Structural defects in MOVPE grown CdTe/GaAs

Ruth Isabel Port

Structural Defects in MOVPE Grown CdTe/GaAs

by

Ruth Isabel Port

This thesis is presented in candidature for the degree of
Doctor of Philosophy

in the
University of Durham

November 1995

Abstract

This work presents a study of the character and distribution of structural defects in (001)CdTe buffer layers grown on GaAs substrates by metal organic vapour phase epitaxy (MOVPE). These are of importance as hybrid substrates for the growth of $Cd_xHg_{(1-x)}Te$ (CMT), a prominent infrared detector material. The 14.6% mismatch between CdTe and GaAs leads to a high density of dislocations at the CdTe/GaAs interface, and threading through the layer. The presence of linear and planar defects is detrimental to the performance of CMT devices and it is desirable to reduce the density of dislocations to below $10^5 cm^{-2}$.

Results of high resolution X-ray diffraction (HRXRD) studies on a series of MOVPE grown CdTe/GaAs epilayers of different thickness and on a single thick layer which was repeatedly etched and remeasured are reported. Threading dislocation density was estimated from HRXRD full width at half maximum (FWHM) using a relationship proposed by Gay, Hirsch and Kelly and was found to decrease rapidly in the initial stages of layer growth. An optimum buffer layer thickness of 8μm is proposed for the subsequent growth of CMT. Rocking curves were recorded from a single thick CdTe/GaAs epilayer for wavelengths in the range 0.69-1.95Å at the Daresbury SRS, and this data is extrapolated to infinite absorption to obtain an estimate of the rocking curve width representative of the surface of a thick layer.

A number of models which attempt to describe the reduction in threading dislocation density with increasing thickness are reviewed and a new model based on the coalescence of like dislocations is developed. The models are compared to published data for layers with misfit in the range 0.23-14.6%. The models previously developed by Tachikawa and Yamaguchi and by Durose and Tatsuoka are shown to be the more appropriate for describing the dislocation density distribution in highly mismatched layers.

Results of the transmission electron microscopy of CdTe/GaAs epilayers, both in plan view and cross-section, showing the character of dislocations threading through thick CdTe buffer layers are presented. Many dipoles composed of 30° type dislocations with Burgers vectors parallel to the interface were observed and found to adopt an orientation whereby the component dislocations had no effect on misfit strain. In cross-section, 30° type dislocations with Burgers vectors inclined to the interface were found to be numerous. 60° and screw type threading dislocations were also observed, but the cross-section projection axis made analysis of these types difficult. The screw and edge components of 30°, 60° and screw type threading dislocations are compared and it is found that the Burgers vector component causing layer tilt is of magnitude $(a_0/2)$ for each type.

Annealing of CdTe/GaAs epilayers under di-methyl cadmium flow was found to have no deleterious effect on layer morphology but did not result in a narrower X-ray rocking curve.

Based upon HRXRD FWHM, 8μm thick CdTe buffer layers grown by MOVPE are estimated to have a dislocation density of about $3x10^8 cm^{-2}$. Even after many of the threading dislocations have been bent over at the CdTe/CMT interface, their density in MOVPE grown CMT/CdTe/GaAs is still greatly in excess of the $10^5 cm^{-2}$ desired. The issues discussed and conclusions drawn in this thesis represent a thorough study of the continuing progress towards high quality MOVPE growth of CMT.

Declaration

I declare that with the exception of those procedures listed below, all the work reported in this thesis was carried out by the candidate. I also declare that none of this work has been previously submitted for any degree and that it is not currently being submitted for any other degree.

Growth of sample layers was carried out by:

Dr Janet E. Hails, D.R.A., Malvern; all CdTe/GaAs epilayers including those annealed, except where indicated in Chapter 3.

Mr John S. Gough, D.R.A., Malvern; CdTe/GaAs epilayers where indicated in Chapter 3.

Mr Andy Graham, D.R.A., Malvern; (CdHg)Te/CdTe/GaAs epilayers.

Dr Sener Oktik, University of Durham; ZnTe/GaAs epilayers.

The assistance of Mr M. J. Soares is acknowledged in obtaining the photoluminescence spectra during the candidate's visit to Aviero.

The etch pit densities reported in Chapter 8 were measured by Mrs A. B. Smith, D.R.A., Malvern.

K Durose
.....

Dr K. Durose
Supervisor

R. Port
.....

R. I. Port
Candidate

ACKNOWLEDGEMENTS

Where shall I start? There are so many people who have made the last three years bearable, and sometimes even enjoyable. I could not have asked anything more of my supervisor, Ken, he was always ready to discuss my work, encouraged me through the second year "I don't have any results" blues and made writing up almost a pleasure. Is this where I am meant to admit to letting that sheep out? But seriously, even without a pot on his leg, Ken was never very difficult to track down. Sincere thanks also to Professor Brian Tanner for explaining so many mysteries to me and to Janet Hails who has tirelessly read this thesis and commented thereupon with copious ink.

There are lots of people in the II-VI group, both past and present, who have helped me over the last three years. I would like to thank them all, in particular Hirokazu Tatsuoka for showing me the TEM ropes and Andy Brinkman for his seemingly endless depth of knowledge. Now for the guys without whom none of this would have been possible: Uncle Norman and David who know the inside of nearly every bit of kit I've ever (tried) to use, and of course Harry, who can make anything except money (or so he says).

Thanks to everyone at the D.R.A. who made my visits so enjoyable, to Janet, Andy, Jean, John, Mike and Dennis in particular, oh and eternal thanks to the person who showed me where to find the key to the milk bottle!

Special thanks to Caroline Moore for the laughs and tears, days and nights spent aligning diffractometers, especially those long nights shut up in a cold tin can, otherwise known as Station 7.6. More than anything else, I want to thank her for her prayers. For the support in prayer of Fiona Smith and Rachel Carrington I am also very grateful. Tamzin Lafford has also been an inspiration and constant reminder of the love of God, a mighty handy contact at Bede Scientific too!

I thank the following bodies for their financial support: the Engineering and Physical Sciences Research Council and the Defence Research Agency.

Finally, my greatest thanks go to my parents for supporting me both financially and psychologically through what must have seemed like a never ending education. Thanks also for educating me in the use of punctuation and grammar, I think I have learnt something useful whilst writing this thesis.

This thesis is dedicated to
Mum and Dad

Man is nothing but:

FAT enough for seven bars of soap,
MAGNESIUM enough for one dose of salts,
IRON enough for one medium-sized nail,
PHOSPHOROUS enough to tip two thousand two hundred matches,
SUGAR enough for seven cups of tea,
POTASH enough to explode one toy crane,
LIME enough to whitewash one chicken coop.

Professor C. E. M. Joad

What is man (O LORD), that you are mindful of him?

Psalm 8 verse 4
The Holy Bible

Contents

CHAPTER 1

Introduction

The theme of this thesis is the study of epitaxial layers grown onto GaAs substrates by metal organic vapour phase epitaxy (MOVPE) for the subsequent growth of $Cd_xHg_{(1-x)}Te$ (CMT). There is considerable interest in the growth of ternary, II-VI, Hg-based semiconductor compounds, in particular CMT, since varying the alloy composition allows the bandgap to be tuned to a broad range of energies. The bandgaps of HgTe and CdTe at room temperature are -0.15eV and 1.44eV respectively[1], enabling solid solutions to be prepared for infrared imaging at both the 3-5μm and 8-14μm atmospheric windows. Details of CMT infrared devices may be found in references 2-6. State-of-the-art device processing requires large area (in excess of $1cm^2$) layers of good structural quality with high standards of compositional, morphological and thickness uniformity.

Device quality epitaxial CMT is commonly grown by liquid phase epitaxy (LPE) onto CdTe or (CdZn)Te (CZT) substrates[7]. Some advantages of using these substrates are: i) the small mismatch, for example, 0.22% for CdTe and 0.015% for $Cd_{0.96}Zn_{0.04}Te$ with $Cd_{0.3}Hg_{0.7}Te$; ii) the similar thermal expansion coefficients of CdTe and HgTe (as shown in table 1.1); and iii) the use of CdTe avoids the introduction of foreign impurity atoms. Unfortunately, both CdTe and CZT substrates contain significant densities of grain boundaries, twins, dislocations and precipitates[7], and are both small in area and relatively expensive.

The lack of cheap II-VI substrates of sufficient quantity and quality has led to the use of alternative substrates, most notably GaAs and InSb. Schmit[8] undertook a study of 24 possible substrates for the growth of CMT and has suggested that InP and GaAs may be the best foreign substrates. Schmit's study did not include InSb, since, to allow for back illuminated devices, only materials transparent over the 3-12μm spectral range were considered. Nevertheless, InSb has the advantages of having a small misfit with CMT (0.19% with $Cd_{0.3}Hg_{0.7}Te$) and a similar thermal expansion coefficient to HgTe and CdTe (table 1.1). However, InSb is thermally unstable at temperatures above the congruent evaporation temperature of 280°C[9].

Material	Lattice parameter / Å	α / $10^{-6}°C^{-1}$	Temperature for which α is quoted / K	Reference for α value
CdTe	6.481	4.70	283	10
HgTe	6.461	4.75	283	10
InSb	6.479	5.04	300	11
GaAs	5.654	6.86	300	12

Table 1.1 Comparison of lattice parameters and linear thermal expansion coefficients, α, of the materials discussed in the text. All lattice parameter values are taken from the ASTM index[13].

GaAs is an attractive substrate for several reasons: i) high quality substrates of large area are available relatively cheaply from commercial sources; ii) GaAs is transparent in the 3-12 μm region[8]; and iii) GaAs/Si wafers are commercially available, offering the possibility of integration of CMT with advanced Si devices, when layer quality allows[14]. Unfortunately, GaAs substrates have several disadvantages, most notably the very large misfit with CMT (14.4% with $Cd_{0.3}Hg_{0.7}Te$) and the much larger thermal expansion coefficient compared with CdTe and HgTe (table 1.1). Also, the out-diffusion of Ga and As from the substrate into the layer[9,15,16] affects the electronic properties of CMT, since Ga and As are electrically active.

CdTe buffer layers are frequently grown onto GaAs substrates prior to the growth of CMT[17], and this serves to reduce the concentration of Ga and As atoms diffusing into the CMT layer. Giess et al.[9] have shown that an 8μm thick CdTe layer is required to reduce the Ga concentration in the active CMT layer to an acceptable level (< 0.01ppm). The large lattice mismatch between CdTe and GaAs gives rise to a dense tangle of dislocations at the interface, with many being forced out of the interfacial plane and into the epilayer to form threading dislocations[18]. These can propagate into the active regions in the CMT and degrade device characteristics[19]. The persistent problem of hillocks on (001) CMT/CdTe/GaAs[14] grown by MOVPE has recently been

addressed by Giess et al.[20], who employed a Na containing final substrate rinse, prior to layer growth.

The aim of the present study has been to investigate the threading dislocations reaching the surface of thick CdTe buffer layers grown on (001)GaAs. From this, it was hoped that an optimum buffer thickness could be determined and methods of threading dislocation density reduction proposed and implemented. A literature study of the generation of dislocations at the interface between mismatched epilayers is presented in Chapter 2. The generally accepted mechanisms for the formation of misfit dislocations, by glide of pre-existing threading dislocations[21] and half-loop nucleation[22,23], are not applicable to layers which display three-dimensional growth or which have a 'critical thickness' of less than a monolayer. The effects of different growth modes on the introduction of misfit dislocations, and mechanisms by which misfit and threading dislocations are introduced into high misfit layers are discussed. All the layers investigated in this thesis were grown by MOVPE, using the growth conditions given in Chapter 3. Examples of the growth defects and inhomogeneities which are observed routinely in MOVPE grown layers are also presented.

It is well reported[24-28] that threading dislocation density in an epilayer decreases with thickness after the maximum number of misfit dislocations have been formed. A number of models have previously been proposed[29-35] to describe this reduction in threading dislocation density and the accompanying reduction in layer strain. Several of these models are reviewed and critically compared in Chapter 5. Three of these models are applied to the specific cases of CdTe/GaAs and ZnTe/GaAs in Chapter 6, where a detailed study of the changes in CdTe/GaAs structural quality with layer thickness is also presented.

The types of dislocation reaching the surface of a thick CdTe buffer layer determine the rate of relaxation of residual strain in thick layers[33]. A study of threading dislocations in thick CdTe buffer layers is presented in Chapter 7 and the findings are related to the earlier calculations and assumptions made in Chapters 5 and 6.

In addition to studying threading dislocations in thick CdTe buffer layers, attempts have been made to reduce the dislocation density for a given

thickness of CdTe buffer, by annealing of CdTe/GaAs layers. The outcome of these annealing studies is reported in Section 8.1.

The findings of Chapters 5 and 6 are brought together in Section 8.2, where the structural quality of two CMT layers grown on CdTe buffer layers of different thicknesses are compared.

REFERENCES FOR CHAPTER 1

1. *Handbook of Physics and Chemistry*, CRC Press, 69th edition, 1988.

2. Bailey R. B., Kozlowski L. J., Chen J., Bui D. Q., Vural K., Edwall D. D., Gil R. V., Vanderwyck A. B., Gertner E. R. and Gubala M. B., *IEEE Transactions on Electron Devices* **38(5)**, (1991), 1104.

3. Blackburn A., Blackman M. V., Charlton D. E., Dunn W. A. E., Jenner M. D., Oliver K. J. and Wotherspoon J. T. M., *Infrared Physics* **22**, (1982), 57.

4. Elliott C. T., *Proc. Jap. Soc. of Infrared Sci. Technol.* 1, (1991), 1.

5. Lanir M. and Riley K. J., *IEEE Transactions on Electron Devices* **29(2)**, (1982), 274.

6. Rode J. P., *Infrared Physics* **24(5)**, (1984), 443.

7. Watson C. C. R., Ph. D Thesis, *Structural Defects in CdTe and Related Materials*, University of Durham (1993).

8. Schmit J. L., *J. Vac. Sci. Technol. A* **4(4)**, (1986), 2141.

9. Giess J., Gough J. S., Irvine S. J. C., Blackmore G. W., Mullin J. B. and Royle A., *J. Cryst. Growth* **72**, (1985), 120.

10. Rolland S., in *Properties of Narrow Gap Cadmium-based Compounds*, Capper P, Ed. (INSPEC, London, 1994), EMIS Datareviews Series No.10, Section A2.3.

11. Madelung O., Schulz M. and Weiss H., Eds., *Technology of III-V, II-VI and non-Tetrahedrally Bonded Compounds*, Landolt-Börnstein Numerical Data and Functional Relationships in Science and Technology, New Series, **volume 17d**, (Springer-Verlag, Berlin, 1984).

12. Sze S. M., *Physics of Semiconductor Devices*, (2nd edition), Wiley, 1981, pp. 850.

13. ASTM Powder Diffraction File.

14. Triboulet R., Tromson-Carli A., Patriarche G., Lorans D. and Nguyen Duy T., *Adv. Mat. for Optics and Elec.* 3, (1994), 239.

15. Giess J., Gough J. S., Irvine S. J. C., Mullin J. B. and Blackmore G. W., *Mat. Res. Soc. Symp. Proc.* **90**, (1987), 389.

16. Blackmore G. W., Jones E. D., Mullin J. B. and Stewart N. M., *Mat. Sci. Eng.* **B16**, (1993), 186.

17. Irvine S. J. C., Gough J. S., Giess J., Gibbs M. J., Royle A., Taylor C. A., Brown G. T., Keir A. M. and Mullin J. B., *J. Vac. Sci. Technol. A* **7(2)**, (1989), 285.

18. Cullis A. G., Chew G., Irvine S. J. C. and Giess J., *Inst. Phys. Conf. Ser.* **87**, Section 2, (1987), 141.

19. Yamamoto T., Miyamoto Y. and Tanikawa K., *J. Cryst. Growth* **72**, (1985), 270.

20. Giess J., Hails J. E., Graham A., Blackmore G., Houlton M. R., Newey J., Young M. L., Astles M. G., Bell W. and Cole-Hamilton D. J., *J. Elec. Mat.* **24(9)**, (1995), in press.

21. Matthews J. W. and Blakeslee A. E., *J. Cryst. Growth* **27**, (1974), 118.

22. People R. and Bean J. C., *Appl. Phys. Lett.* **47(3)**, (1985), 322.

23. People R. and Bean J. C., *Appl. Phys. Lett.* **49(4)**, (1986), 229.

24. Ayers J. E., Schowalter L. J. and Ghandhi S. K., *J. Cryst. Growth* **125**, (1992), 329.

25. Bernardi S., Bocchi C., Ferrari C., Franzosi P. and Lazzarini L., *J. Cryst. Growth* **113**, (1991), 53.

26. Shtrikman H., Raizman A., Oron M. and Eger D., *J. Cryst. Growth* **88**, (1988), 522.

27. Takigawa H., Yoshikawa M. and Maekawa T., *J. Cryst. Growth* **86**, (1988), 446.

28. Yoshikawa M., *J. Appl. Phys.* **63(5)**, (1988), 1533.

29. Dunstan D. J., Young S. and Dixon R. H., *J. Appl. Phys.* **70(6)**, (1991), 3038.

30. Tatsuoka H., Kuwabara H., Nakanishi Y. and Fujiyasu H., *Thin Solid Films* **201**, (1991), 59.

31. Tatsuoka H., Kuwabara H., Nakanishi Y. and Fujiyasu H., *J. Cryst. Growth* **117**, (1992), 554.

32. Ayers J. E., Schowalter L. J. and Ghandhi S. K., *Mat. Res. Soc. Symp. Proc.* **209**, (1991), 661.

33. Durose K. and Tatsuoka H., *Inst. Phys. Conf. Ser.* **134**, Section 9, (1993), 581.

34. Kroemer H., Liu T. Y. and Petroff P. M., *J. Cryst. Growth* **95**, (1989), 96.

35. Tachikawa M. and Yamaguchi M., *Appl. Phys. Lett.* **56(5)**, (1990), 484.

CHAPTER 2

Dislocations in Heteroepitaxial Layers

2.1 Introduction

In this chapter, the concepts fundamental to heteroepitaxial growth, such as critical thickness and misfit dislocation formation, are introduced. Strain relaxation by the introduction of dislocations proceeds differently in high and low misfit systems, this will be discussed together with mechanisms for the formation of threading dislocations. In Section 2.4.2, the methods currently employed to reduce threading dislocation density are reviewed for the case of GaAs/Si which has a misfit of -4.1% (layer in compression). Much less has been published on the reduction of threading dislocations in high misfit II-VI epilayers such as CdTe/GaAs (misfit of -14.6%), however, a brief review is given in Section 2.4.3. The consequences of the anisotropy of the sphalerite lattice and the different types of dislocation which can occur are discussed in Section 2.5.

Consider an epitaxial layer with lattice parameter a_e grown upon an infinitely thick substrate with lattice parameter a_s, where the misfit, f between the substrate and layer is defined by equation 2.1. The convention used in this thesis is to refer to the magnitude of misfit only.

$$f = \frac{a_s - a_e}{a_s} \qquad \text{equation 2.1}$$

If the layer is thin, then it is possible to accommodate the difference in lattice parameter by a biaxial stress in the interfacial plane. The lattice parameter of the epilayer will become equal to that of the substrate parallel to the interfacial plane. The epilayer will also distort along the direction normal to the interface giving a tetragonal distortion as illustrated in figure 2.1a. There are no misfit dislocations in this regime known as pseudomorphic growth. This geometry has a high elastic strain energy since the bond lengths in the epilayer are distorted from their equilibrium values.

At some epilayer thickness known as the critical thickness, h_C, it becomes energetically favourable to reduce this elastic strain energy by the introduction of misfit dislocations, as illustrated in figure 2.1b. Theoretical models for the introduction of misfit dislocations by threading dislocation glide and half-loop nucleation are presented in Section 2.2.1.

The concepts of pseudomorphic growth and critical thickness are not valid for systems with large lattice mismatches, since the two lattices are incoherent at all stages of growth. Different mechanisms for the generation of misfit dislocations may operate in high and low misfit systems. Misfit dislocation generation in high and low misfit systems is reviewed in Sections 2.3 and 2.2 respectively.

2.2 Dislocations and Strain Relaxation in Low Misfit Heteroepitaxial Layers

2.2.1 Theoretical Models for Critical Thickness

The existence of a critical thickness was first considered by Frank and van der Merwe[1], who attempted to model the critical thickness by minimising the energy of a misfit dislocation array at the interface. Since this pioneering work, many models for the generation of misfit dislocations have been proposed. This section gives a brief review of the fundamental aspects of misfit strain relief; more extensive reviews can be found in references 2-4.

Matthews and Blakeslee[5] considered the behaviour of pre-existing threading dislocations under the action of misfit strain. The model relies on the substrate having dislocations which intersect the free surface so that the threading dislocations are replicated in the initially coherent epilayer. The generation of a misfit dislocation segment is illustrated in figure 2.2.

A pre-existing threading dislocation experiences a force F_a due to the lattice mismatch strain. If this force is sufficiently high, the threading dislocation will propagate through the epitaxial layer generating a length of misfit

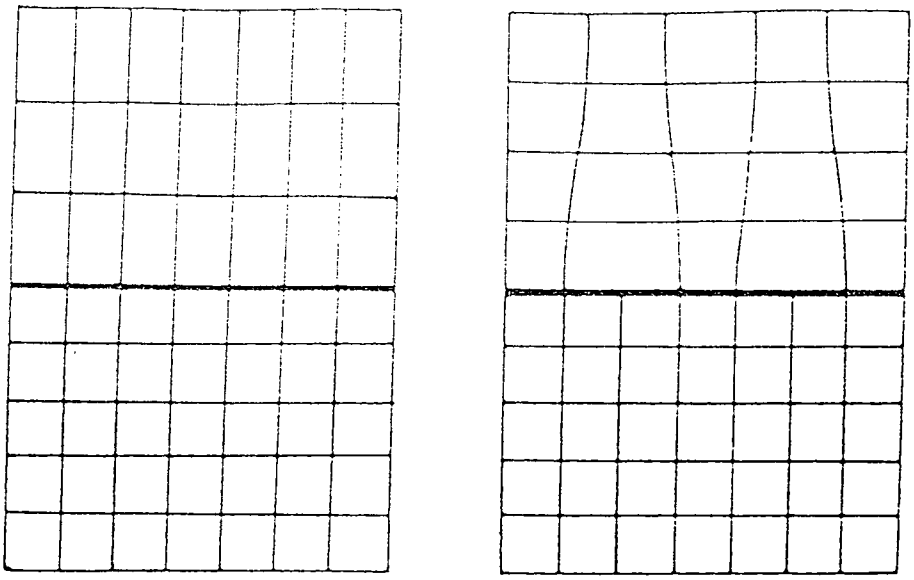

Figure 2.1 Schematic illustration of (a) coherently strained, pseudomorphic lattice mismatched heteroepitaxy and (b) relaxed lattice mismatched heteroepitaxy.

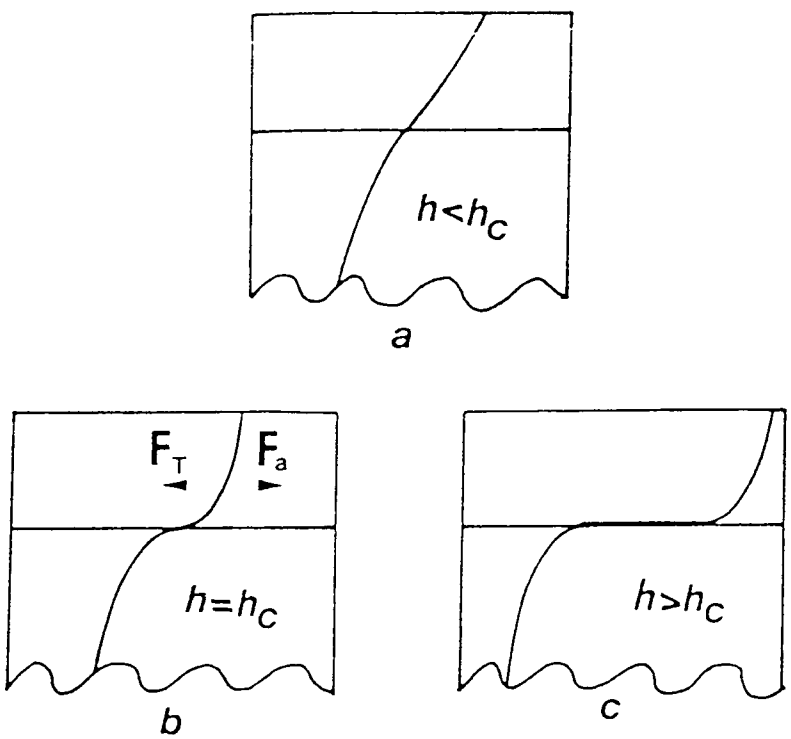

Figure 2.2 Schematic illustration of the Matthews and Blakeslee model of critical thickness. Diagram from Hull and Bean[2].

dislocation at the interface. The misfit dislocation has a self energy[6] which produces a restoring force, F_t upon the propagating dislocation. If $F_a > F_t$ then the threading dislocation will propagate and a misfit segment will be generated, as shown in figure 2.2c. Matthews and Blakeslee[5] defined critical thickness as the thickness at which $F_a = F_t$, figure 2.2b. A full mathematical treatment can be found in references 2-4 which leads to the expression for critical thickness, h_c, given in equation 2.2, where b is the magnitude of the Burgers vector **b**, ν is Poisson's ratio, θ is the angle between **b** and the dislocation line direction ℓ, λ is the angle between **b** and the normal to ℓ and α is a factor intended to account for the dislocation core energy.

$$h_c = \frac{b(1-\nu\cos^2\theta)}{8\pi(1+\nu)\, f\cos\lambda} \ln\left|\frac{\alpha h_c}{b}\right| \qquad \text{equation 2.2}$$

For semiconductor films of the diamond and sphalerite structures, experimental observations such as those described in reference 7 reveal much larger values for the critical thickness than predicted by the Matthews and Blakeslee[5] model. People and Bean[8,9] have calculated h_c for $Ge_xSi_{(1-x)}/Si$ epilayers assuming that misfit dislocation generation is determined solely by energy balance. This gives a better agreement to experimental data than the mechanical equilibrium model of Matthews and Blakeslee.

There are two main reasons for the discrepancy between equilibrium theory and experimental findings for semiconductors. First, the large Peierls-Nabarro frictional stress[6,10] reduces the mobility of dislocations and hence reduces the length of misfit segments that can be formed along the interface. Fox and Jesser[11], invoked a static Peierls stress as an additional restoring force upon threading dislocations in the Matthews and Blakeslee model, thereby increasing the critical thickness predicted. Secondly, semiconductor substrates such as silicon can be produced with very low dislocation densities; homogeneous nucleation of misfit dislocations in addition to glide of pre-existing ones or heterogeneous nucleation, at precipitates or surface defects, may occur for such substrates.

One mechanism for the homogeneous nucleation of misfit dislocations is that of the nucleation of surface half-loops, which is represented schematically in figure 2.3. A growing dislocation-loop of appropriate Burgers vector relaxes the strain energy within the epilayer, E_{strain}. Balancing this is the self energy of the loop, E_{loop}. Other energy terms which should be considered are the energies of steps removed or created in the nucleation process, E_{step}, and the energy of any stacking faults created E_{sf}. The total energy is given by equation 2.3. Note that E_{step} and E_{sf} can be positive or negative depending on their effect relative to the misfit strain.

$$E_{total} = E_{loop} - E_{strain} \pm E_{step} \pm E_{sf} \qquad \text{equation 2.3}$$

The total energy of the loop will pass through an energy maximum at a critical radius which is closely analogous to critical thickness and can be thought of as the activation energy to half-loop formation. This activation energy is large and requires a high misfit strain to activate the process. Heterogeneous nucleation at surface steps or surface imperfections will occur at lower misfit (and for thinner layers), since this process has a lower activation energy[12]. Mathematical treatments of half-loop formation from several different approaches can be found, for example, in references 2,8,9,12-16.

2.2.2 Misfit Dislocations

The dislocations discussed in this thesis are of two types, misfit and threading dislocations, both of which can relieve misfit strain. Misfit dislocations lie parallel to the substrate/layer interface while threading dislocations are inclined to it. From figures 2.2 and 2.3 it is clear that a single dislocation may have both misfit and threading segments. This section deals with those misfit dislocations which are commonly found in (001) oriented heteroepitaxial layers; threading dislocations are discussed further in Chapter 7.

Misfit dislocations are mostly of two types, 90° dislocations (also called Lomer type or edge type) and 60° dislocations. In (001) layers, 60° dislocations have

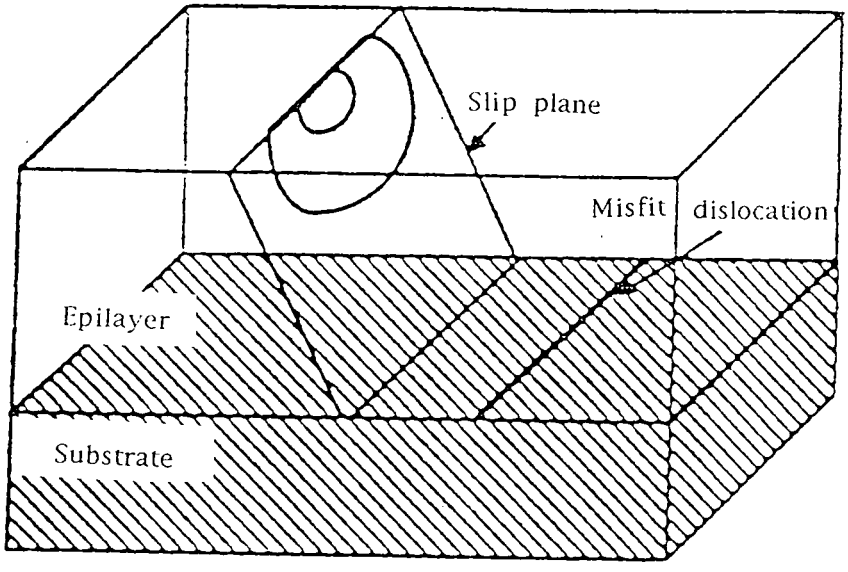

Figure 2.3 Schematic illustration of the generation of a dislocation half-loop in a (001) oriented heterostructure.

<110> line directions in the plane of the interface and <110> Burgers vectors inclined to the interface. They glide on {111} planes and may be formed by glide of threading dislocations or by half-loop nucleation. The Burgers vector of a 60° dislocation can be resolved into three components:(i) a screw component in the interface plane, which has a rotation effect between the substrate and layer ($b_{s\text{-rotate}}$), (ii) an edge component in the interface, which relieves misfit strain ($b_{e\text{-misfit}}$), and (iii) an edge component perpendicular to the interface, which tilts the layer with respect to the substrate ($b_{e\text{-tilt}}$). The resolution of the Burgers vector into these three components is shown in figure 2.4. and their effects are demonstrated in figure 7.15, while the magnitude of the components are compared to those for some threading dislocation orientations in table 7.7. The magnitude of the misfit relieving component of the Burgers vector, $b_{e\text{-misfit}}$ is $(a_o/2\sqrt{2})$.

In (001) layers, 90° dislocations have both their line direction and Burgers vector in the interface plane, both in <110> directions. The whole Burgers vector $(a_o/\sqrt{2})$ relieves misfit strain and this is the most efficient misfit relieving dislocation with a <110> Burgers vector. However, since the (001) plane is not a primary slip plane, these dislocations are sessile, although they may climb in the presence of point defects. 90° misfit dislocations are unlikely to be formed by glide of existing threading dislocations and cannot form by half-loop nucleation at the layer surface.

Nevertheless, it has been proposed by several workers (see for example references 16-18) that 90° misfit dislocations may be formed by the coalescence of two 60° dislocations, and that this process is favourable since twice the misfit strain of a 60° dislocation is relieved. Another mechanism for the generation of 90° dislocations has been proposed by Dregia and Hirth[19] which involves the nucleation of a dislocation at the free surface, glide to the interface where a reaction occurs forming a 90° dislocation and another dislocation, the latter then glides back to the surface leaving a 90° Lomer dislocation in the interface. An alternative nucleation mechanism for 90° misfit dislocations in high misfit systems which display three-dimensional (3-D) growth is presented in Section 2.3.

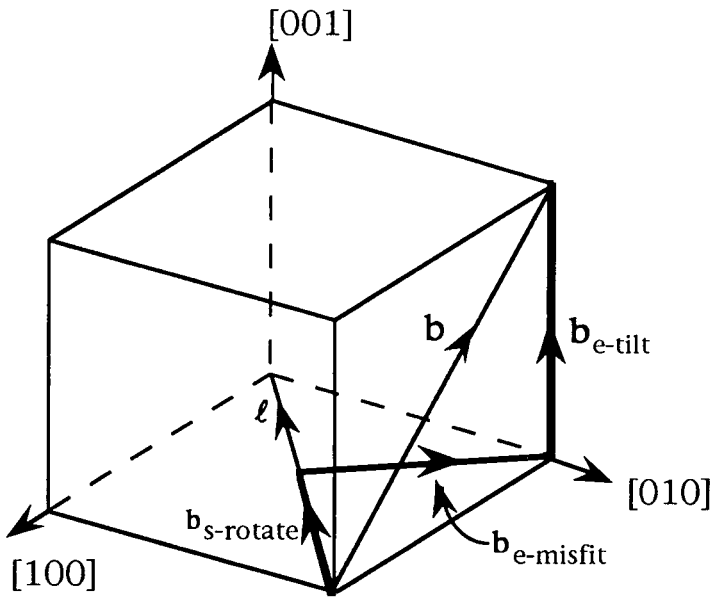

Figure 2.4 Burgers vector components of a 60° type misfit dislocation. The Burgers vector can be resolved into three components, $b_{s\text{-}rotate}$, $b_{e\text{-}tilt}$ and $b_{e\text{-}misfit}$ which produce layer rotation, tilt and misfit relief respectively. Figure 7.15 demonstrates the effect of each component on the layer. The component magnitudes are compared to those for threading dislocations in table 7.7.

2.3 Dislocations and Strain Relaxation in High Misfit Heteroepitaxial Layers

2.3.1 Introduction

The two nucleation mechanisms presented in Section 2.2.1 assumed that growth proceeded by two-dimensional (2-D) layer-by-layer growth and that a critical thickness could be defined at which it became favourable to form misfit dislocations. There are two other modes by which growth can proceed, Stranski-Krastanov and Volmer-Weber. These are both 3-D growth modes and are common for high misfit systems. They are described in Section 2.3.2, and the mechanisms by which misfit dislocations can be formed during 3-D growth are described in Section 2.3.3.

2.3.2 Mechanisms of Epitaxial Growth

Layer-by-layer 2-D growth, Volmer-Weber 3-D growth and Stranski-Krastanov 3-D growth are illustrated in figure 2.5. Layer-by-layer growth proceeds via step-flow and leads to material of high structural quality. Volmer-Weber growth proceeds by the formation of small islands directly on the substrate. Stranski-Krastinov growth occurs when islands are formed on top of a thin uniform layer of deposit. The transition from 2-D to 3-D growth has been studied for $In_xGa_{(1-x)}As/GaAs$[20-24], InAs/GaAs[17] and ZnSe/GaAs[25]. Some of these authors reported that a change in defect structure, most notably an increase in threading dislocation density, accompanies the transition from 2-D to 3-D growth. The generation of misfit dislocations during 3-D island growth and the reason for the increased threading dislocation density will be discussed in the following section.

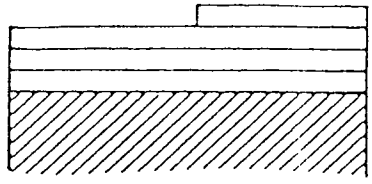

a

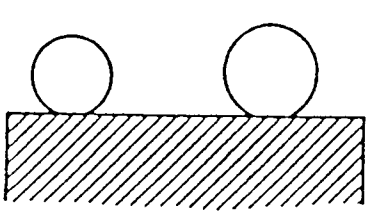

b

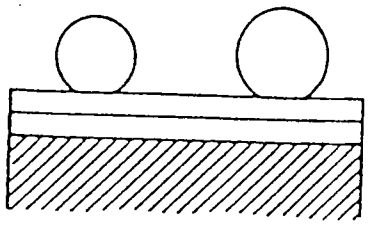

c

Figure 2.5 Schematic illustration of growth modes: (a) layer-by-layer two-dimensional growth; (b) Volmer-Weber three-dimensional growth; (c) Stranski-Krastanov three-dimensional growth.

2.3.3 Misfit Dislocations in High Misfit Systems

The concept of critical thickness is not valid for layers which display 3-D growth since the generation of misfit dislocations often occurs before the islands have coalesced to form a 2-D layer[17,25-29].

As with low misfit layers, 90° and 60° misfit dislocations are the most common in high misfit (001) oriented layers. Studies carried out on GaAs/Si[30,31], CdTe/GaAs[31] and ZnTe/GaAs[32] all found 90° dislocations to be more numerous than 60° dislocations, in contrast to layers which grow by 2-D mode where 60° types dominate. Since 60° dislocations cannot glide in the (001) plane, the chance of two 60° dislocations meeting to form a 90° dislocation cannot account for the high density of 90° misfit dislocations. Many workers have suggested that 90° misfit dislocations are formed at the edges of islands during growth, and indeed this has been observed by high resolution transmission electron microscopy (HRTEM or HREM) for $In_xGa_{(1-x)}As/GaAs$[26] (3-D growth for $x > 0.25$-0.30).

The formation of 90° dislocations at the edge of a growing island can best be imagined best by using the coincidence site lattice (CSL) model described by Matthews[4]. At a coincidence boundary a fraction of the lattice sites in one crystal coincide with a fraction of the lattice sites in the other. It has been shown that coincidence site boundaries are of lower energy than boundaries where the lattice sites do not coincide[33]. The coincidence condition is met when the lattice parameters of the substrate and layer have the relationship given in equation 2.4, where n and m are integers. When n and m are not integral values then the misfit, f between the layer and substrate can be rewritten as equation 2.5.

$$\frac{n}{m} = \frac{a_{epilayer}}{a_{substrate}} \qquad \text{equation 2.4}$$

$$f = \frac{na_{substrate} - ma_{epilayer}}{na_{substrate}} \qquad \text{equation 2.5}$$

As an island grows, its strain increases. As a coincidence condition approaches, it becomes energetically more favourable to assume the coincidence arrangement, thus forming an edge type dislocation, than to strain the island further. This mechanism has been proposed by Kiely et al.[34] for InSb layers on (001)GaAs. A clear diagram from their work is reproduced in figure 2.6 showing how 90° dislocations can form at the edge of a strained island.

When islands coalesce, if the dislocation lines in the two islands do not line up exactly, threading dislocations are likely to be formed by misfit segments being forced away from the interface and into the layer. The generation of threading dislocations at island boundaries has been observed for (InGa)As/GaAs by HRTEM[35]. Since 90° dislocations dominate at the interface, this mechanism would lead to threading dislocations with Burgers vectors parallel to the interface. Such dislocations are not observed in great numbers away from the interface, although they may exist near it in dislocation tangles which cannot be resolved. Threading dislocations with <110> Burgers vectors inclined to the interface are commonly seen and can be generated in large numbers by the half-loop mechanism described in Section 2.2.1. n and m in equation 2.4 are unlikely to be integral values and some residual misfit strain which is not accommodated during the early stages of island growth is probable. After the islands have coalesced, growth proceeds in a 2-D mode and half-loops can be nucleated and glide to the interface to relieve this residual strain. In this way threading dislocations with Burgers vectors inclined to the interface can be generated.

2.4 Threading Dislocation Density Reduction

2.4.1 Introduction

The presence of dislocations in $Cd_XHg_{(1-X)}Te$ (CMT) can affect the overall performance of photovoltaic infra-red focal plane arrays. Shin et al.[36] have reported that the minority carrier lifetime of MBE grown CMT is inversely proportional to dislocation density to the two-third power for

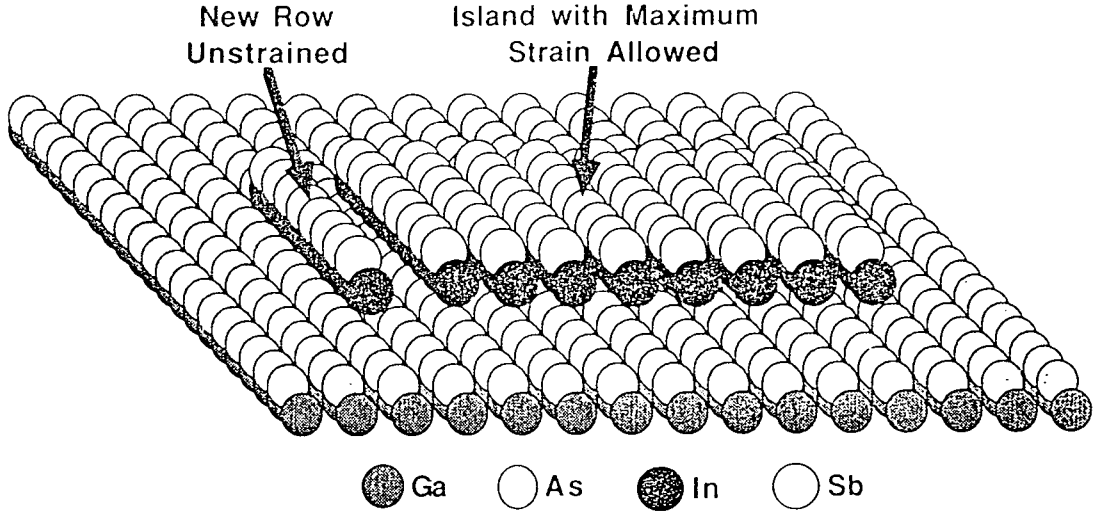

Figure 2.6 Schematic diagram illustrating the formation of an edge type (90°) dislocation at an island edge. Diagram from Kiely et al.[34].

densities greater than $5x10^5cm^{-2}$. Below this density, the minority carrier lifetime was reported to be unaffected by dislocation density. Minority carrier lifetime in the region close to an anodic oxide/CMT interface[37] has been found to be inversely proportional to dislocation densities above $5x10^5cm^{-2}$ and unaffected by densities below $2x10^5cm^{-2}$. It is therefore desirable to decrease dislocation densities in CMT layers to below about 10^5cm^{-2}. In addition, dark current[38,39] has been shown to increase with increasing dislocation density. Dislocations and grain boundaries are electrically active[40], can act as recombination centres[41] and have been found to provide the predominant transport path for diffusion of interstitials and vacancies[42]. The latter observation is of concern for growth on foreign substrates where diffusion of substrate species can result in unintentional doping.

Several workers have shown that misfit strain can be used to force threading dislocations to the edge of a wafer and hence out of the growing layer[43-46], as shown in figure 2.7. This concept has been extended to growth on reduced area substrates and mesas, where the smaller dimensions increase the number of dislocations which reach the edges of the substrate. These methods of threading dislocation reduction are not so useful for high misfit layers since: firstly, misfit dislocations are not usually generated by this mechanism; and secondly, the high density of defects at the interface leads to dislocation tangles which prevent dislocations from gliding great distances.

GaAs/Si is a relatively well studied high misfit (f=4.1%) heteroepitaxial system and a number of different methods, reviewed in Section 2.4.2, are used routinely for the reduction of threading dislocation density. CdTe/GaAs (f=14.6%) has not been so well studied, but some work has been published on the successful reduction in threading dislocation density and is reviewed in Section 2.4.3.

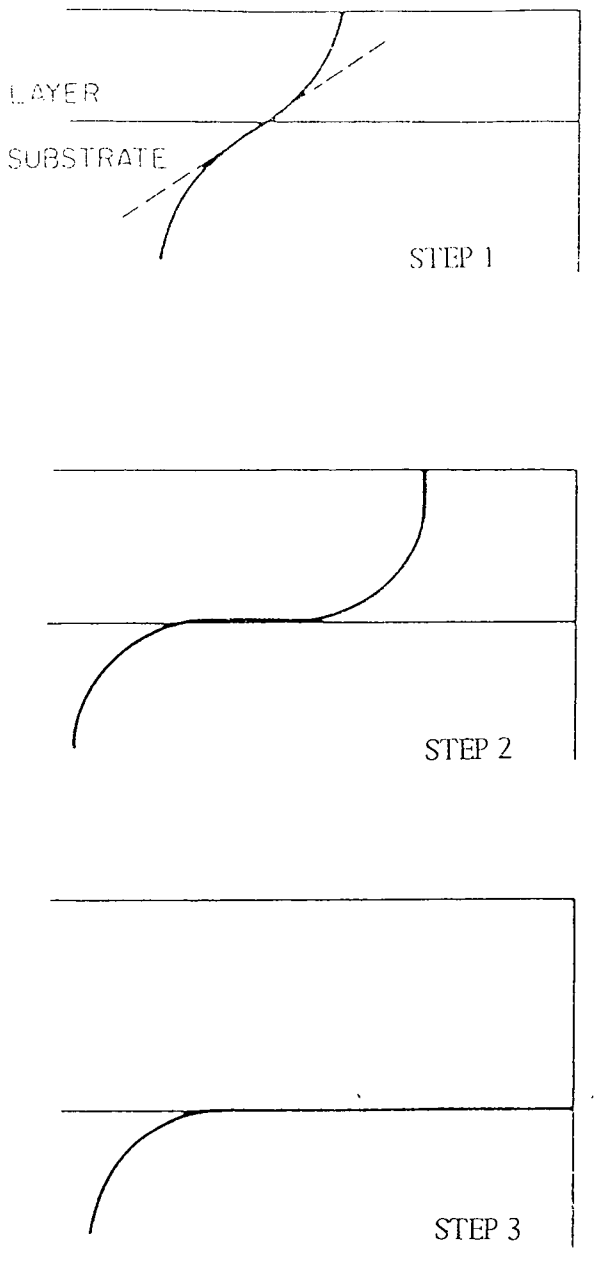

Figure 2.7 Schematic illustration of the removal of a threading dislocation from an epitaxial layer under the influence of misfit strain. This is very similar to the mechanism for the generation of misfit dislocations proposed by Matthews and Blakeslee[5], compare to figure 2.2.

2.4.2 Threading Dislocation Density Reduction in GaAs/Si

Substrate misorientation has been shown to be effective in reducing the threading dislocation density in GaAs/Si epilayers[47]. The mechanism is thought to be due to the nucleation of edge type dislocations at steps which occur on an offcut wafer surface. Fisher and co-workers[47] demonstrated that substrate offcut can be engineered to enhance the formation of 90° dislocations over 60° dislocations. Remembering that 90° dislocations are twice as effective as 60° dislocations at relieving misfit strain and that the formation of 60° misfit dislocations requires the formation of one or two threading dislocations, it is desirable to accommodate misfit strain by 90° rather than by 60° dislocations. The 4.1% misfit of GaAs/Si requires a 90° dislocation every 25 atomic planes. A substrate which is offcut such that there is an atomic step every 25 atomic planes will enhance the formation of 90° misfit dislocations and will increase the probability that dislocations in coalescing islands join up without the formation of threading dislocations. (001) substrates are commonly offcut towards <110> or <100>. An offcut towards a <110> direction will give a staircase of steps in one direction as shown in figure 2.8b. An offcut towards a <100> direction will give staircases in the two orthogonal <110> directions, as shown in figure 2.8c. Fisher et al.[47] have demonstrated the effectiveness of substrate offcut in reducing threading dislocation density. They found that nominally exact oriented substrates gave the poorest epilayers, offcut towards <110> gave better quality layers but that offcut towards <100> gave the best layers.

Strained layer superlattices (SLSs) can interact with threading dislocations and bend them over to accommodate strain[48]. Dislocations can be made to react with each other, resulting in fewer dislocations, or to glide to the edge of the wafer[48] as in figure 2.7. It is important that the individual layers making up the SLS do not exceed the critical thickness for misfit dislocation nucleation and that the final layer of the SLS is lattice matched to GaAs. Examples of the use of SLSs as buffer layers for GaAs/Si can be found in references 49-52. Single interlayers and buffer layers have also been shown to reduce threading dislocation density[53,54].

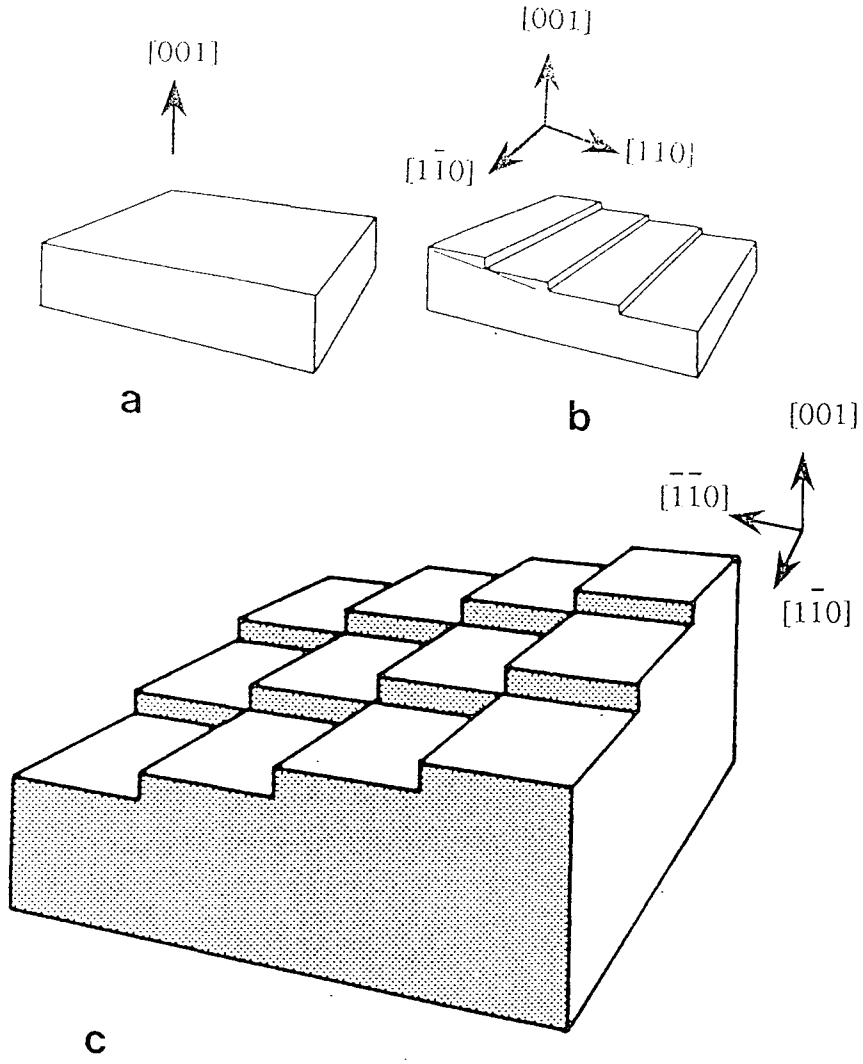

Figure 2.8 Schematic illustration of the effect of offcut on the substrate surface: (a) nominally exact (001) surface; (b) (001) tilted towards <110>; (c) (001) tilted towards <100>. Diagram from Fang et al.[48].

Annealing of GaAs/Si leads to a rearrangement of dislocations and a reduction in threading dislocation density. Annealing aids the conversion of two 60° dislocations into a 90° dislocation and can drastically improve the quality of GaAs grown on Si. A review of the annealing of GaAs/Si is given in Chapter 8.

2.4.3 Threading Dislocation Density Reduction in CdTe/GaAs

In Section 2.4.2, it was explained how an offcut of the substrate towards <100> led to a reduction in threading dislocation density. For CdTe/GaAs with a misfit of 14.6%, a 90° misfit dislocation is required every 8 atomic planes, requiring an offcut of 5.1°. The CdTe and $Cd_xHg_{(1-x)}Te$ epilayers investigated in this thesis were grown on (001) GaAs substrates offcut towards [$\bar{1}$00] about [010] by 3.5° or 2° (Section 3.4.1). Offcut towards [$\bar{1}$00] gives steps in both the [110] and [$\bar{1}\bar{1}$0] directions.

(CdZn)Te/CdTe[55], (HgZn)Te/CdTe[56] and ZnTe/CdTe[57-59] strained layer superlattices have been shown to decrease the threading dislocation density in CdTe buffer layers grown on GaAs substrates. The effectiveness of several SLSs in reducing dislocation density is compared in table 2.1. Petruzzello et al.[56] have calculated the maximum number of threading dislocations per unit area which can be removed from an epilayer by being bent over to form misfit dislocations by a SLS. They assume that the number which can be removed is dependent on the average spacing of dislocations required to relieve the misfit between the CdTe buffer layer and the SLS. Their findings agree well with their experimental observations.

For CMT, more concern has been placed on compositional uniformity and the hillock density[60], with less priority being given to the threading dislocation density of the layers. Indeed, growth of (CdHg)Te by the interdiffused multilayer process[61] (IMP) gives layers of good compositional uniformity but with a higher threading dislocation density[62,63]. This increased density has been traded off with uniformity owing to the need for highly uniform layers for device fabrication.

SLS structure	CdTe/(CdZn)Te*	CdTe/(HgZn)Te@	CdTe/ZnTe#
Reference	Sugiyama[55]	Petruzzello[56]	Sugiyama[59]
Dislocation density without SLS / cm^{-2}	$2x10^8$	$2x10^9$	not given
Dislocation density with SLS / cm^{-2}	$8.2x10^7$	$2x10^8$	not given
Fractional reduction in dislocation density	2.4	10	2
Buffer layer structure	GaAs/CdTe/SLS/ CdTe/SLS/CdTe	GaAs/CdTe/SLS	GaAs/CdTe/SLS /CdTe

Table 2.1 Comparison of the effectiveness of SLSs in reducing the dislocation density in CdTe buffer layers grown on GaAs. Fractional reduction is the ratio of dislocation density without and with SLSs.

* Two SLSs i) 5x(120nmCdTe, 120nm$Cd_{0.97}Zn_{0.03}Te$)
ii) 8x(30nmCdTe, 210nm$Cd_{0.97}Zn_{0.03}Te$)

@ One SLS 200x(80Å$Hg_{0.95}Zn_{0.05}Te$, 20ÅCdTe)

One SLS 5x(500ÅCdTe, 10ÅZnTe)

2.5 Anisotropy in the Sphalerite Lattice

The sphalerite (or zincblende) lattice, consists of two inter-penetrating face centred cubic (f.c.c.) lattices, one of metal atoms and the other of non-metal atoms. The stacking sequence of {111} planes may be represented with Roman (metal) and Greek (non metal) letters. With this notation, the stacking sequence of {111} planes in the sphalerite lattice is AαBβCγAα....., where α,β and γ are located vertically above A, B and C, as shown in figure 2.9. From figure 2.9 it can be seen that {111} planes may be composed of all metal or all non-metal atoms. The convention used throughout this thesis is that {111} planes bounded by metal (e.g. Cd) atoms are referred to as {111}A planes and those bounded by non-metal (e.g. Te) atoms are referred to as $\{\bar{1}\bar{1}\bar{1}\}$B planes. Any two orthogonal <110> directions also display an

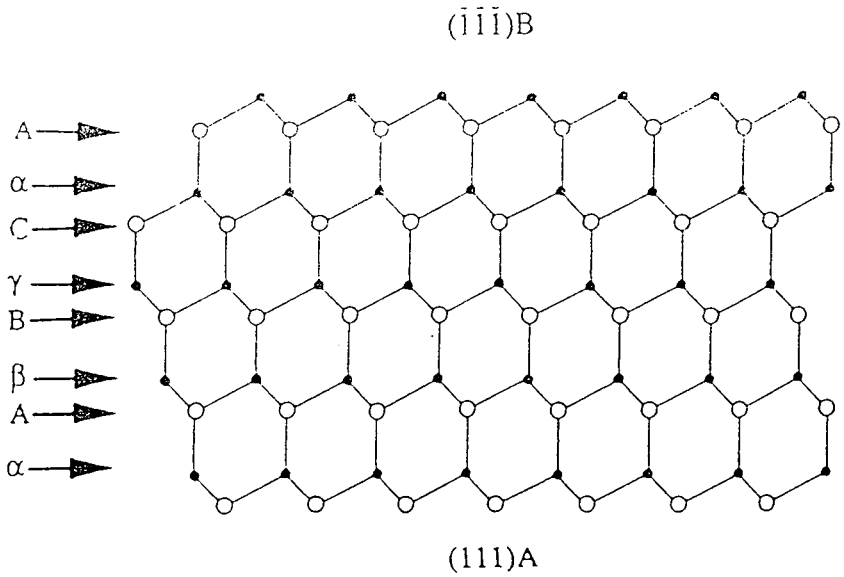

Figure 2.9 {111} plane stacking sequence for the sphalerite lattice and the resulting polar {111}A and {1̄1̄1̄}B surfaces.

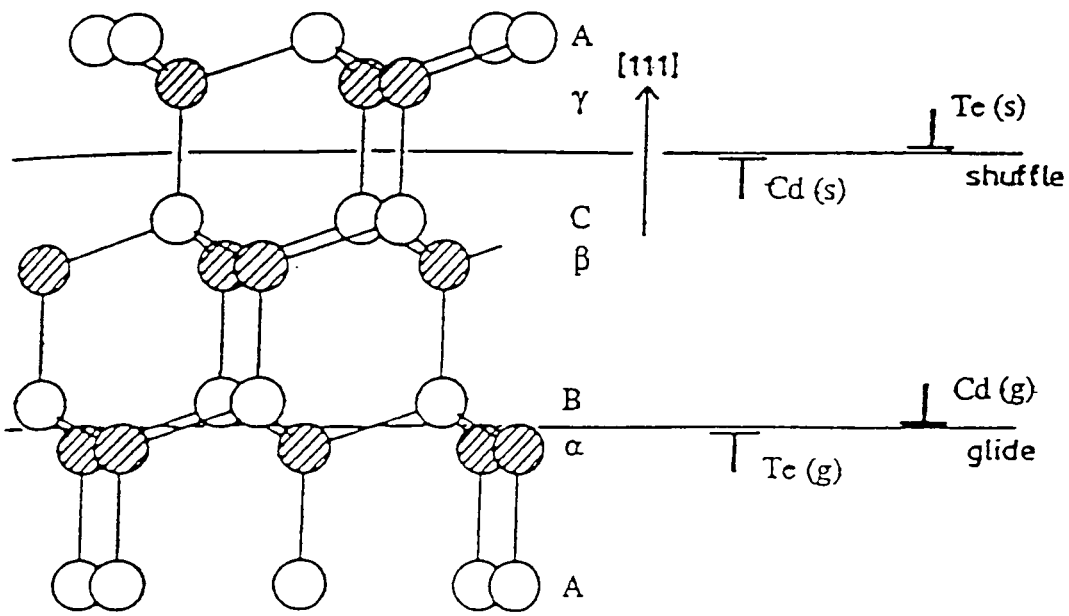

Figure 2.10 Glide and shuffle sets of dislocations in the sphalerite lattice. Dislocations may have a metal or non-metal core.

anisotropy as a result of the orientation of {111}A and $\{\bar{1}\bar{1}\bar{1}\}$B planes relative to them.

The shortest lattice vector in the sphalerite lattice is $(a_0/2)<110>$, this is therefore the most likely Burgers vector for dislocations in materials of this structure. Depending on whether dislocation formation appears to result from the breaking of narrowly or widely spaced {111} planes, dislocations can be classed as a glide or shuffle set respectively (assignment by Hirth and Lothe[6]). Work by Alexander[64] on the dissociation of dislocations suggests that dislocations in the sphalerite lattice are of the glide set, since these can dissociate into partial dislocations, whereas those of the shuffle set cannot, since such a dissociation would lead to a high energy stacking fault[6].

In addition to belonging to the glide or shuffle set, dislocations can also be divided into different classes, according to whether the dislocation core terminates on a metal or a non-metal atom (figure 2.10). Throughout this thesis the convention for labelling α and β type dislocations is: For an α type dislocation (Cd core for glide set), the extra half-plane ends on a {111}A directed plane (i.e. (111), $(\bar{1}\bar{1}1)$, $(\bar{1}1\bar{1})$ or $(1\bar{1}\bar{1})$); for a β type dislocation (Te core for glide set), the extra half-plane ends on a $\{\bar{1}\bar{1}\bar{1}\}$B directed plane (i.e. $(\bar{1}\bar{1}\bar{1})$, $(11\bar{1})$, $(1\bar{1}1)$ or $(\bar{1}11)$). This is the convention proposed by Suzuki, Takeuchi and Yoshinaga[65].

More thorough reviews of dislocations, may be found in texts by Hirth and Lothe[6], Read[66], Kelly and Groves[67] and Cottrell[68].

2.6 Conclusions

Conventional theories of the nucleation of misfit dislocations and critical thickness, such as those by Matthews and Blakeslee[5] and People and Bean[8,9] cannot be applied directly to high misfit layers, particularly those which display 3-D island growth mode. It is clear that the early stages of layer relaxation and the resulting misfit dislocation network are governed by growth mode.

The most common misfit dislocations in CdTe/GaAs are 90° type with both ℓ and **b** lying in the interface and it is thought that these dislocations are nucleated at the edge of growing islands. 60° dislocations are more likely to be formed by half-loop generation after a complete covering of the overlayer has grown. Threading dislocations are likely to be formed by the misalignment of dislocations when islands meet, and also as a consequence of half-loop generation.

A number of methods for the reduction of threading dislocation density in GaAs/Si have been described including misorientation of the substrate, annealing and the use of strained layer superlattices. A few of these methods have been successfully applied to CdTe/GaAs by other workers and these have also been reviewed.

REFERENCES FOR CHAPTER 2

1. Frank F. C. and van der Merwe J. H., *Proc. Roy. Soc. A* **198**, (1949), 216.

2. Hull R. and Bean J. C., *Critical Reviews in Solid State and Materials Science* **17(6)**, (1992), 507.

3. Matthews J. W., in *Epitaxial Growth Part B,* Matthews J W, Ed. (Academic Press, Inc., New York, 1975), Chapter 8.

4. Matthews J. W., in *Dislocations in Solids,* Nabarro F R N, Ed. (North Holland, Amsterdam, 1979), vol. 2, Chapter 7.

5. Matthews J. W. and Blakeslee A. E., *J. Cryst. Growth* **27**, (1974), 118.

6. Hirth J. P. and Lothe J., *Theory of Dislocations*, McGraw-Hill, 1968.

7. Marée P. M. J., Olthof R. I. J., Frenken J. W. M., van der Veen J. F., Bulle-Lieuwma C. W. T., Viegers M. P. A. and Zalm P. C., *J. Appl. Phys.* **58**, (1985), 3097.

8. People R. and Bean J. C., *Appl. Phys. Lett.* **47(3)**, (1985), 322.

9. People R. and Bean J. C., *Appl. Phys. Lett.* **49(4)**, (1986), 229.

10. Hull D. and Bacon D. J., *Introduction to Dislocations*, (3rd edition), Pergamon Press, 1989International Series on Materials Science and Technology, volume 37, chapter 1.

11. Fox B. A. and Jesser W. A., *J. Appl. Phys.* **68**, (1990), 2801.

12. Fitzgerald E. A., Watson G. P., Proano R. E., Ast D. G., Kirchner P. D., Pettit G. D. and Woodall J. M., *J. Appl. Phys.* **65(6)**, (1989), 2220.

13. Eaglesham D. J., Kvam E. P., Maher D. M., Humphreys C. J. and Bean J. C., *Phil. Mag. A* **59(5)**, (1989), 1059.

14. Hull R. and Bean J. C., *J. Vac. Sci. Technol. A* **7**, (1989), 2580.

15. Kamat S. V. and Hirth J. P., *J. Appl. Phys.* **67**, (1990), 6844.

16. Marée P. M. J., Barbour J. C., van der Veen J. F., Kavanagh K. L., Bulle-Lieuwma C. W. T. and Viegers M. P. A., *J. Appl. Phys.* **62(11)**, (1987), 4413.

17. Trampert A., Tournié E. and Ploog K. H., *Appl. Phys. Lett.* **66(17)**, (1995), 2265.

18. Chang K. H., Bhattacharya P. K. and Gibala R., *J. Appl. Phys.* **66(7)**, (1989), 2993.

19. Dregia S. A. and Hirth J. P., *J. Appl. Phys.* **69**, (1991), 2169.

20. Price G. L., *Phys. Rev. Lett.* **66(4)**, (1991), 469.

21. Hsu C. C., Wilson I. H. and Wang S. M., *Appl. Phys. Lett.* **66(5)**, (1995), 604.

22. Lentzen M., Gerthsen D., Förster A. and Urban K., *Appl. Phys. Lett.* **60(1)**, (1992), 74.

23. Snyder C. W., Mansfield J. F. and Orr B. G., *Phys. Rev. B* **46(15)**, (1992), 9551.

24. Snyder C. W., Orr B. G. and Munekata H., *Appl. Phys. Lett.* **62(1)**, (1993), 46.

25. Guha S., Munekata H., LeGoues F. K. and Chang L. L., *Appl. Phys. Lett.* **60(26)**, (1992), 3220.

26. Guha S., Madhukar A. and Rajkumar K. C., *Appl. Phys. Lett.* **57(20)**, (1990), 2110.

27. George T., Weber E. R., Nozaki S., Wu A. T., Noto N. and Umeno M., *J. Appl. Phys.* **67**, (1990), 2441.

28. Trampert A., Tournié E. and Ploog K. H., *Inst. Phys. Conf. Ser.* **in press**, (1995).

29. Tamura M., Yodo T., Saitoh T. and Palmer J., *J. Cryst. Growth* **150**, (1995), 654.

30. Otsuka N., Choi C., Kolodziejski L. A., Gunshor R. L., Fischer R., Peng C. K., Morkoç H., Nakamura Y. and Nagakura S., *J. Vac. Sci. Technol. B* **4(4)**, (1986), 896.

31. Eaglesham D. J., Aindow M. and Pond R. C., *Mat. Res. Soc. Symp. Proc.* **116**, (1988), 267.

32. Bauer S., Rosenauer A., Link P., Kuhn W., Zweck J. and Gebhardt W., *Ultramicroscopy* **51**, (1993), 221.

33. Hasson G., Bos J.-Y., Herbeuval I., Biscondi M. and Goux C., *Surface Science* **31**, (1972), 115.

34. Kiely C. J., Chyi J. I., Rockett A. and Morkoç H., *Phil. Mag. A* **60**, (1989), 321.

35. Gerthsen D., Tillmann K. and Lentzen M., in *Festkörperprobleme/ Advances in Solid State Physics,* Helbig R, Ed. (Vieweg, Braunschweig, Wiesbaden,), vol. 34, pp 275.

36. Shin S. H., Arias J. M., Edwall D. D., Zandian M., Pasko J. G. and Dewames R. E., *J. Vac. Sci. Technol. B* **10(4)**, (1992), 1492.

37. Yamamoto T., Miyamoto Y. and Tanikawa K., *J. Cryst. Growth* 72, (1985), 270.

38. Szilagyi A. and Grimbergen M. N., *J. Crsyt. Growth* 86, (1988), 912.

39. Norton P. W. and Erwin A. P., *J. Vac. Sci. Technol. A* 7(2), (1989), 503.

40. Hirth J. P. and Ehrenreich H., *J. Vac. Sci. Technol. A* 3(1), (1985), 367.

41. Tregilgas J. H., *J. Vac. Sci. Technol.* 21(1), (1982), 208.

42. Archer N. A., Palfrey H. D. and Willoughby A. F. W., *J. Cryst. Growth* 117, (1992), 177.

43. Matthews J. W., Blakeslee A. E. and Mader S., *Thin Solid Films* 33, (1976), 253.

44. Matthews J. W. and Blakeslee A. E., *J. Cryst. Growth* 32, (1976), 265.

45. Rozgonyi G. A., Petroff P. M. and Panish M. B., *Appl. Phys. Lett.* 24(6), (1974), 251.

46. Mader S. R., *US Patent* , (1974), No 3,788,890.

47. Fisher R., Neuman D., Zabel H., Morkoç H., Choi C. and Otsuka N., *Appl. Phys. Lett.* 48, (1986), 1223.

48. Fang S. F., Adomi K., Iyer S., Morkoç H., Zabel H., Choi C. and Otsuka N., *J. Appl. Phys.* 68(7), (1990), R31.

49. Shinohara M., *Appl. Phys. Lett.* 52, (1988), 543.

50. El-Masry N., Tarn J. C. L., Humphrey T. P., Hamaguchi N., Karam N. H. and Bedair S. M., *Appl. Phys. Lett.* 51, (1987), 1608.

51. El-Masry N. A., Tarn J. C. and Karam N. H., *J. Appl. Phys.* 64(7), (1988), 3672.

52. Soga T., Hattori S., Sakai S., Takeyasu M. and Umeno M., *J. Appl. Phys.* 57, (1985), 4578.

53. Shiba Y., Asai K., Kamel K. and Katahama H., *Jpn. J. Appl. Phys.* 34, (1995), 1466.

54. Hashimoto A., Sugiyama N. and Tamura M., *Inst. Phys. Conf. Ser.* 117, (1991), 403.

55. Sugiyama I., Hobbs A., Saito T., Ueda O., Shinohara K. and Takigawa H., *J. Cryst. Growth* 117, (1992), 161.

56. Petruzzello J., Olego D., Chu X. and Faurie J. P., *J. Appl. Phys.* 66(7), (1989), 2980.

57. Mullins J. T., Clifton P. A., Brown P. D., Brinkman A. W. and Woods J., *J. Cryst. Growth* **101**, (1990), 100.

58. Clifton P. A., Mullins J. T., Brown P. D., Russell G. J., Brinkman A. W. and Woods J., *J. Cryst. Growth* , 93, (1988), 726.

59. Sugiyama I., Hobbs A., Ueda O., Shinohara K. and Takigawa H., *Appl. Phys. Lett.* **58(24)**, (1991), 2755.

60. Giess J., Hails J. E., Graham A., Blackmore G., Houlton M. R., Newey J., Young M. L., Astles M. G., Bell W. and Cole-Hamilton D. J., *J. Elec. Mat.* **24(9)**, (1995), in press.

61. Tunnicliffe J., Irvine S. J. C., Dosser O. D. and Mullin J. B., *J. Cryst. Growth* **68**, (1984), 245.

62. Edwall D. D., Gertner E. R. and Bubulac L. O., *J. Cryst. Growth* **86**, (1988), 240.

63. Shigenaka K., Uemoto T., Sugiura L., Ichizono K. and Hirahara K., *J. Cryst. Growth* **117**, (1992), 37.

64. Alexander H., *J. de Physique (Paris) Colloque* **40**, (1979), C6-1.

65. Suzuki T., Takeuchi S. and Yoshinaga H., *Dislocation Dynamics and Plasticity*, Springer Series in Materials Science, 1985; **12**, Chapter 7.

66. Read W. T., *Dislocations in Crystals*, London: McGraw-Hill, 1968.

67. Kelly A. and Groves G. W., *Crystallography and Crystal Defects*, London: Longman, 1970.

68. Cottrell A. H., *Dislocations and Plastic Flow in Crystals*, Oxford: Clarendon Press, 1953.

CHAPTER 3

Epitaxial Growth of CdTe, (CdHg)Te and ZnTe on GaAs by MOVPE

3.1 Introduction

In this chapter the growth of some II-VI epitaxial layers is discussed. A brief literature review of the epitaxial growth of CdTe and (CdHg)Te (CMT) is given in Section 3.2. The principles of metalorganic vapour phase epitaxy (MOVPE) will be outlined briefly in Section 3.3 prior to a description of the specific growth conditions employed in the present study. Details of the orientation of GaAs substrates used in this work are summarised in Section 3.4 along with a description of non-uniformities in the layer thickness which have been encountered.

3.2 Literature Review of the Epitaxial Growth of CdTe and CMT

3.2.1 Introduction

The following sections are in no way an exhaustive review of the growth of CdTe and CMT. Many reviews have been published on this topic and these are referred to in the text. The epitaxial growth of CdTe and CMT will be dealt with in separate sections although it should be kept in mind that CdTe is often used as a buffer layer prior to the growth of CMT when hybrid substrates are employed.

3.2.2 Epitaxial Growth of CdTe

Reviews of the growth of CdTe by liquid phase epitaxy (LPE)[1], vapour phase epitaxy (VPE)[2] and molecular beam epitaxy (MBE)[3] all appear in a single volume published by the Institute of Electrical Engineers. A further review by Franzosi and Bernardi[4] on the X-ray rocking curve widths of epitaxial

CdTe should be read with caution since rocking curve widths are quoted without reference to the thickness of the layer in question; the importance of this will become apparent in later chapters.

CdTe can be grown on a variety of substrates by a number of different growth techniques and is frequently used as a buffer layer for the subsequent growth of CMT. CdTe may adopt either the (111) or (001) orientation on (001)GaAs as has been reported for growth by MBE[5], hot wall epitaxy (HWE)[6-8] and MOVPE[9-11]. The temperature at which the CdTe is grown and the temperature at which the GaAs substrate is heat cleaned prior to growth have been shown to be factors in determining the orientation with which CdTe grows on (001)GaAs[9]. By depositing a thin layer of ZnTe, which always adopts the (001) orientation on (001)GaAs, Feldman et al.[12] have demonstrated growth of (001)CdTe/ZnTe/GaAs. In a separate study, Feldman et al.[13] found that by introducing the Te precursor first into an MOVPE reactor, the (001)CdTe orientation was always obtained.

High quality CdTe is best grown on matched or nearly lattice matched substrates. Hwang et al.[14] have used photoassisted MBE to deposit homoepitaxial CdTe on (001)CdTe substrates. High quality CdTe layers have been grown on nearly lattice matched (001)InSb substrates by Wood et al.[15], they found that the cleaning procedure for the substrates was essential in determining the structural quality of the epilayers. Highly lattice mismatched substrates have also been used. For instance the difference in the lattice parameters of CdTe and Si is 19% and yet $\{\bar{1}\bar{1}\bar{1}\}$B CdTe has been grown on (001)Si by MBE[16] and (001)CdTe onto (001)Si by HWE[17]. Sapphire, which has a hexagonal structure, has also been used as a substrate for CdTe growth, both {111}A and $\{\bar{1}\bar{1}\bar{1}\}$B CdTe have been deposited on (0001)sapphire[18].

3.2.3 Epitaxial Growth of CMT

In this section a brief review of the epitaxial growth of CMT is presented. A more thorough review of the structural quality of epitaxial CMT is given in Section 8.2. Recent reviews of the growth of CMT can be found for example

in references 19-21. X-ray rocking curve widths of epitaxial CMT reviewed by Bernardi and Franzosi[22] should be treated with the same caution as those of CdTe cited in the previous section.

Lattice matched (CdZn)Te [≈4.5%Zn] and Cd(TeSe) [≈4%Se] are common substrates for the epitaxial growth of CMT and CdTe. A comparison of CMT grown by LPE on CdTe and (CdZn)Te has been made by Bell et al.[23], they found that growth on (CdZn)Te substrates gave layers of superior structural quality to those grown on CdTe substrates, this is a consequence of the poorer initial quality of CdTe substrates and the lattice matching of (CdZn)Te. CMT grown on CdTe and Cd(TeSe) substrates by MOVPE using the interdiffused multilayer process[24] (IMP) has been compared by Bhat et al.[25,26], while direct alloy growth (DAG) of CMT by MOVPE has been compared by Bevan et al.[27] for (CdZn)Te and Cd(TeSe) substrates.

GaAs is also a popular substrate for the MOVPE growth of CMT despite there being a large misfit. Many authors have reported on the use of CdTe buffer layers on GaAs for the subsequent growth of CMT, for example, Triboulet et al.[28] have written a review on 'GaAs substrates for the MOVPE growth of CMT layers' outlining the current problems associated with CMT growth on GaAs. An even greater misfit exists between CMT and Si; the use of GaAs and CdTe buffer layers has allowed CMT of surprisingly good structural quality to be grown on Si substrates[16,29]. The use of CdTe as a buffer layer between GaAs and CMT is the major subject of this thesis.

3.3 MOVPE Growth of Some II-VI Epilayers

3.3.1 Introduction

In the following subsection the principles of MOVPE growth will be outlined. Specific details will be kept to a minimum since a number of well written texts are available on MOVPE reaction kinetics[30], growth mechanisms[31] and vapour transport[32]. Concise reviews on the fundamental principles of MOVPE can be found in references 33-35. A very extensive book review on

the theory and practice of MOVPE by Stringfellow may be found in reference 36.

Later subsections present the specific substrate preparation methods and growth conditions employed for the II-VI epilayers which were studied in this work. For all of the layers investigated, (001)GaAs substrates were used, the reasons for this choice of substrate were outlined in Chapter 1.

3.3.2 Principles of MOVPE

MOVPE is known also as organometallic vapour phase epitaxy (OMVPE), organometallic chemical vapour deposition (OMCVD) and metalorganic vapour phase deposition (MOCVD); the name MOVPE will be used throughout the present work. As the name suggests, MOVPE is epitaxial growth from the vapour phase by means of the pyrolysis of organometallic precursors. A schematic diagram of an MOVPE growth system is shown in figure 3.1. For the case of II-VI semiconductor growth, group II and VI covalent alkyls, for example di-methyl cadmium {also written as $Cd(CH_3)_2$, DMCd or Me_2Cd} and di-*iso*-propyl telluride {also written as $Te[CH(CH_3)_2]_2$, DiPTe or Pr^i_2Te}, are introduced into the reactor in a hydrogen carrier gas. The gas flows over the heated susceptor on which the substrate is placed and the organometallics crack. Group II and VI atoms are epitaxially deposited onto the substrate while the breakdown products are flushed out of the reactor in the H_2 gas stream. A detailed study of the pyrolysis reactions of Pr^i_2Te and Me_2Cd, with and without Hg has been carried out by Hails[37]. Reaction mechanisms and the implications for MOVPE growth have been proposed by Hails in the same publication.

Because of the need to maintain a high Hg partial pressure in the reactor, along with the high toxicity and stability of Me_2Hg, elemental Hg is almost universally used as the Hg source for CMT growth. Hg may be introduced either from an external source, or from an independently heated boat upstream of the susceptor (the latter is shown in figure 3.1).

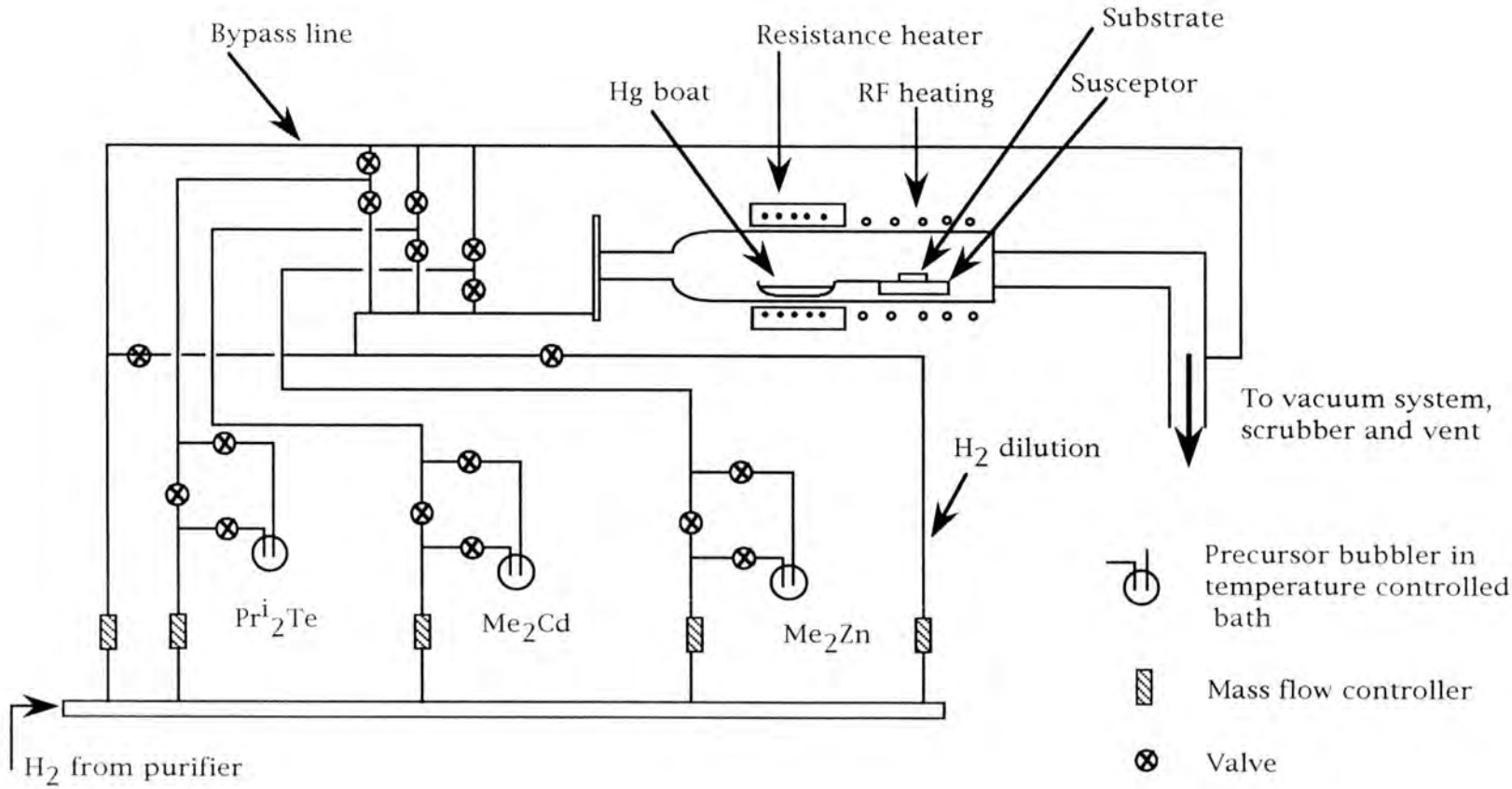

Figure 3.1 Schematic diagram of the MOVPE growth system

Two techniques are commonly used for MOVPE growth of CMT: 1) the DAG method, whereby the cadmium and tellurium precursors and mercury are continuously fed into the reactor and 2) the IMP[24] technique, whereby individual layers of HgTe and CdTe are grown and interdiffuse during growth. Compositional control is achieved by varying the Cd, Te and Hg partial pressure for DAG and by adjusting the relative thicknesses of the CdTe and HgTe layers in the IMP technique. The IMP technique is shown schematically in figure 3.2 with the thicknesses of individual HgTe and CdTe layers being t_1 and t_2 respectively. The composition of $Cd_xHg_{(1-x)}Te$ grown by the IMP technique depends on t_1 and t_2 according to equation 3.1.

$$x = \frac{t_2}{(t_1 + t_2)} \qquad \text{equation 3.1}$$

The lateral and depth compositional uniformity of layers grown by the IMP technique have been reported to be superior to those grown by the DAG method by a number of authors[38-40]. IMP is now the more common method for MOVPE growth of CMT.

3.3.3 Experimental

3.3.3.1 MOVPE Growth of CdTe on GaAs*

GaAs (001) substrates (offcut 3.5° towards [$\bar{1}$00] about [010]) were prepared according to the flowchart given in figure 3.3. The substrates were degreased in trichloroethylene, etched for 5 minutes at 40°C in 5:1:1 H_2SO_4:H_2O:H_2O_2, rinsed in deionised water and in boiling propan-2-ol (IPA). The substrates were finally dried in IPA vapour before loading into the MOVPE reactor. The IPA was treated with $NaBH_4$ according to reference 41 to reduce the formation of pyramidal hillocks which have been extensively reported for CdTe and CMT growth on (001)GaAs (see for example

* Except where indicated, CdTe buffer layers investigated in this thesis were grown by Dr J. E. Hails, onto substrates prepared by Mr A. Graham, both at Defence Research Agency, Malvern, UK.

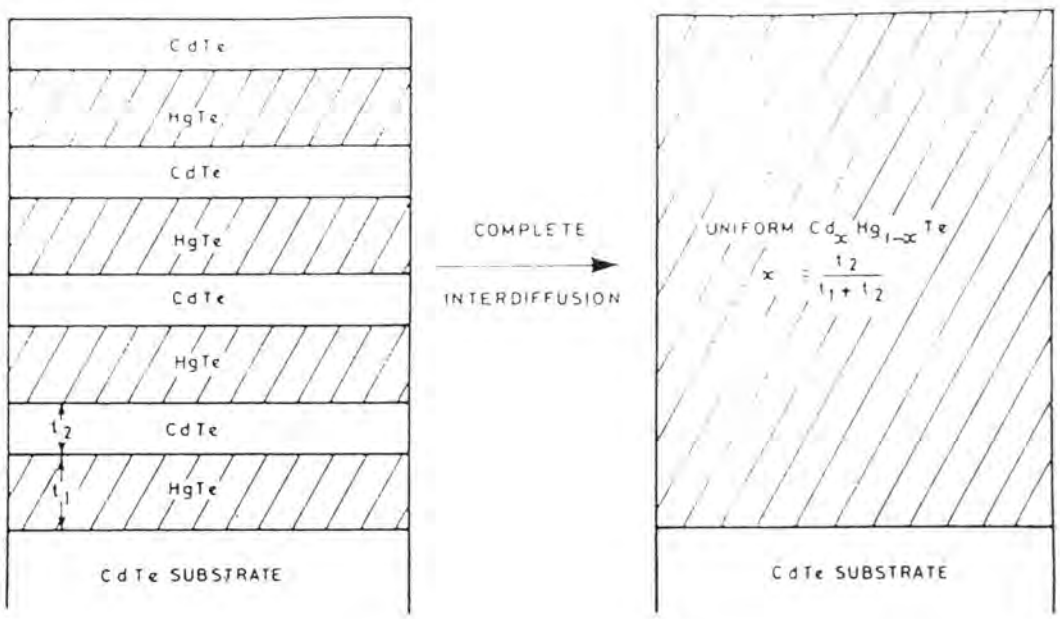

Figure 3.2 Schematic diagram of CMT growth by the interdiffused multilayer process. Individual thin layers of HgTe and CdTe are grown and allowed to interdiffuse. Diagram from Tunnicliffe et al.[24].

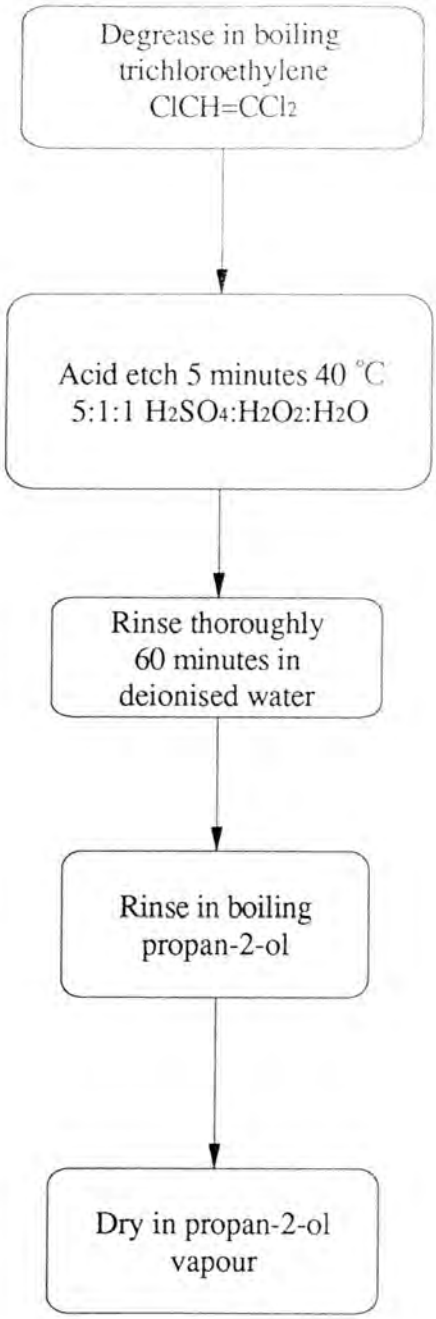

Figure 3.3 GaAs substrate preparation for growth of CdTe buffer layers.

references 42 and 43). Examples of these hillocks, which still occur but with reduced density, are shown in figure 3.4. Another common problem associated with MOVPE grown CdTe and CMT on GaAs is the formation of polycrystalline lumps of a range of sizes which are thought to be caused by dust contamination from gas phase reaction during growth; an example of these features is shown in figure 3.5. These features can be reduced and in some cases virtually eliminated by, for example, careful control of the growth conditions, high standards of glassware cleanliness (both in the reactor and for substrate preparation) and careful handling of the etched substrate prior to loading into the MOVPE reactor.

The CdTe layers investigated in Chapters 6 and 7 were grown according to the flowchart given in figure 3.6, but with the growth of CMT omitted. A boat containing elemental Hg was present during growth of the buffer layers but was not heated. The substrates were heated to 385°C for 20 minutes before cooling to 320°C. The tellurium precursor, $Pr^{i}_{2}Te$, was passed into the reactor to ensure that the CdTe layer was deposited in the (001) orientation[13] rather than {111}. Growth was initiated by switching the cadmium precursor, Me_2Cd, into the reactor. After a fraction of a micron of CdTe had been deposited, the temperature was raised to 370°C and the desired thickness of CdTe buffer was deposited.

The CdTe layers were shiny with occasional matte patches, their surface morphology is shown in figures 3.7a-c. The surface does not show crystallographically aligned faceted hillocks as in figure 3.4, but rather more rounded features whose average size increases as the layer thickens. CdTe buffer layer thicknesses were mapped for layers thicker than 1μm, and showed a thickness variation of between 10 and 17% over an area 30mmx10mm for all layers. Reasons for the thickness variation are given in Section 3.4.

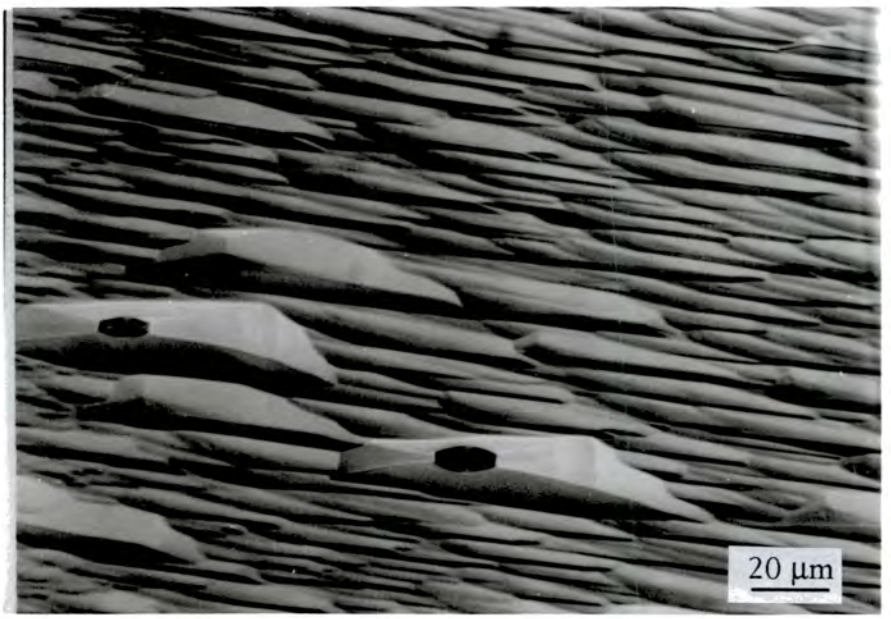

Figure 3.4 Normarski interference micrograph of hillocks on an 18µm thick (001)CdTe/GaAs epilayer. The epilayer was grown by Mr J. S. Gough, D.R.A., Malvern.

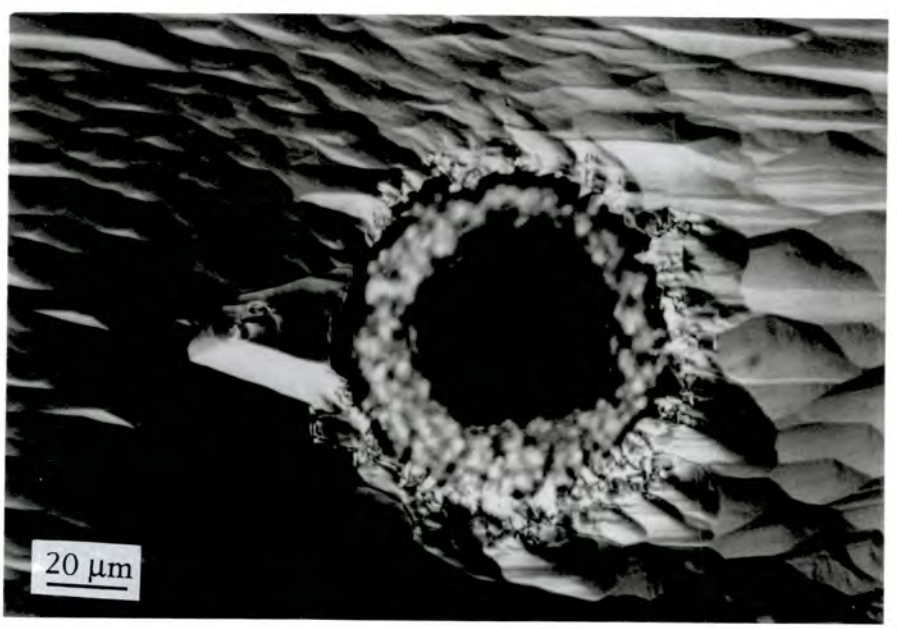

Figure 3.5 Polycrystalline lumps on an 18µm thick (001)CdTe/GaAs layer, the feature is 45µm high. The epilayer was grown by Mr J. S. Gough, D.R.A., Malvern.

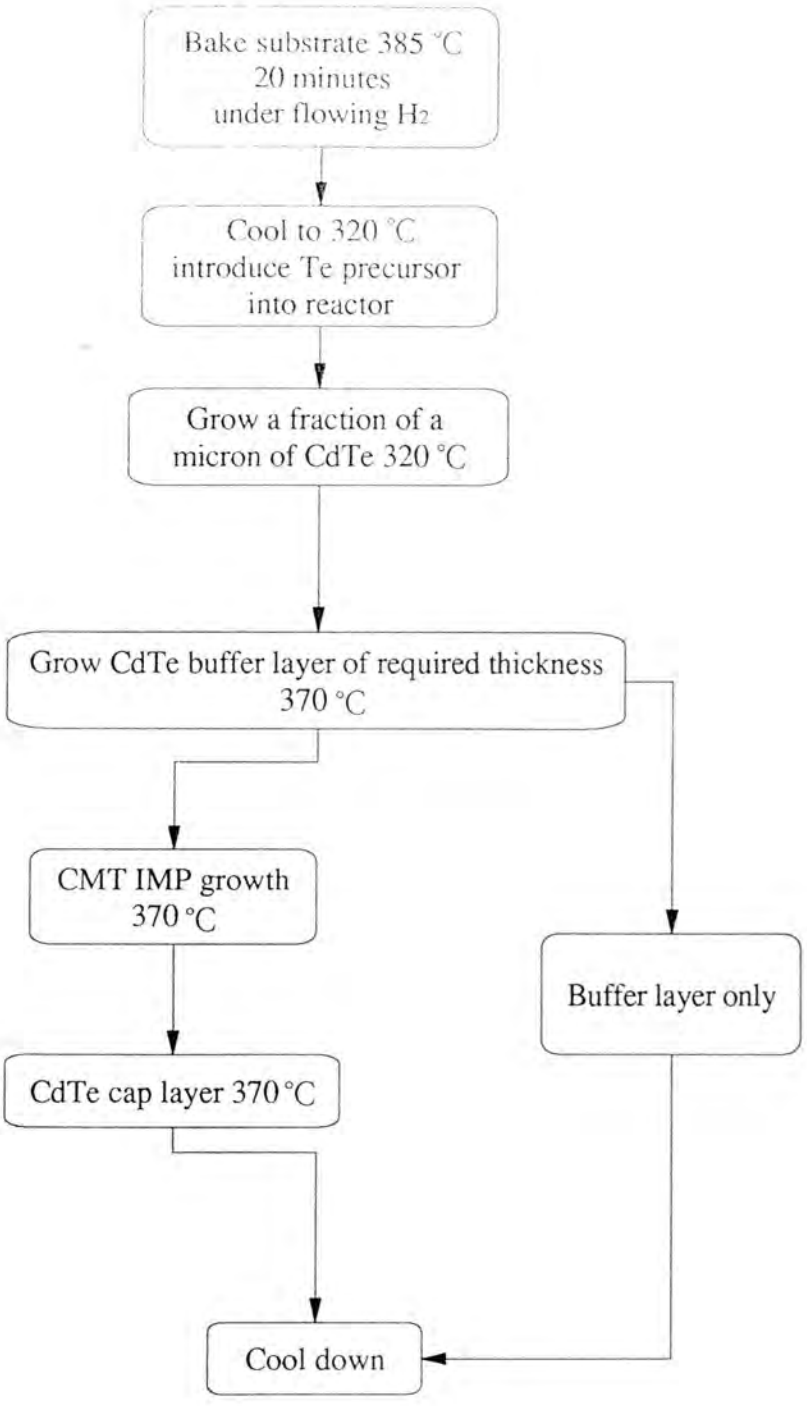

Figure 3.6 Growth conditions for growth of CdTe buffer layers with and without CMT layer.

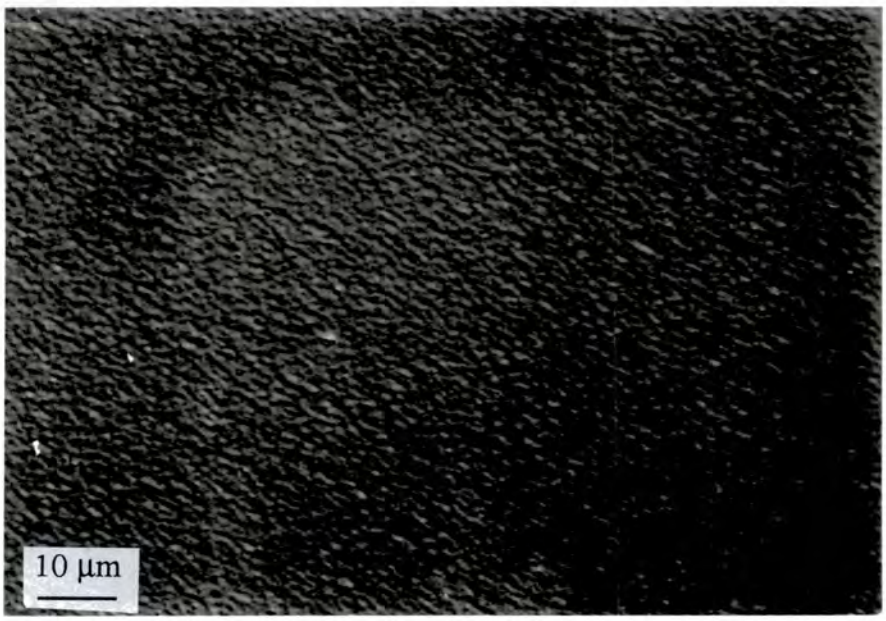

Figure 3.7a Surface morphology of a 0.60µm thick (001)CdTe/GaAs epilayer.

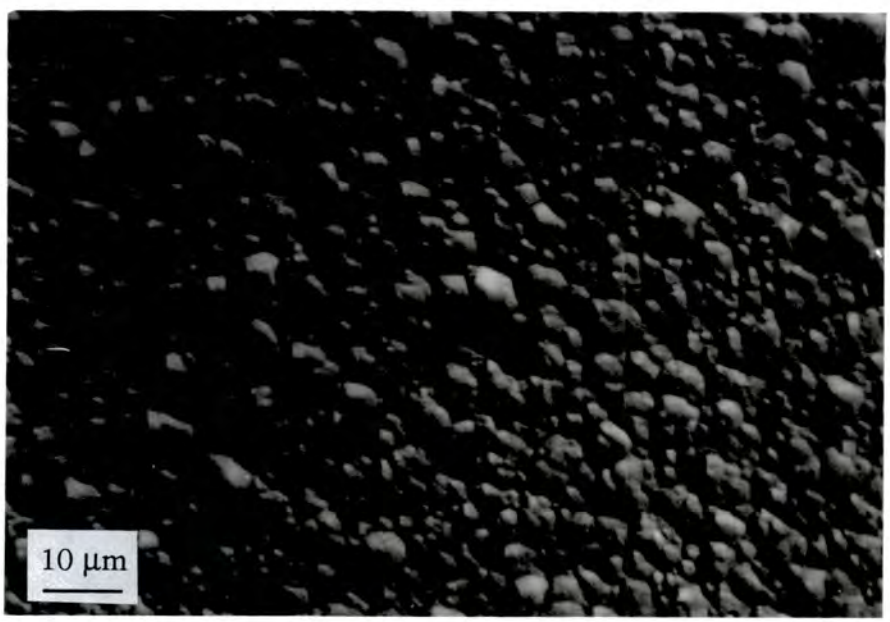

Figure 3.7b Surface morphology of a 4.0µm thick (001)CdTe/GaAs epilayer.

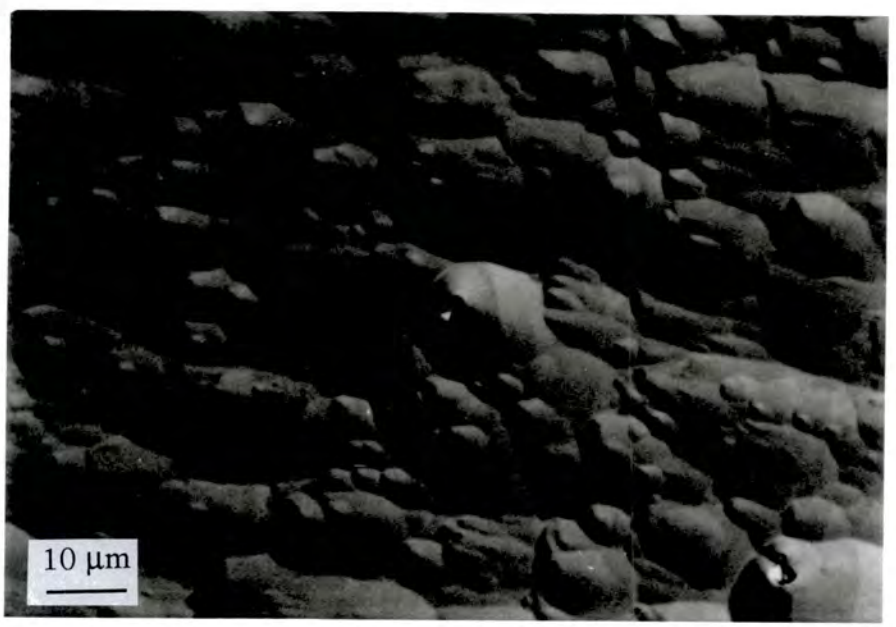

Figure 3.7c Surface morphology of a 24.5µm thick (001)CdTe/GaAs epilayer.

3.3.3.2 MOVPE Growth and Annealing of CdTe on GaAs[#]

A separate series of CdTe/GaAs epitaxial layers were grown to investigate the effect of interrupted growth and *in-situ* annealing. The results of this study can be found in Section 8.1. The CdTe buffer layers were annealed under a cadmium overpressure according to the flow chart given in figure 3.8. One standard buffer layer was also grown, without interruption of growth or annealing. The GaAs substrates used for this study were offcut 2° towards [$\bar{1}$00] about [010] and were prepared as before (flowchart in figure 3.3). From the gas flows used, if DMCd were to be completely pyrolysed at the annealing temperature, then the resulting Cd partial pressure would be 0.655 Torr. CdTe layers were annealed at 420°C and 470°C for 60 minutes and 20 minutes respectively and showed the same surface morphology as layers grown without a thermal anneal. For these layers no Hg was present in the reactor during growth.

3.3.3.3 MOVPE Growth of CMT on CdTe/GaAs[$]

CMT layers were grown onto (001)GaAs substrates (offcut 2° towards [$\bar{1}$00] about [010]) buffered with either 6.5 or 11μm thick CdTe. The substrates were prepared as before (flow chart in figure 3.3). The precursors Me_2Cd and Pr^i_2Te were used and the growth carried out as described in figure 3.6. The individual thicknesses of the HgTe and CdTe layers along with the resulting composition uniformity are summarised in table 3.1.

[#] Layers described in Sections 3.3.3.2 and 8.1 were grown by Dr J. E. Hails on substrates prepared by Mr A. Graham, both at Defence Research Agency, Malvern, UK.

[$] The CMT layers investigated in this thesis were grown by Mr A. Graham, Defence Research Agency, Malvern, UK.

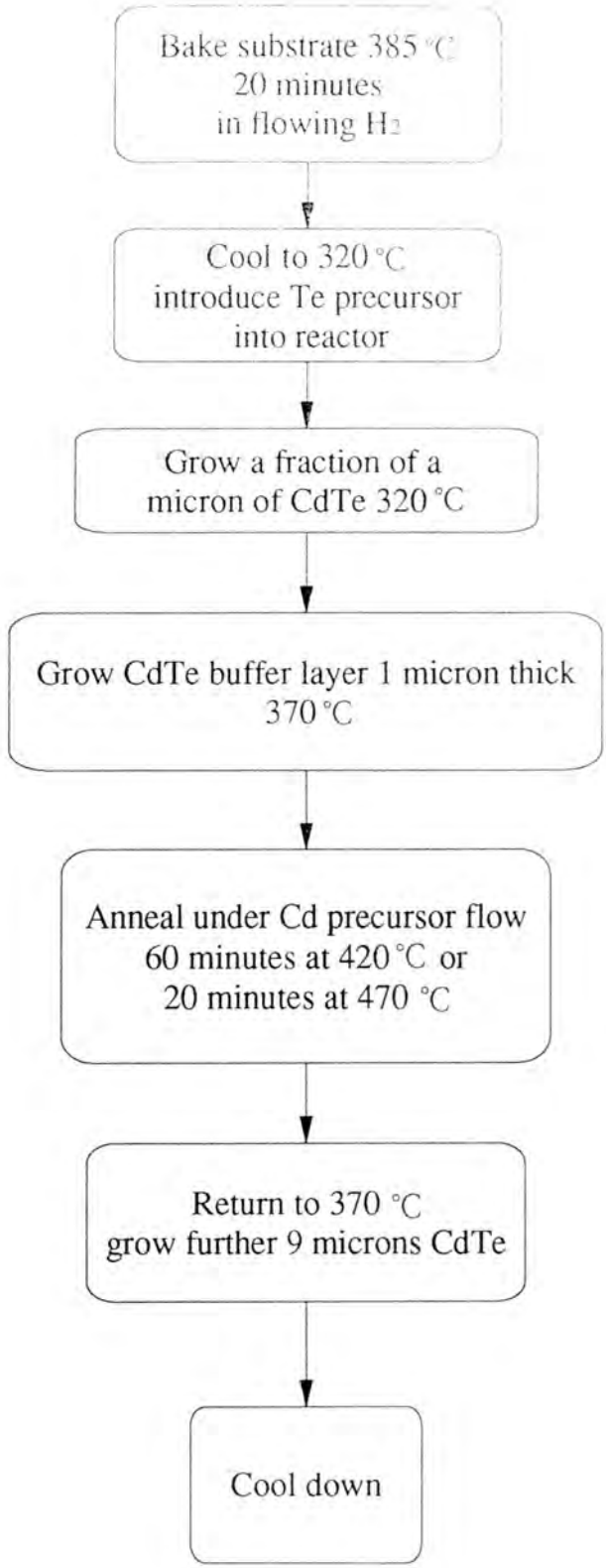

Figure 3.8 Growth conditions for growth and annealing of CdTe buffer layers.

CdTe buffer thickness /μm	CMT thickness /μm	HgTe IMP thickness, t_1 /μm	CdTe IMP thickness, t_2 /μm	%Cd composition by mole fraction, x, over a 30mmx10mm area
6.5	12.2	0.109	0.033	0.220-0.245
11	11	0.091	0.037	0.280-0.315

Table 3.1 Growth details of CMT ($Cd_xHg_{(1-x)}Te$) layers grown by the IMP technique and investigated in Section 8.2. Composition determined by t_1 and t_2 according to equation 3.1.

3.3.3.4 MOVPE Growth of ZnTe on GaAs*

A ZnTe epilayer was grown on a nominally exact (001)GaAs substrate which was prepared according to the flow chart in figure 3.9. It should be noted that the IPA used for the final rinse of the etched substrate was not treated with $NaBH_4$. The substrate was baked at 368°C for 30 minutes prior to growth of the epilayer with di-methyl zinc (also written as $Zn(CH_3)_2$, DMZn or Me_2Zn) and di-*iso*-propyl telluride as precursors. The thickness of the ZnTe layer ranged from 1.4 to 3.2μm over a 12mmx12mm area.

3.4 Additional Considerations Concerning Growth of II-VI Epilayers

3.4.1 Substrate Orientation

Because of the anisotropy of the sphalerite lattice, wafers must be labelled to show the orientation of {111}A and $\{\bar{1}\bar{1}\bar{1}\}$B planes. There are two conventions used for labelling wafers, namely the European/Japanese and the United States' conventions; the former is used throughout the present work. Two 'flats' are given on wafers which indicate the orientation of the substrate, as shown in figure 3.10. Unfortunately, the substrate offcut is quoted, for

* The ZnTe layers investigated in this thesis were grown by Dr S. Oktik, Department of Physics, University of Durham.

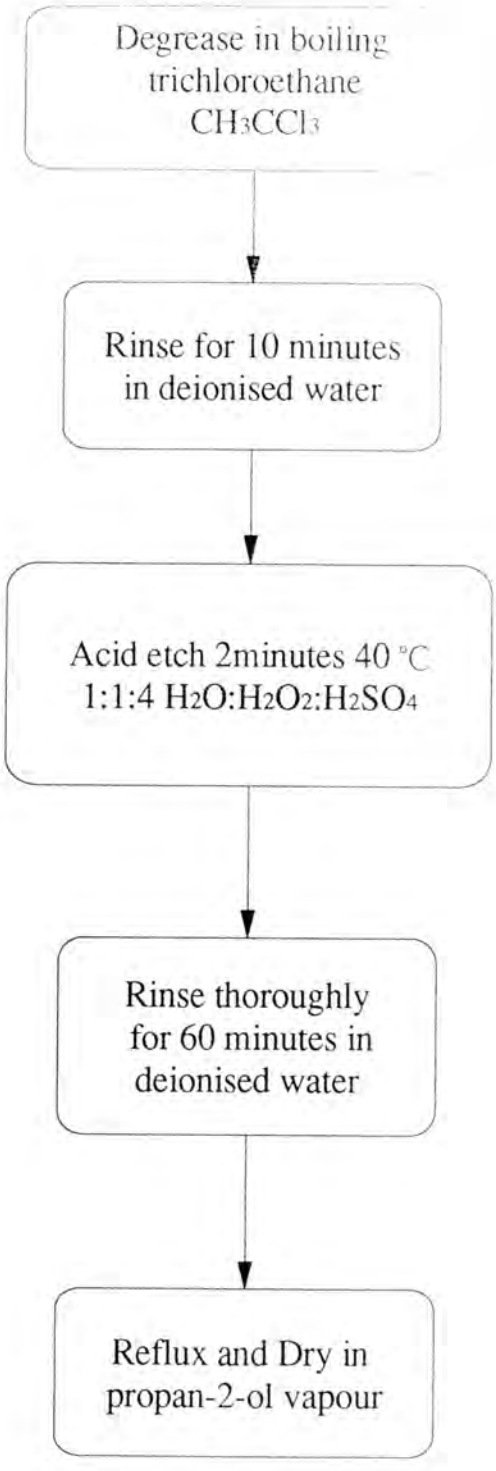

Figure 3.9 GaAs substrate preparation for growth of ZnTe layers.

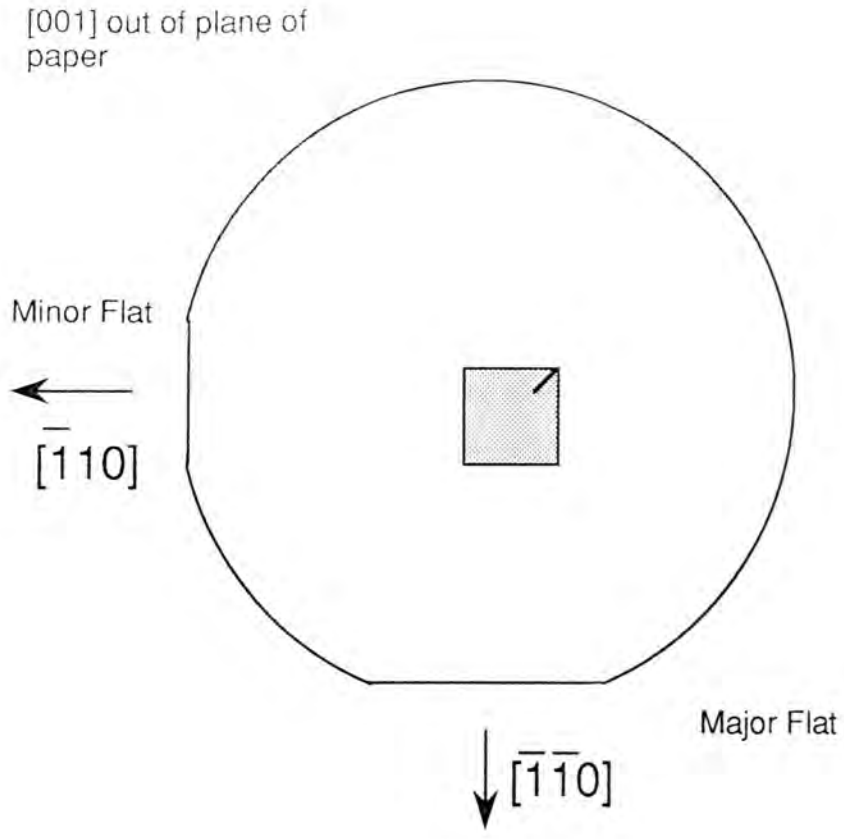

Figure 3.10 Diagram showing the European and Japanese convention for wafer labelling. All small samples cleaved from the main wafer were marked with a single scratch as indicated in the diagram. In this way all characterisation was carried out under known orientation conditions.

example, as being "towards the nearest <110> direction" by the manufacturer, i.e. the exact direction of offcut is not known. For the substrates used in this work, the direction of offcut has been determined by Laue back-reflection X-ray diffraction, which is described in Section 4.2.4. The resulting Laue pattern allows the direction and magnitude of the offcut relative to the major and minor flats to be determined. The offcuts of the substrates used for the growth of CdTe, annealed CdTe, CMT and ZnTe are summarised in table 3.2.

Layer	Magnitude of offcut	Direction towards which offcut occurs	Axis about which offcut occurs
CdTe/GaAs	3.5°	[$\bar{1}$00]	[010]
Annealed CdTe/GaAs	2°	[$\bar{1}$00]	[010]
CMT/CdTe/GaAs	2°	[$\bar{1}$00]	[010]
ZnTe/GaAs	nominally exact		

Table 3.2 Direction and magnitude of substrate offcut for layers described in Section 3.3. A diagram illustrating the direction of offcut can be found in figure 7.19.

3.4.2 Epilayer Thickness Uniformity

Many factors affect the thickness uniformity of layers grown by MOVPE. Three causes of thickness variation over the area of a wafer were observed during this study. Figure 3.11 shows the effect of non-uniform carrier gas flow into the MOVPE reactor, the area of the substrate upstream and on the side of greatest mass flow was found to be the thickest region and that of poorest crystalline quality. The thickness plot shown in figure 3.12a shows the effect of a cold air 'draught' passing one side of a MOVPE reactor which was housed in a fume extraction cupboard. The thickest part of the layer was the furthest from where the cold air was drawn under the fume cupboard window, i.e. at the hottest part of the susceptor. Figure 3.12b shows the effect of stopping the cold air intake in the region of the reactor wall. The result

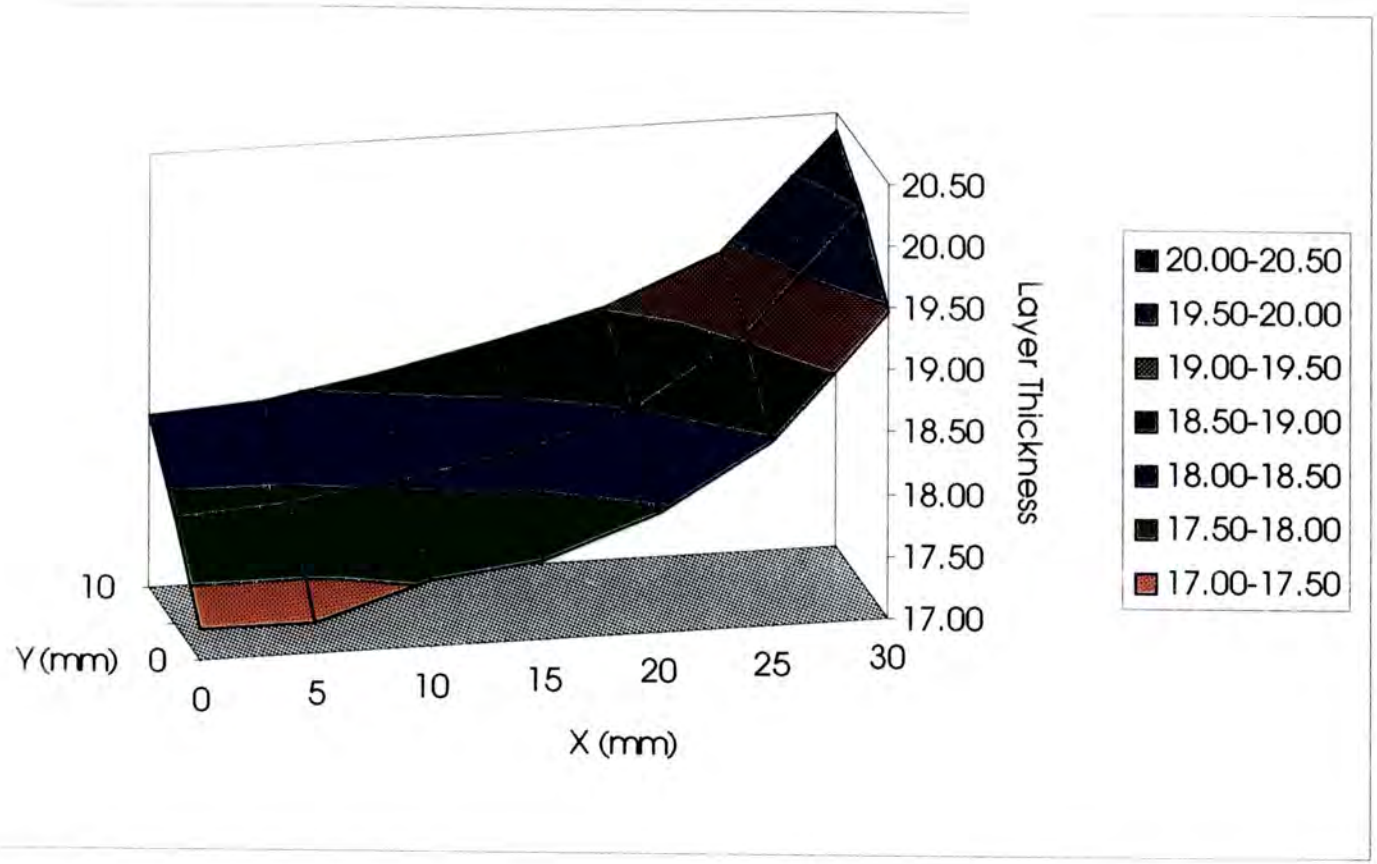

Figure 3.11 Thickness map showing the effect of non uniform carrier gas flow. The thickest region is upstream and on the side of greatest mass flow. The layer thickness is given in microns. This (001) CdTe/GaAs epilayer was grown by Mr J. S. Gough, Defence Research Agency, Malvern.

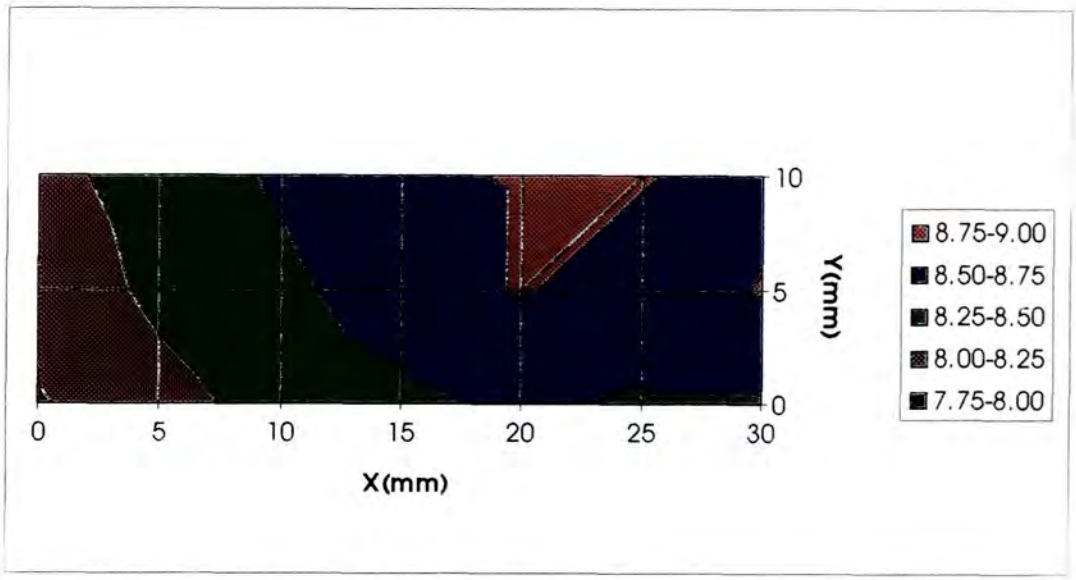

a

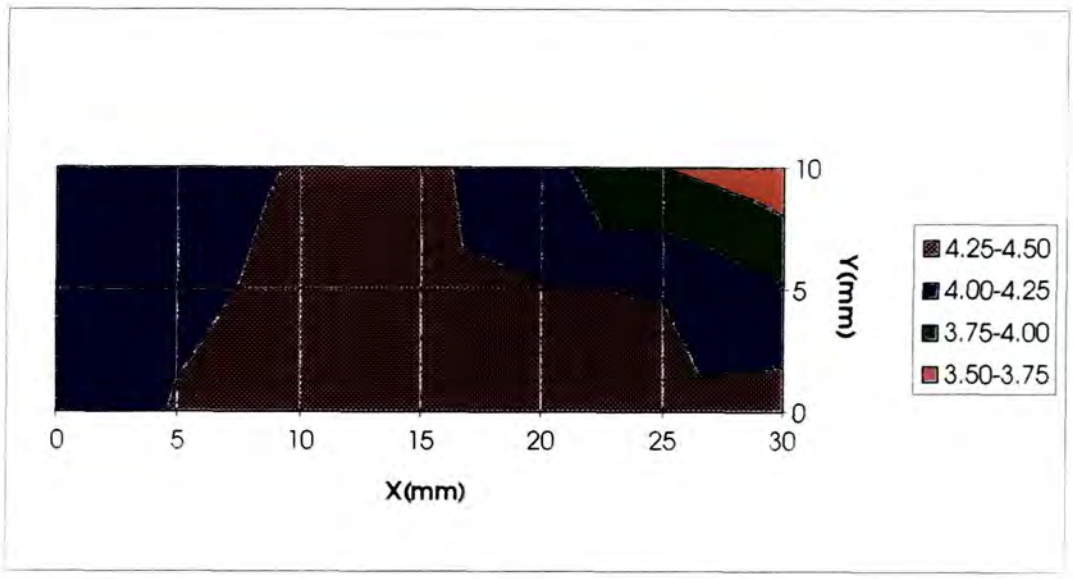

b

Figure 3.12 Thickness maps showing (a) the effect of a cold draught on the outside of the MOVPE reactor wall. The thinnest region, nearest the bottom of the page is closest to the source of the draught, and (b) when the source of the draught is removed, a larger region of uniform thickness is grown. The (001) CdTe/GaAs epilayers thicknesses are given in microns.

was a greater region of uniform thickness with the thickest region nearest the fume cupboard window. A greater effect of temperature fluctuation was seen for ZnTe/GaAs growth, when the susceptor had a temperature gradient along its length. This is illustrated in figure 3.13, again the thickest region of the layer corresponded to the higher substrate temperature. In this case there was a doubling in thickness between the upstream and downstream regions over just 10mm.

3.5 Conclusions

MOVPE of Te based II-VI compounds is a mature technology but it is not without technical problems. IMP growth gives good compositional control of CMT although some authors report that the IMP technique results in a higher dislocation density. Despite this, IMP is now the standard technique for growth of CMT. Data on the thickness uniformity of MOVPE layers presented here shows that CdTe epitaxy (and epitaxy of other compounds) still requires process optimisation. The thickness variation also demonstrates that routine mapping of layer thickness and uniformity is required to ensure that structural and electrical characterisation is carried out on layer portions of known thickness and composition.

A significant advance in CdTe and CMT MOVPE has been the reduction in hillock densities in layers grown on (001) oriented substrates. Giess et al.[41] have demonstrated that treatment of IPA (used for the final rinse in substrate preparation) with $NaBH_4$ reproducibly reduces hillock densities to less than $10cm^{-2}$.

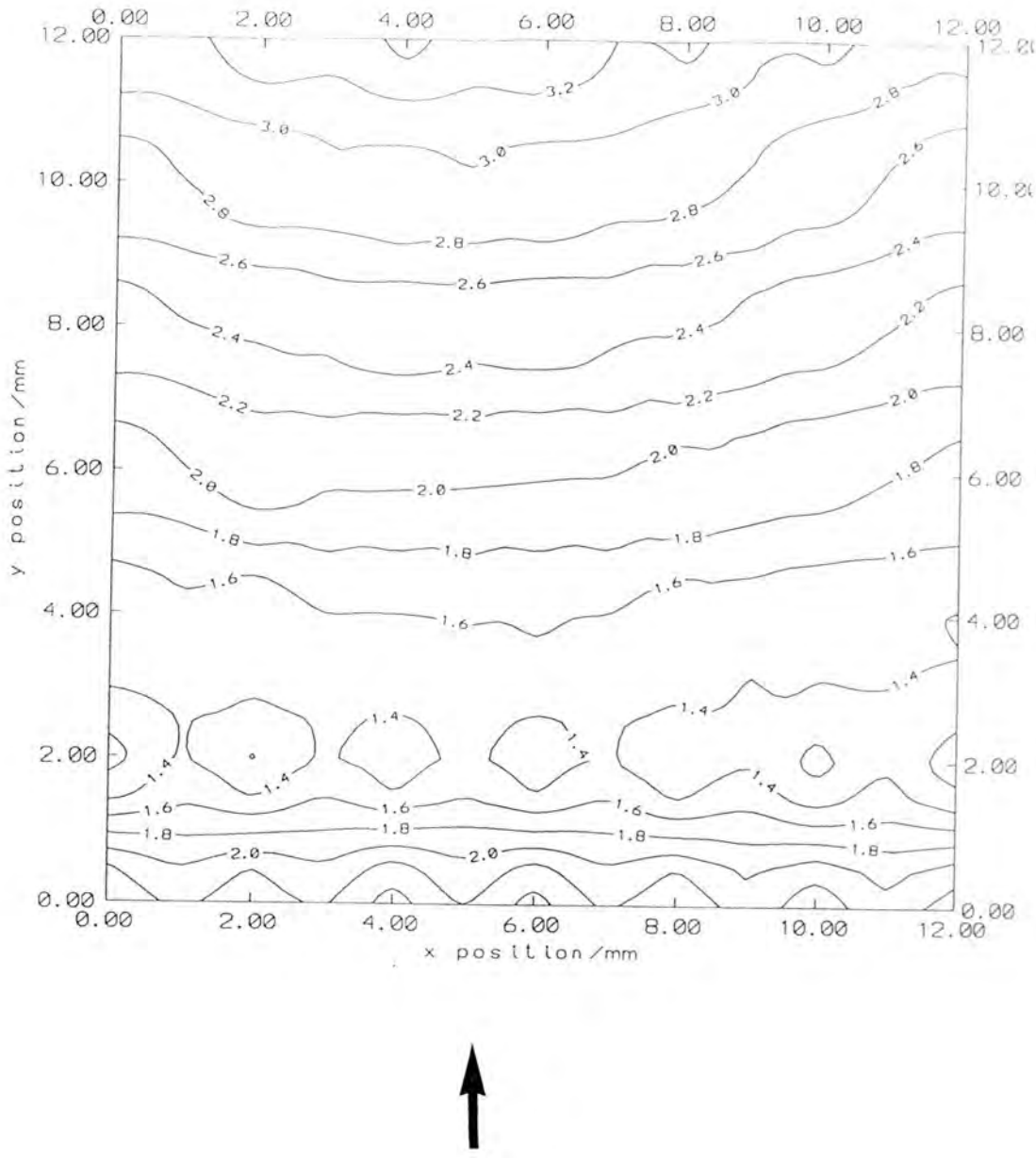

Figure 3.13 The effect of a susceptor temperature gradient on epilayer thickness for a ZnTe epilayer. The thickest region corresponds to the greatest susceptor temperature. The layer thickness is given in microns. The layer thickness was measured by DCXRD of the GaAs substrate recorded through the buffer layer (Section 4.4). Arrow indicates direction of gas flow and increasing temperature.

REFERENCES FOR CHAPTER 3

1. Astles M. G., in *Properties of Narrow Gap Cadmium-based Compounds,* Capper P, Ed. (INSPEC, London, 1994), EMIS Datareviews Series No.10, Section B1.2.

2. Irvine S. J. C., in *Properties of Narrow Gap Cadmium-based Compounds,* Capper P, Ed. (INSPEC, London, 1994), EMIS Datareviews Series No.10, Section B1.3.

3. Magnea N. and Pautrat J. L., in *Properties of Narrow Gap Cadmium-based Compounds,* Capper P, Ed. (INSPEC, London, 1994), EMIS Datareviews Series No.10, Section B1.4.

4. Franzosi P. and Bernardi S., in *Properties of Narrow Gap Cadmium-based Compounds,* Capper P, Ed. (INSPEC, London, 1994), EMIS Datareviews Series No.10, Section B5.7.

5. Faurie J. P., Reno J., Sivananthan S., Sou I. K., Chu X., Boukerche M. and Wijewarnasuriya P. S., *J. Vac. Sci. Technol. A* **4(4)**, (1986), 2067.

6. Tatsuoka H., Kuwabara H., Fujiyasu H. and Nakanishi Y., *J. Appl. Phys.* **65(5)**, (1989), 2073.

7. Tatsuoka H., Kuwabara H., Nakanishi Y. and Fujiyasu H., *J. Appl. Phys.* **68(9)**, (1990), 4592.

8. Korenstein R. and MacLeod B., *J. Cryst. Growth* **86**, (1988), 382.

9. Cullis A. G., Chew G., Irvine S. J. C. and Giess J., *Inst. Phys. Conf. Ser.* **87**, Section 2, (1987), 141.

10. Brown P. D., Hails J. E., Russell G. J. and Woods J., *Appl. Phys. Lett.* **50**, (1987), 1144.

11. Brown P. D., Hails J. E., Russell G. J. and Woods J., *J. Cryst. Growth* **86**, (1988), 511.

12. Feldman R. D., Austin R. F., Dayem A. H. and Westerwick E. H., *Appl. Phys. Lett.* **49**, (1986), 797.

13. Feldman R. D., Kisker D. W., Austin R. F., Jeffers K. S. and Bridenbaugh P. M., *J. Vac. Sci. Technol. A* **4(4)**, (1986), 2234.

14. Hwang S., Harper R. L., Haris K. A., Giles N. C., Bicknell R. N., Cook Jr J. W. and Schetzina J. F., *J. Vac. Sci. Technol. A* **6**, (1988), 2821.

15. Wood S., Greggi Jr J., Farrow R. F. C., Takei W. J., Shirland F. A. and Noreika A. J., *J. Appl. Phys.* **55**, (1984), 4225.

16. Sporken R., Lange M. D., Sivananthan S. and Faurie J. P., *Appl. Phys. Lett.* **59**, (1991), 81.

17. Kuo T. C., Chi Y. T., Ghosh P. K., G K. P. and Beasock J., *Thin Solid Films* **197**, (1991), 107.

18. Thomson J., Woodhouse K. T. and Dineen C., *J. Cryst. Growth* **77**, (1986), 452.

19. Astles M. G., in *Properties of Narrow Gap Cadmium-based Compounds,* Capper P, Ed. (INSPEC, London, 1994), EMIS Datareviews Series No.10, Section A1.2.

20. Irvine S. J. C., in *Properties of Narrow Gap Cadmium-based Compounds,* Capper P, Ed. (INSPEC, London, 1994), EMIS Datareviews Series No.10, Section A1.3.

21. Arias J. M., in *Properties of Narrow Gap Cadmium-based Compounds,* Capper P, Ed. (INSPEC, London, 1994), EMIS Datareviews Series No.10, Section A1.4.

22. Bernardi S. and Franzosi P., in *Properties of Narrow Gap Cadmium-based Compounds,* Capper P, Ed. (INSPEC, London, 1994), EMIS Datareviews Series No.10, Section A5.11.

23. Bell S. L. and Sen S., *J. Vac. Sci. Technol. A* **3**, (1985), 112.

24. Tunnicliffe J., Irvine S. J. C., Dosser O. D. and Mullin J. B., *J. Cryst. Growth* **68**, (1984), 245.

25. Bhat I. B., Fardi H., Ghandhi S. K. and Johnson C. J., *J. Vac. Sci. Technol. A* **6**, (1988), 2800.

26. Bhat I. B., *J. Cryst. Growth* **117**, (1992), 1.

27. Bevan M. J., Doyle N. J., Greggi J. and Snyder D., *J. Vac. Sci. Technol. A* **8**, (1990), 1049.

28. Triboulet R., Tromson-Carli A., Patriarche G., Lorans D. and Nguyen Duy T., *Adv. Mat. for Optics and Elec.* **3**, (1994), 239.

29. Edwall D. D., Bajaj J. and Gertner E. R., *J. Vac. Sci. Technol. A* **8**, (1990), 1045.

30. Stringfellow G. B., in *Handbook of Crystal Growth vol. 3, Thin Films and Epitaxy Part B: Growth Mechanisms and Dynamics,* Hurle D T J, Ed. (Elsevier Science B. V., Amsterdam, 1994).

31. Stringfellow G. B., *J. Cryst. Growth* **68**, (1984), 111.

32. Jensen K. F., in *Handbook of Crystal Growth vol. 3, Thin Films and Epitaxy Part B: Growth Mechanisms and Dynamics,* Hurle D T J, Ed. (Elsevier Science B. V., Amsterdam, 1994).

33. Kuech T. F. and Jensen K. F., in *Thin Film Processes II*, Vossen J L, Kern W, Eds. (Academic Press, Inc., San Diego, 1991).

34. Kisker D. W. and Kuech T. F., in *Handbook of Crystal Growth vol.3, Thin Films and Epitaxy Part A: Basic Techniques*, Hurle D T J, Ed. (Elsevier Science B. V., Amsterdam, 1994).

35. Williams J. O., in *Growth and Characterisation of Semiconductors*, Stradling R A, Klipstein P C, Eds. (Adam Hilger, Institute of Physics Publishing Ltd, Bristol, 1990).

36. Stringfellow G. B., *Organometallic Vapor-Phase Epitaxy: Theory and Practice*, San Diego: Academic Press Inc., 1989.

37. Hails J. E., *Advanced Materials for Optics and Electronics* **3**, (1994), 151.

38. Edwall D. D., Gertner E. R. and Bubulac L. O., *J. Cryst. Growth* **86**, (1988), 240.

39. Irvine S. J. C., Mullin J. B., Giess J., Gough J. S., Royle A. and Crimes G., *J. Cryst. Growth* **93**, (1988), 732.

40. Shigenaka K., Uemoto T., Sugiura L., Ichizono K. and Hirahara K., *J. Cryst. Growth* **117**, (1992), 37.

41. Giess J., Hails J. E., Graham A., Blackmore G., Houlton M. R., Newey J., Young M. L., Astles M. G., Bell W. and Cole-Hamilton D. J., *J. Elec. Mat.* **24(9)**, (1995), in press.

42. Cinader G., Raizman A. and Sher A., *J. Vac. Sci. Technol. B* **9(3)**, (1991), 1634.

43. Million A., Di Cioccio L., Gailliard J. P. and Piaguet J., *J. Vac. Sci. Technol. A* **6(4)**, (1988), 2813.

CHAPTER 4

Theory of Characterisation and Experimental Techniques

4.1 Introduction

The aim of this chapter is to describe the experimental techniques which have been used to characterise the layers whose growth was described in Chapter 3. The specific experimental conditions used are also given in this chapter except for X-ray diffraction studies, where a number of different arrangements have been used and for which details are given alongside the data as it is presented.

The theory of X-ray and electron diffraction is not given in this chapter since many reviews have been written on this matter. Only the principles of diffraction as they apply to semiconductor characterisation will be presented.

4.2 X-ray Diffraction

4.2.1 Introduction

A perfect crystal can diffract X-rays since their wavelengths are of the order of the interplanar spacing of a crystal lattice. For a given wavelength, constructive interference occurs at particular angles of incidence given by the well known Bragg equation (equation 4.1), where n is the order of diffraction, λ is the X-ray wavelength, θ_B is the Bragg angle and d is the interplanar spacing. Equation 4.1 can be rewritten as equation 4.2 where n has been incorporated into d to give d_{hkl} for an hkl reflection from a cubic unit cell (equation 4.3).

$$n\lambda = 2d \sin\theta_B \qquad \text{equation 4.1}$$

$$\lambda = 2d_{hkl} \sin\theta_B \qquad \text{equation 4.2}$$

$$d_{hkl} = \frac{1}{\sqrt{h^2 + k^2 + l^2}} \qquad \text{equation 4.3}$$

Bragg's law and how equation 4.2 is satisfied in regions of perfect and distorted lattice is the basis for all the X-ray and electron diffraction contrast reported in this thesis.

A number of X-ray diffraction techniques have been used in the present study and are described in the following sections. The Kinematical and Dynamical theories of X-ray diffraction will not be described, but can be found in references 1 and 2 respectively.

4.2.2 High Resolution X-ray Diffraction

4.2.2.1 Introduction

High resolution X-ray diffraction involves the illumination of a specimen crystal with a monochromatic X-ray beam where the angle of incidence is varied about the specimen Bragg angle and the resulting diffraction profile is called a rocking curve. The first crystal is the reference crystal which is set to satisfy the Bragg condition and diffracts only a narrow band of wavelengths which reach the second crystal, the specimen. The technique could more accurately be called double axis X-ray diffraction since more than one crystal reflection can be used to monochromate the X-ray beam, this would lead to a narrower band of wavelengths reaching the specimen. A pair of slits is usually positioned between the reference and specimen crystals to remove the $K\alpha_2$ characteristic line of the X-ray tube, leaving only the $K\alpha_1$ line to reach the specimen. A schematic diagram of a high resolution diffractometer as used in the present work is given in figure 4.1. The arrangement shown is known as the parallel non-dispersive (+n,-n) configuration. Other configurations which may be adopted for HRXRD have been reviewed by Hudson[3] along with a discussion of their relative merits.

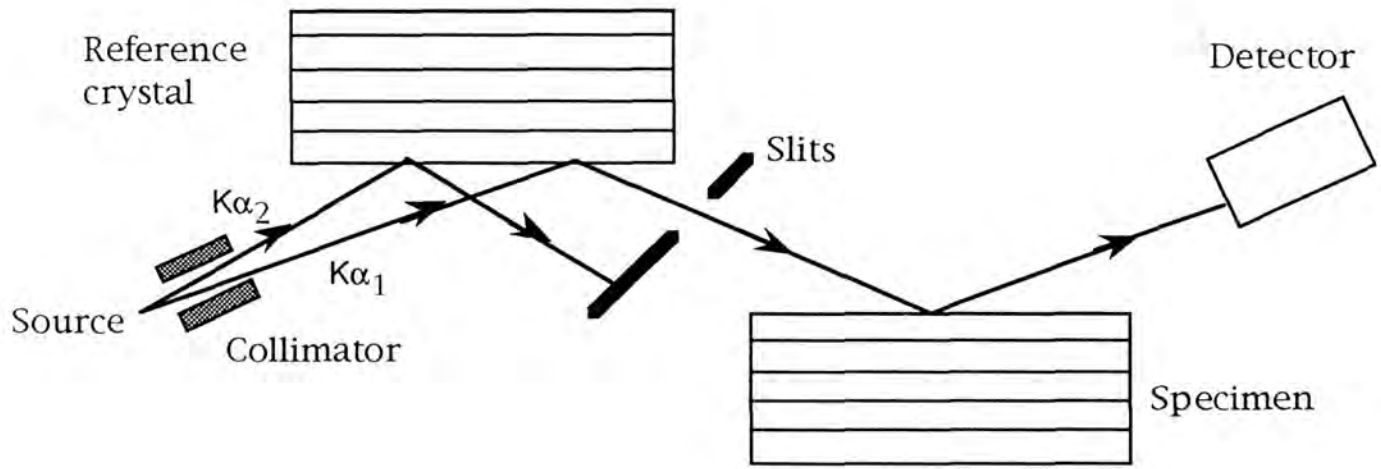

Figure 4.1 High Resolution X-ray Diffractometer in parallel non-dispersive (+n, -n) configuration. The $K\alpha_2$ characteristic line of the X-ray source is removed by a pair of slits between the reference and specimen crystals.

The structural quality of semiconductor crystals can be assessed by measuring the full width at half maximum (FWHM) of the HRXRD rocking curve. An estimation of dislocation density can also be obtained from FWHM and this is discussed in Section 4.2.2.3. Assuming that the reference and specimen crystals are of the same lattice parameter and are not tilted relative to each other (the effects of these situations are discussed in Section 4.2.2.2), then the broadening of a rocking curve from its intrinsic width arises from local lattice tilts (mosaic spread) and variation in lattice parameter (lattice dilatations). Since a high resolution diffractometer operates with an open detector, scattered intensity is collected from the specimen over all angles within its aperture. Broadening due to tilts and dilatations cannot be distinguished by HRXRD.

4.2.2.2 Experimental Broadening of Rocking Curves

When the reference and specimen crystals do not have the same interplanar spacing the HRXRD FWHM increases, since different wavelengths satisfy the Bragg condition as the specimen is rotated about its mean position relative to the reference crystal. The broadening of the rocking curve, $\delta\theta$ is given in equation 4.4 (for the so-called parallel setting) where θ_1 and θ_2 are the Bragg angles of the specimen and reference crystals, and $\delta\lambda/\lambda$ is the fractional spread in wavelength of the X-rays reaching the specimen.

$$\delta\theta = \left|\tan\theta_1 - \tan\theta_2\right| \left(\frac{\delta\lambda}{\lambda}\right) \qquad \text{equation 4.4}$$

If $\delta\lambda/\lambda$ is taken to be the intrinsic width of the $K\alpha_1$ line, the effect of using a GaAs reference crystal and a CdTe specimen would be to broaden the CdTe rocking curve by 8 arcseconds for $CoK\alpha_1$ radiation. The use of an InSb reference crystal which has almost the same lattice parameter as CdTe would give no significant broadening.

Rocking curves can also be broadened if there is an angular offset between the diffracting planes of the reference and specimen crystals.

Schwarzchild[4] derived an expression (equation 4.5) for the broadening of a rocking curve, $\delta\theta$, by an angular offset of reference and specimen, ϕ_c, and a vertical beam divergence, ϕ_v (ϕ_v is measured from the horizontal to the furthest vertical extent of the beam), where θ_1 and θ_2 have the same meanings as in equation 4.4.

$$\delta\theta = \phi_c \, \phi_v + \frac{1}{2}\left|\tan\theta_1 - \tan\theta_2\right| \phi_v^2 \qquad \text{equation 4.5}$$

If the reference and specimen crystals are of the same lattice parameter, then the second term of equation 4.5 is zero and the broadening is simply given by the product of the angular offset and vertical beam divergence (both in radians). The tilt offset also results in a slight shift in the measured Bragg angle and a decrease in peak height. By altering the crystal tilt and measuring the rocking curve, the maximum peak height will be obtained when the X-ray beam is normal to the diffracting planes. Firstly, the reference is aligned by this method, then the specimen is aligned similarly with the diffracted intensity from the reference. This process is referred to as tilt optimisation in later chapters and minimises ϕ_v. It is estimated that an offset of up to 0.5° may still be present after this optimisation which would lead to a broadening of the rocking curve of 6 arcseconds. This is negligible compared to the rocking curve widths of over 100 arcseconds which were recorded for CdTe/GaAs. Limiting the vertical extent of the beam using horizontal slits between the reference and specimen drastically reduces ϕ_v and the rocking curve broadening. The second term in equation 4.5 is very small compared to the first for a well aligned (small ϕ_v) specimen even when a large difference in Bragg plane spacing between reference and specimen exists. All of these assumptions are valid only for the so-called parallel (+n, -n) and (+n, -m) settings which have been used throughout the present work.

4.2.2.3 Estimation of Dislocation Density from FWHM

An equation relating the density of excess dislocations of one sign in tilt boundaries with HRXRD FWHM was proposed by Gay, Hirsch and Kelly[5] in

1953. A modified form of this equation is given in equation 4.6. The modifications allow for rocking curve broadening other than that due to mosaic spread. If it is assumed that rocking curves and all broadening factors are Gaussian in shape[5,6], then, according to the properties of Gaussian distributions, the square of the standard deviation (i.e. variance) of the measured rocking curve is equal to the sum of the squares of the standard deviations of all the broadening factors.

$$D = \frac{\left(\beta^2 - B^2\right)}{9b^2_{e\text{-}tilt}} \qquad \text{equation 4.6}$$

If it is assumed that the only broadening effects are due to mosaic spread (FWHM=β) and intrinsic broadening (FWHM=B) then there are only two terms in the summation. Note also that FWHM is directly proportional to standard deviation and therefore the sum of the squares of FWHM may be treated in the same way as the sum of the squares of standard deviations. In the present work B was evaluated for each layer using the software program RADS* .

Equation 4.6 has been used by several authors to estimate the dislocation density of semiconductor films[6-9], however there are disagreements as to the value of $b_{e\text{-}tilt}$ (whether the whole magnitude of the Burgers vector or just the tilt component should be used) and on whether to correct for broadening by factors other than mosaic spread (many authors ignore B in equation 4.6). The values of dislocation density obtained from equation 4.6 have been found to be an overestimate compared to etch pit density[10]; this may be due to the penetration of X-rays into the more dislocated interfacial regions of a layer or due to rocking curve broadening by lattice dilatations which would increase the value of β^2 used. For layers which are known to have considerable lattice dilatations compared to mosaic spread, an estimate of the FWHM due to dilatations should be made using triple axis diffractometry and an additional correction term included in equation 4.6.

---

* RADS is a dynamical simulation package available from Bede Scientific Instruments Ltd.

Rocking curve broadening due to lattice dilatations is negligible compared to mosaic spread for the layers investigated in the present work (Section 6.2).

4.2.3 Triple Axis X-ray Diffraction

4.2.3.1 Introduction

A double axis X-ray diffractometer uses an open detector and collects diffracted intensity from the specimen for all angles within its aperture. As the specimen is moved about its mean position, regions of different relative tilt and lattice parameter will satisfy the Bragg condition. An open detector cannot resolve these two effects. If an analyser crystal is mounted before the detector on a "third" axis concentric with the "second" (specimen) axis and may be scanned independently of the specimen, then diffracted intensity can be measured as a function of diffracted angle. This diffraction arrangement is termed triple axis mode and is shown schematically in figure 4.2. Detailed descriptions of the alignment procedure and scanning modes of a triple axis diffractometer are given in reference 3.

Triple axis diffractometry enables lattice tilts and dilatations to be distinguished. If all the crystals in figure 4.2 are set to their Bragg condition then a high intensity of X-rays will reach the detector. For a perfect specimen crystal, rotation about its axis (axis 2) will result in no intensity reaching the detector. If the specimen is made up of regions of different relative tilt i.e. it has a mosaic spread, then as it is rotated about axis 2, different regions will satisfy the Bragg condition. The rocking curve so obtained gives a measure of the mosaic spread. Regions of different lattice parameter will not contribute since they will scatter X-rays through a different angle which will not be "transmitted" by the analyser crystal.

Lattice dilatations can be measured independently of lattice tilts if the analyser is scanned at twice the rate of the specimen (this is known as a θ-2θ scan). As the scan proceeds, regions of the specimen which are tilted with respect to each other will diffract, but the Bragg condition at the analyser

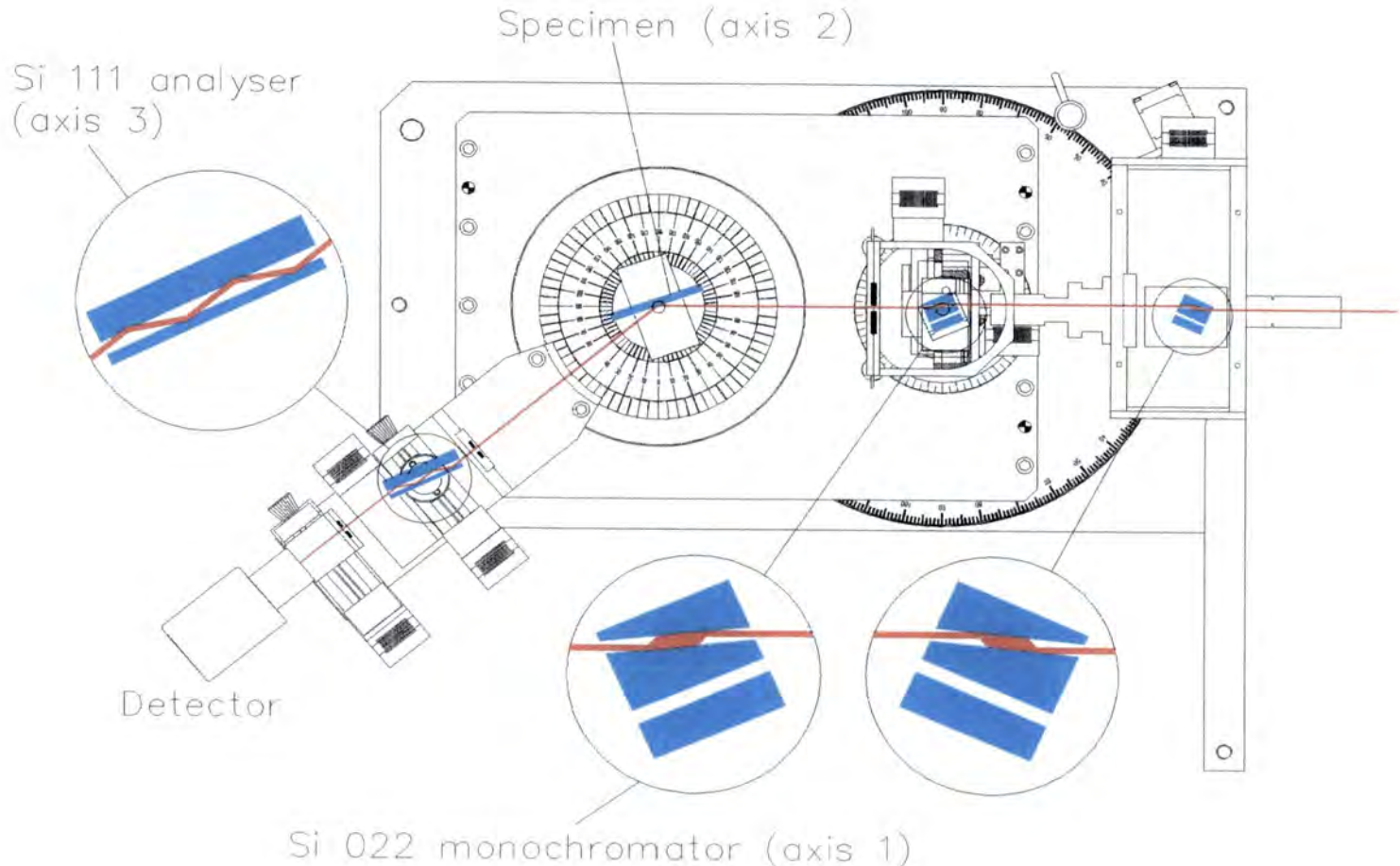

Figure 4.2 Schematic diagram of a Bede D3 diffractometer fitted with a triple axis stage. Diagram courtesy of Bede Scientific Instruments Ltd.

crystal will not be satisfied. Regions of different lattice parameter will diffract when the Bragg condition is satisfied and the diffracted intensity would be "transmitted" by the analyser which moves with the diffraction angle, 2θ.

Triple axis diffraction can be used in two ways, either to record the two scans described above and hence resolve lattice tilts and dilatations, or to record a full reciprocal space map. A reciprocal space map of the scattering around a reciprocal lattice point can be obtained from a series of scans which are coupled so as to trace out a grid in reciprocal space. This is described in references 3,11 and 12.

4.2.3.2 Transforming from Real to Reciprocal Space

Reciprocal space mapping involves recording scattered X-ray intensity as a function of the angular positions of the specimen (ψ) and analyser (φ) crystals. These real space parameters can be transformed into reciprocal space using the relationships given in equations 4.7 and 4.8. The derivation of these equations is described in references 3,11,12. ΔQ_z and ΔQ_y are the components of the deviation of the scattering vector from the "ideal" and can be calculated by a software package from $\Delta\varphi$ and $\Delta\psi$; a map of scattered intensity in reciprocal space can then be produced. Broadening in the ΔQ_y direction is due to mosaic spread while broadening in the ΔQ_z direction is due to lattice dilatations.

$$\Delta Q_z = \frac{\Delta\varphi \cos\theta_B}{\lambda} \qquad \text{equation 4.7}$$

$$\Delta Q_y = \frac{\left(2\Delta\psi - \Delta\varphi\right) \sin\theta_B}{\lambda} \qquad \text{equation 4.8}$$

4.2.4 Laue Back Reflection Diffraction

In Laue diffraction unfiltered radiation is directed at a single crystal and the diffracted intensity is recorded on photographic film. The Bragg angle is fixed for each set of crystal planes and each set will satisfy the Bragg condition for wavelengths given by equation 4.2, according to d_{hkl} and θ. Each diffracted beam has a different wavelength. Laue photographs can be recorded in transmission or back reflection mode depending on the position of the photographic film relative to the source and specimen. For the present work, unfiltered radiation from a copper X-ray tube was used with the film placed between the source and specimen in the back reflection geometry, as shown in figure 4.3.

All the planes of a zone axis diffract beams which lie on the surface of a cone. The axis of the cone is the zone axis and the semiapex angle is equal to the angle between the transmitted beam and the zone axis. The Laue geometry and the interception of the diffracted beams with the film are shown in figure 4.4. If the zone axis is exactly perpendicular to the transmitted beam, then the cone will intersect the film in a straight line passing through its centre. If the zone axis is inclined at an angle of between 45° and 90° to the beam, then the cone intersects the film in a hyperbola. The orientation of the zone axis relative to the beam can be determined since the diffracting plane normals always bisect the angle between the incident and diffracted beam. If the distance between the film and specimen is known, then the magnitude of the inclination can also be measured using a Greninger chart, details of this procedure can be found in reference 13.

Figure 4.5 is a typical Laue back reflection photograph of the CdTe/GaAs epilayers studied in later chapters. The specimen was mounted 3cm from the film in a known orientation determined from the flats on the wafer. From the position of the hyperbolae relative to the film and the wafer flats, the offcut direction and magnitude of substrates were determined.

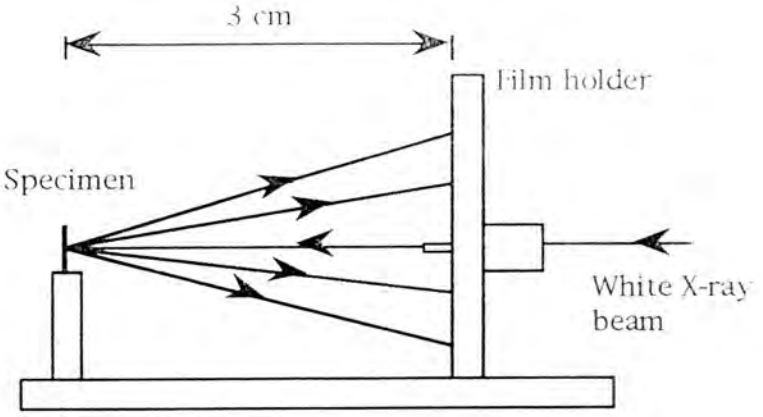

Figure 4.3 Laue back reflection geometry.

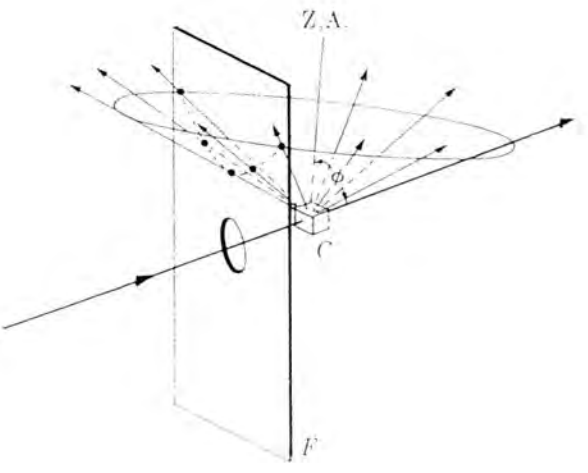

Figure 4.4 Formation of hyperbolae in Laue back reflection diffraction. C=crystalline specimen, Z.A.=zone axis, F=film. Diagram from reference 13.

Figure 4.5 Laue back reflection diffraction pattern of a (001)GaAs substrate offcut 3.5° towards [$\bar{1}$00] about [010].

4.2.5 Double Crystal X-ray Topography

A detailed description of X-ray topography (XRT) theory and methods is not given here but can be found in references 2 and 14. Double crystal X-ray topography (DCXRT), in reflection geometry, is configured similarly to HRXRD except that a larger incident beam is used and the diffracted intensity is recorded on photographic film rather than by a detector. An image of the diffracted X-ray intensity exiting the specimen is recorded and shows contrast according to strain variations and tilt misorientations.

A dislocation has a strain field associated with it which produces contrast in the topographic image in a similar way to the production of images in transmission electron microscopy. X-ray diffraction is approximately 1000 times more sensitive to strain than electron diffraction and this leads to broader images of dislocations. This puts an upper limit on the density of dislocations at which individual dislocations can be imaged by XRT. For highly dislocated materials, TEM is more useful for dislocation imaging and in this sense the two methods are complementary. Regions which are misoriented with respect to each other will show topographic contrast since the narrow wavelength band "passed" by the reference crystal in DCXRT will not satisfy the Bragg condition for all regions. This has been utilised in the present study to investigate the distribution and size of tilt domains in CdTe/GaAs epilayers. It should be noted that CdTe/GaAs layers have residual strain[15] and may be bowed, which may result in only a small region of the specimen being correctly oriented for Bragg diffraction. This in turn reduces the size of the topograph obtained, despite the large area of the incident beam.

4.3 Transmission Electron Microscopy

4.3.1 Introduction

Transmission electron microscopy (TEM) is the most widely used technique for the observation of dislocations and other crystal defects such as stacking

faults, twins, grain boundaries and voids. In particular the technique can be used for imaging dislocations in highly dislocated films where individual dislocations cannot be imaged by XRT. All the TEM investigations presented in this thesis were carried out on a JEOL JEM 200CX operating at 200keV. The de Broglie wavelength of the electrons[16] is 2.5 pm and they can be diffracted by crystal planes according to Bragg's law (equation 4.2). The Bragg angles are very small compared with those of X-ray diffraction and different diffraction conditions can be obtained by relatively small tilt adjustments of the specimen. The Kinematical and Dynamical theories of electron diffraction are analogous to those for X-ray diffraction and are presented in reference 16. The application of the Kinematical and Dynamical theories to faulted crystals and the determination of the nature of dislocations, stacking faults and other crystal defects are also to be found in the reference by Hirsch et al.[16].

The Burgers vector of a dislocation can be determined by attempting to image the dislocation under different diffraction conditions. If the dislocation has a Burgers vector **b**, line direction ℓ, and the diffraction vector operating is **g**, then for a perfect screw dislocation, the dislocation will be invisible for $\mathbf{g}\cdot\mathbf{b}=0$. For a perfect edge dislocation to be invisible then both $\mathbf{g}\cdot\mathbf{b}$ and $\mathbf{g}\cdot\mathbf{b}\times\ell$ must be equal to zero. A general dislocation will be effectively invisible when $(1/8)(\mathbf{g}\cdot\mathbf{b}\times\ell) \lesssim 0.08$, this is discussed by Hirsch et al. in reference 16 and by Gandais et al. in reference 17. More recently, Ngan[18], has proposed a useful test to distinguish between $g.b=0$ and $\neq 0$. The test is that for $\mathbf{g}\cdot\mathbf{b}=0$, the dislocation residual contrast appears on both sides of the $\mathbf{s}=0$ line (**s** is the deviation from the exact Bragg condition), while for $\mathbf{g}\cdot\mathbf{b}\neq 0$, the residual contrast moves from one side of the line to the other when the beam is tilted in the plane containing **g** and the vertical microscope axis. The inclination of a dislocation with respect to the TEM foil can be determined by noting the contrast of the dislocation ends in bright and dark field imaging. This is briefly described in Chapter 7 where the technique is used, it is discussed in more detail in reference 16.

4.3.2 Image Rotation and Polarity Determination

In order to determine the direction of the diffraction vector, **g** in relation to the image, the relative rotation of the diffraction pattern and image must be determined. The relative rotation is caused by the different lens currents used to focus the diffraction pattern and image onto the film. The rotation must be calibrated using, for example Orthorhombic α-molybdenum trioxide crystals, for each magnification used[19]. The crystals have a long edge perpendicular to [100], as shown in figure 4.6, which corresponds to a short spot separation in the diffraction pattern[20] (also shown in figure 4.6). There is a 180° uncertainty in indexing [100] and [$\bar{1}$00], and a rotation of 180° between image and diffraction pattern introduced by the objective lens. If one of the diffraction spots is underfocussed and compared to the image, then it can be seen whether or not a 180° rotation exists in addition to the rotation caused by the intermediate and projector lenses. The knowledge of this relative rotation allows dislocation directions in plan view TEM to be inferred (Chapter 7) and is needed for polarity determination in XTEM.

The non equivalence of [110] and [$\bar{1}$10] directions in the sphalerite lattice was discussed in Section 2.5; this can have a large influence on the defect structure which is found in the two orthogonal directions. Brown et al.[19,21] have shown that microdiffraction in XTEM can be used to determine the sense of advancing {111}A planes; from this the [110] and [$\bar{1}$10] direction can be distinguished.

Microdiffraction was carried out for orthogonal [110] and [$\bar{1}$10] beam directions according to the method described by Brown[19]. The microdiffraction pattern shown in figure 4.7 is from the GaAs substrate of a (001)CdTe/GaAs epilayer with the beam direction into the plane of the paper. In figure 4.7, a {911} and a {11 1 1} reflection are strong, as is the [004]. A dark cross can be seen in the {002} diffraction spot; the vector from the central spot to the spot with the deficiency cross gives the sense of the advancing {111}A planes in the substrate. When the microdiffraction pattern is superimposed on the XTEM image (requiring a knowledge of the relative rotation of the image and diffraction pattern described above), then

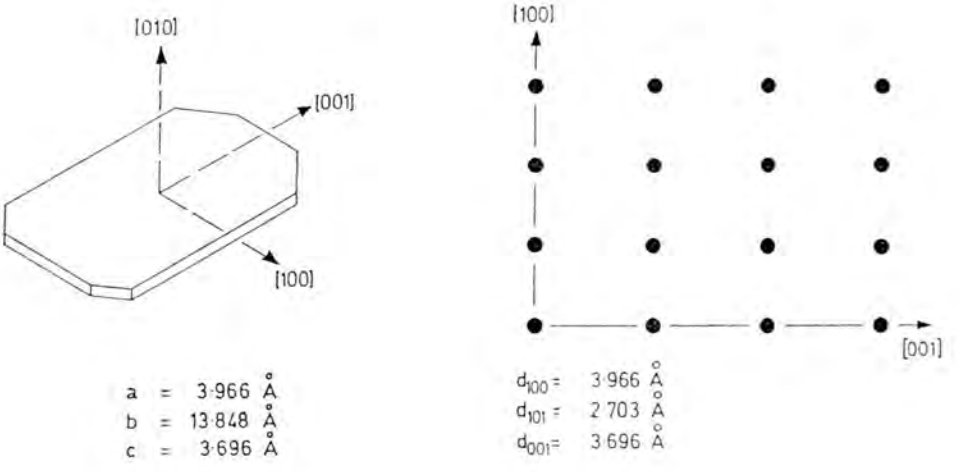

Figure 4.6 Schematic illustration of a single crystal of α-molybdenum trioxide and its diffraction pattern used to calibrate the relative rotation of the diffraction pattern and image. Diagram from reference 20.

the sense of the advancing A planes can be established relative to the substrate/layer interface. Figure 4.7 shows the deficiency cross in the direction of the CdTe layer which is known to be (001) oriented, which gives a beam direction of $[\bar{1}10]$ into the plane of the paper.

4.3.3 TEM Specimen Preparation

Plan view specimens were prepared so that the top of the epitaxial layer was investigated by TEM. A small (2.5mmx2.5mm or less) piece of material was mounted layer side down on a copper grid and was "dimpled" using a VCR Group D500i Dimpler to a thickness of approximately 20μm. The specimen was then thinned to perforation from the substrate side only, in an Ion Tech ion beam milling machine at 77K using Ar^+ ions. An accelerating voltage of 6kV was used with an ion current of approximately 20μA and a beam incidence of 16°. After perforation, the specimen was thinned for a further 10 minutes with 4kV accelerating voltage, 5μA ion current and 16° beam incidence. Argon ion thinning has been shown to produce dislocation loops in CdTe[22-24] even when cooled to 77K. Chew and Cullis[23] have shown that iodine reactive ion sputtering gives superior quality TEM specimens. Therefore, before being examined by TEM, the plan view specimens were thinned for 10 minutes from the substrate side and 5 minutes from the layer side at room temperature in a modified Ion Tech ion beam milling machine with iodine sources. The thinning conditions employed were an accelerating voltage of 4kV, ion current of 4μA and beam incidence of 16°.

Cross-section TEM specimens were prepared using a similar method to Brown[19]. As-grown samples were cleaved to produce two thin strips of material with orthogonal cross-section projections. They were glued layer to layer and fixed between two blocks of polycrystalline silicon to form a Si/substrate/layer/layer/substrate/Si sandwich. The sandwich was mechanically polished using 12μm alumina slurry until it was approximately 0.5mm thick. A 3.05mm diameter disk was cut out and one side was polished using 5μm, 3μm and finally 0.3μm diamond slurry. This polished side was stuck face down onto a slotted copper disc and thinned to 100μm thickness

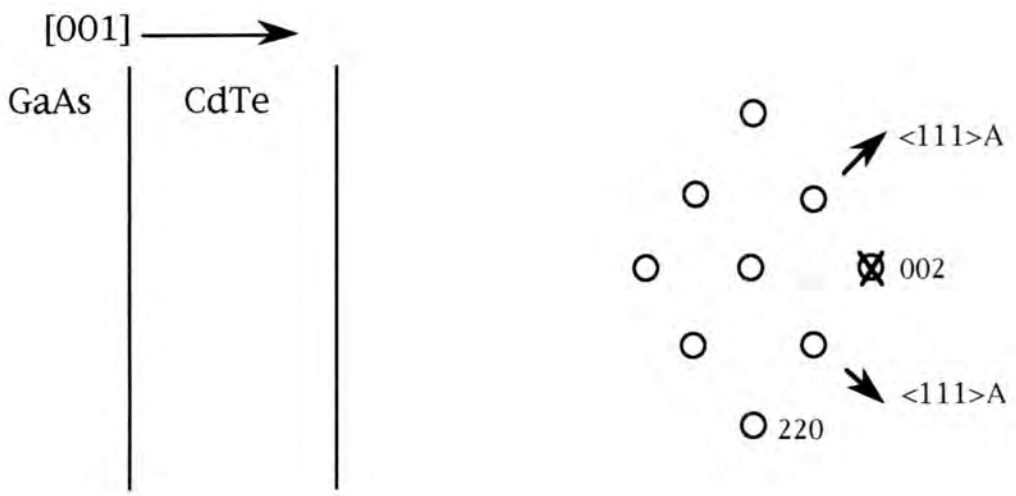

Figure 4.7 (a) Microdiffraction pattern of (001)CdTe/GaAs in cross section, showing a dark cross in the [002] diffraction spot caused by destructive interference from the interaction of a pair of doubly diffracted {911} and {11 1 1} reflections with the directly scattered [002] beam. (b) The dark cross is in the CdTe epilayer and gives the sense of the advancing {111}A planes. The beam direction is determined to be [$\bar{1}$10] into the plane of the paper.

with 3μm slurry and a "flatting" tool on a VCR Group dimpler. A further 70μm was removed using 0.3μm slurry and a "dimpling" tool. The 30μm thick specimen was then thinned to perforation from both sides using Ar^+ ions at 77K, with the guns set at the initial conditions given for the plan view specimens. After perforation the samples were thinned for a further 10 minutes from both sides using gun conditions of 4kv and 5μA. As for the plan view specimens, to remove Ar^+ thinning damage, iodine reactive ion sputtering with 4KV accelerating voltage, 4μA ion current and 16° beam incidence was used at room temperature for 10 minutes from each side of the specimen.

4.4 Epitaxial Layer Thickness Determination

4.4.1 Thickness Determination by Infrared Transmission

When light is incident on an interface, intensity is reflected and transmitted. The ratio of these components is determined from Fresnel's equations, and the effect will occur at each interface encountered. If light is incident on a single epilayer on a thick substrate then the light transmitted will contain a direct component which has not undergone reflection together with components which have been reflected by the layer/substrate and layer/air interfaces. The effective path difference between these components is dependent on the thickness and refractive index of the epilayer. This path difference leads to constructive and destructive interference fringes which depend on wavelength.

Making the approximation that refractive index is constant with wavelength over the wavenumber range 500-4000cm^{-1}, the film thickness can be calculated from the spacing of adjacent constructive interference maxima. Equation 4.9 gives the relationship between fringe spacing (difference in wavenumber between adjacent constructive interference maxima), refractive index of the epilayer and thickness. This formula is derived by considering the reflectance and transmission of a thin film[25,26]. In equation 4.9, t is the layer thickness, n is the refractive index of the layer,

υ_N is the wavenumber at the N^{th} maximum and υ_{N+1} is the wavenumber at the $(N+1)^{th}$ maximum.

$$t = \frac{1}{2n_{layer}\left|\upsilon_N - \upsilon_{N+1}\right|} \qquad \text{equation 4.9}$$

Infrared transmission spectra were recorded for CdTe/GaAs and CMT/CdTe/GaAs epilayers using a Bio-rad Fourier transform infrared spectrometer. Examples of spectra recorded for 23.5μm and 4.1μm CdTe/GaAs epilayers are shown in figure 4.8. Thickness maps were generated from spectra recorded at points on a grid over the area of a wafer. This was discussed in relation to thickness non-uniformities in Section 3.4.2.

4.4.2 Thickness Determination by X-ray Absorption

The thickness of a thin semiconductor layer on a substrate can be determined from the absorption of X-rays by the epilayer. If an X-ray rocking curve is recorded for a substrate with and without an epilayer, then the difference in integrated intensity allows the layer thickness to be calculated from equation 4.10. In equation 4.10, I(0) is the integrated intensity of a clean substrate, I(x) is the integrated intensity of the rocking curve recorded through the overlayer, t is the layer thickness, μ is the linear absorption coefficient of the overlayer at the X-ray wavelength used, and θ_B is the Bragg angle for diffraction by the substrate. Absorption of X-rays is discussed in greater detail in Section 6.4 where a complex form of equation 4.10 is derived. It is very important that the accelerating voltage and current of the X-ray generator are the same when obtaining I(0) and I(x), and that the beam size is not altered. This method of thickness determination was used to map the thickness of a ZnTe/GaAs epilayer investigated in Section 6.6.

$$I(x) = I(0)\exp\left[-2\mu t \operatorname{cosec}\theta_B\right] \qquad \text{equation 4.10}$$

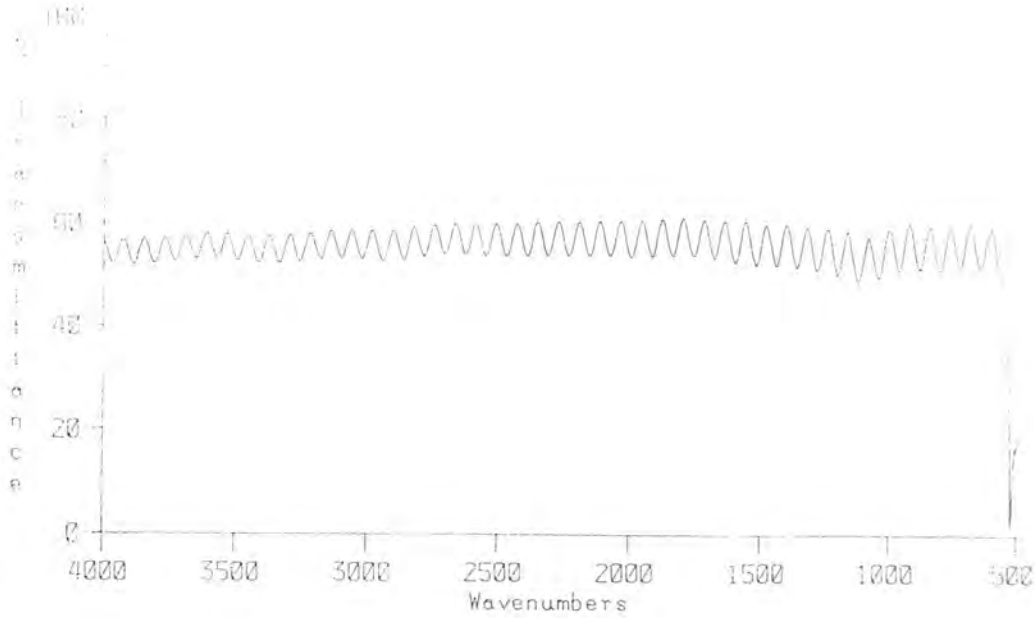

Figure 4.8a Fourier transform infrared transmission spectrum of a 23.5μm thick CdTe/GaAs epilayer.

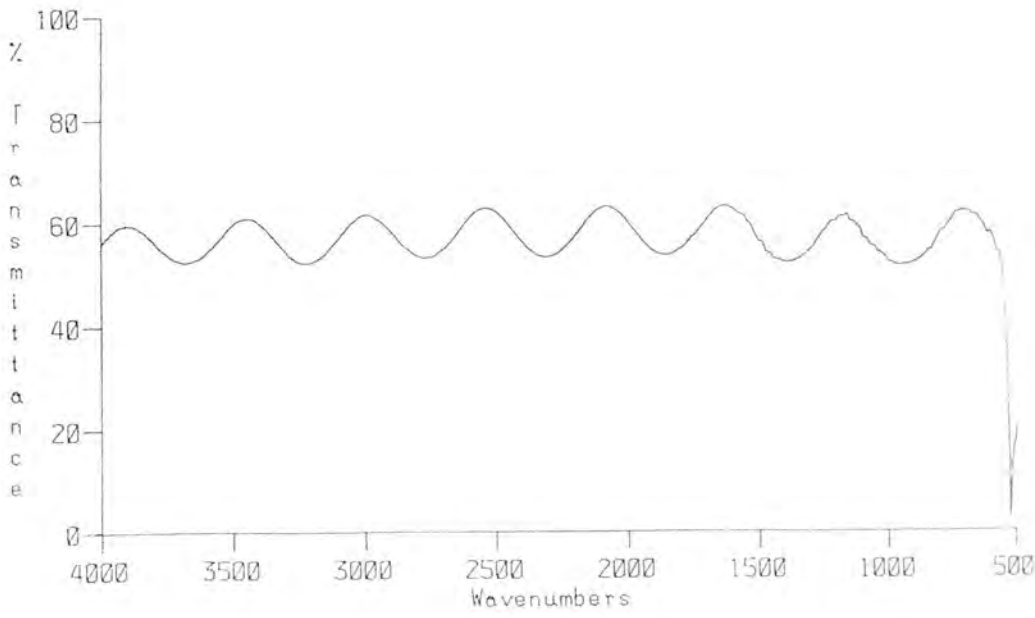

Figure 4.8b Fourier transform infrared transmission spectrum of a 4.1μm thick CdTe/GaAs epilayer.

4.5 Photoluminescence Spectroscopy

Photoluminescence (PL) is the emission of light by a material as a result of being illuminated by light of photon energy greater than its band gap. Photons are emitted due to an electronic transition between two states, the initial high energy state, E_i and final lower energy state E_f. In the most simple case the wavelength, λ of the emitted photon is given by equation 4.11 and is determined by the difference in energies of the initial and final electronic states.

$$\frac{hc}{\lambda} = |E_i - E_f| \qquad \text{equation 4.11}$$

Impurity and defect related luminescence generally dominate at low temperature, where transitions usually occur from the lowest energy exited state. In semiconductor materials many transitions involve excitons which are either free or bound to impurities. Examples of radiative transitions which can occur in semiconductors are given in figure 4.9. Any of the transitions can occur with the emission of one or more phonons, the energy of the emitted photon is decreased from that of equation 4.11 by the energy of the phonon(s). A general review of photoluminescence characterisation of semiconductors can be found in reference 27.

Luminescence from (001)CdTe/GaAs epilayers in the edge and near edge wavelength region were studied using a Spex dispersive monochromator with a grating of 1200 groves per mm and detected with a photomultiplier tube fitted with an extended cathode. The samples were mounted on a cold finger of a helium flow cryostat and were excited at 4.2K with an Ar^+ ion laser operating at 514nm. The data is presented and discussed in Section 6.5*.

* Photoluminescence spectra were collected at the University of Aviero with the help of M. J. Soares and interpreted with the help of M. C Carmo (also at the University of Aviero). Additional advice on interpretation was sought from D. P. Halliday, University of Durham.

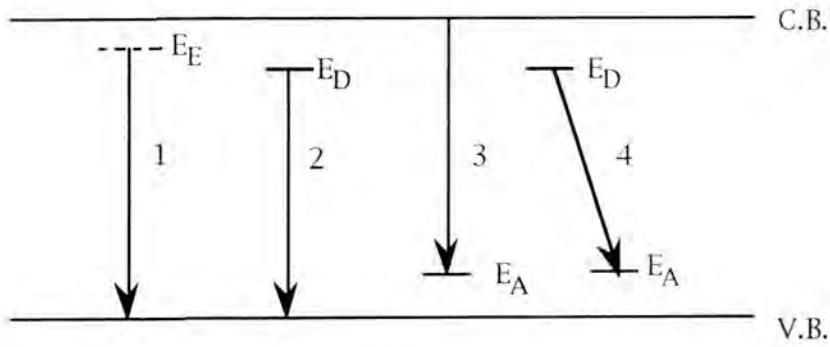

Figure 4.9 Schematic illustration of radiative transitions in semiconductors. C.B.=conduction band, V.B.=valance band.

1. Exciton decay from exciton level E_E. Free exciton recombination is denoted by X, recombination of an exciton bound to a neutral donor is denoted by D°X and recombination of an exciton bound to a neutral acceptor is denoted by A°X.

2. Donor to free hole transition. If transition is from a neutral donor then transition is denoted by D°h.

3. Free electron to acceptor transition. If transition is to a neutral donor then transition is denoted by eA°.

4. Donor acceptor pair recombination. Transition denoted by DAP.

REFERENCES FOR CHAPTER 4

1. Azároff L. Z., *Elements of X-Ray Crystallography*, New York: McGraw Hill, 1968.

2. Tanner B. K., *X-ray Diffraction Topography*, Oxford: Pergamon Press, 1976.

3. Hudson J. M., Ph. D Thesis, *Specular and Diffuse X-Ray Scattering Studies of Surfaces and Interfaces*, University of Durham (1994).

4. Schwarzchild M. M., *Phys. Rev.* **32**, (1928), 162.

5. Gay P., Hirsch P. B. and Kelly A., *Acta Metallurgica* **1**, (1953), 315.

6. Qadri S. B. and Dinan J. H., *Appl. Phys. Lett.* **47**, (1985), 1066.

7. Monfroy G., Sivananthan S., Faurie J. P. and Reno J. L., *J. Vac. Sci. Technol. A* **7(2)**, (1989), 326.

8. Lischka K., Fantner E. J., Ryan T. W. and Sitter H., *Appl. Phys. Lett.* **55(13)**, (1989), 1309.

9. Ayers J. E., Schowalter L. J. and Ghandhi S. K., *J. Cryst. Growth* **125**, (1992), 329.

10. Watson C. C. R., Ph. D Thesis, *Structural Defects in CdTe and Related Materials*, University of Durham (1993).

11. Tanner B. K. and Bowen D. K., *J. Cryst. Growth* **126**, (1993), 1.

12. Bowen D. K., *Fundamentals of Triple Axis Measurements*, Application Note #5 Rev.1 (Bede Scientific Instruments Ltd., 1992).

13. Cullity B. D., *Elements of X-ray Diffraction*, (2nd edition), Addison-Wesley, 1978, Cohen M, Ed. Addison-Wesley Series in Metallurgy and Materials.

14. Bowen D. K., in *Advances in X-Ray Analysis*, Barrett C S, Ed. (Plenum press, New York, 1990), vol. 33, 13.

15. Tatsuoka H., Kuwabara H., Nakanishi Y. and Fujiyasu H., *J. Appl. Phys.* **67(11)**, (1990), 6860.

16. Hirsch P. B., Howie A., Nicholson R. B., Pashley D. W. and Whelan M. J., *Electron Microscopy of Thin Crystals*, London: Butterworths, 1965.

17. Gandais M., Hihi A., Willaime C. and Epelboin Y., *Phil. Mag. A* **45**, (1982), 387.

18. Ngan A. H. W., *Phil. Mag. A* **71(6)**, (1995), 1209.

19. Brown P. D., Ph. D Thesis, *Structural defects in II-VI epitaxial layers*, University of Durham (1988).

20. Kay D. H., Ed., *Techniques for Electron Microscopy*, (Blackwell Scientific Publications, Oxford, 1965).

21. Brown P. D., Durose K., Russell G. J. and Woods J., *J. Cryst. Growth* **101**, (1990), 211.

22. Cullis A. G., Chew N. G. and Hutchison J. L., *Ultramicroscopy* **17**, (1985), 203.

23. Chew N. G. and Cullis A. G., *Ultramicroscopy* **23**, (1987), 175.

24. Lu G., *Phil. Mag. Lett.* **68**, (1993), 1.

25. Vasícek A., *Optics of Thin Films*, Amsterdam: North Holland, 1960.

26. Heavens O. S., *Thin Film Physics*, London: Methuen & Co Ltd., 1970.

27. Lightowers E. C., in *Growth and Characterisation of Semiconductors*, Stradling R A, Klipstein P C, Eds. (Adam Hilger, Institute of Physics Publishing Ltd, Bristol, 1990).

CHAPTER 5

Models of Strain Relaxation and Threading Dislocation Reduction in Heteroepitaxial Layers

5.1 Introduction

In Chapter 2, the concepts of critical thickness and the introduction of misfit dislocations to relieve misfit strain in heteroepitaxial layers were reviewed. In this chapter, the relaxation of heterolayers and the change in dislocation density with layer thickness are investigated in greater detail. Two models[1-3] describing the reduction of residual layer strain with increasing layer thickness are reviewed in Section 5.2. Experimental data which has been published in the literature for three heterosystems with misfits of 0.23%, 4.1% and 14.6% are compared with the two models. In Section 5.3, three different approaches for describing the reduction of threading dislocation density with increasing layer thickness which is observed in heterolayers, especially highly mismatched ones[4], are reviewed[5-7]. Section 5.4 is dedicated to the development of a new geometrical model for the reduction of threading dislocation density with increasing layer thickness.

5.2 Strain Relaxation Models

5.2.1 Geometrical Model for Low Misfit Systems

The accepted models for plastic relaxation of strained epitaxial layers put forward by van der Merwe[8], Matthews and Blakeslee[9] and People and Bean[10,11] are based on strain energy considerations (see Section 2.2.1). The strain energy of the layer, the strain energy of a dislocation and the mechanism by which the first misfit dislocation is formed are considered and a prediction of the thickness at which relaxation will occur is made. All the models agree reasonably well with experiment, although critical

thickness is usually underestimated, and all predict that critical thickness is inversely proportional to strain. The models do not however aim to describe relaxation above critical thickness. Relaxation may take place either completely and discontinuously at critical thickness or perhaps smoothly. Dunstan et al.[1] take a purely geometric approach to predict critical thickness and the manner of relaxation above critical thickness. This model is described and discussed in the remainder of this section.

Dunstan's model[1] considers a perfectly crystalline substrate with a pseudomorphic strained layer of thickness h and strain ε. Misfit dislocations are postulated to form at the heterointerface and relax the strain in the layer. The strain field of a dislocation at the interface of a layer of thickness h decays within a lateral distance mh[12]. A dislocation can therefore only relax strain in the layer over a lateral distance mh; outside this region there is assumed to be no relaxation. For a dislocation with Burgers vector **b**, the average relaxation in the relaxed region is $|\mathbf{b}|/mh$. To a first approximation it is assumed that there is a uniform relaxation within the relaxed region of $\Delta\varepsilon=|\mathbf{b}|/mh$. This is illustrated in figure 5.1a.

There are two key observations to be made. Firstly, that a dislocation will not form if the relaxation due to a dislocation exceeds the strain in the layer i.e. if $|\mathbf{b}|/mh > \varepsilon$: this prevents the sign of the strain being reversed. Secondly, the formation of a dislocation within a width mh requires that dislocations will form in all other regions of width mh in order to preserve translational symmetry. The second observation is allowed since a perfectly crystalline substrate is assumed, containing no preferential sites for dislocation nucleation. The condition for critical thickness occurs when the relaxation afforded by a dislocation equals the strain in the layer. The condition for critical thickness is given in equation 5.1 and agrees with accepted models[8-11]. The model predicts complete discontinuous relaxation at critical thickness h_c, as illustrated in figures 5.1b and 5.2a.

$$h_c=\frac{|\mathbf{b}|}{m\varepsilon} \qquad \text{equation 5.1}$$

If the random nature of dislocation generation is taken into account, then dislocations may form anywhere and there will be gaps between relaxed regions of any width up to a maximum of mh (a separation greater than mh would cause another dislocation to form). The effect of the random generation of dislocations is shown in figure 5.1c. Dunstan makes an analysis of the statistical distribution of the widths of unrelaxed regions and calculates that at critical thickness only three quarters of the original misfit strain is relieved. If it is assumed that a partially relaxed layer may be treated in the same way as a pseudomorphic one, then a new critical thickness can be calculated for the residual strain. In this case, if 75% strain had been relieved at critical thickness, then the partially relaxed layer could be considered to be a layer with a uniform strain of $\varepsilon/4$. A critical thickness four times as large as for the original layer is calculated from equation 5.1. A stepwise relaxation is predicted as shown in figure 5.2b.

If a further refinement is made, assuming that there is a statistical distribution of gaps between dislocations and that wider gaps will relax at smaller thicknesses than narrower gaps, then the stepwise reduction in strain is smoothed after initial relaxation, as shown in figure 5.2c. The relaxation of a strained layer is then given by equations 5.2 and 5.3 where ε_0 is the mismatch and (1-f) the fraction of strain relieved abruptly at critical thickness.

$$\varepsilon(h)=\varepsilon_0 \qquad h<h_c \qquad \text{equation 5.2}$$

$$\varepsilon(h)=\frac{f\varepsilon_0 h_c}{h} \qquad h\geq h_c \qquad \text{equation 5.3}$$

Equation 5.3 predicts that, as the thickness of the relaxing layer is increased, the strain will reduce to zero. However, a thin film can support a finite strain up to its elastic limit. Plastic relaxation therefore continues to the elastic limit of the material after which a residual strain will remain. The model is not expected to apply for thicknesses greater than those at which the residual strain can be supported by the material (the residual strain region). No account has been taken of the existence of substrate defects, which may act as preferential nucleation sites for dislocations. It is expected

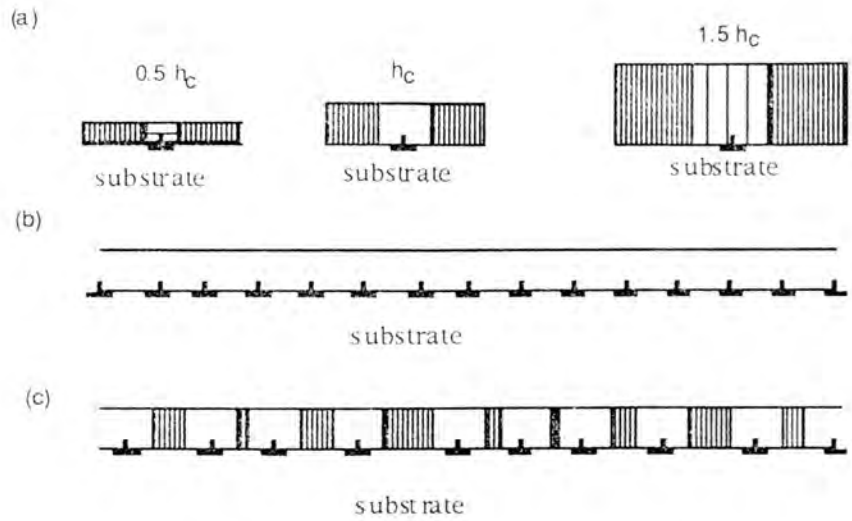

Figure 5.1 (a) Strain relaxation around a misfit dislocation below, at and above critical thickness h_c. Vertical hatching represents in-grown strain, horizontal hatching represents strain of the opposite sign. Density of hatching is proportional to strain. (b) Full and discontinous relaxation at critical thickness. (c) Randomly distributed misfit dislocations with unstrained regions all less than mh wide.

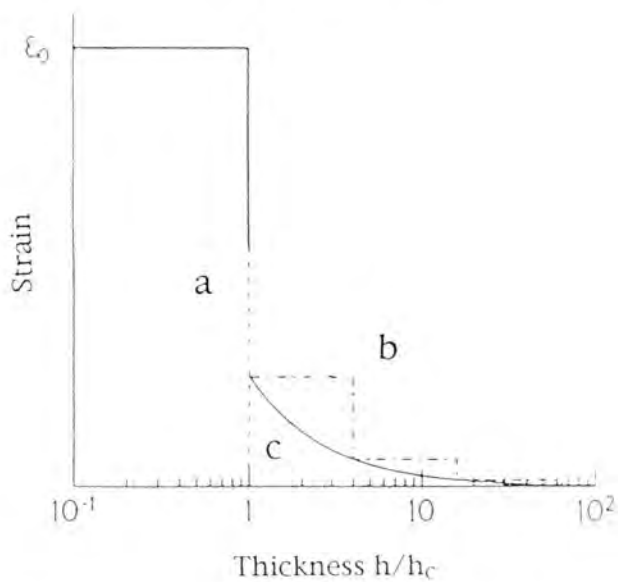

Figure 5.2 Strain relaxation as a function of layer thickness. (a) Full and discontinous relaxation-dashed line. (b) Stepwise relaxation for a layer assumed to be homogeneous after each step-dot dashed line. (c) Smoothing effect of layer strain inhomogeneity-solid line.

therefore, that some relaxation will occur below the critical thickness predicted by this model due to nucleation of dislocations at substrate imperfections. Other limitations of this model are that the magnitude of the misfit must be less than 5% (to ensure that dislocations are not so close that their strain fields interact) and that the growth mode must be layer-by-layer two-dimensional growth.

The thickness range over which this model is applicable is very small as is demonstrated by Dunstan et al. in their subsequent work[13]. Three sets of experimental data, taken from published literature have been used to test this model. Data for the material system ZnSe/GaAs with misfit 0.23% is taken from Yokogawa et al.[14] and was recorded at room temperature. Data for GaAs/Si with misfit of 4.1% is taken from Huang et al.[15] at a temperature of 87°C and, for the case of CdTe/GaAs with misfit 14.6%, the data is taken from Tatsuoka et al.[16]. For CdTe/GaAs, the temperature dependence of the thermal expansion coefficient was taken into account and the strains quoted are for the growth temperature of 300°C[17].

Figure 5.3 shows strain plotted against reciprocal thickness for the three sets of data. Dunstan has proposed that a Universal Relaxation Law exists[18,19] whereby $\varepsilon = k|\mathbf{b}|/h$ with $k|\mathbf{b}| = 0.83$ nm, this universal law is also plotted in figure 5.3. It is clear that none of the data sets follow the relationship given in equation 5.3. All the data sets include measurements for thicknesses greater than the critical thickness. The critical thickness of (001) ZnSe on GaAs is about 150 nm [20,21]. The data from Yokogawa et al.[14] is in the thickness range 150-700 nm. It is possible that all of the data points, except that of the thinnest layer, lie in the residual strain region where the model in question is not valid; indeed figure 5.3 shows that the data for ZnSe/GaAs deviates from the universal relaxation law for thicker layers but lies very close to the theoretical line for the thinnest layer. The model is only valid for two-dimensional layer-by-layer growth which is the case for ZnSe/GaAs but not for GaAs/Si or CdTe/GaAs both of which display three-dimensional growth and do not follow the relaxation law proposed by Dunstan et al..

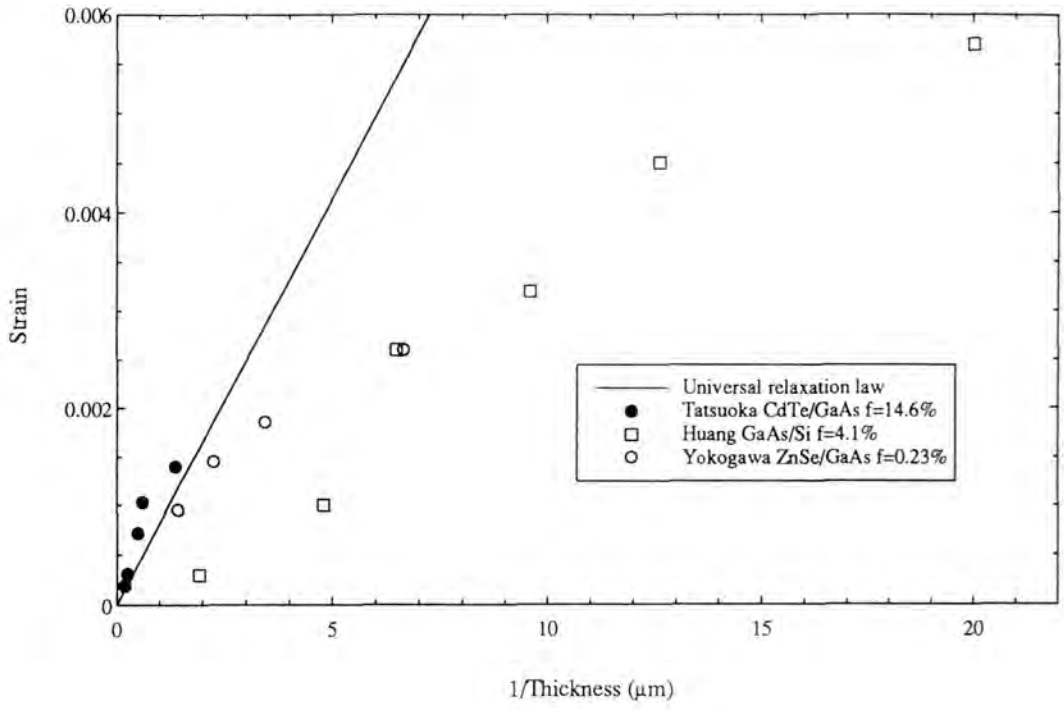

Figure 5.3 Strain vs thickness for three epitaxial systems of different misfit. The solid line shows the universal relaxation law predicted by Dunstan et al.[1]. Data for CdTe/GaAs and GaAs/Si are not valid for this model since both display three dimensional growth. The ZnSe/GaAs data are entering the residual strain region and are beginning to deviate from the universal relaxation law.

The model developed by Dunstan et al. provides a useful rule of thumb, but must be treated with caution to ensure that the system under investigation lies within the narrow window of applicability between critical thickness and the onset of the residual strain region. Dunstan stated in his original paper that the model was valid for systems with misfit less than about 5%. This is likely to be an overestimate of the limiting strain since the onset of three-dimensional growth may occur well below a misfit of 5% (for example $In_xGa_{(1-x)}As$ on GaAs has a transition at x=0.4 which corresponds to a misfit of 2.8% [22]).

The model assumes that long straight misfit dislocations are formed at the heterointerface and that strain is relieved only by this mechanism. Thus layer strain decreases and misfit dislocation density increases as a layer grows. No account has been taken of the strain relieving properties of threading dislocations; the model is therefore unlikely to describe accurately materials which contain many threading dislocations. This observation also lends weight to the argument that layers with 5% misfit are outside the applicability range of the model since systems with such a large misfit usually contain a high density of threading dislocations (for example GaAs/Si f=4.1% [23], InP/GaAs f=3.8% [24]).

5.2.2 Residual Strain Relaxation Model

The theories for strain relaxation of heteroepitaxial layers by van der Merwe[8], Matthews and Blakeslee[9], People and Bean[10,11] (Section 2.2.1) and by Dunstan et al[1] (Section 5.2.1), all assume that strain is relaxed by misfit dislocations which lie in the interface between the substrate and layer. If this is the only means of strain relaxation then the strain in the layer must be homogeneous over epilayer thickness, i.e. strain is constant along the growth direction. Homogeneous strain has been reported by Stolz et al.[25], for the GaAs/Si system, but inhomogeneous strain has been reported by Soga et al.[26] and Huang et al.[15] for GaAs/Si (f=4.1%), Schaffer et al.[27] for InAs/GaAs (f=7%) and by Tatsuoka et al.[28] for

CdTe/GaAs (f=14.6%). In the case of inhomogeneous strain, a relaxation mechanism which operates outside the heterointerface must be in operation.

Tatsuoka et al.[2,3] proposed a new model for strain relaxation to account for strain inhomogeneity within epilayers. They proposed that misfit dislocations are found not only at the heterointerface, but are also distributed throughout the layer. Their own experiments on CdTe/GaAs grown by hot wall epitaxy have confirmed the existence of misfit dislocations at the heterointerface[28], and later work indicated the generation of misfit dislocations in the bulk of the film by the bending over of threading dislocations[2].

Consider an epitaxial film divided into monolayers, the strain in the nth layer being $\varepsilon(n)$ and the number of misfit dislocations generated per unit length in the nth layer being N(n) (figure 5.4). The number of misfit dislocations in the (n+1)th layer is, in the simplest case, proportional to the strain in the nth layer, as given by equation 5.4, where A is the generation rate of misfit dislocations. When N(n+1) dislocations are generated per unit length in the (n+1)th layer, the strain in the (n+1)th layers is given by equation 5.5 where b_{eff} is the misfit component of the misfit dislocation Burgers vector. Combining equations 5.4 and 5.5 gives an expression for the residual strain in the layer as a function of the number of monolayers (equation 5.6).

$$N(n+1)=A\varepsilon(n) \qquad \text{equation 5.4}$$

$$\varepsilon(n+1)=\varepsilon(n)-N(n+1)b_{eff} \qquad \text{equation 5.5}$$

$$\varepsilon(n)=\varepsilon(1)(1-Ab_{eff})^{n-1} \qquad \text{equation 5.6}$$

The data of Section 5.2.1 are reapplied here[14,15,17], with the number of monolayers, n, being replaced with the expression $n=h/(a_o/2)$ in equation 5.6, a_o being the layer lattice parameter and assuming $n>>1$. Figure 5.5 is a plot of the natural logarithm of strain versus layer thickness for the same three systems which were used in Section 5.2.1. A straight line

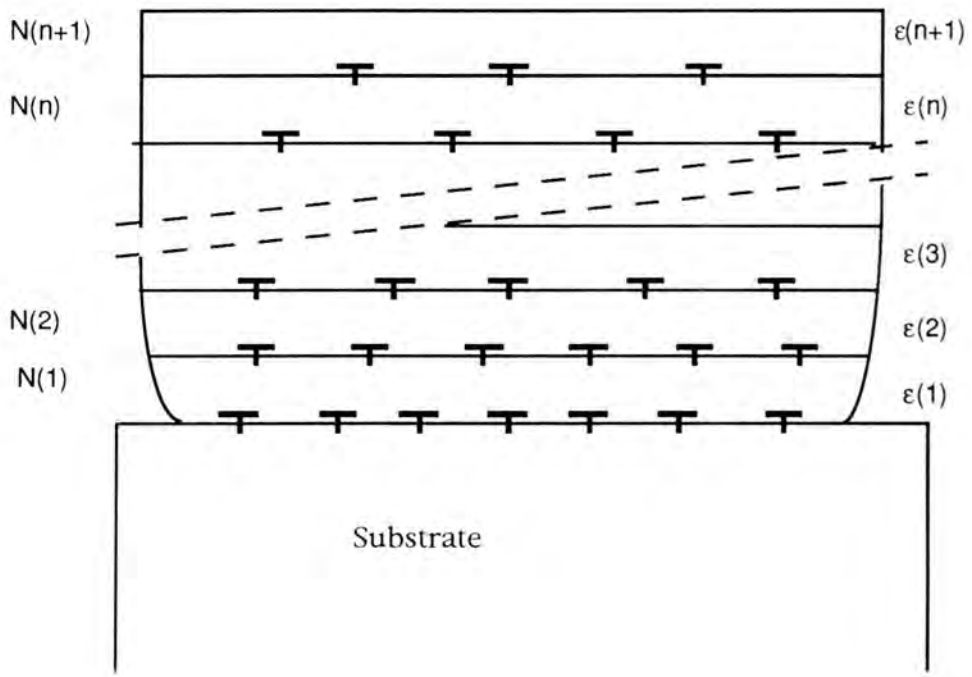

Figure 5.4 Schematic illustration of strain relaxation due to a distribution of misfit dislocations along the growth direction from Tatsuoka et al. [2,3].

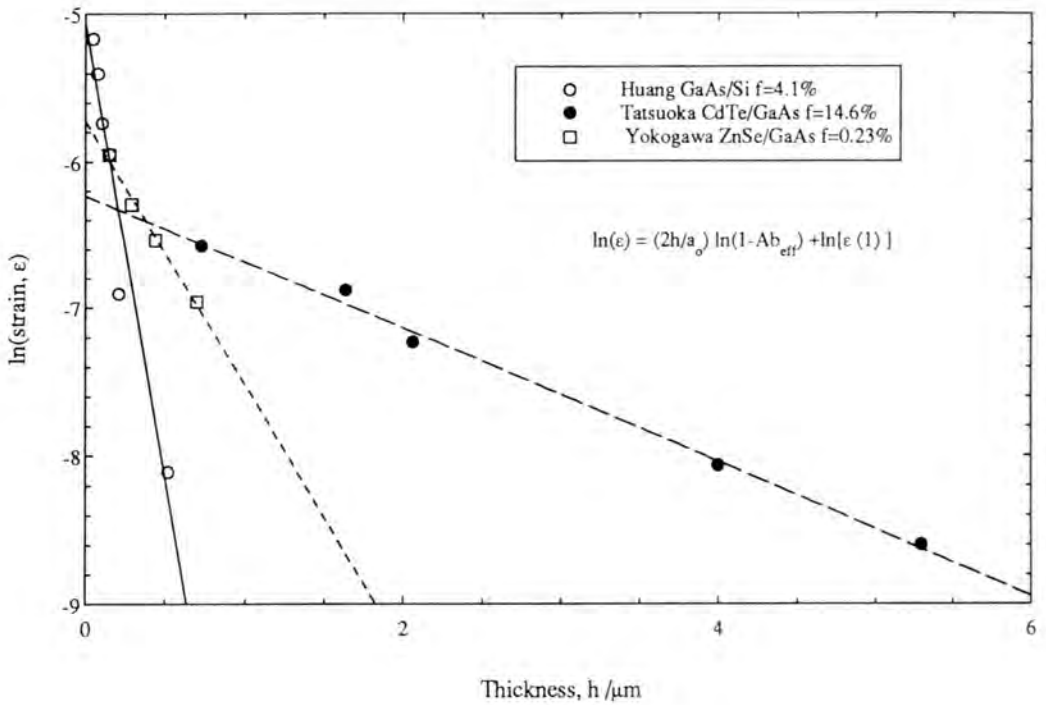

Figure 5.5 Data fit for Tatsuoka et al.'s residual strain relaxation model[2,3] for epitaxial systems of different misfit. Values of ε (1) and A for best fit lines are given in table 5.1.

with an intercept equal to the logarithm of the strain in the first monolayer is expected if equation 5.6 is followed. The values of $\varepsilon(1)$ and A obtained by fitting equation 5.6 to the data are given in table 5.1.

Source of data	$\varepsilon(1)/\ 10^{-3}$	$Ab_{eff}/\ 10^{-3}$	$A/10^3 cm^{-1}$	variance $/10^{-3}$
Yokogawa[14] ZnSe/GaAs	3.3	0.51	2.5	2.5
Huang[15] GaAs/Si	6.3	1.7	8.7	100
Tatsuoka[16,17] CdTe/GaAs	2.0	1.5	6.4	5.6

Table 5.1 Parameters for Tatsuoka et al.'s model of strain relaxation obtained from experimental curves shown in figure 5.5. (Note that variance has been calculated using the natural logarithm of strain rather than strain itself.)

Figure 5.5 shows that equation 5.6 fits the experimental data quite well. In the case of CdTe/GaAs the value for $\varepsilon(1)$ is close to the strain predicted at the interface if the interface layer is treated as a coincidence boundary [29]. If the lattice parameters of the substrate and layer have the relationship given in equation 5.7, where n and m are integers, then a fraction of the atoms in the layer lattice coincide with atom sites in the substrate lattice. When n and m are not exactly integer values then the misfit, f, between the layer and substrate can be rewritten as equation 5.8.

$$\frac{a_{epilayer}}{a_{substrate}} = \frac{n}{m} \qquad \text{equation 5.7}$$

$$f = \frac{na_{substrate} - ma_{epilayer}}{na_{substrate}} \qquad \text{equation 5.8}$$

Remembering that the data for CdTe/GaAs is calculated at the growth temperature of 300°C, the lattice parameters of the substrate and layer must also be calculated at 300°C. Thermal expansion coefficients of 6.86×10^{-6} $°C^{-1}$ for GaAs[30] and 4.5×10^{-6} $°C^{-1}$ for CdTe[31] are taken, giving lattice parameters at the growth temperature of 5.663Å and 6.489Å respectively. Equation 5.8 with n=8 and m=7 gives a value of strain at the interface using the coincidence lattice of -2.6×10^{-3} (negative sign indicates compressive strain) which compares favourably with the value of 2.0×10^{-3} obtained from the experimental fit. When misfit is calculated for GaAs/Si using equation 5.8, the value is a huge underestimate of that obtained from fitting equation 5.6. This is not surprising since the coincidence model is usually only useful for values of m up to 10 (for values greater than this, the layer will grow pseudomorphically rather than strain to divide the interface into units ma_0 in length), for GaAs/Si, n=23 and m=24.

The model seems unphysical in that misfit dislocations are not often seen in the bulk of a layer except when there are compositional variations in a ternary or quaternary compound semiconductor or in strained layer superlattices, see for example Yoshikawa[4]. The model also predicts unrealistically low generation rates for misfit dislocations. Using the values of A and $\varepsilon(1)$ from table 5.1 and substituting into equations 5.4 and 5.6, the number of misfit dislocations generated per unit length is of the order of $10cm^{-1}$, which is much less than is observed in CdTe/GaAs.

The model has been developed by Durose and Tatsuoka[6] such that residual strain is relieved by a distribution of threading dislocations; this is reviewed in Section 5.3.1.

5.2.3 Conclusions

The two models described in Sections 5.2.1 and 5.2.2 cater for different growth regimes. Dunstan's simple geometrical model[1] assumes that there is homogeneous strain in the layer with misfit dislocations forming only at the heterointerface, thus relieving strain in the entire layer. The model can

only be applied to low misfit systems which display two-dimensional layer-by-layer growth. In the original paper, Dunstan set an upper limit of 5% for the misfit for which the geometrical model is valid. The misfit at which transition from layer-by-layer growth to three-dimensional Stranski-Krastanov growth occurs depends on the material system and the growth conditions. The growth of $In_xGa_{(1-x)}As$ on GaAs has a transition at x=0.4 which corresponds to a misfit[22]. of 2.8% The growth of ZnSe/GaAs which has a misfit of only 0.23% can display three-dimensional Stranski-Krastanov growth or two-dimensional layer-by-layer growth depending on the initial substrate surface stoichiometry[32]. The growth mode of a layer is fundamental in determining whether the relaxation of the layer can be described using Dunstan's formula.

This geometrical model does not take into account relaxation due to the bending over of dislocations threading from the substrate. There will therefore be some relaxation observed before the critical thickness predicted by the model. Since no substrate is defect free, relaxation is expected to occur before the predicted h_c in all cases. At large thicknesses, a strain will be reached which can be supported by the layer material, this is know as residual strain and is the lower strain limit of applicability for the model. Dunstan has observed that relaxation continues after the residual strain limit is reached[13] but makes no attempt at including this in the model. The model by Tatsuoka et al.[2,3] aims to describe relaxation after the residual strain limit is reached and the strain is necessarily inhomogeneous with depth. The models by Dunstan (Section 5.2.1) and Tatsuoka (Section 5.2.2) are therefore mutually exclusive in their applicability.

The model by Tatsuoka et al. has been found to describe the data considered the present study reasonably well, (figure 5.5). Critical thickness must have been exceeded and the residual strain region entered for the model to apply. The model is particularly useful for high misfit systems and is the most applicable for the CdTe/GaAs layers investigated in this thesis. CdTe/GaAs displays three-dimensional Volmer-Weber growth[33] and has a critical thickness (if one can use this expression for 3D growth) of less than one

monolayer. Dunstan's geometrical model is not applicable to the CdTe/GaAs layers studied in this thesis.

The model by Dunstan et al. is extended to multilayer structures in the original paper[1] and has been extended to graded buffer layers by Dunstan[34]. The residual strain relaxation model has been developed by Durose and Tatsuoka[6] such that residual strain is relieved by a distribution of threading dislocations; this is reviewed in Section 5.3.1.

5.3 Threading Dislocation Reduction Models

5.3.1 Model for Reduction of Residual Strain by Threading Dislocations

In Section 5.2.2 a model for the reduction of residual strain was described which accounted for the reduction in strain as a layer thickened by proposing that threading dislocations were bent over to produce misfit segments, the density of which was calculated to be approximately 10 cm^{-1} for CdTe/GaAs; this is a gross underestimate. A mechanism by which inhomogeneous strain may be present within a layer has been developed by Durose and Tatsuoka[6].

Threading dislocations can be imagined as opposite ends of a half-loop with Burgers vector **b**. The half-loop's Burgers vector determines whether an extra half-plane exists in the direction of the layer or substrate. For example, consider an extra half-plane in the substrate for a layer in compression as illustrated in figure 5.6. Outside the half-loop, the layer is in compression, inside the half-loop the layer experiences strain relief. As a layer thickens, provided the half-loop continues to grow with threading segments inclined to the interface at less than 90°, then more of the layer will experience strain relief. This is illustrated in figure 5.7 where the region of the layer labelled Δh is less strained than the region h_1 below it. Thus as a threading dislocation propagates through a layer, it imparts the strain relieving component of its Burgers vector to that layer as illustrated in figure 5.8. A

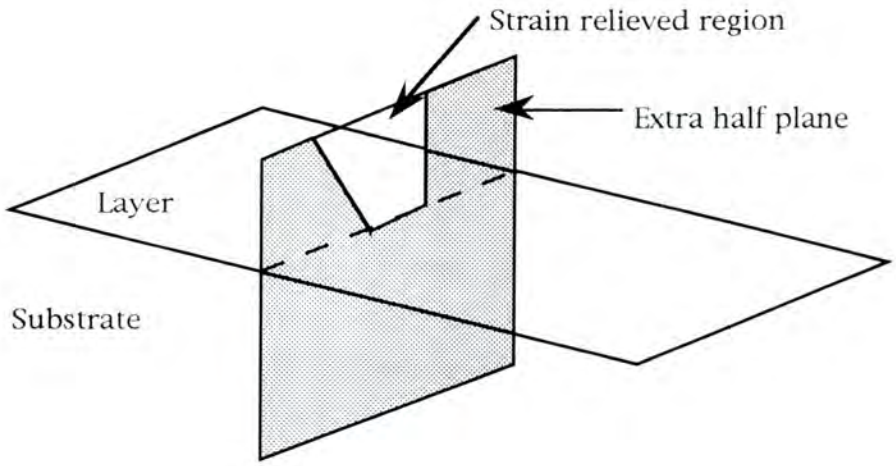

Figure 5.6 Strain relief by a dislocation half loop for a layer in compression.

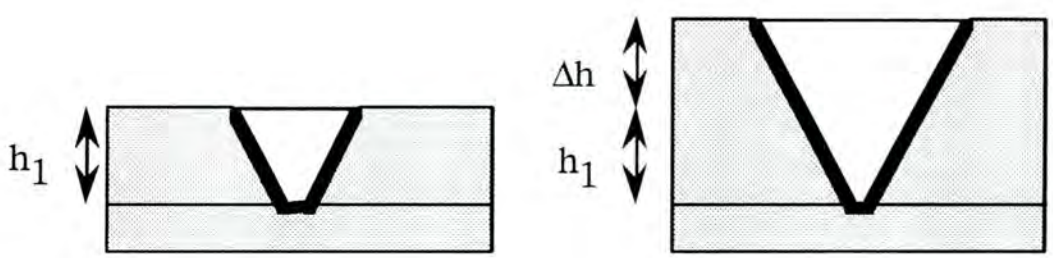

Figure 5.7 Strain relief afforded by threading segments of a dislocation half-loop as a layer in compression thickens. The 'extra half-planes' are shaded.

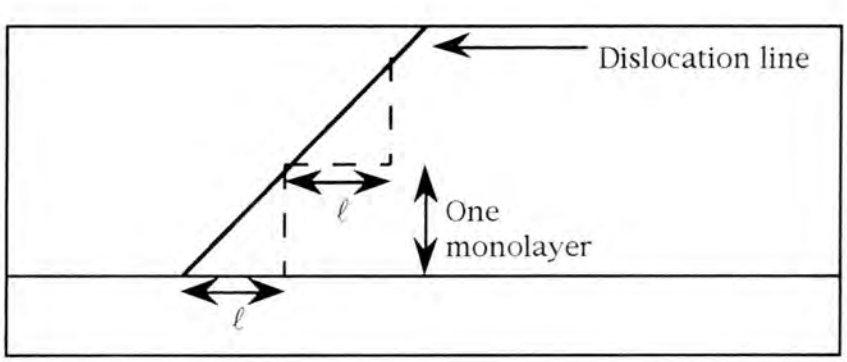

Figure 5.8 Schematic illustration of a threading dislocation acting as a misfit dislocation of length ℓ passing through consecutive monolayers.

threading dislocation may therefore act as a misfit dislocation of length equal to its projected length on a plane parallel to the interface. Durose and Tatsuoka have reworked the expression of Tatsuoka et al.[2,3] in equation 5.6 so that strain relief is afforded by threading dislocations of projected length ℓ on planes parallel to the interface[6]. The development of the model is outlined below.

From equations 5.4 and 5.6, the number of misfit dislocations generated per unit length is given by equation 5.9 assuming n>>1. If N(n) is rewritten as an equivalent number of threading dislocations of projected length ℓ, then the threading dislocation density D(n) is given by equation 5.10. The factor of 2 in the nominator of equation 5.10 comes from the consideration of dislocations in two orthogonal <110> directions.

$$N(n) \approx A\varepsilon(1)(1-Ab_{eff})^n \qquad \text{equation 5.9}$$

$$D(n) \approx \frac{2A\varepsilon(1)}{\ell}(1-Ab_{eff})^n \qquad \text{equation 5.10}$$

Equation 5.10 indicates that the threading dislocations in layer n relieve a fraction Ab_{eff} of the strain in the previous layer, (n-1). As the threading dislocations pass through layer n, the threading dislocation density is also reduced by a fraction Ab_{eff}. This reduction is thought to be due to threading dislocations meeting and annihilating under the influence of residual strain. The maximum number of threading dislocations which can be removed as $n \rightarrow \infty$ is $2A\varepsilon(1)/\ell$. Once this limit is reached, further threading dislocation density reduction is not expected and there will remain a constant background threading dislocation density $D(\infty)$ which is independent of thickness. Equation 5.10 may then be rewritten as equation 5.11 where $D(1)=2A\varepsilon(1)/\ell$.

$$D(n) \approx D(1)(1-Ab_{eff})^n + D(\infty) \qquad \text{equation 5.11}$$

In this study six sets of data from the literature[16,35-38] will be compared with equation 5.11. The misfits of the literature data sets chosen range from 0.23% to 14.6% and the details are summarised in table 5.2.

It should be noted that b_{eff} may not have the same value here as for the residual strain relaxation model in Section 5.2.2; the misfit dislocations in Section 5.2.2 and the threading dislocations in this section may have different misfit relieving Burgers vector components owing to their different orientation. It will be assumed that the threading dislocations have the same misfit relieving component as a 60° misfit dislocation lying in the interface. This small approximation is discussed more fully in Section 7.5.

Reference	System	$a_{substrate}$/Å	a_{layer}/Å	Misfit/%
Muggleberg [35]	ZnSe/GaAs	5.654	5.667	0.23
Horikawa [36]	InP/GaAs	5.654	5.869	3.80
Ayers [37]	GaAs/Si	5.431	5.654	4.11
Kudlek [38]	ZnTe/GaAs	5.654	6.103	7.94
Tatsuoka[16]	CdTe/GaAs	5.654	6.481	14.6

Table 5.2 Summary of literature data and lattice parameters of substrates and layers. All lattice parameter values are taken from the ASTM index[39] and were measured at room temperature.

Dislocation density may be calculated from values of Full Width at Half Maximum (FWHM) expressed in units of radians from High Resolution X-Ray Diffraction (HRXRD) rocking curves using a relationship by Gay et al.[40]. The effect of intrinsic broadening, B (also in radians) on FWHM, β is subtracted from the measured value of FWHM so that only broadening due to dislocation tilt components is included (equation 5.12). It should be noted that in all cases, data are for binary compounds which are not expected to

display any significant lattice parameter variations which would contribute to rocking curve broadening. A nominal value of 20 arcseconds is taken for B. The values of b_{tilt} used in equation 5.12 assume that a threading dislocation has the same Burgers vector tilt component as a 60° misfit dislocation ($b_{tilt}=(a_o/2)$ - see Section 2.2.2). The validity of this assumption is discussed in Section 7.5 in the light of Burgers vector analysis of threading dislocations in CdTe/GaAs. The validity of equation 5.12 is discussed in Sections 4.2.2.3 and 6.4.4.

$$D=\frac{\left(\beta^2-B^2\right)}{9b_{tilt}^2} \qquad \text{equation 5.12}$$

The papers by Muggleberg[35] and Horikawa and co-workers[36] gave values of FWHM of 004 HRXRD rocking curves as a function of layer thickness. Data for CdTe/GaAs[16] was received by personal communication from Dr H Tatsuoka[17]. The data for GaAs/Si included as-grown and annealed samples and the data were recorded as dislocation density as a function of layer thickness. In the papers by Ayers et al.[37] and Kudlek et al.[38], the authors assumed that the threading dislocations were of 60° type but used the full magnitude of the Burgers vector to calculate the dislocation density, rather than just the component which imparts a tilt to the layer. In both these cases FWHM was calculated from the published data and dislocation density recalculated using equation 5.12 with $b_{tilt}=(a_o/2)$.

For all six sets of data, a best value of $D(\infty)$ was determined before a graph of $\ln[D(n)-D(\infty)]$ versus number of monolayers was plotted. The fits for ZnSe/GaAs, InP/GaAs and ZnTe/GaAs are shown in figure 5.9, those for as-grown and annealed GaAs/Si are shown in figure 5.10; the fit parameters are summarised in table 5.3.

Source	D(1) /10^9cm^{-2}	A /10^4cm^{-1}	D(∞) /10^8cm^{-2}	Variance
Muggleberg[35] ZnSe/GaAs	0.65	0.79	0.74	0.031
Horikawa[36] InP/GaAs	1.6	1.1	1.2	0.036
Ayers PGA[37] GaAs/Si	1.3	1.8	1.0	0.012
Ayers as-grown[37] GaAs/Si	3.2	2.1	2.3	0.064
Kudlek[38] ZnTe/GaAs	0.72	0.69	0.12	0.019

Table 5.3 Parameters for equation 5.11 from figures 5.9 and 5.10. Note that variance has been calculated using the natural logarithm of [D(n)-D(∞)] rather than [D(n)-D(∞)] itself.

All the literature data fitted equation 5.11 reasonably well with the exception of the data for CdTe/GaAs. This is surprising since it was with this very data, (the details of which have been confirmed by the original author[17]), that the model in question was developed. It should, however, be noted that in the original paper by Durose and Tatsuoka, D(∞) was taken as the dislocation density of the thickest layer for CdTe/GaAs where a layer of 15μm was included in the data set, but was neglected for all other systems. If the linear fits published in the original paper are compared with those in figures 5.9 and 5.10, there appears to be a significant need for the term D(∞) in all cases. Since D(∞) appears in a logarithmic term, its value has little effect on the goodness of fit, but it seems that it should not be neglected altogether. D(∞) can be described as the limiting dislocation density below which dislocation density will not fall simply by increasing layer thickness. It is difficult to ascribe a thickness at which D(∞) can be said to have been reached. Even for layers a thick as 180 μm, Tachikawa and Yamaguchi[41] have recorded dislocation density still decreasing with increasing thickness.

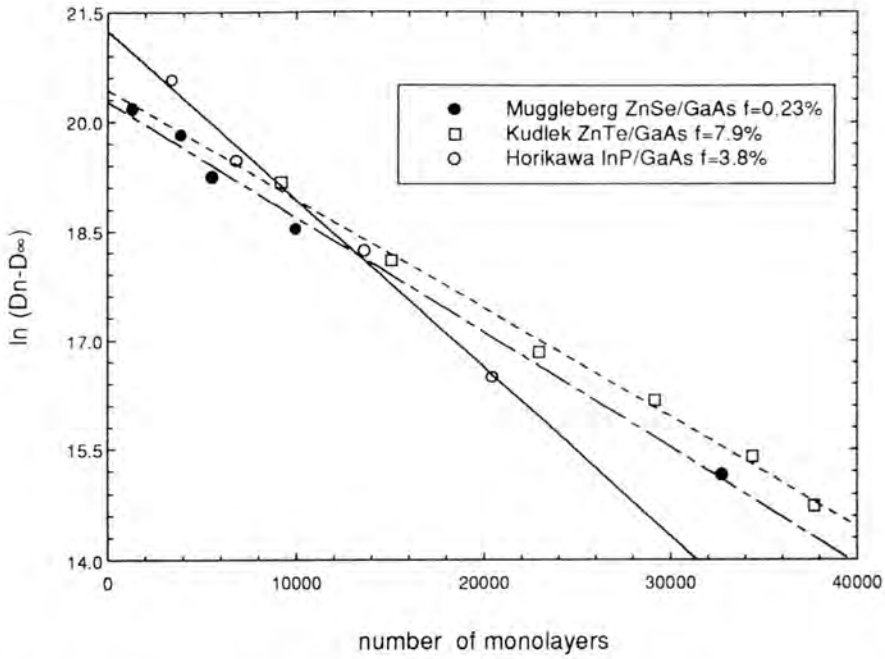

Figure 5.9 Data fit for model by Durose and Tatsuoka[5] where threading dislocations relieve strain. Data for three epitaxial systems with different misfits are shown. Values of D(∞) are given in table 5.3.

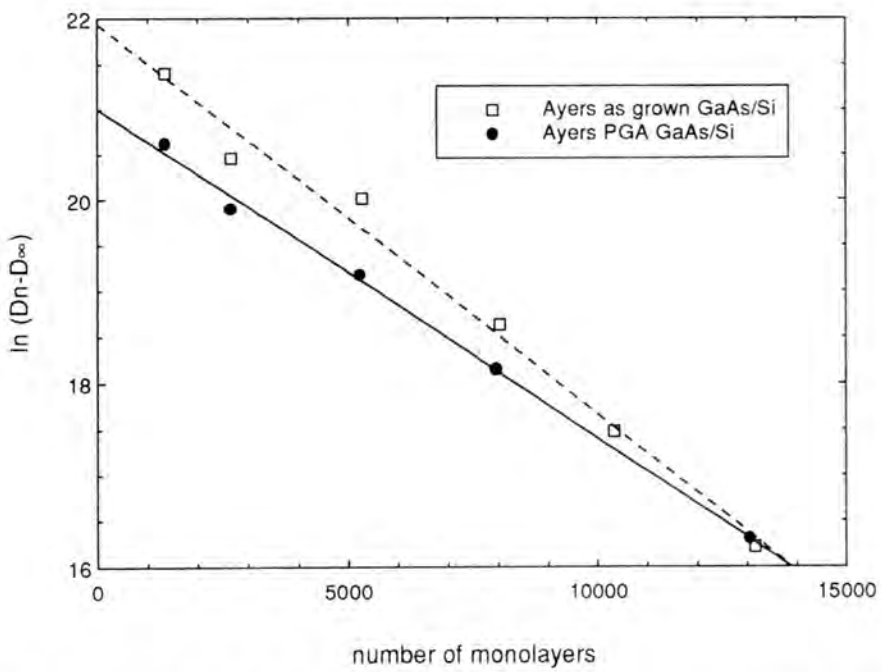

Figure 5.10 Data fit for model by Durose and Tatsuoka[5] where threading dislocations relieve strain. Data for as grown and post growth annealed (PGA) GaAs/Si are shown. Values of D(∞) are given in table 5.3.

The original paper stated that Ab_{eff} was proportional to misfit; there is no evidence of this relationship in the present work despite using much of the same data sources. The discrepancy is likely to be due to the neglect of the $D(\infty)$ term by Durose and Tatsuoka which greatly influenced the slope of their $\lg[D(n)]$ versus n plots. The gradient of the linear plot is the sole determinator in the value of A obtained.

The effect of post-growth thermal annealing on the structure of GaAs on Si is to reduce the threading dislocation density. The value of $D(\infty)$ is calculated to be smaller by a factor of 2 after annealing and the maximum possible reduction $D(1)$ is reduced to 40% of the as-grown value. Ayers et al.[37] have discussed the effects of post-growth thermal annealing for GaAs/Si and have suggested that annealed dislocation density will be proportional to the lattice mismatch. Annealing of CdTe/GaAs is discussed in greater detail in Section 8.1.

5.3.2 Half-Loop Mechanism for the Annihilation of Threading Dislocations

A mechanism for the reduction of threading dislocation density with increasing thickness has been proposed by Ayers et al.[5]. The energetics of the model are similar to the approach taken by Matthews and Blakeslee[9]. The forces acting on threading dislocations are considered and an equilibrium condition is determined. Although the validity of the energetics of the model have been acknowledged by previous workers in the field, the mechanism by which half-loops are formed and the geometry of the dislocation density reduction mechanism are uncertain and seem unphysical; for this reason the description of the mechanism of half-loop formation will be quoted directly from the original text[5]. The geometrical problems involved with this mechanism of half-loop formation and glide will be discussed later in this section.

"In this paper we propose an explanation for the thickness dependence of the threading dislocation densities in mismatched heteroepitaxial materials, based on a half-loop mechanism for the annihilation of misfit dislocations. In developing this model, it is assumed that a relatively high density of threading dislocations is introduced during lattice relaxation by some means. Neighbouring threading dislocations will often have opposing Burgers vectors; they will therefore attract one another and coalesce. Upon coalescence, a half-loop such as the one shown in figure (5.11) will be formed. The strain and line tensional forces acting on this half-loop will determine whether it glides back to the interface, preserving the two original threading dislocations, or glides to the surface and disappears."

Assuming that half-loops have been formed as described in the previous paragraph then energetic calculations may be carried out. Figure 5.11 indicates that there is a force F_g acting on the misfit segment of the half-loop due to the strain in the layer. There are also line tensional forces F_l on the two threading segments of the half-loop owing to the line energy of the dislocations. If the misfit segment is of length L, then a critical half-loop size L_C, which depends on layer thickness, can be defined for which the forces are balanced (equation 5.13).

$$2F_l = F_g \qquad \text{when } L = L_c \qquad \text{equation 5.13}$$

Some half-loops will have $L>L_C$ and will glide to the interface, conserving the two threading segments; others will have $L<L_C$ and will glide to the surface and disappear. Half-loops with $L=L_C$ will be in equilibrium and the number in equilibrium will determine the threading dislocation density at a particular thickness.

Ayers et al. use expressions for the magnitude of the glide component of the strain force acting on the misfit segment, and for the line tension in the threading segments (which are assumed to be of screw type) to determine an expression for L_C. The resulting expression indicates that the equilibrium half-loop size is inversely proportional to the strain in the film. Two assumptions are then made.

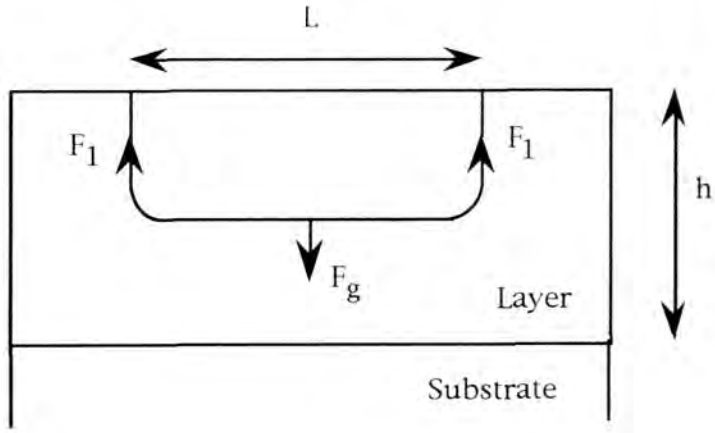

Figure 5.11 Formation of a half-loop by the coalescence of threading dislocations as described by Ayers et al.[4]. F_l is the line tensional force on a threading segment. F_g is the force acting on a misfit segment due to the layer strain.

1) The average misfit dislocation segment length at the interface is proportional to L_C and therefore that the threading dislocation density is inversely proportional to L_C.
2) The strain in a layer in equilibrium is related to its thickness according to a relationship derived by Matthews[42].

From these two assumptions an equation linking threading dislocation density with layer thickness is derived which is reproduced in equation 5.14; where ν is the Poisson ratio, δ is the part of the mismatch relieved by dislocations, f is the misfit, α is a geometrical factor greater than unity, b is the modulus of the Burgers vector and R is equal to one half of the film thickness or one half the average dislocation spacing, whichever is smaller.

$$D = \frac{\left((1+\nu)(1-2\nu)|\delta|\sqrt{2}\right)\ |\ln[2\pi|f|/(1-\nu)]|}{\alpha b h(1-\nu)^3[|\ln(R/b)+1|]} \qquad \text{equation 5.14}$$

For the case of thick highly mismatched films, two simplifying assumptions can be made. Firstly, that most of the mismatch is accommodated by dislocations (δ = f); secondly, that the lateral spacing of threading dislocations is much less than the film thickness ($R=1/2\sqrt{D}$). Ayers et al. claim that these assumptions are good for mismatch greater than about 0.3% and thicknesses greater than about 1μm. With these assumptions, equation 5.14 may be simplified as shown in equation 5.15.

$$D = \frac{\left((1+\nu)(1-2\nu)|f|\sqrt{2}\right)\ |\ln[2\pi|f|/(1-\nu)]|}{\alpha b h(1-\nu)^3[1-\ln(2b\sqrt{D})]} \qquad \text{equation 5.15}$$

Equation 5.15 predicts that dislocation density is inversely proportional to thickness and directly proportional to misfit, (ignoring the weak logarithmic dependence on $\sqrt{D}$). A plot of threading dislocation density versus reciprocal thickness will yield a straight line plot passing through the origin if equation 5.15 is followed. It should be pointed out that although Ayers et al. assumed that the threading dislocations were of screw type in

formulating equation 5.14, they claim that the nature of the dislocations does not greatly effect the final relationship.

Dislocation densities were calculated as described in Sections 4.2.2.3 and 5.3.1 using data from the same literature sources. Figure 5.12 demonstrates how threading dislocation density varies with reciprocal thickness for the cases of ZnSe/GaAs, ZnTe/GaAs and CdTe/GaAs. Figure 5.13 shows the fit of GaAs/Si data, both as-grown and after post-growth thermal annealing, to equation 5.15. Data for InP/GaAs are also shown in figure 5.13.

ZnSe/GaAs heterostructures have a misfit of 0.23%; this is less than the value given by Ayers et al. for the approximations made in formulating equation 5.15. For thin layers, equation 5.15 is expected to overestimate dislocation density since δ ,the fraction of the misfit strain relieved by dislocations, is less than f for low misfit thin layers which are incompletely relaxed. The simplifying approximation $\delta = f$ was made in formulating equation 5.15. Figure 5.12 shows that the data for ZnSe/GaAs deviates from linearity to dislocation densities less than those predicted by the simple $D \alpha (1/h)$ relationship predicted in equation 5.15.

Intermediate misfit systems such as GaAs/Si (f=4.1%) and InP/GaAs (f=3.8%) follow the reciprocal relationship between dislocation density and thickness reasonably well, although none of the data sets give a line which passes through the origin. InP/GaAs gives a negative intercept with the ordinate axis; this suggests a negative dislocation density as thickness tends to infinity. Both sets of GaAs/Si data give positive intercepts with the ordinate axis; if this value of intercept is taken as a $D(\infty)$ value, then the values obtained are, in both cases, at least an order of magnitude less than those determined for the model by Durose and Tatsuoka (Section 5.3.1). The model by Ayers et al. does not allow for dislocation density levelling off for thick layers; indeed if the model were followed accurately, the dislocation density would tend to zero for thick layers. If threading dislocation density were to level off for thick layers then the nature of a reciprocal thickness plot means that it would have little effect on the gradient of the best fit line and therefore little effect on the ordinate intercept. With these points in mind, it

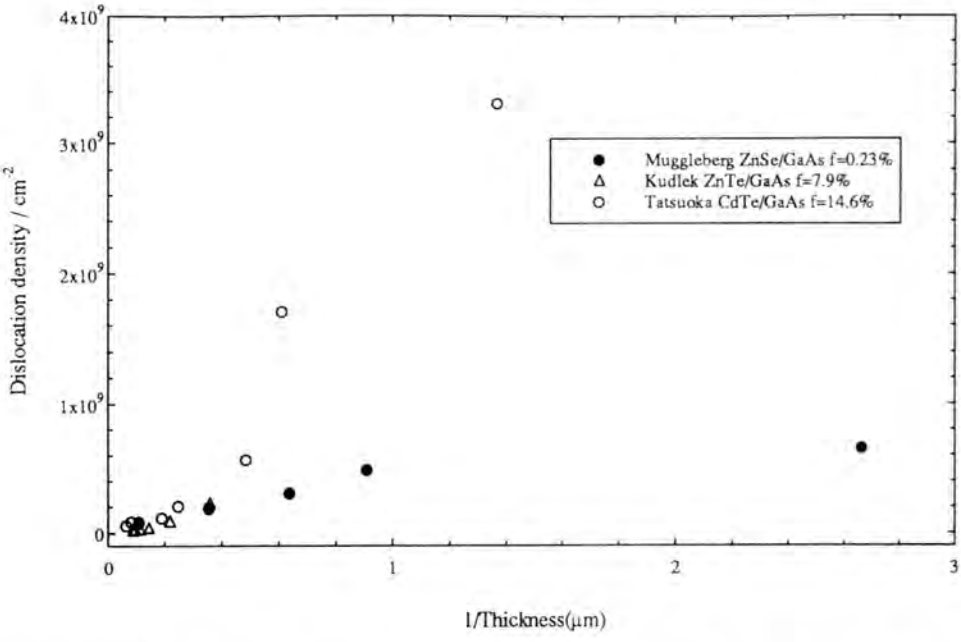

Figure 5.12 Dislocation density versus reciprocal thickness for three epitaxial systems with different misfits. If the relationship predicted by Ayers et al.[4] (equation 5.15) is followed, linear plots passing through the origin are expected.

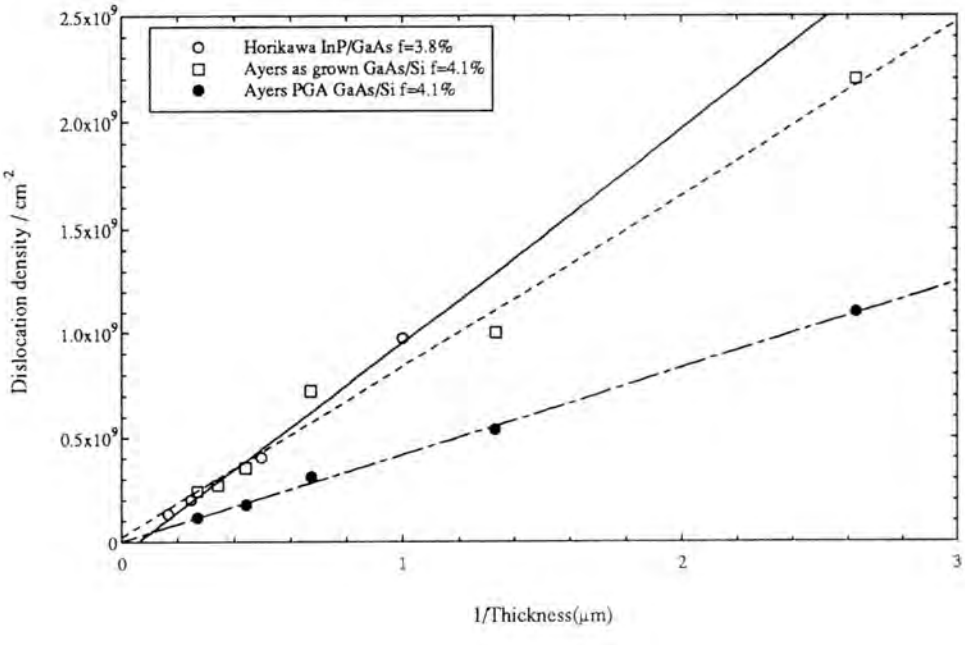

Figure 5.13 Dislocation density versus reciprocal thickness for as grown and post-growth annealed (PGA) GaAs/Si and for InP/GaAs. If the relationship predicted by Ayers et al.[4] (equation 5.15) is followed, linear plots passing through the origin are expected.

is not surprising that there is an apparent discrepancy between the two estimates of D(∞). A comparison is given in table 5.4. No goodness of fit details are given since the large values of dislocation density give very unhelpful values for variance. Goodness of fit can be judged by eye from figure 5.13.

Source	Half-loop model Ayers et al. [5] D(∞) / 10^7cm^{-2}	Residual Strain Relief model Durose and Tatsuoka[6] D(∞) / 10^7cm^{-2}
Ayers as-grown[37] GaAs/Si	2.4	23
Ayers PGA[37] GaAs/Si	0.23	10
Horikawa[36] InP/GaAs	-5.9	12

Table 5.4. Comparison of dislocation density at infinite epilayer thickness predicted by figure 5.13 (half-loop mechanism) and figures 5.9 and 5.10 (Residual strain relaxation mechanism).

High misfit systems such as ZnTe/GaAs (f=7.9%) and CdTe/GaAs (f=14.6%) do not follow the reciprocal thickness dependence as is clear from figure 5.12. Although the mechanism proposed by Ayers et al. for the formation of half-loops by threading dislocations is unclear, it is certain that threading dislocations must be able to glide. In high misfit systems, the density of dislocations, both misfit and threading, makes it almost impossible for unhindered glide to occur. For thin layers in particular, any mechanism which includes significant dislocation glide is unlikely. Failure of the half-loop model for such high misfit systems is not therefore surprising. In most circles, GaAs/Si with a misfit of 4.1% is considered to be a high misfit system, and displays a tangle of dislocations near to the interface[23] similar to CdTe/GaAs[43] and ZnTe/GaAs[44]. It is not clear from the half-loop model alone why it should fail for misfits of 7.9% and 14.6% but not for 4.1%, when the

dislocation geometry in the three cases is so similar. A possible explanation is discussed in Sections 5.3.3 and 5.3.4.

The mechanism proposed for the formation of half-loops seems to be confused, since one would expect that if threading dislocations were to coalesce, their geometry would form a half-loop as shown in figure 5.14. The occurrence of opposite Burgers vectors, assuming that coalescing dislocations have line directions of the same sense, suggests that dislocations are being formed which add to misfit strain, in numbers comparable to those relieving misfit. Obviously this cannot be the case. A much more likely occurrence is the coalescence of dislocations with the same Burgers vector, to form a half-loop as illustrated in figure 5.14; this incidentally may be treated in the same way as the half-loop described by Ayers et al. and would yield the same expression (equation 5.14).

5.3.3 Models for the Annihilation Kinetics of Threading Dislocations

A binary recombination mechanism has been proposed by Kroemer et al.[7]. If D(h) is the areal threading dislocation density, (number per unit area) and dislocations meet and react as expressed in equation 5.16, then according to reaction kinetics, the rate of change of threading dislocation density is given by equation 5.17, where λ is a constant with units of length. Integration of equation 5.17 yields equation 5.18 where D(0) is the primary dislocation density, (dislocation density at h=0).

$$D + D \xrightarrow{\lambda} \text{annihilation} \qquad \text{equation 5.16}$$

$$\frac{dD}{dh} = -\lambda D^2 \qquad \text{equation 5.17}$$

$$D(h) = \frac{D(0)}{1+D(0)\lambda h} \qquad \text{equation 5.18}$$

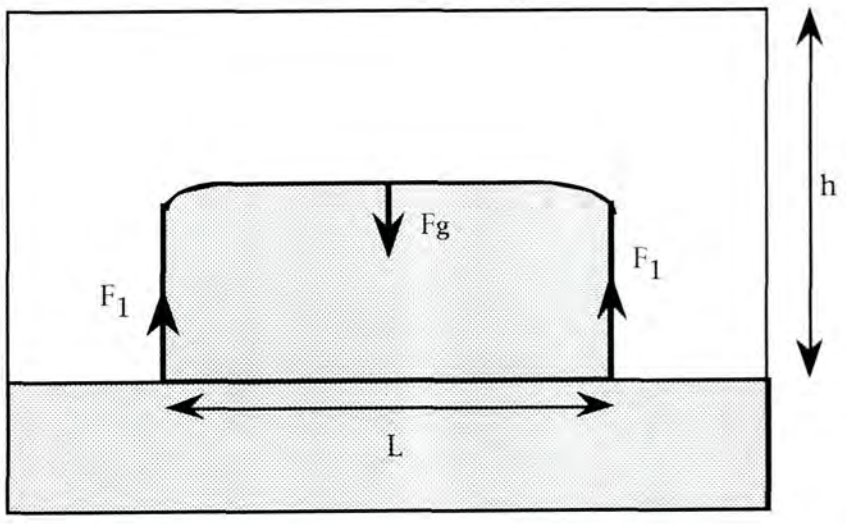

Figure 5.14 Schematic illustration of the geometry of half-loops expected to be formed by the coalescence of threading dislocations having the same Burgers vector. The 'extra half-plane' is shaded. This is for a layer in compression.

Chandra et al.[45] compared equation 5.18 with their data for the case of $Cd_xHg_{(1-x)}Te/Cd_yZn_{(1-y)}Te$ with x=0.2 and y=0.95 (nearly lattice matched). They defined a normalised density function D(h)D(0)/[D(0)-D(h)], which is related to thickness as given in equation 5.19. Chandra et al. plotted the logarithm of the normalised density function versus reciprocal thickness, but the plot gave a gradient of -1.53 rather than -1 as predicted by equation 5.19. D(0) was taken to be the dislocation density of the substrate, which is a valid assumption for a nearly mismatched system.

$$\frac{D(h)\ D(0)}{D(0)-D(h)} = \frac{1}{\lambda h} \qquad \text{equation 5.19}$$

Attempts have been made to compare this binary recombination model with the data sets described in table 5.2. In each case D(0) has been treated as an unknown parameter since none of the heterostructures are lattice matched, and it is expected that there will be a greater dislocation density at the interface than is present in the substrate.

Intermediate misfit systems, GaAs/Si (f=4.1%) and InP/GaAs (f=3.8%) agreed very favourably with equation 5.18. This is not surprising since $D(0)\lambda h >> 1$ and equation 5.18 approximates to $D(h)=1/\lambda h$. This is the same relationship as in equation 5.15, (which was derived for the half-loop annihilation mechanism[5] proposed by Ayers et al.) and the data fitted equation 5.15 well, with the exception of a non zero intercept. Large misfit systems such as ZnTe/GaAs (f=7.9%) and CdTe/GaAs (f=14.6%) deviate from the relationship of equation 5.18 for all but the thinnest layers.

A more thorough kinetic mechanism has been proposed by Tachikawa and Yamaguchi[41]. In this case a second mechanism for threading dislocation density reduction is proposed in addition to the binary recombination mechanism. They suggest that, "Annihilation is caused by the deflection of dislocations followed by a reaction with other dislocations or by movements outside the crystal. The deflection reaction occurs when the dislocation is scattered by something, for example a point defect or local stress in the crystal." Therefore, in addition to the reaction described by equation 5.16, there is a second reaction (equation 5.20) which involves only one

dislocation and whose reaction rate depends on the concentration of the 'scattering' matter (n/cm^{-3}) and the capture cross-section (σ/cm^2). The rate of change of threading dislocation density is now given by equation 5.21 where $n\sigma = a$. Integration of equation 5.21 yields equation 5.22 where D(0) is the primary dislocation density, (dislocation density at h=0).

$$D \xrightarrow{n\sigma} \text{annihilation} \qquad \text{equation 5.20}$$

$$\frac{dD}{dh} = -aD - \lambda D^2 \qquad \text{equation 5.21}$$

$$D(h) = \frac{1}{([1/D(0)] + [\lambda/a])\exp(ah) - [\lambda/a]} \qquad \text{equation 5.22}$$

From equation 5.21, it is clear that the additional mechanism will become more significant for lower dislocation densities, i.e. for thicker layers. When equation 5.22 is used to fit the data for high misfit systems, a much improved fit is achieved, particularly for thicker layers. Figures 5.15-5.18 show the fits of equations 5.18 (simple binary recombination mechanism) and 5.22 ('unimolecular' and 'bimolecular' recombination mechanisms) to the systems GaAs/Si, InP/GaAs, ZnTe/GaAs and CdTe/GaAs respectively. Table 5.5 compares the values of the constants λ and a obtained by fitting equations 5.18 and 5.22 to five sets of data.

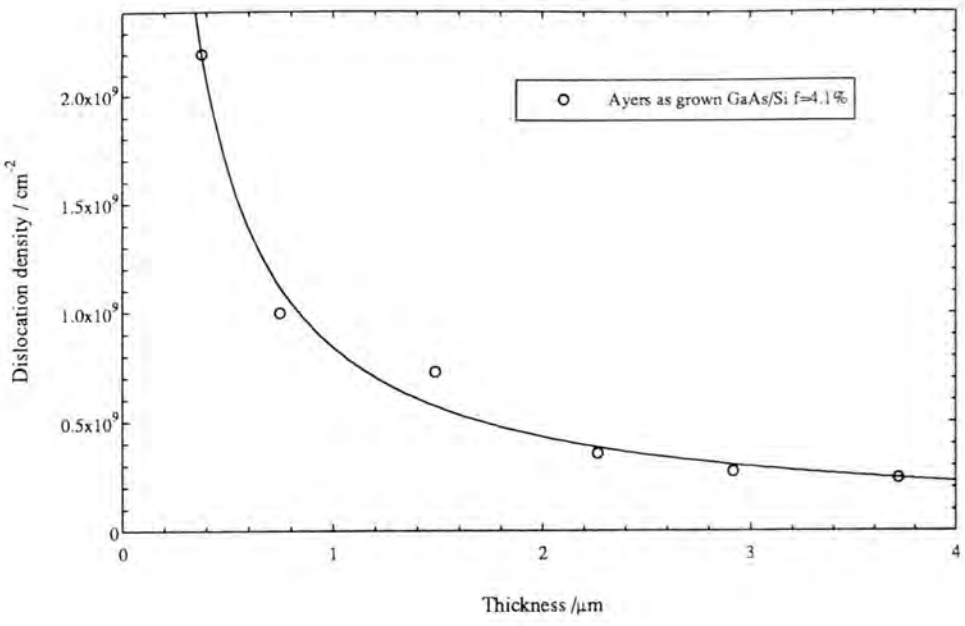

Figure 5.15 Comparison of data for as grown GaAs/Si with equation 5.18 (simple binary recombination mechanism). There is no visible change in fit when compared with equation 5.22 (both 'unimolecular' and 'bimolecular' recombination mechanisms).

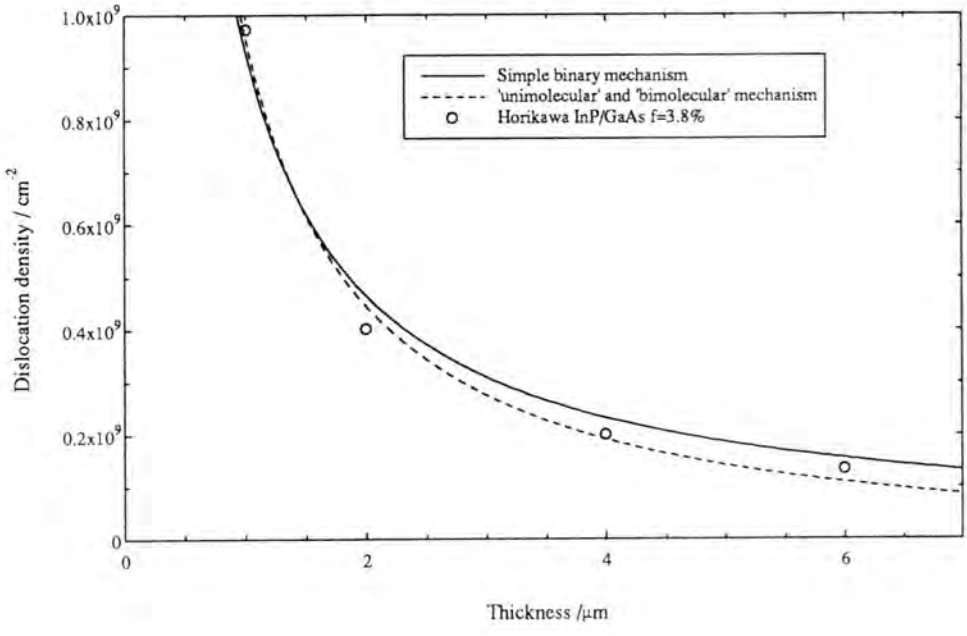

Figure 5.16 Comparison of data for InP/GaAs with equation 5.18 (simple binary recombination mechanism) and with equation 5.22 (both 'unimolecular' and 'bimolecular' recombination mechanisms).

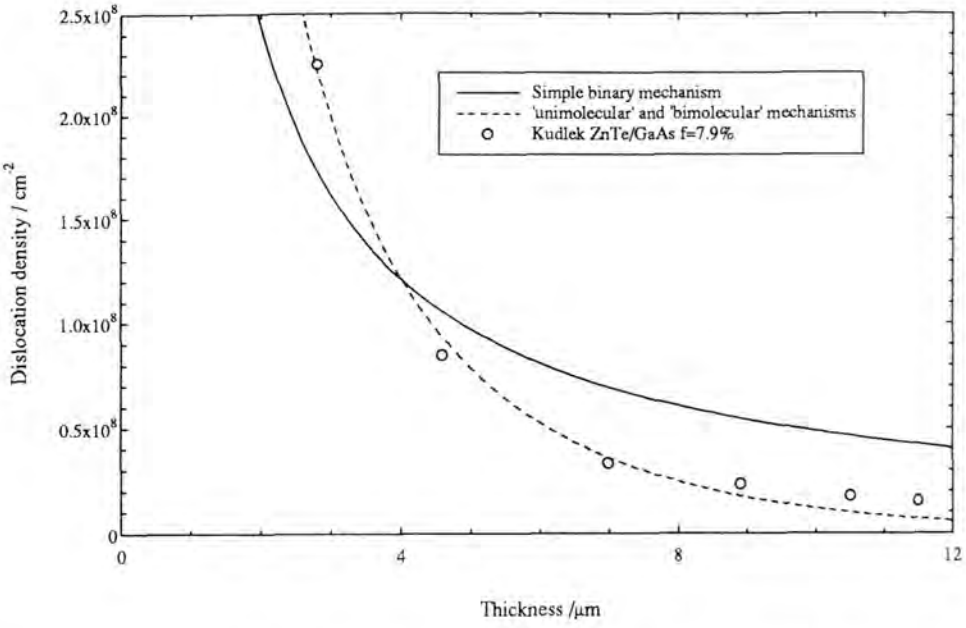

Figure 5.17 Comparison of data for ZnTe/GaAs with equation 5.18 (simple binary recombination mechanism) and with equation 5.22 (both 'unimolecular' and 'bimolecular' recombination mechanisms).

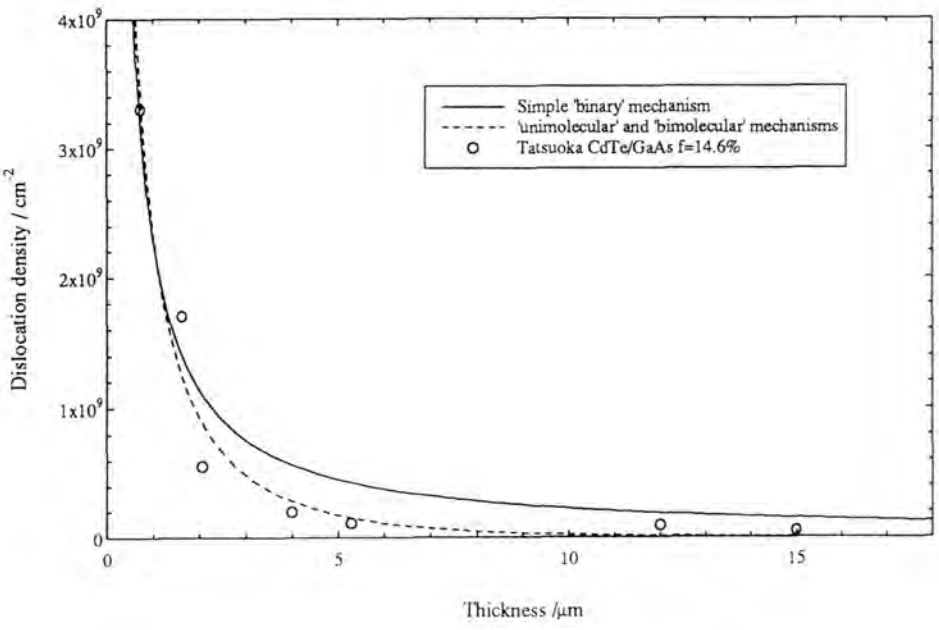

Figure 5.18 Comparison of data for CdTe/GaAs with equation 5.18 (simple binary recombination mechanism) and with equation 5.22 (both 'unimolecular' and 'bimolecular' recombination mechanisms).

	Equation 5.18	Equation 5.22	
	λ/ 10^{-5} cm	λ/ 10^{-5} cm	a/ 10^{3} cm^{-1}
Horikawa [36] InP/GaAs	1.1	0.97	1.4
Ayers [37] GaAs/Si	1.2	1.2	-0.55
Ayers PGA [37] GaAs/Si	2.4	2.4	-0.1
Kudlek [38] ZnTe/GaAs	2.1	0.96	3.4
Tatsuoka [16] CdTe/GaAs	0.44	0.35	4.1

Table 5.5. Comparison of first (a) and second (λ) order rate constants derived from equations 5.18 and 5.22.

Table 5.5 indicates that the additional annihilation mechanism makes relatively little difference to the best value of λ obtained, compared to the simple binary recombination mechanism, except for ZnTe/GaAs which gave a particularly poor fit to equation 5.18, (figure 5.17). The additional term in the rate equation gave no observable change in best fit for GaAs/Si. Negative values for the first order rate constant, a, were obtained for both as-grown and annealed GaAs/Si. This suggests that either dislocation multiplication sources are operating as the layer thickens or that threading dislocations are being spontaneously generated; the later is not permitted since dislocations may not begin or end within a crystal[46]. Since the magnitude of the constant a, is in both cases small compared to the values for the other systems, and since the goodness of fit is not adversely affected by neglecting this term, it is acceptable to ignore this first order term. The possibility of negative rate constants in relation to the generation of threading dislocations is discussed in Section 5.3.4.

It has already been noted that equation 5.18 approximates to $D(h) \propto 1/(\lambda h)$ for thick layers. This suggests that dislocation density is independent of the initial dislocation density D(0) and that a reduction in D(0) will not lead to a proportional reduction in D(h). In order to achieve a significant reduction in D(h), which is a major aim for all high misfit systems, then an increase in λ (and a) is required. Strained layer superlattices are employed to increase the parameter a by increasing the strain encountered by threading dislocations and hence increasing the probability of deflection of dislocations to the edge of the layer.

5.3.4 Discussion and Conclusions

The model described in Section 5.3.1, developed by Durose and Tatsuoka[6], has been found to describe the data considered in this study reasonably well. Critical thickness had been exceeded in all cases. They suggested that a levelling off of dislocation density will occur for thick layers, the dislocation density at this level being termed $D(\infty)$. The original paper neglects the term $D(\infty)$ for all but one set of data. The work carried out in the study presented in Section 5.3.1 suggests that $D(\infty)$ should be included for all systems and that dislocation density is expected to level off for thick layers, although it is difficult to predict at what thickness this might occur. Care should also be taken when consulting the summary table contained in the original paper. There are a number of errors in the units given, and the neglect of the term $D(\infty)$ has had quite a large effect on the values of the parameters quoted.

The expression derived by Ayers et al.[5] predicting the relationship between dislocation density and layer thickness can be used to describe intermediate misfit systems of thicknesses in the range 1-5μm. Care must be taken for thick layers since extrapolation of the reciprocal thickness plot can give negative dislocation densities. The high misfit systems investigated in this study do not follow the relationship predicted by the half-loop mechanism, that is $D \propto (1/h)$. The geometrical basis of the mechanism for half-loop formation is unsure and has been discussed in Section 5.3.2.

The very simple 'bimolecular' annihilation model by Kroemer et al.[7] and later by Chandra et al.[45] approximates to the half-loop model in its prediction of the dislocation density versus thickness relationship. This demonstrates the great care which must be taken when fitting data to model expressions. It is the expression which is being fitted to a particular set of data, not the model itself. Therefore, the fact that the dislocation density for the GaAs/Si samples considered in this study displays a reciprocal relationship with thickness, does not reveal the details of the mechanism of threading dislocation density reduction, or what affects it.

A more advanced kinetic model developed by Tachikawa and Yamaguchi[41] has also been presented in Section 5.3.3 which includes a 'unimolecular' threading dislocation density reduction mechanism. The additional term improves the agreement with the literature data for high misfit systems but has little effect on the fit parameters for systems which followed a reciprocal thickness relationship.

There are other mechanisms by which threading dislocation density can be reduced which were not considered by Kroemer et al.[7], Chandra et al.[45] or Tachikawa and Yamaguchi[41]. One very significant process which can lead to the reduction of dislocation density is the combination of two threading dislocations followed by the re-emission of a single dislocation. This is expected to occur when dislocations with non equivalent Burgers vectors coalesce. Figure 5.19 shows schematically the mechanisms by which threading dislocation density can be reduced. If the original dislocations have density D_1 and dislocations formed by re-emission have density D_2, then the equations governing the rate of change of D_1 and D_2 are given in equations 5.23-5.27.

$D_1 \xrightarrow{a}$ annihilation — equation 5.23

$2D_1 \xrightarrow{b}$ annihilation — equation 5.24

$2D_1 \xrightarrow{c} D_2$ coalescence + re-emission — equation 5.25

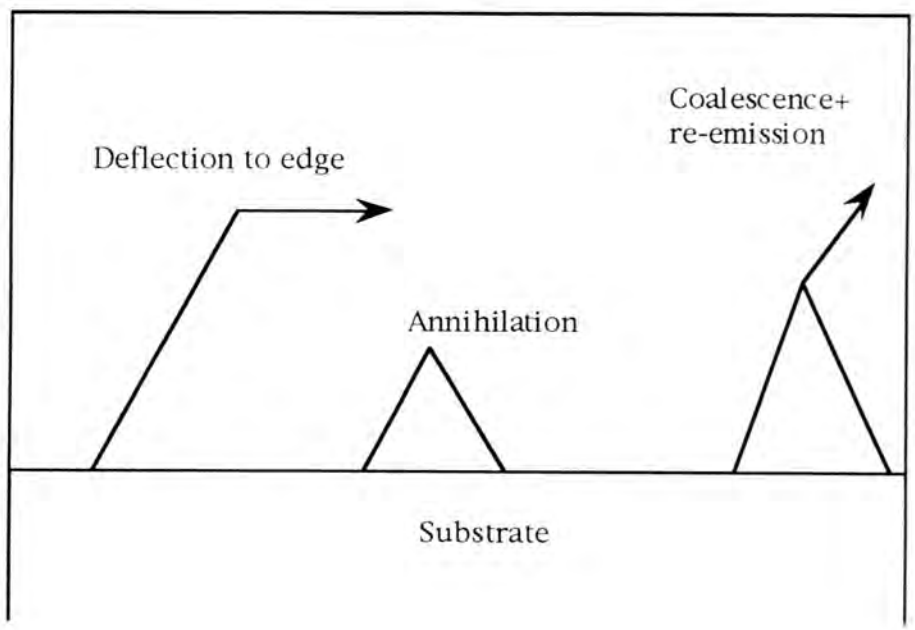

Figure 5.19 Schematic illustration of threading dislocation reactions which lead to a reduction in threading dislocation density.

$$\frac{dD_1}{dh} = -aD_1 - bD_1^2 - cD_1^2 \qquad \text{equation 5.26}$$

$$\frac{dD_2}{dh} = +\frac{cD_1^2}{2} \qquad \text{equation 5.27}$$

Total dislocation density D is the summation of densities D_1 and D_2. The rate of change of dislocation density is the summation of the rates of change of D_1 and D_2 and is given in equation 5.28. For an overview of reaction kinetics see for example Atkins[47] or Frost and Pearson[48].

$$\frac{dD}{dh} = -aD_1 - bD_1^2 - \frac{cD_1^2}{2} \qquad \text{equation 5.28}$$

It is clear that many refinements to the kinetic models can be made to account for the many different types of reaction which may occur, each having a different rate constant. The dislocations which are re-emitted may go on to react with others, and so on. Each additional mechanism will bring another constant. Without knowing the interdependence of the constants it would be futile to attempt to fit increasingly complex expressions with more and more unknown constants to literature data. However, the simple approaches taken by the authors reviewed here are satisfactory in describing threading dislocation density reduction with increasing thickness.

It seems that no one model can yield an expression which describes reduction in threading dislocation density with increasing thickness for all the data sets considered in this limited study. Each model has its own advantages, whether being accuracy of fit within a limited number of systems, or general applicability to a wide range of systems with, perhaps, a less accurate fit. It appears from this study that the expressions derived from models by Durose and Tatsuoka[6] and by Tachikawa and Yamaguchi[41] are applicable to most systems while expressions derived by Ayers et al.[5] and Kroemer et al.[7] are accurate only for misfits in the region of 4% and for layers whose thicknesses lie within the range 1-5μm.

5.4 New Geometrical Model for Threading Dislocation Density Reduction

5.4.1 Introduction

In the following section a new geometrical model, describing the reduction in threading dislocation density with increasing layer thickness will be introduced and developed. The model is based on the premise that threading dislocations confined to oppositely inclined planes will meet at a certain layer thickness and that there will be a probability of them reacting.

5.4.2 Development of a New Geometrical Model

Consider an array of threading dislocations emanating from a (001) heterointerface, each lying on a {111} plane inclined at 54° 44' to the interface. Let the dislocations also be contained in one of the two {110} planes which are perpendicular to the interface. Neglecting dislocation glide and climb, a thickness will be reached where adjacent dislocations meet. At this thickness a fraction of interactions will lead to coalescence and termination of threading dislocation propagation, while other meeting events will result in no reaction. (No account is taken of coalescence with re-emission of a threading dislocation here). Figure 5.20 illustrates the geometry under consideration.

A number of simplifying assumptions are made in the initial development of this model.

1) When dislocations meet geometrically, there is a probability of annihilation which is independent of layer thickness.

2) When dislocations meet they either do not react and continue in their original direction or they coalesce and do not propagate any further. There is no re-emission after coalescence.

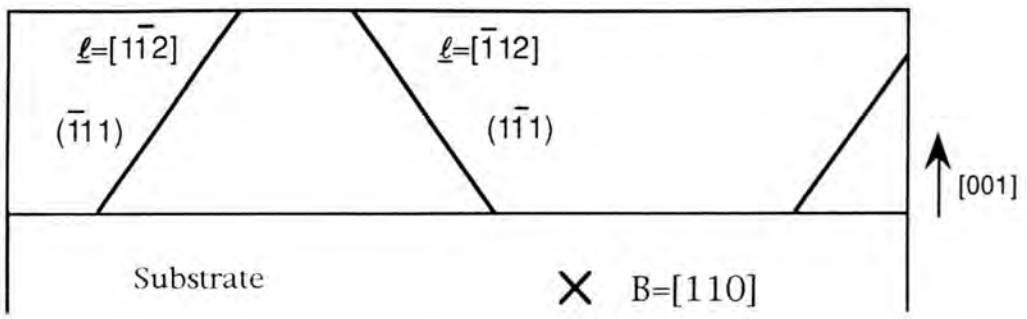

Figure 5.20 Schematic illustration of the geometry of threading dislocations considered in developing a new geometrical model for the annihilation of threading dislocations (see Section 5.4).

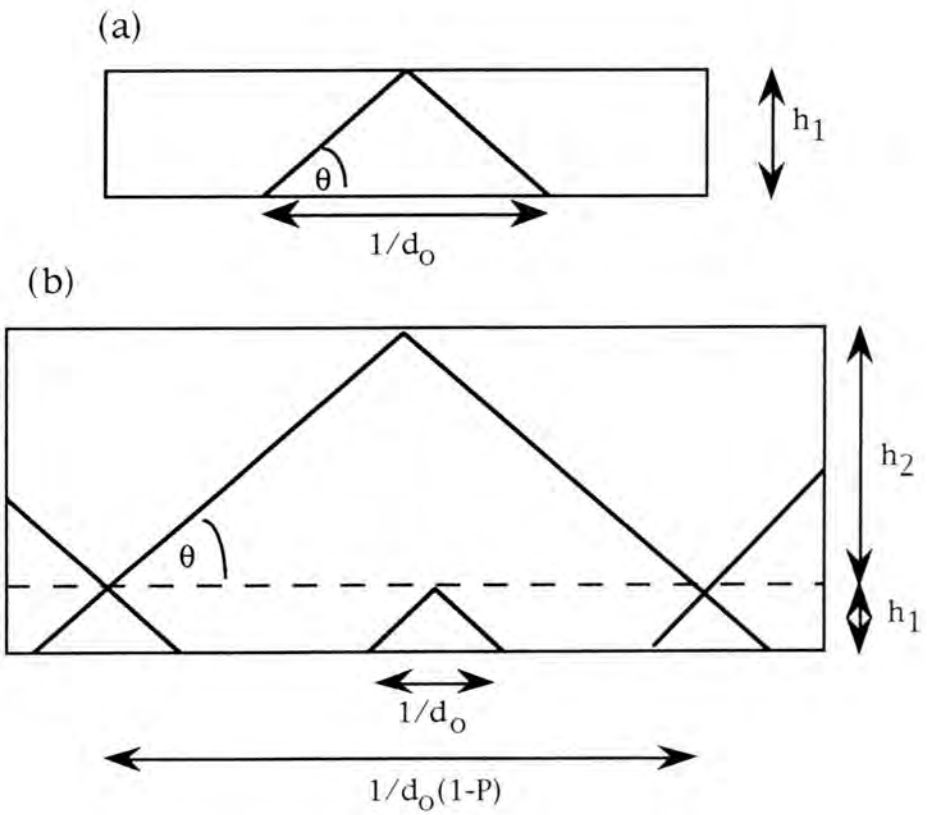

Figure 5.21 Schematic illustration of threading dislocation annihilation, showing (a) the first thickness and (b) the second thickness at which annihilation may occur.

3) Dislocation line directions are confined to a {111} plane and a {110} plane. This means that they have a <112> line direction and that linear dislocation density can be considered.

4) Dislocations on oppositely inclined {111} planes are present in equal numbers.

5) On average, the dislocations are evenly spaced.

6) There is no glide of threading dislocations.

7) Neither dislocation interaction energies nor the effect of lattice strain energy are taken into account in this model.

Let the linear threading dislocation density in the [110] plane at the interface be d_o cm^{-1}. The spacing of threading dislocations at the interface will be $(1/d_o)$ cm. In an ordered array, each dislocation propagating on a $(\bar{1}11)$ plane will be adjacent to two threading dislocations propagating on $(1\bar{1}1)$ planes. The separation of adjacent threading dislocations propagating on oppositely inclined {111} planes will, on average, be $(1/d_o)$ cm.

The film thickness h_1 at which these two dislocations meet is determined from figure 5.21a, and is given by $h_1=(\tan\theta/2d_o)$, where $\theta = 54° 44'$ and is the inclination of the {111} plane to the interface. Let the probability of reaction resulting in no further propagation of either threading dislocation be P. If the linear threading dislocation density at the interface is d_o, then the threading dislocation density at h_1 will be $d_o(1-P)$ cm^{-1} and the average spacing of threading dislocations at h_1 will be $[1/\{d_o(1-P)\}]$ cm.

The next annihilation event will occur at a thickness h_2 greater than h_1 as determined from figure 5.21b. If the probability of annihilation with no further propagation is again P, then the threading dislocation density at h_1+h_2 will be $d_{h_1}(1-P)$ which has the value $d_o(1-P)^2$. This geometrical approach may be continued in a similar manner and the result is

summarised in table 5.5, where m is the number of thicknesses at which annihilation events may have occurred.

Thickness	Thickness	Linear dislocation density
0	0	d_o
h_1	$\frac{\tan\theta}{2d_o}$	$d_o(1-P)$
h_1+h_2	$\frac{\tan\theta}{2d_o}\left[1+\frac{1}{(1-P)}\right]$	$d_o(1-P)^2$
$h_1+h_2+h_3$	$\frac{\tan\theta}{2d_o}\left[1+\frac{1}{(1-P)}+\frac{1}{(1-P)^2}\right]$	$d_o(1-P)^3$
$\sum_{n=1}^{m} h_n$	$\frac{\tan\theta}{2d_o}\sum_{n=1}^{m}\frac{1}{(1-P)^{n-1}}$	$d_o(1-P)^m$

Table 5.5 Summary of layer thicknesses at which threading dislocations meet and corresponding threading dislocation densities.

In general, at a thickness $\frac{\tan\theta}{2d_o}\sum_{n=1}^{m}\frac{1}{(1-P)^{n-1}}$, the linear threading dislocation is $d_o(1-P)^m$ where m is the number of thicknesses reached at which coalescence may occur. The expression $\frac{\tan\theta}{2d_o}\sum_{n=1}^{m}\frac{1}{(1-P)^{n-1}}$ is the summation of a geometric progression. A common theorem for the summation of a geometric progression is given in equation 5.29.

For $S_n = a+ar+ar^2+\cdots ar^{n-1}$; $S_n = \frac{a(1-r^n)}{(1-r)}$ equation 5.29

In this case, $S_n = 1+\frac{1}{(1-P)}+\frac{1}{(1-P)^2}+\cdots\frac{1}{(1-P)^{n-1}}$ equation 5.30

With a=1 and r=1/(1-P), equation 5.29 gives an expression for the summation term in table 5.5 as given in equation 5.31 (after rearranging).

$$S_n = \frac{[1-(1-P)^m]}{P(1-P)^{m-1}} \qquad \text{equation 5.31}$$

The expression for thickness then becomes:

$$h = \frac{\tan\theta}{2d_o}\left[\frac{1-(1-P)^m}{P(1-P)^{m-1}}\right] \qquad \text{equation 5.32}$$

The expression for linear threading dislocation density from table 5.5 is:

$$d=d_o(1-P)^m \qquad \text{equation 5.33}$$

Substituting d_O from equation 5.33 into equation 5.32 gives equation 5.34.

$$h = \frac{(1-P)\tan\theta}{2dP}\left[1-(1-P)^m\right] \qquad \text{equation 5.34}$$

Substituting m from equation 5.33 into equation 5.34 gives an expression linking threading dislocation density and layer thickness as given in equation 5.35.

$$h = \frac{(1-P)\tan\theta}{2dP}\left[1-(1-P)^{\frac{1}{\ln(1-P)}\ln\left|\frac{d}{d_o}\right|}\right] \qquad \text{equation 5.35}$$

Equation 5.35 is for a two-dimensional model. In order to compare an expression with literature data, an areal (three-dimensional) dislocation density must be obtained.

The separation of [110] planes is $a_o\sqrt{2}$, where a_o is the bulk lattice parameter of the layer. In a square centimetre of layer, there will be $\sqrt{2}/a_o$ [110] planes and $\sqrt{2}/a_o$ [1$\bar{1}$0] planes, (when a_o is given in cm units), each plane has d dislocations per centimetre. The areal dislocation density is given by the number of dislocations in the two planes ($2d\sqrt{2}/a_o$) divided by the area of the sampling region, which in this case is 1 cm^2. The areal dislocation density, D is given in equation 5.36.

$$D = \frac{2d\sqrt{2}}{a_o} \qquad \text{equation 5.36}$$

Substituting for d in equation 5.35 and noting that $D_o=(2d_o\sqrt{2}/a_o)$, an expression between areal dislocation density and layer thickness is reached which is given in equation 5.37.

$$h=\frac{(1-P)\sqrt{2}\tan\theta}{a_oDP}\left[1-(1-P)^{\frac{1}{\ln(1-P)}\ln\left|\frac{D}{D_o}\right|}\right] \qquad \text{equation 5.37}$$

5.4.3 Discussion

There are two unknown parameters in equation 5.37, D_o, which is expected to be of weak influence since it appears only in a logarithmic term and P which must have a value in the range $0\rightarrow1$ since it is a probability. The angle θ is known to be 54° 44'. Equation 5.37 can be written more simply by collecting several constants together, this is shown in equation 5.38.

$$x = \frac{a}{y}\left[1-b^{\frac{1}{\ln b}\ln\left|\frac{y}{c}\right|}\right]$$

$$\text{where } a=\frac{(1-P)\sqrt{2}\tan\theta}{a_oP},\ b=(1-P) \text{ and } c=D_o \qquad \text{equation 5.38}$$

An attempt was made to compare equation 5.38 with literature data. The data of Tatsuoka et al.[16,17] was chosen owing to the large thickness range over which experiments had been performed and because there were the greatest number of data points. The result is shown in figure 5.22. For CdTe/GaAs, where the layer is in compression, there are four Burgers vectors which are expected to dominate in each <110> projection, these are, for the [110] projection, $[0\bar{1}1]$, [101], $[10\bar{1}]$ and $[0\bar{1}\bar{1}]$. The probability of adjacent dislocations having the same Burgers vector (and thus being able to form a closed half-loop as illustrated in figure 5.14) is 0.25x0.25, therefore P is taken to be 0.0625. A value of $1x10^{12}$ cm^{-2} was taken for D_o since this was the

value used for the dislocation annihilation mechanism models described in Section 5.3.3. It is difficult to determine D_0 theoretically since the confinement length of misfit dislocation segments, which determines the number of threading segments, is not known.

The model gives a reasonable agreement with the data for thicknesses greater than about 2μm, the model greatly underestimates the threading dislocation density for thinner layers. One obvious reason for this discrepancy is that the large misfit for CdTe/GaAs leads to a tangle of dislocations near the interface which extends at least 1μm into the layer. It is unreasonable to suppose that a geometrical annihilation mechanism such as the one proposed here can occur near the interface of such greatly mismatched layers. For comparison, the fit for ZnSe/GaAs[35] (f=0.23%) is shown in figure 5.23, where a better fit for thin layers is observed.

During best fit determination, it was noticed that the goodness of fit was not affected much by the values of b or c in equation 5.38, the parameter a, had by far the greatest effect in determining how well equation 5.38 described the experimental data. The value of fit parameter a from figure 5.22 is 10^7 m^{-1}. The value expected from equation 5.38 with P=0.0625 and $D_O=10^{12}$ cm^{-2} is $a=4.6\times10^{10}$ m^{-1}. There is a discrepancy of over three orders of magnitude between the expected value and that obtained from the best fit. The limitations and assumptions made in arriving at equation 5.37 will now be discussed.

The major simplifying assumption made was that all the threading dislocations were contained in the [110] or [1$\bar{1}$0] plane and a {111} plane. This geometry requires that the dislocation line direction is of a <112> type which, given the almost exclusive <101> Burgers vectors in the sphalerite structure, would mean that the threading dislocations were exclusively 30° or 73°13' types. Many such dislocations have been observed in [110] and [1$\bar{1}$0] cross-section TEM projections (Section 7.4), however they are by no means exclusive, and 60° type dislocations with the same Burgers vectors but with <101> line directions also occur (Section 7.4). The model developed in Section 5.4.2 did not take into account any dislocations which were not in

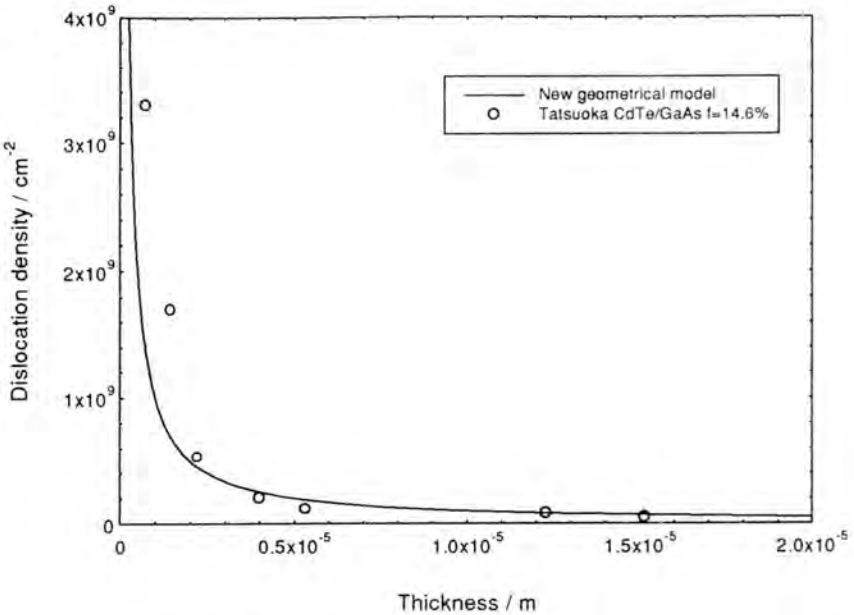

Figure 5.22 Data fit for new geometrical model which is developed in Section 5.4. Experimental data is for CdTe/GaAs. The expression used to fit the data is given in equation 5.38 with $a=10^7 m^{-1}$, b=0.994 and $c=10^{12}$ cm^{-2}.

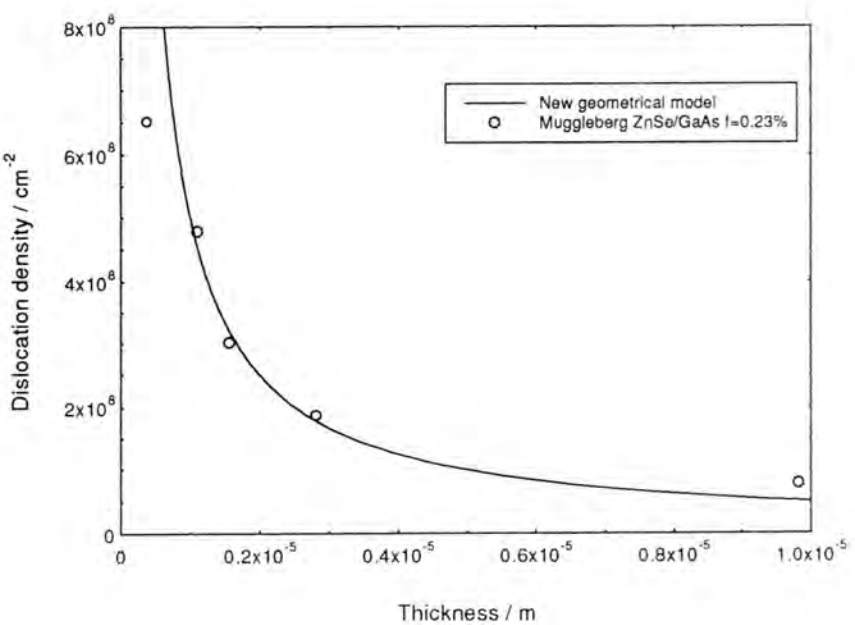

Figure 5.23 Data fit for new geometrical model which is developed in Section 5.4. Experimental data is for ZnSe/GaAs. The expression used to fit the data is given in equation 5.38 with $a=5x10^6 m^{-1}$, b=0.994 and $c=10^{12}$ cm^{-2}.

the [110] or [1$\bar{1}$0] planes. It is not easy to develop a geometrical linear threading dislocation density model if such dislocations are included.

If threading dislocation annihilation were to be controlled by geometry as suggested in the development of this model, then a much more complex model for threading dislocations with ℓ=<101> would be required, for two major reasons. Firstly, each ℓ=<101> is contained in two {111} planes and can therefore meet and react with threading dislocations on either of these two planes. The simple model developed here only allowed threading dislocations to react with others on one {111} plane. The second complication arises from the fact that dislocations of different character could meet and coalesce if they had the same Burgers vector, and this would occur at a different height above the interface than would be the case for two dislocations of the same type; this is illustrated in figure 5.24.

In Section 5.3.4, the possibility of dislocation reaction with the re-emission of a threading dislocation was discussed. It is very likely that such reactions will occur; however reactions of this kind have not been included in the model.

Substrate offcut greatly influences the relative numbers of 90° and 60° misfit dislocations which are formed, there is also likely to be an anisotropy in dislocation types in the two orthogonal [110] directions[33]. Any anisotropy in misfit dislocations is likely to affect the character and spacing of threading dislocations which originate at the interface[49]. Anisotropy of threading dislocation character and geometry is investigated in Section 7.4.

The threading dislocations were assumed to be evenly distributed, enabling specific layer thicknesses at which threading dislocations could meet and coalesce to be defined. The expression presented in equation 5.34 gives discrete thicknesses at which threading dislocation density will be reduced. The random nature of the generation of threading dislocations means that some dislocations are closer together than the average, while others are further apart. Refinement of equation 5.34 to include a distribution of

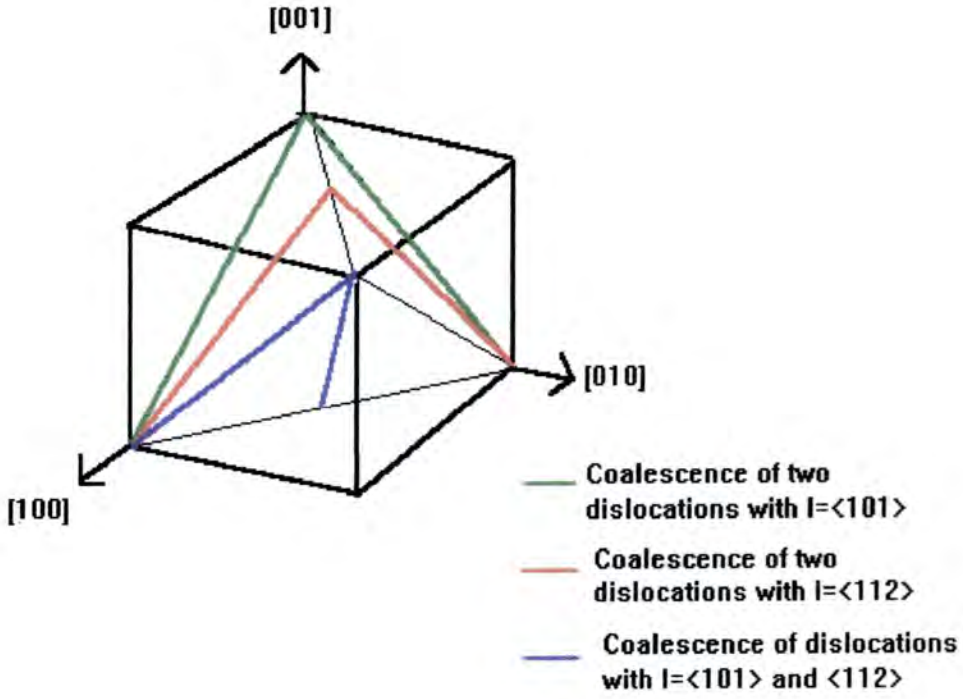

Figure 5.24 Schematic illustration of the height at which dislocations meet depending on their line direction. The initial separation of <101> and <112> shown here is half that of two <101>'s or two <112>'s. For the same initial separation, those with <112> and <101> line directions will meet at a height twice that at which two <101>'s or two <112>'s will meet.

dislocation spacings would have a smoothing effect on the thickness function in a similar way to the work by Dunstan et al.[1] (Section 5.2.1).

It has already been noted that equation 5.38 contains 3 unknown constants, of which only the constant a, has a significant effect on the fit of the equation to the data. If the term $\ln(d/d_0)$ can be considered to be a constant since it is a logarithmic term and is slowly varying, then equation 5.38 approximates to $x \alpha (1/y)$, that is an inverse relationship between threading dislocation density and layer thickness. This was the relationship predicted by Ayers et al.[5] and by Kroemer et al.[7], for thick layers.

5.5 Conclusions

The simple geometrical model for strain relief by Dunstan et al.[1] predicts that critical thickness is inversely proportional to misfit strain in agreement with models by van der Merwe[8], Matthews and Blakeslee[9] and People and Bean[10]. Dunstan and co-workers have developed the geometrical model to describe relaxation of strain above critical thickness and predict that strain is inversely proportional to layer thickness with the constant of proportionality equal to 0.83nm. The expression derived using this model is only applicable within the very small thickness range above critical thickness and below the residual strain regime. The model can only be applied to low misfit systems which display two-dimensional layer-by-layer growth. The very specific conditions which must be met for applicability of this model resulted in none of the literature data examined in this work following the relationship predicted by Dunstan et al..

The model developed by Tatsuoka et al.[2,3] to account for inhomogeneous residual strain in thick layers suggested that threading dislocations were bent over to form misfit segments at all depths within a layer. The expression derived through this approach was found to agree with literature data for misfits of 0.23%, 4.1% and 14.6%. The model is particularly useful for high misfit systems and is the most applicable for the CdTe/GaAs layers

investigated in this thesis. The geometrical model of Dunstan et al. cannot be applied to CdTe/GaAs layers since they display three-dimensional growth.

The model for inhomogeneous residual strain by Tatsuoka et al.[2,3] and the further developments by Durose and Tatsuoka[6] appear to be widely applicable to systems with misfit in the range 0.23% - 14.6% which have exceeded critical thickness. The model relies on the strain relieving properties of threading dislocations to relieve strain according to the earlier model by Tatsuoka et al.. The study conducted in Section 5.3.1 supports the suggestion of Durose and Tatsuoka that a constant background dislocation density will be reached for thick layers, although it cannot be predicted at what thickness this level might be said to have been reached.

A mechanism for the annihilation of threading dislocations by the formation of half-loops suggested by Ayers et al.[5] was discussed in Sections 5.3.2 and 5.3.4. The model predicted that threading dislocation density should be proportional to misfit and inversely proportional to layer thickness. Despite the geometry of the mechanism by which half-loops were formed being unclear and improbable, the expression derived by Ayers et al. was found to be applicable to systems with misfits of 3.8% and 4.1% with thicknesses in the range 1-5μm, although none of the plots gave a graph which passed through the origin. Extrapolation of the reciprocal thickness plots were found to give negative dislocation densities for thick layers in some cases. The model is not applicable to high misfit systems where glide of dislocations is hindered, nor to low misfit layers which are not completely relaxed.

The very simple 'bimolecular' annihilation model by Kroemer et al.[7] was found to approximate to the half-loop model proposed by Ayers et al.[5] in its prediction that threading dislocation density is inversely proportional to layer thickness. A more advanced kinetic model developed by Tachikawa and Yamaguchi[41] was presented in Section 5.3.3 which includes a 'unimolecular' threading dislocation density reduction mechanism. This introduces extra terms into the equation relating threading dislocation density to layer thickness which led to an improvement in fit for high misfit systems. There

was little effect on the data which could be well described by only the binary recombination mechanism.

The new geometrical model which was developed in Section 5.4.2 and discussed in Section 5.4.3 was found to approximate to the relationship predicted by Ayers et al. and Kroemer et al.; that is that threading dislocation density is inversely proportional to layer thickness. The many approximations made in developing the new model leads to a large discrepancy between the theoretical value of the constant of proportionality and that which is found experimentally.

It has not been possible to test exhaustively each model reviewed in this chapter. What is apparent, however, is that each model has a series of conditions which must be met for the model to be applicable. This limited study suggests that the models by Tatsuoka et al.[2], Durose and Tatsuoka[6] and Tachikawa and Yamaguchi[41] are the most suitable to be applied to the CdTe/GaAs heteroepitaxial system which is the major subject of this thesis.

The observation that quite different approaches can predict the same relationship between two parameters demonstrates the great care which must be taken when fitting data to model expressions. It is the expression which is being fitted to a particular set of data, not the model itself. The observation that a particular set of data may be accurately described by a given equation does not in itself mean that the model from which the expression was derived is the correct mechanism for strain relief or threading dislocation density reduction.

REFERENCES FOR CHAPTER 5

1. Dunstan D. J., Young S. and Dixon R. H., *J. Appl. Phys.* **70(6)**, (1991), 3038.

2. Tatsuoka H., Kuwabara H., Nakanishi Y. and Fujiyasu H., *Thin Solid Films* **201**, (1991), 59.

3. Tatsuoka H., Kuwabara H., Nakanishi Y. and Fujiyasu H., *J. Cryst. Growth* **117**, (1992), 554.

4. Yoshikawa M., *J. Appl. Phys.* **63(5)**, (1988), 1533.

5. Ayers J. E., Schowalter L. J. and Ghandhi S. K., *Mat. Res. Soc. Symp. Proc.* **209**, (1991), 661.

6. Durose K. and Tatsuoka H., *Inst. Phys. Conf. Ser.* **134**, Section 9, (1993), 581.

7. Kroemer H., Liu T. Y. and Petroff P. M., *J. Cryst. Growth* **95**, (1989), 96.

8. van der Merwe J. H., *J. Appl. Phys.* **34**, (1962), 123.

9. Matthews J. W. and Blakeslee A. E., *J. Cryst. Growth* **27**, (1974), 118.

10. People R. and Bean J. C., *Appl. Phys. Lett.* **47(3)**, (1985), 322.

11. People R. and Bean J. C., *Appl. Phys. Lett.* **49(4)**, (1986), 229.

12. Timoshenko S. P. and Goodier J. N., *Theory of Elasticity*, New York: McGraw Hill, 1951, chapter 3.

13. Dunstan D. J., Kidd P., Howard L. K. and Dixon R. H., *Appl. Phys. Lett.* **59(26)**, (1991), 3390.

14. Yokogawa T., Sato H. and Ogura M., *Appl. Phys. Lett.* **52(20)**, (1988), 1678.

15. Huang Y., Yu P. Y., Charasse M. N., Lo Y. and Wang S., *Appl. Phys. Lett.* **51(3)**, (1987), 192.

16. Tatsuoka H., Kuwabara H., Fujiyasu H. and Nakanishi Y., *J. Appl. Phys.* **65(5)**, (1989), 2073.

17. Tatsuoka H., Personal Communication, (1995).

18. Dunstan D. J., Kidd P., Beanland R., Sacedón A., Calleja E., González L., González Y. and Pacheco F. J., *Mater. Sci. Technol.* **in press**, (1995).

19. Dunstan D. J., HCMS Consortium Meeting University of East Anglia UK, (1994).

20. Heinke H., Möller M. O., Hommel D. and Landwehr G., *J. Cryst. Growth* **135**, (1994), 41.

21. Wolf K., Jilka S., Rosenauer A., Schütz G., Stanzl H., Reisinger T. and Gebhardt W., *J. Phys. D: Appl. Phys.* **28**, (1995), A120.

22. Lentzen M., Gerthsen D., Förster A. and Urban K., *Appl. Phys. Lett.* **60(1)**, (1992), 74.

23. Takagi Y., Yonezu H., Hachiya Y. and Pak K., *Jpn. J. Appl. Phys.* **33**, (1994), 3368.

24. Lazzarirni L., Nasi L., Normamn C. E., Salviati G. and Bertoni S., *J. Cryst. Growth* **126**, (1993), 133.

25. Stolz W., Guimaraes F. and Ploog K., *J. Appl. Phys.* **63**, (1988), 492.

26. Soga T., Hattori S., Sakai S. and Umeno M., *J. Cryst. Growth* **77**, (1986), 498.

27. Schaffer W. J., Lind M. D., Kowalczyk S. P. and Grant R. W., *J. Vac. Sci. Technol. B* **1**, (1983), 688.

28. Tatsuoka H., Kuwabara H., Nakanishi Y. and Fujiyasu H., *J. Appl. Phys.* **67(11)**, (1990), 6860.

29. Matthews J. W., in *Dislocations in Solids,* Nabarro F R N, Ed. (North Holland, Amsterdam, 1979), vol. 2, Chapter 7.

30. Sze S. M., *Physics of Semiconductor Devices,* (2nd edition), Wiley, 1981, pp. 850.

31. Cleveland Crystals Incorporated, *Internal Report,* (Ohio USA, 1984).

32. Guha S., Munekata H., LeGoues F. K. and Chang L. L., *Appl. Phys. Lett.* **60(26)**, (1992), 3220.

33. Cheng T. T., Aindow M., Jones I. P., Hails J. E., Williams D. J. and Astles M. G., *J. Cryst. Growth* **135**, (1994), 409.

34. Dunstan D. J., *Semicond. Sci. Technol.* **6**, (1991), A76.

35. Muggleberg C., Diplomarbeit Thesis Thesis, *Herstellung und Characterisierung von ZnSe und (ZnMn)Se MBE Strichten,* Humboldt Universität zu Berlin (1992).

36. Horikawa H., Ogawa Y., Kawai Y. and Sakuta M., *Appl. Phys. Lett.* **53(5)**, (1988), 397.

37. Ayers J. E., Schowalter L. J. and Ghandhi S. K., *J. Cryst. Growth* **125**, (1992), 329.

38. Kudlek G., Presser N., Gutowski J., Hingerl K., Abramof E., Pesek A., Pauli H. and Sitter H., *J. Cryst. Growth* **117**, (1992), 290.

39. ASTM Powder Diffraction File

40. Gay P., Hirsch P. B. and Kelly A., *Acta Metallurgica* **1**, (1953), 315.

41. Tachikawa M. and Yamaguchi M., *Appl. Phys. Lett.* **56(5)**, (1990), 484.

42. Matthews J. W., *Phil. Mag. A* **13**, (1966), 1207.

43. Durose K., Turnbull A. and Brown P., *Mat. Sci. Eng.* **B16(1-3)**, (1993), 96.

44. Bauer S., Rosenauer A., Link P., Kuhn W., Zweck J. and Gebhardt W., *Ultramicroscopy* **51**, (1993), 221.

45. Chandra D., Tregilgas J. H. and Goodwin M. W., *J. Vac. Sci. Technol. B* **9(3)**, (1991), 1852.

46. Hull D. and Bacon D. J., *Introduction to Dislocations*, (3rd edition), Pergamon Press, 1989International Series on Materials Science and Technology, volume 37, chapter 1.

47. Atkins P. W., *Physical Chemistry*, (3rd edition), Oxford University Press, 1988, chapter 28.

48. Frost A. A. and Pearson R. G., *Kinetics and Mechanism*, (International Edition), New York: John Wiley, 1961, chapter 10.

49. Fang S. F., Adomi K., Iyer S., Morkoç H., Zabel H., Choi C. and Otsuka N., *J. Appl. Phys.* **68(7)**, (1990), R31.

CHAPTER 6

Depth Resolved Studies of Epitaxial CdTe/GaAs and ZnTe/GaAs

6.1 Introduction

The variation in the characteristics of an epitaxial layer with layer thickness have been observed to occur in both low and high misfit systems. Variations in the electrical properties of CdTe/InSb epilayers have been studied by Ashenford et al.[1] who found a reduction in carrier densities in the region closest to the substrate. Kudlek et al.[2] observed a gradient in the density of acceptor sites in ZnTe/GaAs layers as a result of out-diffusion of As from the substrate. Structural changes with layer thickness are a common finding of HRXRD studies and variations in strain and dislocation density with thickness have been reported for many magnitudes of misfit as is apparent from the data discussed in Chapter 5.

The aim of this chapter is to present depth resolved data concerning the structural quality of CdTe/GaAs and ZnTe/GaAs epilayers, the study has been undertaken using a variety of experimental methods. The opening section serves to confirm work by other authors that, for highly mismatched layers, the major contribution to HRXRD rocking curve broadening comes from mosaic tilts. HRXRD studies carried out on CdTe/GaAs epilayers as a function of thickness and X-ray wavelength are presented in Sections 6.3 and 6.4 respectively. A brief presentation of the changing character of the photoluminescence spectrum of CdTe/GaAs layers with thickness is given in Section 6.5 and compared to the dislocation distribution described in Section 6.3. Finally, the variation of FWHM with layer thickness is investigated for a single ZnTe/GaAs layer in Section 6.6 and a comparison of the findings with those for CdTe/GaAs is also made.

6.2 Triple Axis X-ray Diffraction of CdTe/GaAs

The contributions of mosaic tilts and variations in lattice parameter (lattice dilatations) to X-ray rocking curve widths can be separated by the use of triple axis diffraction (see Section 4.2.3). The use of both a channel cut collimator (CCC) crystal and a channel cut analyser (CCA) crystal results in significant attenuation of the X-ray beam but can be tolerated for the intense, narrow diffraction peaks of near perfect semiconductor crystals such as Si and III-V compounds. This is not the case for highly dislocated crystals such as epitaxial CdTe/GaAs which contains a high defect concentration due to the large lattice mismatch of 14.6%. The HRXRD rocking curves of such layers are broad and weak in intensity and the intensity of radiation reaching the detector after up to nine Bragg reflections is so low as to be almost indistinguishable from background radiation. In cases such as this, a compromise must be reached which allows a detectable level of radiation to fall on the detector whilst still retaining much of the advantages of triple axis diffraction. Hudson[3] investigated dislocated epitaxial $Hg_{(1-x)}Mn_xTe$/ GaAs in triple axis mode by removing the CCC and replacing it with a pin hole collimator. The resulting increase in intensity striking the sample allowed meaningful detection of scattered radiation as a function of angle using a CCA, although a beam conditioner "streak" was introduced. The removal of the CCC seriously disrupts the alignment of an optimised diffractometer and an alternative method is desirable. In the study presented in the following section, an alternative method of increasing diffracted intensity was employed which did not interfere with diffractometer alignment, but which did result in a loss of resolution.

6.2.1 Experimental Details

Triple axis X-ray diffraction was described in Section 4.2.3. In this section the specific experimental conditions employed in this study are described.

The triple axis data presented in this study were collected with a Bede Direct Drive Diffractometer (D3) system. The incident beam was collimated by a two reflection Si 022 CCC. A second CCC (also a two reflection Si 022 channel) was

mounted on the first axis to monochromate the beam (the $CuK\alpha_1$ line was selected). After these four reflections the angular divergence of the beam was approximately 12" and the wavelength dispersion was $\Delta\lambda/\lambda=1.3x10^{-4}$.

The samples were mounted on the second axis as illustrated in figure 6.1 with indexing according to the European and Japanese wafer labelling convention. The beam direction projected onto the $[\bar{1}00]$ direction and tilt optimisation of the sample (001) planes was carried out as described in Section 4.2.2.2. The axis of rotation of the second axis was aligned with the sample surface to ensure that the incident beam did not traverse the sample on rotation. The samples were oriented at the Bragg angle for 004 reflection of $CuK\alpha_1$ radiation. The two samples investigated by triple axis X-ray diffraction were 8.7 and 4.3 μm thick, as calculated from FTIR fringe spacing (Section 4.4.1).

In high resolution mode a CCC is used to select diffracted intensity as a function of angle but this results in severe attenuation of the beam as outlined in the previous section. Two sets of parallel slits 1mm wide were placed between the specimen and the detector, the first at a distance of 186mm from the centre of the second axis and the second at a distance of 310mm[4]. The detector was then displaced from its central position to effectively reduce the second slit to a width of 0.6mm as illustrated in figure 6.2. In this way the detector is no longer "open" as is the case for HRXRD, but has a limited acceptance angle dependent on the distance between the second slit and the specimen. In this case the acceptance angle of the detector is 400" which is much greater than the 7" achieved with a Si 111 CCC analyser. The large acceptance angle means that a $\theta/2\theta$ scan will result in lattice dilatations and to a much lesser extent mosaic tilts contributing to the rocking curve width. The aim of this study was to determine whether lattice dilatations or mosaic tilts were the dominant factor in broadening HRXRD rocking curves. The loss of resolution is acceptable, therefore, since high resolution reciprocal space mapping is not an aim of the study.

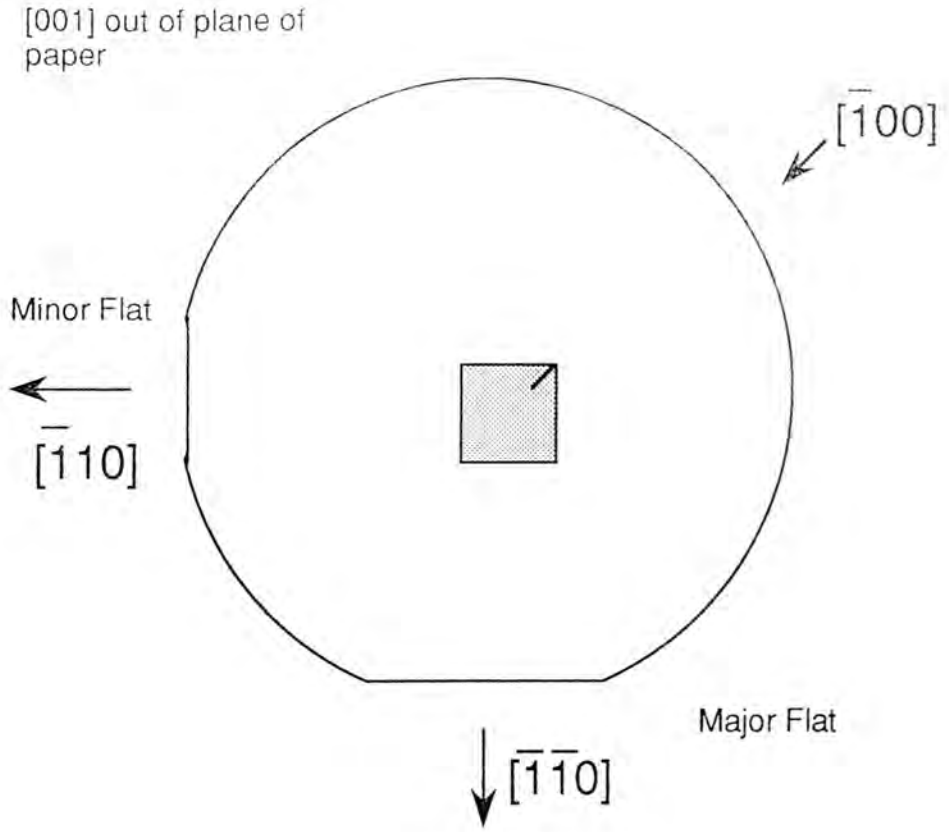

Figure 6.1 Illustration of the orientation of sample mounting for XRD measurements carried out in Chapter 6 on CdTe/GaAs epilayers. The wafer indexing is according to the European and Japanese convention. The beam direction projects onto [$\bar{1}$00].

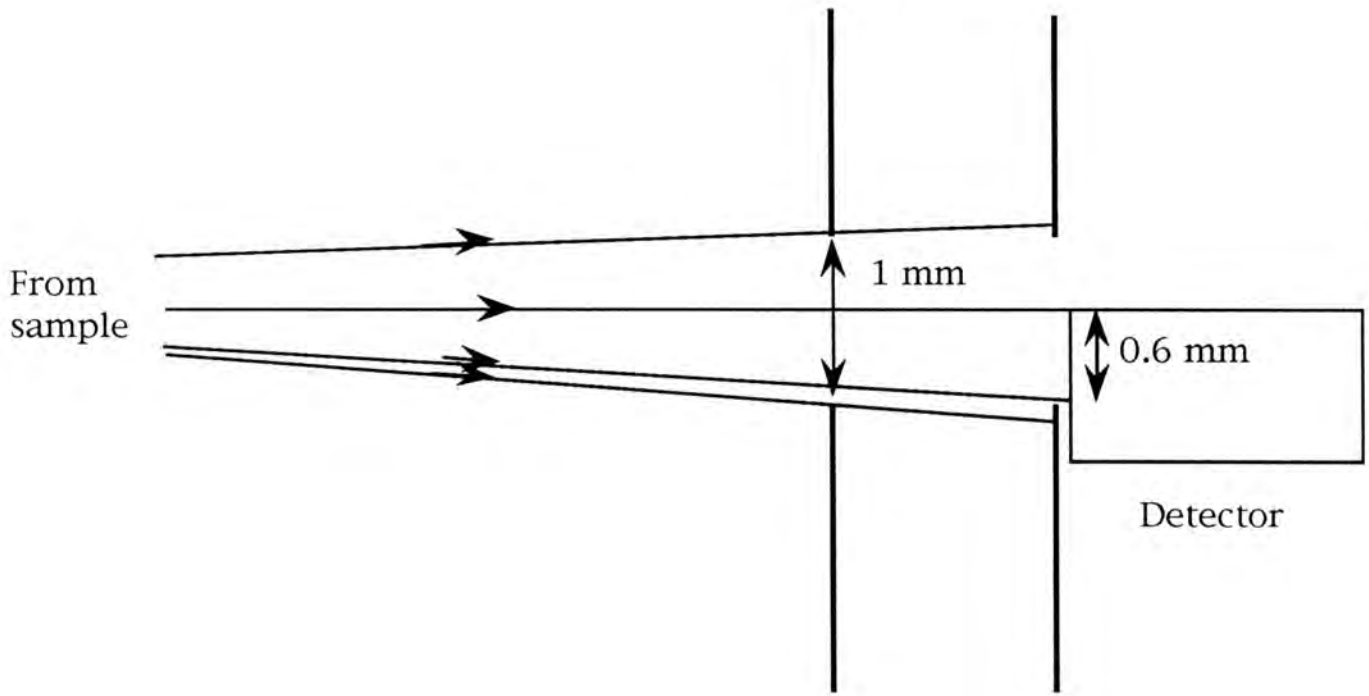

Figure 6.2 Schematic diagram of the reduction in angular acceptance of the detector by the inclusion of two 1mm slits and displacement of the detector.

6.2.2 Results and Discussion

Figure 6.3 shows a single HRXRD scan with an open detector (broadening due to both tilts and dilatations) compared with a $\theta/2\theta$ scan (broadening due to dilatations only, in the ideal case) for an 8.7μm thick layer of CdTe/GaAs. The full width at half maximum (FWHM or β) is 300 arcseconds for contributions from lattice tilts and dilatations and 95 arcseconds for a $\theta/2\theta$ scan with reduced acceptance angle of detector. It is clear that a significant amount of the broadening of the HRXRD rocking curve is due to tilts, which do not contribute to such a great extent in a $\theta/2\theta$ scan. A reciprocal space map (see Section 4.2.3.2) is shown for a 4.3 μm layer in figure 6.4. The axes are of the same scale and the isointensity contours shown are for the logarithm of the diffracted intensity. The comparison of the "sharpness" of the Bragg diffraction peak should be judged according to the spacing of the contours rather than the extent of the final contour due to the nature of logarithmic plotting. It can be seen from figure 6.4 that the spacing of the contours in the ΔQ_z direction (lattice dilatations) is much closer than in the ΔQ_y direction (tilts), again this shows that the tilt distribution is considerably broader than that of the lattice dilatation distribution. A conventional HRXRD scan with an open detector corresponds to a scan along the ΔQ_y direction (constant detector position) with intensity being integrated along a line inclined at the Bragg angle to the ΔQ_y axis[5]. The "tail" on the lower right hand side of the Bragg peak is termed an "analyser streak" and would be greatly reduced if an analyser crystal rather than slits was used[6].

Similar investigations have been carried out by Keir et al.[7] on 4.4μm thick CdTe buffer layers grown on GaAs by MOVPE. They found that samples with HRXRD rocking curve widths of 289" and 612" gave widths of 40" and 44" respectively in $\theta/2\theta$ scan mode. Hudson[3] investigated a 7μm thick $Hg_{(1-x)}Mn_xTe$ layer grown on a $Cd_{0.96}Zn_{0.04}Te$ substrate and recorded a FWHM of 68" for a $\theta/2\theta$ scan compared to 207" for a θ only scan (fixed detector position with acceptance angle determined by setting of analyser crystal, broadening in this case is due to tilts only). It should be noted that Hudson used a channel cut analyser and Keir et al. used a high quality Si crystal to select the diffracted beam angle reaching the detector, both

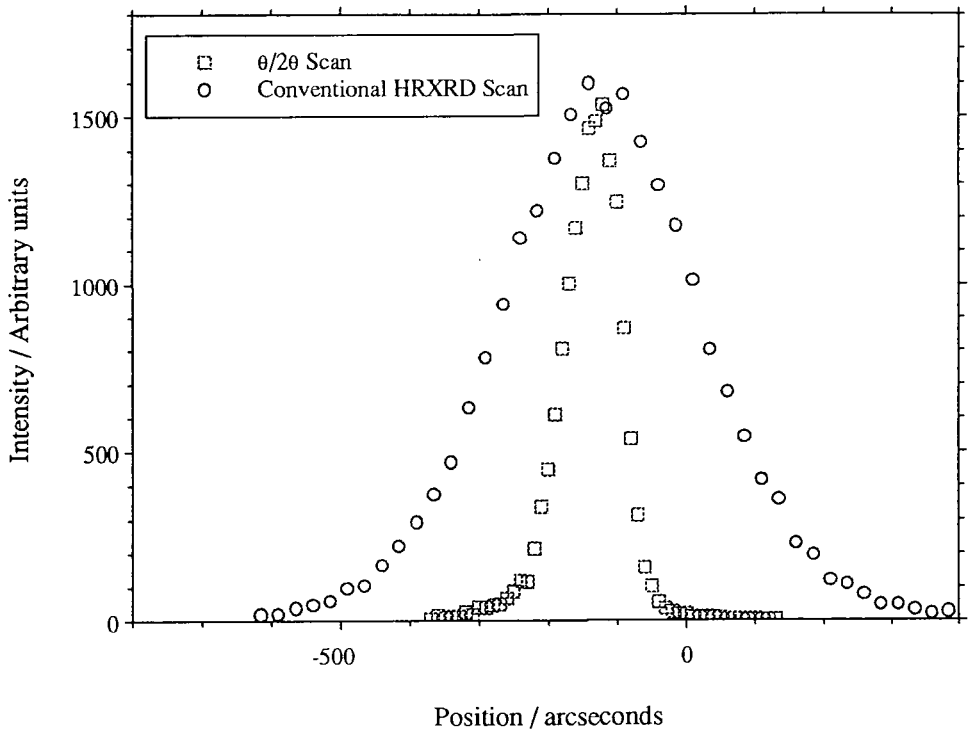

Figure 6.3 Demonstration of the contribution to HRXRD rocking curve broadening due to subgrain (mosaic) tilts. Conventional HRXRD scan broadening includes contributions due to both tilts and lattice dilatations. The sample is (001)CdTe/GaAs and is 8.7μm thick. The θ/2θ scan was conducted with a 0.6mm slit reducing the acceptance angle of the detector to 400", broadening for this case is due mainly to lattice dilatations, although tilts contribute to a small degree.

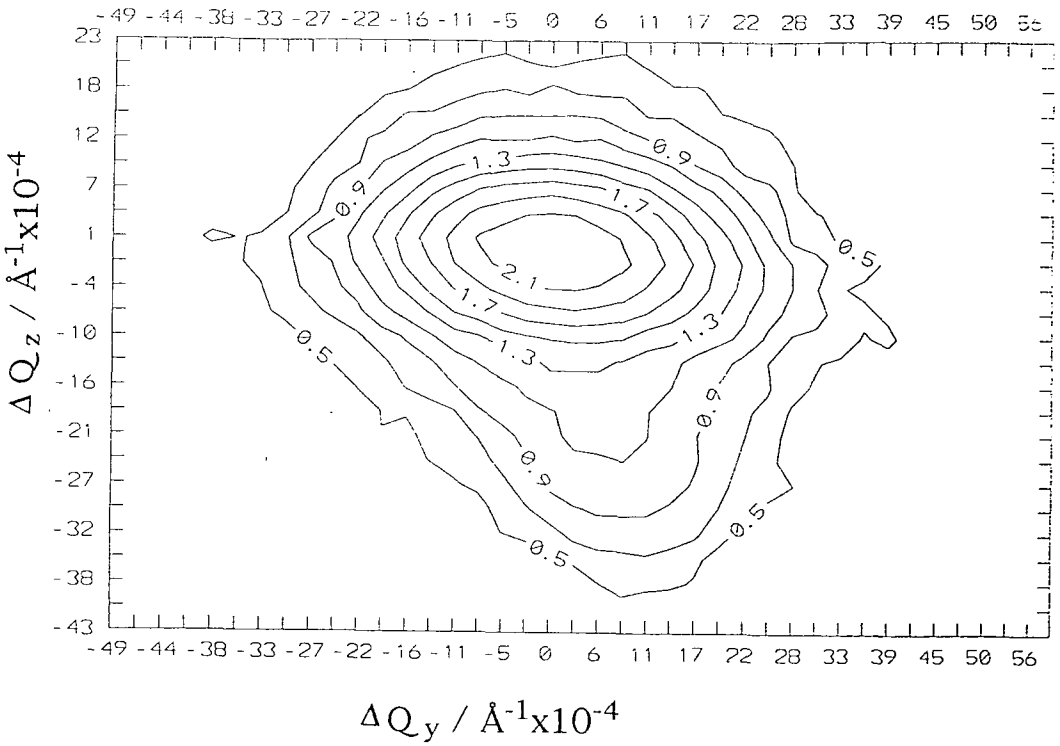

Figure 6.4 Reciprocal space plot of the scatter around the (004) reciprocal lattice point of a 4.3μm layer of (001)CdTe/GaAs. Spacing of the contours indicates the sharpness of the peak. Broadening in the ΔQ_z direction is due to lattice dilatations (and tilts to a lesser extent). Broadening in the ΔQ_y direction is due to mosaic tilts (and lattice dilatations to a lesser extent).

methods giving a far greater angle specificity than the narrow slit geometry used in the present study.

From this study and comparison with work by other authors, it is clear that there is a greater contribution to the width of a conventional HRXRD rocking curve from mosaic tilts than from lattice dilatations. The limitations of using shielding slits instead of an analyser crystal means that the width of the $\theta/2\theta$ scan shown in figure 6.3 still contains contributions from tilts. The acceptance angle of the detector in this study has been estimated to be about 400" compared to an acceptance angle of 7" for a Si 111 channel cut analyser crystal. With this in mind, it is reasonable to suppose that if it were possible to undertake an investigation of these highly defective layers using an analyser crystal, then the width of the $\theta/2\theta$ scan thus recorded would not be significantly broader than the intrinsic width (16" by dynamical simulation).

It is proposed that to a reasonable approximation, the FWHM of a HRXRD rocking curve is due to tilts. In all calculations of dislocation density using the relationship by Gay et al.[8], it will be assumed that broadening is due totally to tilts once the effects of instrumental broadening and intrinsic rocking curve width have been taken into account.

6.3 Conventional High Resolution X-ray Diffraction of Epitaxial CdTe/GaAs

6.3.1 Experimental Details

High Resolution X-ray Diffraction (HRXRD) was described in Section 4.2.2. In this section the specific experimental conditions employed in this study are described, together with the conditions for etching CdTe in order to obtain depth resolved information.

HRXRD rocking curves were recorded on a Bede Model 150 Diffractometer using Co$K\alpha_1$ radiation, the $K\alpha_2$ component being removed by a slit placed between the reference and specimen crystals. The symmetric 004 CdTe

reflection was used in the non-dispersive setting with an InSb (001) crystal as reference. From Section 4.2.2.2, the broadening effect of the difference in lattice parameter of reference and layer is reduced by 8" when using an InSb reference crystal rather than the more common GaAs reference. This is assuming that the fractional spread in wavelength of the X-rays reaching the specimen is 2.6×10^{-4}, the intrinsic width of the $K\alpha_1$ line[6]. A beam size of 2.5mmx0.3mm was used, with the incident beam projecting onto $[\bar{1}00]$ as shown in figure 6.1, tilt optimisation of the sample (001) planes was carried out as described in Section 4.2.2.2.

The rocking curves of five MOVPE grown (001)CdTe/GaAs layers of thickness 25, 8.7, 4.3, 0.6 and 0.3 μm were recorded. The layer thicknesses were calculated according to Section 4.4.1, growth details are given in Section 3.3.3.1. A profile of FWHM as a function of depth in a layer was obtained from HRXRD rocking curves recorded after progressive etching with a 3%bromine in 1:1 ethylene glycol/methanol solution. Lacomit varnish was used to mask one region of the sample while the rest was etched. The etch depth was measured after removal of the mask using a Tencor alpha-step 200. Etching was carried out at temperatures of between 17 and 21°C. Great care was taken to record rocking curves from the same position on the sample after each etch.

Errors in FWHM were calculated assuming a Gaussian distribution of tilts and that the error in the intensity recorded at any angular position is $\sqrt{N}$ where N is the intensity in counts per second. The uncertainty is small for all but the broadest and lowest intensity peaks. Uncertainties in layer thickness for the five as-grown samples were estimated from the uncertainty in measuring the spacing of fringes in the FTIR transmission spectra and from the thickness inhomogeneity of the samples (Section 3.4.2); the uncertainty is again small. The uncertainties for the etched layers are much greater due to non-uniform etching (despite the use of an etch solution containing ethylene glycol to increase the etch viscosity and approach a diffusion limited etch reaction). Etch depth was recorded for three positions on the sample and the range of values was taken as the uncertainty.

6.3.2 Results and Discussion

The 004 peak widths of rocking curves recorded after repeated etching are plotted with respect to distance from the CdTe/GaAs interface, from now on called thickness, in figure 6.5. For comparison, the FWHM of a series of (001)CdTe/GaAs layers grown by hot wall epitaxy (HWE)[9] are also plotted. The effects of experimental broadening and intrinsic width have not been removed from the FWHM values for either set of data.

The widths of the rocking curves decrease with increasing thickness for layers grown by both MOVPE and HWE. The most rapid decrease occurs during the first two microns of growth; the rate of decrease slows as the layer thickens but a constant value of FWHM is not reached even at a thickness of 25μm. The layers grown by HWE have narrower rocking curves than a layer of the same thickness grown by MOVPE. The difference between HWE and MOVPE is less significant for thick layers than for thin ones. A comparison of FWHM for thick (001)CdTe/GaAs grown by MOVPE, conventional HWE and HWE using a gold tube radiation shield is shown in table 6.1.

Growth method	Source of data	FWHM/arcseconds	Thickness/μm
MOVPE	Present work	122	25
MOVPE	Irvine et al.[10]	137	11.7
HWE	Tatsuoka et al.[9]	145	15
HWE gold tube radiation shield	Hwang et al.[11]	89	15

Table 6.1 Comparison of HRXRD FWHM for thick CdTe/GaAs epilayers grown by three different techniques. The effects of instrumental broadening and intrinsic width have not been accounted for. The choice of radiation wavelength and reference crystal are not the same for all measurements; the table is for approximate comparison only.

One of the major differences between HWE and other vapour growth techniques is that growth proceeds in thermodynamic equilibrium, a detailed review by Lopez-Otero can be found in reference 12. In HWE, polycrystalline CdTe is used as the source material at one end of a quartz tube while the substrate is placed on the open end of the tube. Resistance windings heat the source, the 'hot' wall of the tube and the substrate independently. The hot wall maintains the vaporised source atoms at constant thermal equilibrium as the layer grows. In contrast, thermodynamic equilibrium is not maintained above a layer growing by MOVPE. The comparison of growth by these two methods suggests that the layers grown by MOVPE are not as relaxed and that a process which encourages movement towards equilibrium relaxation, such as annealing, may improve the layer quality. The observation that the difference between HWE and MOVPE layers is less for thicker layers may be due to movement towards equilibrium during growth, the thicker layers having a longer growth time.

The choice of CdTe buffer layer thickness for the subsequent growth of $Cd_xHg_{(1-x)}Te$ (CMT) by MOVPE has increased in recent years. From 1989 buffer layers were typically 3-4μm thick[7,13-15], now buffer layers 6μm thick[16] are routinely grown. From the present study it is estimated that FWHM reduces from 520" to 350" as buffer layer thickness increases from 4μm to 6μm, a further reduction to 300" is expected on increasing to 8μm. Recent work by Nishino et al.[17] found that the minimum etch pit density (EPD) was obtained when the CdTe buffer layer and CMT layer were both at least 8μm thick, little reduction in EPD was observed for buffer layers thicker than 8μm. The choice of buffer layer thickness depends not only on the crystallographic quality but also on the surface morphology which worsens with increasing thickness. There is a trade off between the desire for good quality material and uniform morphology. The variation in surface morphology with layer thickness has been demonstrated in Section 3.3.3.

A comparison between the FWHM of the etched thick layer and those of the five layers of different thicknesses is made in figure 6.6. The FWHM of the series of five layers follows the same trend with thickness as the repeatedly

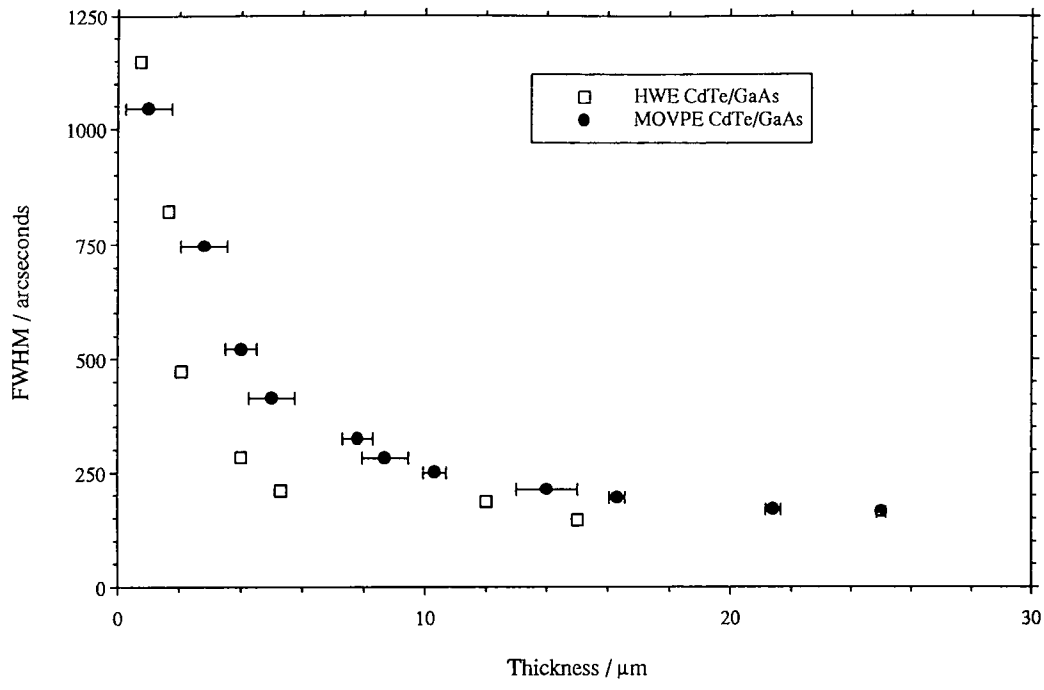

Figure 6.5 Comparison of HRXRD FWHM versus thickness for a 25μm CdTe/GaAs layer grown by MOVPE, which has been repeatedly etched and remeasured, and for a series of seven CdTe/GaAs layers grown by HWE, data from Tatsuoka et al.[9].

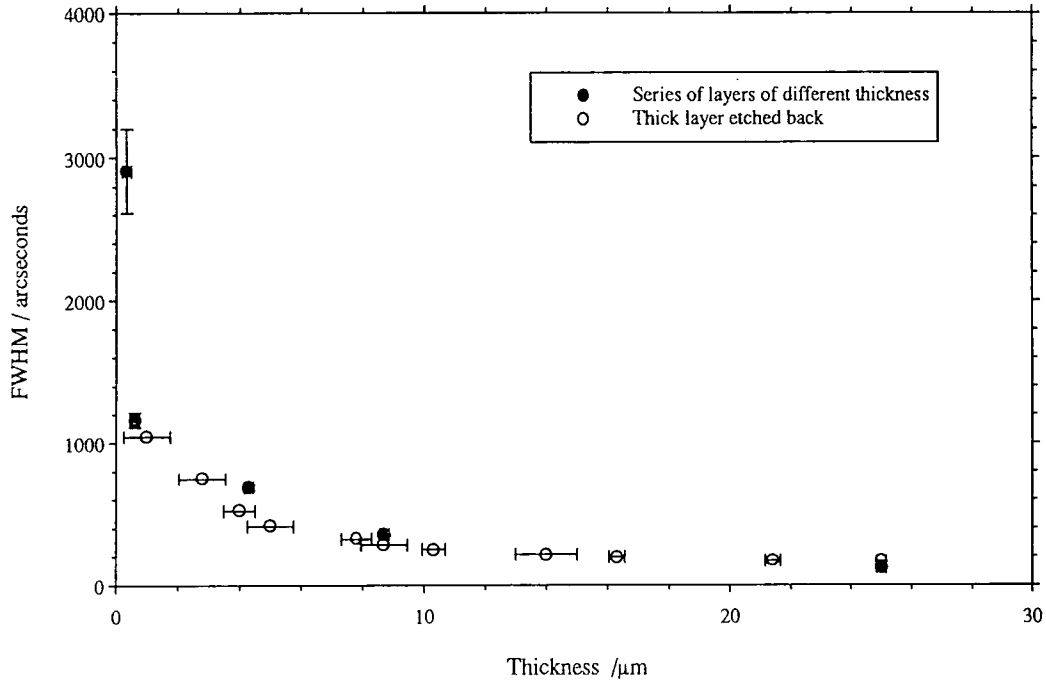

Figure 6.6 Comparison of HRXRD FWHM versus thickness for a 25μm MOVPE grown (001)CdTe/GaAs layer, which has been repeatedly etched and remeasured, and for a series of five layers grown to different thicknesses.

etched sample. The FWHM of the 8.7 and 4.3μm layers appear to be slightly greater than for a thick layer that has been etched back to these two respective thicknesses. The difference is very small and care must be taken in drawing any conclusions. It should be mentioned however, that if movement towards equilibrium strain distribution occurs during extended growth as suggested in the discussion of MOVPE and HWE, then a layer grown to say 4μm would be expected to be of poorer structural quality than the first 4μm of a layer which has been grown to 25μm. The difference is small, however, and suggests that if post-growth annealing is to be successful for CdTe/GaAs grown by MOVPE, then annealing temperatures greater than the growth temperature will be required, this is investigated in Section 8.1.

The FWHM values presented in figure 6.5 were used to estimate the threading dislocation density as a function of layer thickness. The method of calculating threading dislocation density from values of FWHM using the relationship by Gay et al.[8] (equation 6.1) was outlined in Section 4.2.2.3 and Chapter 5. Again it was assumed that a threading dislocation has the same Burgers vector tilt component as a 60° misfit dislocation (see Section 2.2.2). B was taken to be the intrinsic width of a rocking curve as predicted by dynamical simulation using the software program RADS (available from Bede Scientific Instruments Ltd.); experimental broadening was neglected since the apparatus was operating in non-dispersive mode with an almost lattice matched reference crystal. It was shown from triple axis experiments (Section 6.2) that the HRXRD FWHM may be assumed to be totally due to tilts, with no contribution from lattice dilatations, intrinsic and experimental broadening having been removed.

$$D=\frac{\left(\beta^2-B^2\right)}{9b_{tilt}^2} \qquad \text{equation 6.1}$$

The study of models which predict the relationship between threading dislocation density and layer thickness, which was presented in Chapter 5, suggested that the relationships predicted by Durose and Tatsuoka[18] and by Tachikawa and Yamaguchi[19] were the most likely to be applicable to the high misfit system of CdTe/GaAs. It is expected that the model by

Ayers et al.[20] which predicts that threading dislocation density is inversely proportional to thickness will not be followed. Figure 6.7 shows best fit lines for relationships predicted by Ayers et al.[20], Durose and Tatsuoka[18] and by Tachikawa and Yamaguchi[19]. All three lines are plotted using the same axes so that the variance of each fit may be meaningfully compared to the others. Note that $D(\infty)$ was taken to be $6.5 \times 10^7 cm^{-2}$ and best fits for the models by Ayers et al. and by Tachikawa and Yamaguchi were obtained individually, before being replotted on the axes required by the Durose and Tatsuoka model. The point for the 25μm layer was excluded from the calculation of best fit for the model by Durose and Tatsuoka but was included in the best fit calculations of the other two models. The data point for the 25μm layer was omitted from the fit to the Durose and Tatsuoka model since, in the absence of other layers of such large thickness, it was not clear whether layers deviate from the model as their densities approach the order of $D(\infty)$. The best fit line for the Ayers plot was obtained by fitting equation 6.2 rather than equation 6.3 since a straight line passing through the origin could not be drawn through more than two of the data points. The variances of the best fits for the three models are compared in table 6.2.

$$D = \frac{a}{h} + b \quad \text{where a and b are constants} \qquad \text{equation 6.2}$$

$$D = \frac{a}{h} \quad \text{where a is a constant} \qquad \text{equation 6.3}$$

Model	Half-loop model	Strain relief by threading dislocations	'Bimolecular' and 'Unimolecular' annihilation
Reference	Ayers et al.[20] modified-see equations 6.2 and 6.3	Durose and Tatsuoka[18]	Tachikawa and Yamaguchi[19]
Variance/ $(\ln[cm^{-2}])^2$	3.9	0.5	0.8

Table 6.2 Comparison of the variance of best fit lines for three models reviewed in Chapter 5.

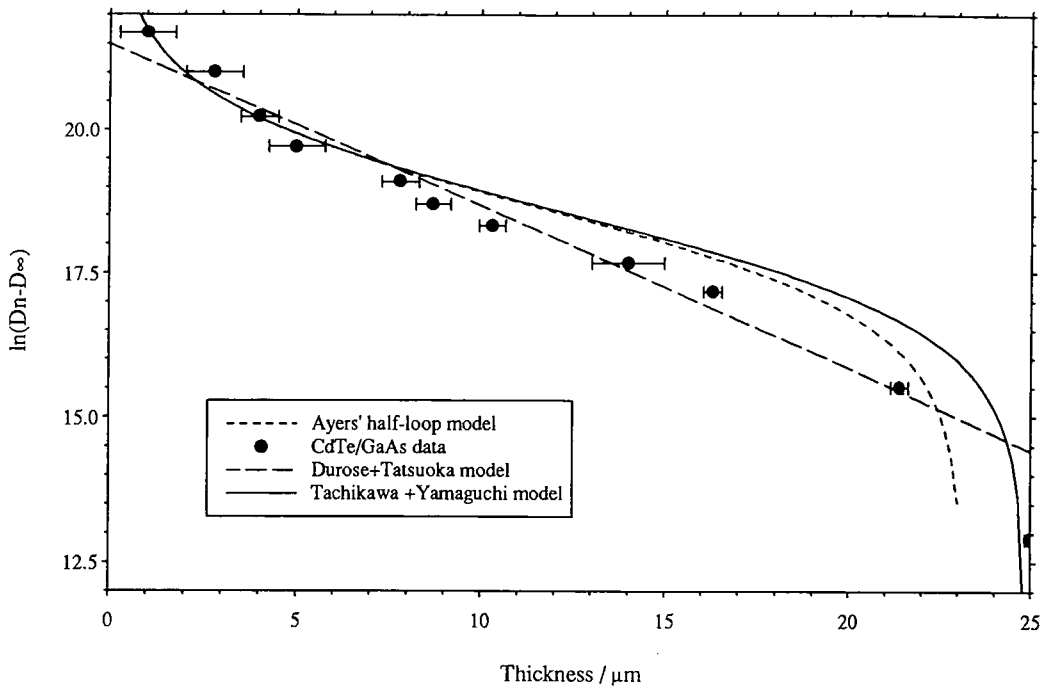

Figure 6.7 Dislocation density data calculated from DCXRD FWHM versus thickness for 25μm a (001)CdTe/GaAs epilayer which has been repeatedly etched and remeasured. Comparison of best fit lines for relationships predicted by Ayers et al.[20] (half-loop model), Durose and Tasuoka[18] (strain relief by threading dislocations) and by Tachikawa and Yamaguchi[19] ('unimolecular' and 'bimolecular' annihilation mechanisms), $D(\infty)=6.5\times10^{7}cm^{-2}$. Note that the agreement with Ayers' expression (equation 6.3) is very poor and a modified expression (equation 6.2) has been used in this graph.

As was predicted from the review in Chapter 5, the best fit lines are indeed obtained for the relationships by Durose and Tatsuoka and by Tachikawa and Yamaguchi. The data does not show an inverse relationship between thickness and threading dislocation density as was predicted by Ayers et al.

6.4 Synchrotron High Resolution X-ray Diffraction

6.4.1 Introduction

The HRXRD experiments presented in Sections 6.2 and 6.3 were carried out at a fixed wavelength which was determined by the X-ray source tube. The triple axis investigations of Section 6.2 were carried out using the $CuK\alpha_1$ line, while the HRXRD studies of Section 6.3 used the $CoK\alpha_1$ line. Synchrotron radiation is a source of white X-rays and a particular wavelength may be selected by the use of a monochromator crystal. In this section a series of HRXRD experiments carried out at different wavelengths are presented, the depth penetration properties of X-rays are reviewed and the experimental conditions used in the study summarised.

6.4.2 Depth Penetration of X-rays

When X-rays encounter any form of matter, they are partly transmitted and partly absorbed. The fractional decrease in the intensity, I, of an X-ray beam as it passes through a homogeneous substance is proportional to the distance traversed, x,[21,22]. The differential form of this relationship is given in equation 6.4 and on integration gives equation 6.5 where μ is the linear absorption coefficient of the material, I(0) is the incident intensity and I(x) is the intensity after passing through a thickness x of material.

$$\frac{dI}{I} = -\mu dx \qquad \text{equation 6.4}$$

$$I(x) = I(0)\exp[-\mu x] \qquad \text{equation 6.5}$$

μ is proportional to density ρ, therefore the quantity μ/ρ is a constant for a given element and is called the mass absorption coefficient. The mass absorption coefficient of a compound is simply the weighted average of the mass absorption coefficients of its constituent elements. If w_1,w_2 etc. are the weight fractions of elements 1, 2, etc. in the compound and $(\mu/\rho)_1$, $(\mu/\rho)_2$ etc. are their mass absorption coefficients, the expression for the mass absorption coefficient of the compound is given in equation 6.6. The mass absorption coefficient is also dependent on wavelength as indicated in equation 6.6. Equation 6.5 can then be re-written in terms of the mass absorption coefficient and density of the compound (equation 6.7).

$$\left(\frac{\mu}{\rho}\right)_{cpd,\lambda} = \sum_{i=1}^{n} w_i \left(\frac{\mu}{\rho}\right)_{i,\lambda} \qquad \text{equation 6.6}$$

$$I(x) = I(0)\exp\left[-\left(\frac{\mu}{\rho}\right)_{cpd,\lambda} \rho_{cpd} x\right] \qquad \text{equation 6.7}$$

The values of mass absorption coefficient for the elements are only tabulated for wavelengths corresponding to the characteristic lines of commonly used X-ray sources. Since white beam radiation is used in this experiment, the mass absorption coefficient of CdTe, calculated from equation 6.6 for the wavelengths tabulated in the International Tables of Crystallography[23], must be extrapolated to obtain values of $(\mu/\rho)_{cpd}$ for non-characteristic wavelengths. Extrapolation in this manner is valid only if carried out away from the absorption edges of Cd and Te. Figure 6.8 shows the fit of a polynomial of order 5 to $(\mu/\rho)_{cpd}$ for CdTe calculated from equation 6.6. The absorption edges of Cd and Te occur at 0.464Å and 0.390 Å for the K absorption edge, and at 3.503Å and 2.855Å for the L absorption edge respectively[23]. Wavelengths in the range 0.69 $\rightarrow$ 1.95Å are used in the present work; no absorption edge occurs in this range.

If an X-ray beam is considered to undergo Bragg reflection as shown in figure 6.9, where θ is the Bragg angle of the diffracting planes, and ω is the angle of offcut of the substrate about an axis perpendicular to the plane of

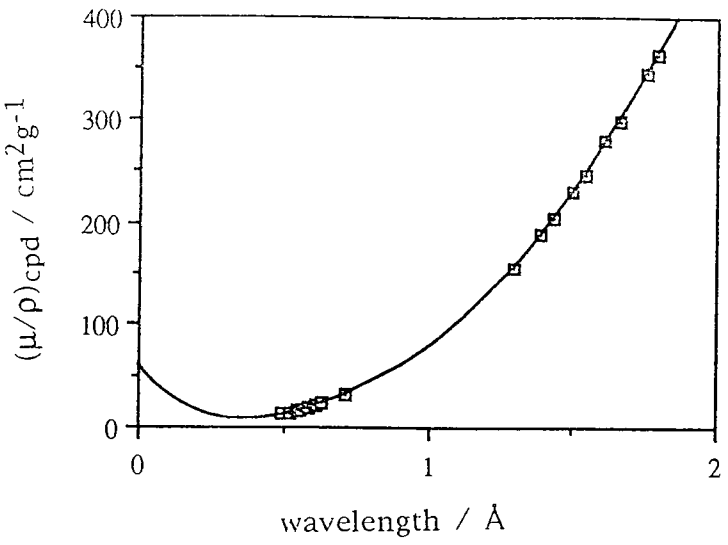

Figure 6.8 Mass absorption coefficient of CdTe as a function of wavelength. The curve shown is a polynomial of order 5. The curve fit may be used to determine mass absorption coefficients for nontabulated wavelengths in the region between the two clusters of points. No absorption edges occur in this region. The behaviour of the polynomial curve at low wavelength is an artefact of the polynomial and does not describe the relationship between mass absorption coefficient and wavelength. The equation of the polynomial is:

$$(\mu/\rho)_{cpd} = 59 - 345\,\lambda + 774\,\lambda^2 - 718\,\lambda^3 + 380\,\lambda^4 - 73\,\lambda^5 \qquad cm^2g^{-1}$$

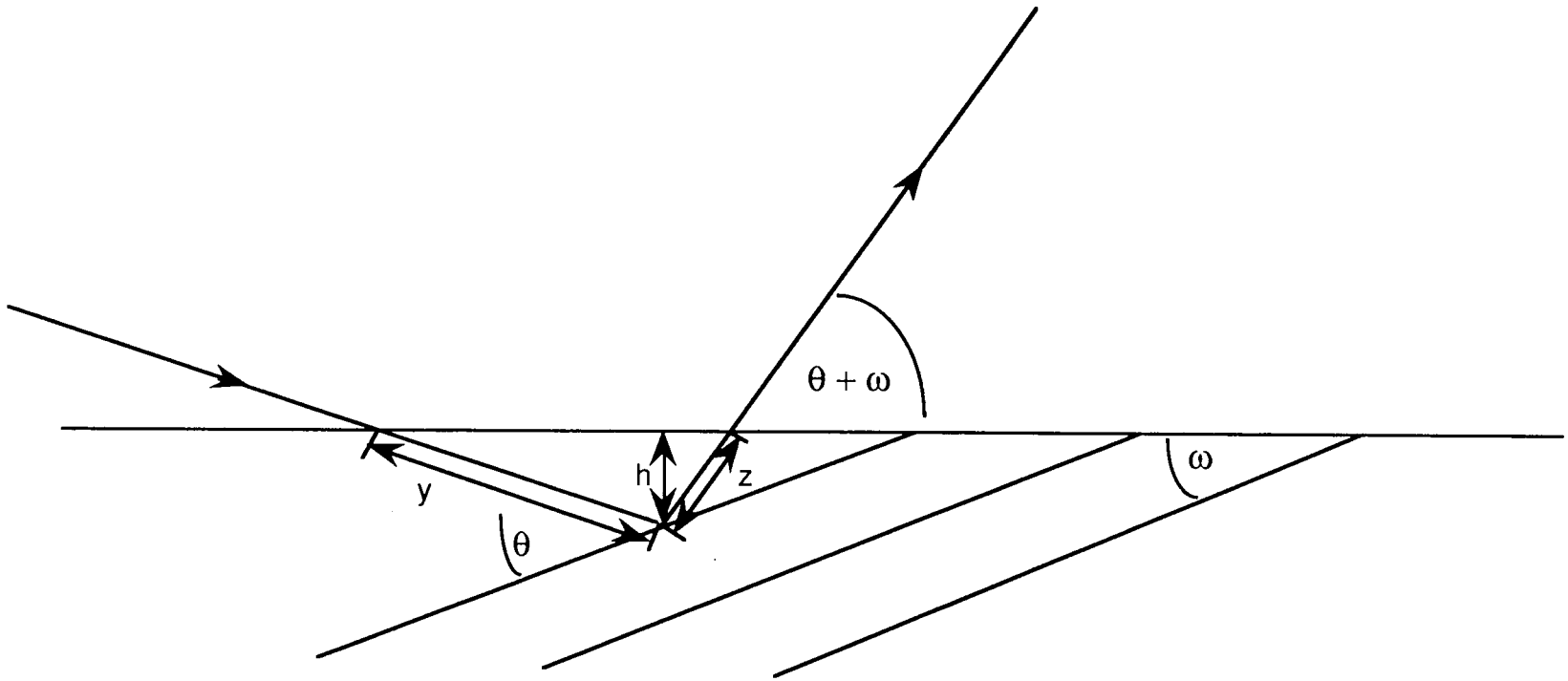

Figure 6.9 Schematic illustration of the path traversed by an X-ray beam undergoing 004 Bragg reflection for a sample with offcut ω about an axis perpendicular to the plane of the paper.

the figure, then equation 6.7 may be expressed as given in equations 6.8 and 6.9.

$$I(x) = I(0)\exp\left[-\left(\frac{\mu}{\rho}\right)_{cpd,\lambda}\rho_{cpd}(y+z)\right] \qquad \text{equation 6.8}$$

$$\ln\left|\frac{I(x)}{I(0)}\right| = -\left(\frac{\mu}{\rho}\right)_{cpd,\lambda}\rho_{cpd}\,h\left[\frac{2\sin\theta\cos\omega}{\sin(\theta-\omega)\sin(\theta+\omega)}\right] \qquad \text{equation 6.9}$$

For a given fractional reduction in intensity [I(x)/I(0)], the depth to which X-rays will penetrate in order to be attenuated by the given amount, will be dependent on wavelength since $(\mu/\rho)_{cpd}$ varies with wavelength. Selection of a long wavelength which undergoes strong attenuation will give a more surface sensitive measurement than a short wavelength which has a smaller mass attenuation coefficient and thus penetrates further for a given fractional reduction in intensity.

6.4.3 Experimental Details

The experimental configuration used in this study is illustrated in figure 6.10. The main difference between this arrangement and that described in Section 4.2.2 and used in other HRXRD experiments reported in this chapter, is that the Si (111) reference crystal no longer diffracts only one intense wavelength (such as CuKα_1 or CoKα_1) but all wavelengths satisfying equation 6.10. The wavelength whose diffraction contributes to the recorded rocking curve is selected by setting the specimen at the Bragg angle for (004) diffraction.

$$n\lambda = 2d\sin\theta_B \qquad \text{equation 6.10}$$

The angular position of the Si(111) strain relieved reference crystal was calibrated using the K absorption edge of Zirconium (Zr) which occurs at 0.6887Å. The accuracy with which this can be set is estimated to be 1'. Other wavelengths were selected by rotating the first axis from this calibrated

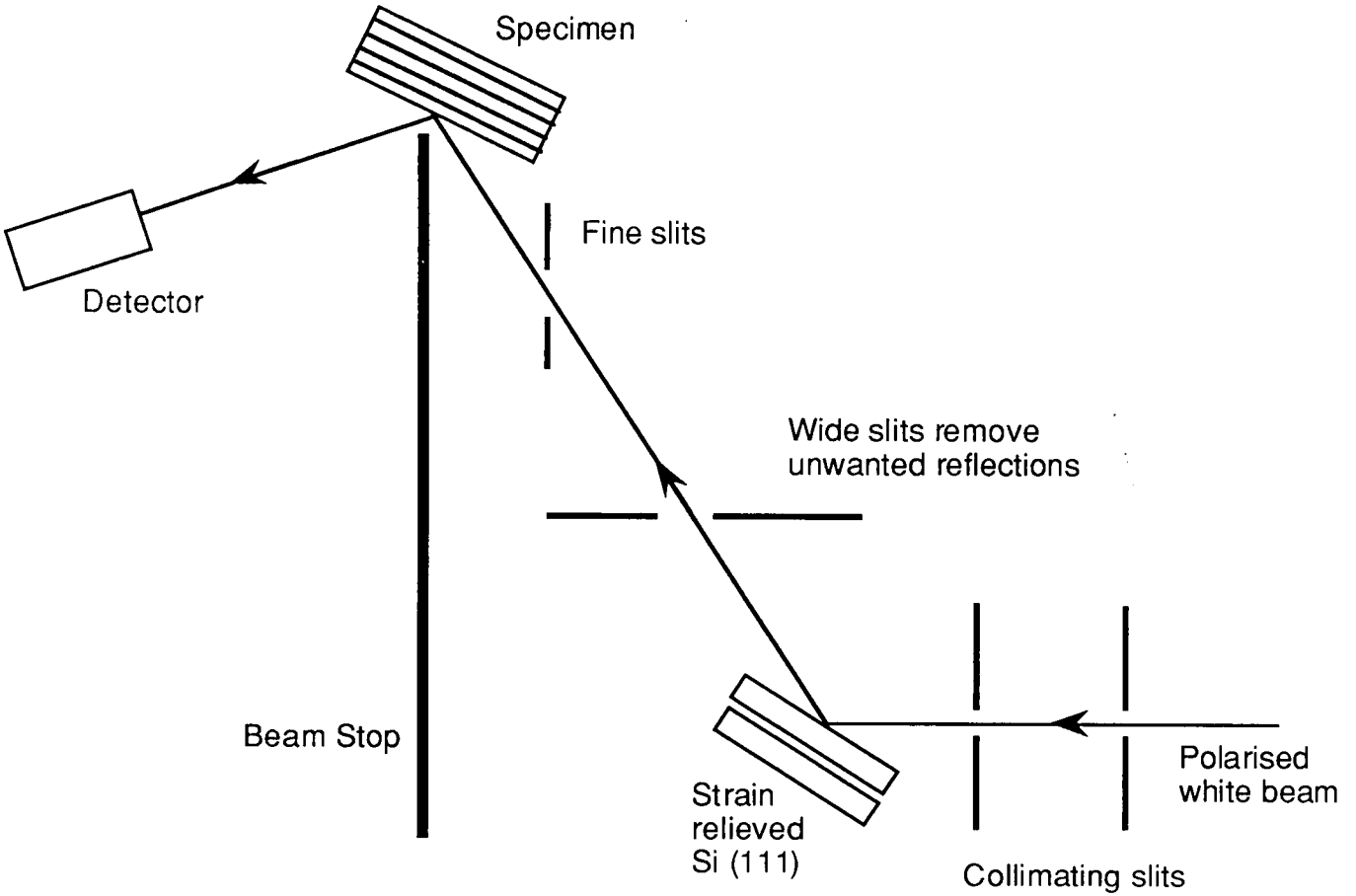

Figure 6.10 Experimental configuration for HRXRD using a white beam source. Wavelength contributing to rocking curve is determined by the angular settings of the Si(111) crystal and specimen. See text for details.

position using a vernier scale; the extra uncertainty of this procedure being estimated to be 1'. The uncertainty in setting the wavelength to contribute to the HRXRD rocking curve is calculated from the propagation of uncertainty in θ_B from equation 6.10. The wavelengths selected in this investigation are listed in table 6.3 together with the Si reflection used, the uncertainty in wavelength and the linear absorption coefficient of CdTe at each wavelength.

Wavelength λ / Å	Si reflection hkl	λ uncertainty/Å	$(\mu/\rho)\,\rho$ / μm^{-1}
0.69	333	0.06	0.017
0.85	333	0.03	0.030
1.25	333	0.04	0.082
1.95	111	0.16	0.258

Table 6.3 Summary of the wavelengths selected using Si (111) reference crystal, the reflection used to select the wavelength and the uncertainty in selecting the wavelength. The linear attenuation coefficient of CdTe at each of the wavelengths is also given, having been calculated from equation 6.6 from the mass attenuation coefficients of Cd and Te[23] and the density of CdTe. The density of CdTe was taken to be 5.856 gcm^{-3} as given in the table of X-ray density, reference 24. This value was confirmed for single crystal CdTe from the atomic masses of Cd and Te[24] and the lattice parameter of CdTe at room temperature[25].

The beam reaching the sample was 0.5mmx3.5mm in size and projected onto the [$\bar{1}$00] direction as shown in figure 6.1. The sample investigated was the 25μm thick (001)CdTe/GaAs epitaxial layer of figures 6.5 and 6.6. Although the first axis was tilt optimised, the poor alignment equipment on Station 7.6 at Daresbury Laboratory did not allow for the desired tilt optimisation of the sample; the broadening effect of the misorientation of diffracting planes is described in Section 4.2.2.2. The effect of this possible misorientation will be the same for all scans and is expected to be small due to the narrow angular divergence of the synchrotron source.

6.4.4 Results and Discussion

The rocking curves obtained from the 25μm CdTe/GaAs layer at the four wavelengths given in table 6.3 are shown in figure 6.11. The relative intensities of the peaks are arbitrary on the scale used. The curves are not as smooth as those recorded by conventional methods owing to the larger incident beam size which was used in this case (the incident beam was 0.5mmx3.5mm rather than 0.3mmx2.5mm as used in Section 6.3). The use of a larger beam increases the chance of sampling an area which is tilted significantly with respect to the majority of the sample. The particular area sampled in this experiment was also investigated by Double Axis X-ray Topography and was found to contain regions of large misalignment (full analysis and discussion is given in Section 7.2).

It has been stated by many authors[22,26-28] that the mosaic tilt distribution which contributes to rocking curve broadening is Gaussian in nature. This is the expected distribution for tilted grains randomly oriented about a mean position. Curve fitting was carried out for the CdTe/GaAs layers examined in Sections 6.2-6.5 and rocking curves were found to be Gaussian when recorded with small area incident beams. In order to determine values of FWHM for the rocking curves shown in figure 6.11, Gaussian lineshapes were fitted to the more uniform side of the curve. The FWHM of a Gaussian distribution is related to its standard deviation by the relation given in equation 6.11, where β is the FWHM and σ the standard deviation. From these curve fits a 'best estimate' of the FWHM was obtained. The recorded FWHM of the curves including 'shoulders' etc. were also evaluated and the differences between these values and the 'best fit' values were taken to be the uncertainties in FWHM which are shown in figures 6.12 and 6.14.

$$\beta = 2\sqrt{2\ln 2}\,\sigma \qquad \text{equation 6.11}$$

The relationship between FWHM and the wavelength at which the rocking curve was recorded is better seen in figure 6.12. It is noted that as wavelength increases the rocking curve width recorded decreases. This is

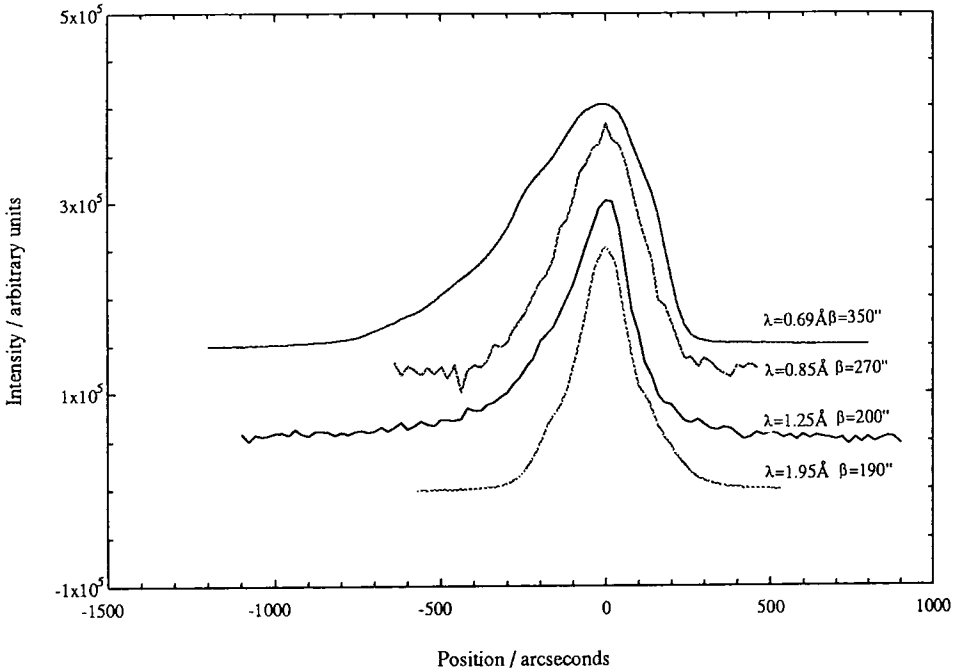

Figure 6.11 HRXRD rocking curves recorded at four wavelengths for a 25μm layer of (001)CdTe/GaAs. The values of FWHM (β) are calculated from fitting Gaussian line shapes to the most uniform side of the curve.

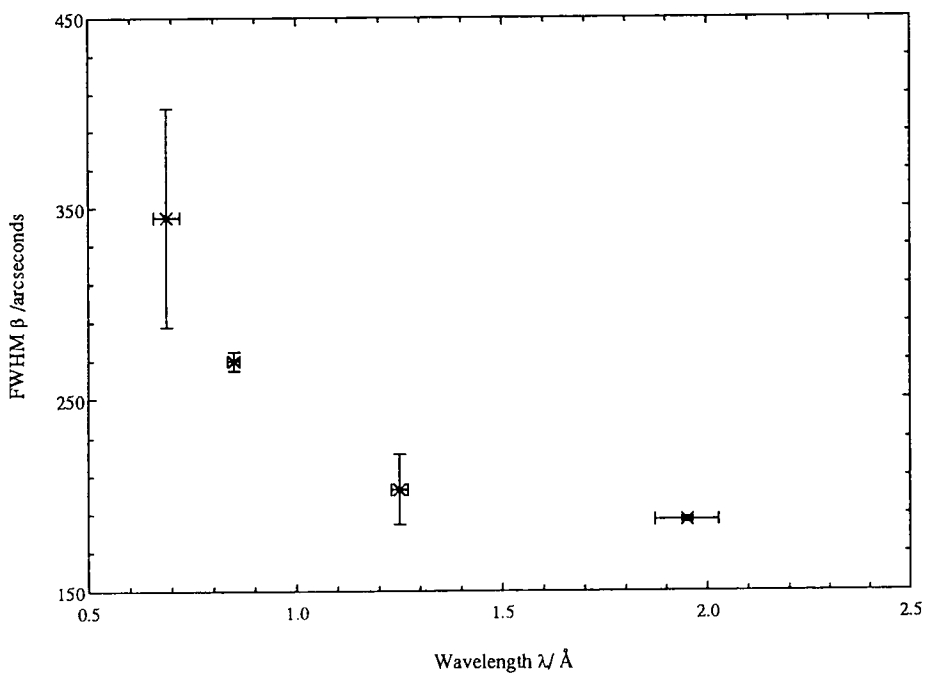

Figure 6.12 HRXRD FWHM recorded at four wavelengths for the 25μm CdTe/GaAs layer of figures 6.5 and 6.6. Uncertainty in FWHM is the difference between Gaussian fit FWHM and that measured from figure 6.11 including 'shoulders'. Uncertainty in wavelength is determined by the accuracy of setting the Si(111) crystal and calibration using the Zr absorption edge, further details are given in the text.

because the absorption coefficient of CdTe increases with wavelength, as illustrated in figure 6.8; and penetration, for a given reduction in intensity, decreases. Broadening of rocking curves with increasing penetration of the probing beam suggests that, within a thick layer, there is an inhomogeneity in mosaic tilt distribution. This is very different from nearly lattice matched layers where relaxation is said to occur at the heterointerface with the entire layer being relaxed to the same extent (this was discussed in comparing two strain relaxation models in Section 5.2.3).

If a layer is considered to be made up of individual monolayers (figure 6.13) each with a Gaussian distribution of tilts with mean angular position $\bar{\theta}$, then the contribution to the measured rocking curve from a given monolayer is determined solely by the attenuation of the beam in traversing the path yz. The intensity, I_θ of the diffracted beam at an angle θ is given by the summation in equation 6.12 where $A_{\theta\lambda}$ contains the structure factor and other diffraction terms which affect intensity, $N_{\bar{\theta}n}$ is the number of tilt domains at $\bar{\theta}$ in the nth layer and σ_n is the standard deviation of the mosaic spread of the nth layer. Other parameters in equation 6.12 are μ, the linear absorption coefficient, h the perpendicular distance from the surface to layer n, and θ_B is the Bragg angle for the chosen wavelength. Note that the absorption term (exponential term) is given for ω=0 in equation 6.9.

$$I_\theta = \sum_{n=1}^{m} A_{\theta\lambda} N_{\bar{\theta}n} \exp\left[-\frac{1}{2}\left(\frac{\theta-\bar{\theta}}{\sigma_n}\right)^2\right] \exp\left[-2\mu(\lambda)h\,\mathrm{cosec}\theta_B\right] \qquad \text{equation 6.12}$$

Equation 6.12 is Kinematical in approach and does not take into account extinction or rediffraction. The contribution from each monolayer is dependent on the wavelength of the incident photons, thus equation 6.12 is different for each wavelength chosen, with only $N_{\bar{\theta}n}$, $\bar{\theta}$, σ_n and h being independent of wavelength. Since only four wavelengths have been used in this study, a very large approximation would be required in order to extract the value of σ_n at four specific depths, h. The approximation would be such that equation 6.12 would need to be re-written as a summation of four contributions from layers several microns in thickness (the depth to which an X-ray beam may penetrate whilst still giving a significant diffracted

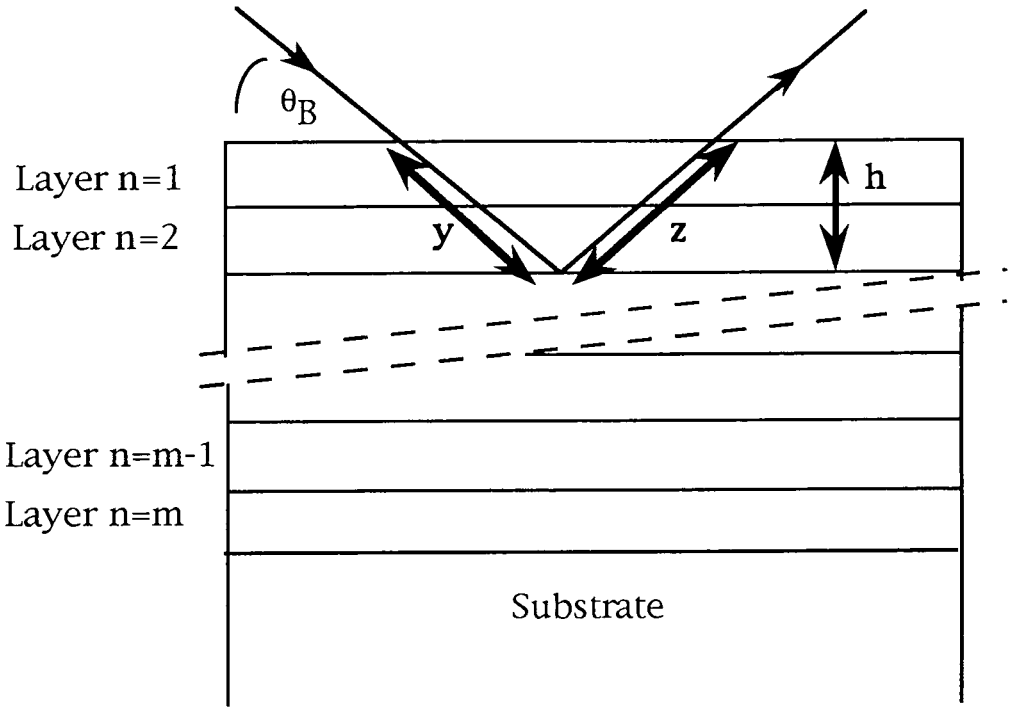

Figure 6.13 Schematic diagram of the division of a layer into monolayers each having a Gaussian distribution of subgrain tilts. Contribution to diffracted intensity from each monolayer depends on the attenuation in traversing a distance (y+z). Note that for a symmetric reflection as shown in the figure, y=z.

intensity). When this is compared to the actual thickness of a monolayer (3.24Å for (001) CdTe) it is clear that this approximation is not valid. An additional problem is the complexity of the term $A_{\theta\lambda}$ which, despite the synchrotron source being plane polarised parallel to the sample surface, is still heavily wavelength and geometry dependent.

A value of FWHM for the top surface of the 25μm layer can be estimated from the current data by extrapolation of FWHM to infinite absorption. The FWHM from figure 6.12 are plotted against the reciprocal of the linear absorption coefficients (from table 6.3) in figure 6.14. The uncertainties in FWHM were calculated as described earlier, and the uncertainties in μ were calculated from the uncertainties in λ (table 6.3), assuming the polynomial relationship between $(\mu/\rho)_{cpd}$ and λ determined in figure 6.8. The value of FWHM for the surface layer of the 25μm CdTe/GaAs layer calculated from figure 6.14 is 170". This value is greater than the FWHM of 163" obtained for the same layer by conventional HRXRD using $CoK\alpha_1$ radiation(λ=1.789Å, $\mu=0.21\mu m^{-1}$). In principle, the FWHM representative of only the surface of the layer, should be much less than that obtained for a beam which penetrates into the more dislocated region of the layer. The discrepancy between the expected relative values and those obtained, is thought to arise from the fact that the specimen could not be tilt optimised, and hence every rocking curve was broadened owing to the offset of the diffracting planes. This would not be a problem on a well equipped diffractometer and it is expected that repetition of this experiment at a synchrotron station with automated alignment of specimen tilt would enable the surface FWHM to be obtained for a series of layers.

When undertaking any X-ray study, the effect of the penetration of the X-rays must be considered. The most commonly used X-ray tube is Copper ($CuK\alpha_1$ λ = 1.541Å)[23]; this was the source used for data presented in Section 6.2. Data presented in Sections 6.3, 6.6, 8.1.4.2 and 8.2.3 were collected using a Cobalt tube ($CoK\alpha_1$ λ=1.789Å)[23]. For 95% attenuation [I(x)/I(0) = 0.05 in equation 6.9], the penetration depths h for 004 reflection of CdTe and GaAs with ω=0 using $CuK\alpha_1$ and $CoK\alpha_1$ radiation are summarised in table 6.4.

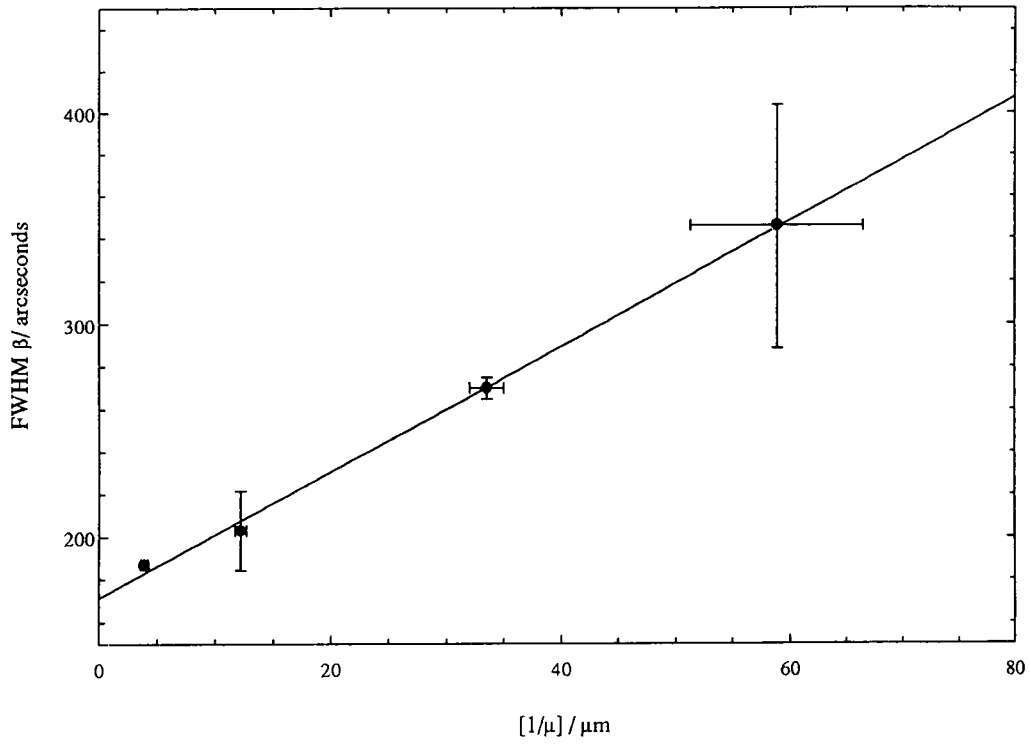

Figure 6.14 HRXRD FWHM of a 25μm thick (001)CdTe/GaAs epilayer recorded at four different wavelengths plotted against the reciprocal of linear absorption coefficient. Intercept with the ordinate axis gives an estimate of the FWHM of the surface layer. Intercept occurs at 172 arcseconds.

Source	$CuK\alpha_1$	$CoK\alpha_1$
Wavelength / Å	1.541	1.789
Penetration depth in CdTe / μm	4.8	3.8
Penetration depth in GaAs / μm	22	17

Table 6.4 Comparison of penetration depths of $K\alpha_1$ lines of Cu and Co for 95% attenuation. The penetration depths have been calculated from equation 6.9. The linear attenuation coefficients of CdTe and GaAs were calculated from equation 6.6 from the mass attenuation coefficients of Cd, Te, Ga and As[23] and the densities of CdTe ($5.856 gcm^{-3}$) and GaAs ($5.316 gcm^{-3}$), reference 24. The values were confirmed for single crystal CdTe and GaAs as described in the caption of table 6.3.

It can be seen from table 6.4 that the penetration depth of X-rays is most significant for compounds composed of the lighter elements such as Ga and As. Investigation of Si, P, S, Zn, Ga, As and Se based compounds, all of which have atomic number less than 35, will include information from regions of the sample well away from the surface. Since the region near the interface is expected to be more dislocated than the surface region for mismatched layers, the FWHM of layers composed of the lighter elements will be greater for a given surface dislocation density than a layer composed of heavier elements. This should be borne in mind when using the formula of Gay et al.[8] to calculate dislocation density from FWHM; the effect of X-ray penetration can give an overestimate of dislocation density, this is more significant for compounds of low average atomic mass (for further discussion of the formula by Gay et al. see Section 4.2.2.3). $CoK\alpha_1$ was selected for all the conventional HRXRD presented in this thesis since its long wavelength gives more surface sensitive information than the more commonly used $CuK\alpha_1$ radiation.

6.5 Photoluminescence of CdTe/GaAs

6.5.1 Introduction

Photoluminescence (PL) was described in Section 4.5, including the details of the experimental apparatus used in this study. Thickness dependence studies of the photoluminescence spectra of CdTe/GaAs layers have been carried out by a number of workers. Taguchi et al.[29] have studied MOVPE layers of thickness 0.22-3.5μm, 0.7-15μm layers grown by HWE have been studied by Tatsuoka et al.[9] and layers of thickness 0.8-6.8μm grown by HWE with a gold tube radiation shield have been studied by Hwang et al.[11]. The work presented in this section extends to thicker layers than those previously reported, and shows the behaviour of the photoluminescence spectra of a wide range of thicknesses in both the exciton and donor acceptor pair regions.

6.5.2 Results and Discussion

Photoluminescence (PL) spectra of the five CdTe/GaAs layers investigated in Section 6.3 (of thickness 25, 8.7, 4.3, 0.6 and 0.32 μm) were obtained at a temperature of 4.2K. The details of the experimental apparatus are described in Section 4.5. Spectra in the donor acceptor pair (DAP) region (8000-9000Å) were recorded for all five layers and are shown in figure 6.15. Excitonic features (7750-7830Å) were only visible for layers of thickness ≥ 4.3μm as shown in figure 6.16. The increase in excitonic emission with increasing thickness is expected, given the accompanying reduction in dislocation density[9,30] (Section 6.3).

While the DAP bands in the thinnest samples were broad and featureless, those from the thickest sample had structure. Two peaks in the DAP band of the 25μm layer are tentatively assigned to transitions involving As acceptors. These are an eA° (free electron to neutral acceptor) line at 1.5152eV (8181Å) and a donor acceptor transition at 1.5074eV (8223Å); the donor involved in this transition has not been identified. These assignments

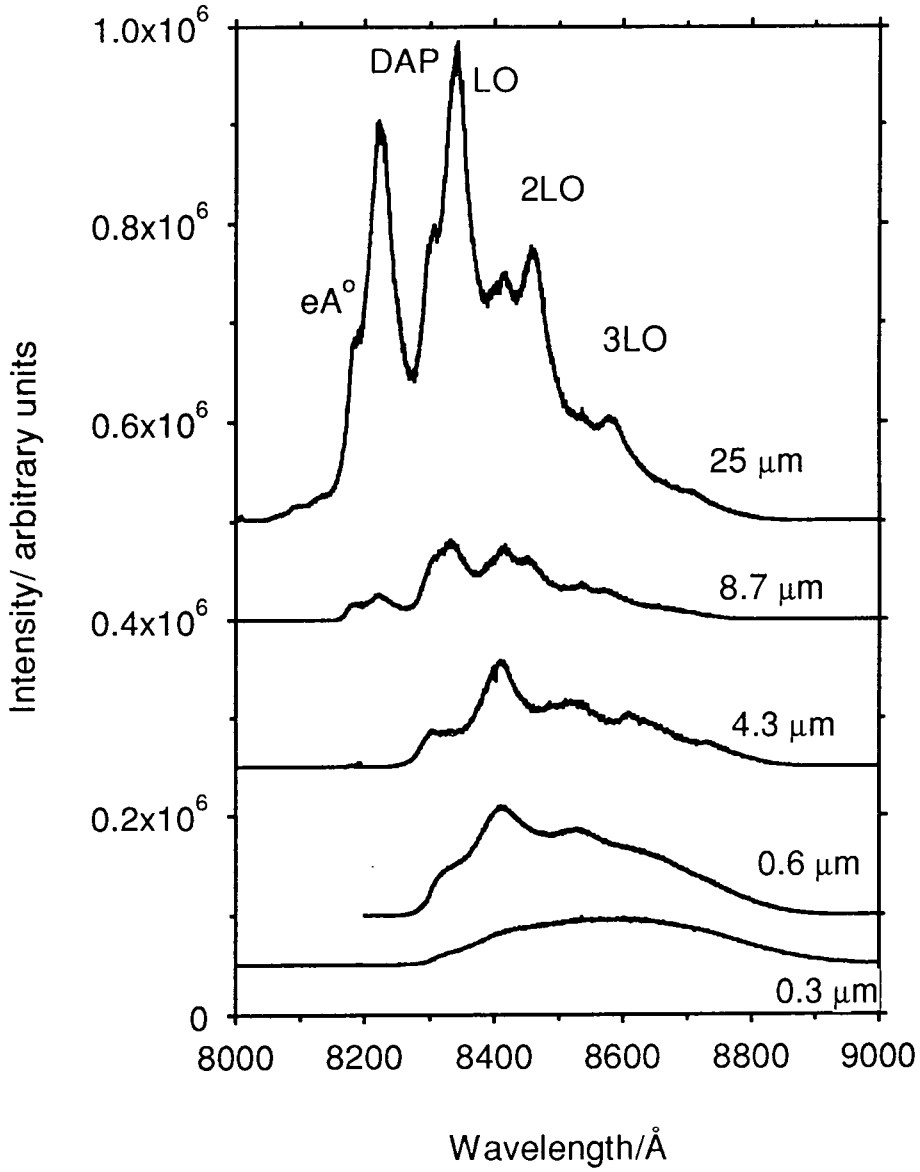

Figure 6.15 Photoluminescence spectra of CdTe/GaAs layers of different thicknesses. The spectra are of the donor acceptor pair region.

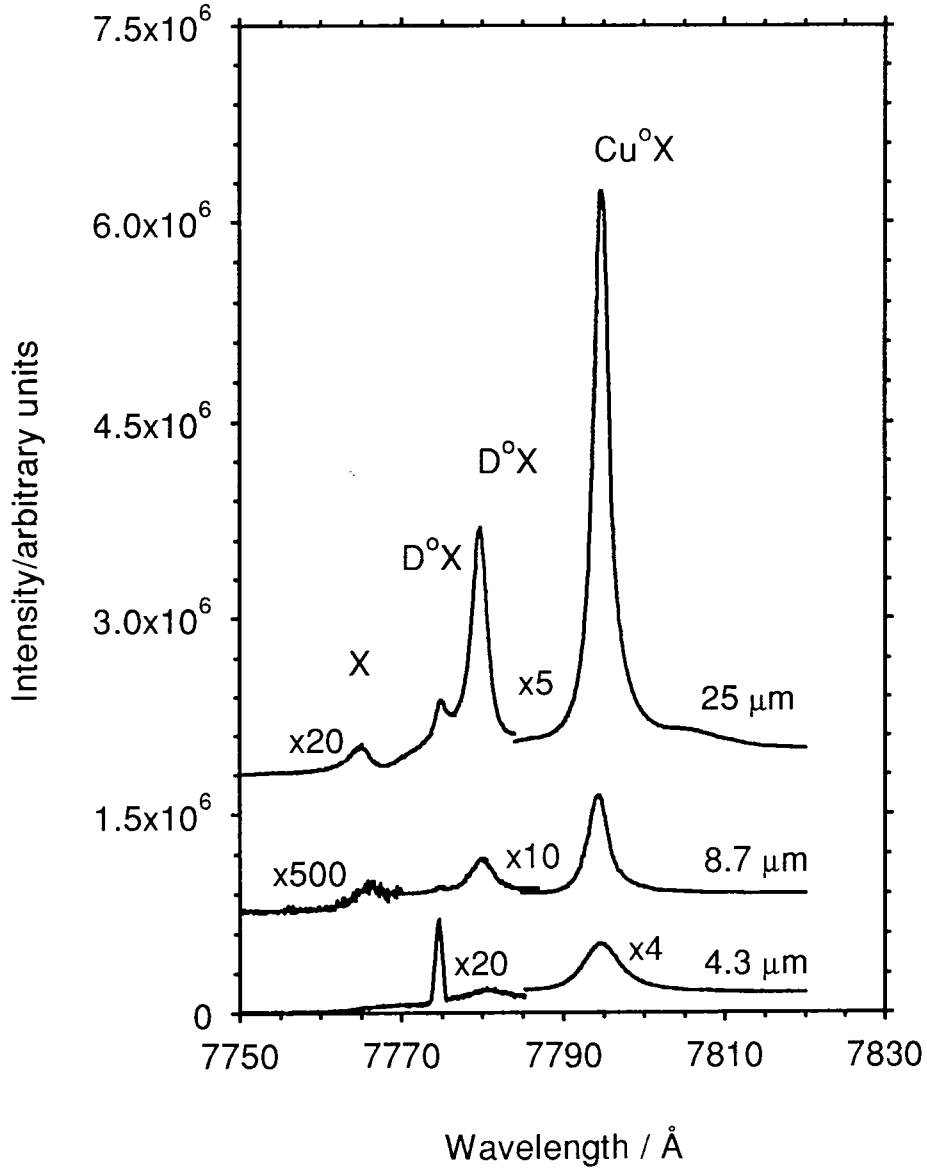

Figure 6.16 Photoluminescence spectra of CdTe/GaAs layers of different thicknesses. The spectra are of the exciton region, assignments are given in the text.

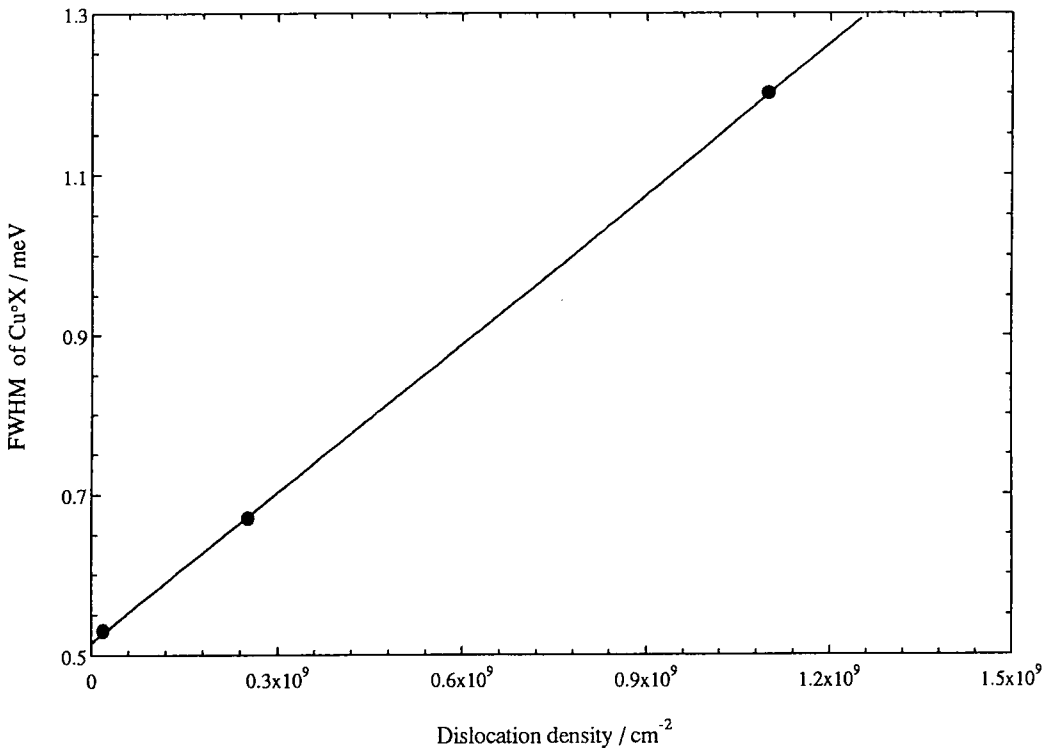

Figure 6.17 FWHM of Cu°X line versus dislocation density estimated from HRXRD FWHM .

were made after comparison with those of Molva et al.[31]. The two lines are replicated at intervals of 21meV (LO phonon replicas).

The dominant feature of the exciton region is the A°X (recombination of an exciton bound to a neutral acceptor) transition at 1.5902eV (7795Å), attributed to Cu by Francou et al.[32]. Other features observed in the spectrum of the thickest layer and to a lesser extent in the two thinner layers are the free exciton line, X at 1.5963eV (7765Å) and two peaks due to D°X (recombination of an exciton bound to a neutral donor) transitions at 1.5943eV (7775Å) and 1.5932eV (7780Å). It is possible that Ga donors are present due to outdiffusion from the substrate (Chapter 1), however, the D°X peaks cannot be definitely assigned since most D°X peaks in CdTe overlap in this region[32].

The FWHM of the A°X transition line (assigned to Cu) increases with decreasing layer thickness as is clear from figure 6.16. The FWHM of the A°X line is plotted against threading dislocation density (from Section 6.3) in figure 6.17. A high dislocation density may lead to a greater distribution of acceptor environments and hence a greater range of exciton binding energies, thus broadening the peak. An alternative explanation for the increase in FWHM with decreasing thickness is that the thinner layers are more strained than thicker ones, and the lines are broadened under the influence of this strain. This is expected to be a less significant effect for CdTe/GaAs, which displays a relatively slow reduction in strain with increasing thickness compared to lower misfit systems (illustrated in Section 5.2.2, figure 5.5).

6.6 High Resolution X-ray Diffraction of ZnTe/GaAs

6.6.1 Introduction

The lattice parameters of ZnTe and GaAs are 6.1026Å and 5.654Å respectively[25], giving a misfit of 7.94% which is approximately half that between CdTe and GaAs (14.6%). ZnTe buffer layers have been used for the growth of CdTe on (001)GaAs to ensure (001) growth rather than (111)[33].

ZnTe is a popular buffer layer for ternary compounds containing Zn[34], for example Brown et al.[35] have investigated $Hg_xZn_{(1-x)}Te$ with a ZnTe buffer layer. ZnTe-CdTe strained layer superlattices grown on GaAs substrates by HWE[36] and by MOVPE[37,38] have been investigated by a number of workers as a threading dislocation filter for the subsequent growth of $Cd_xHg_{(1-x)}Te$ or HgTe:ZnTe superlattices.

In this section an alternative method for studying the thickness dependence of HRXRD FWHM is used. Instead of measuring the FWHM of a series of layers of different thickness or one thick layer repeatedly etched, one layer of (001)ZnTe/GaAs of non-uniform thickness was investigated. Thickness and FWHM were recorded over the inhomogeneous sample and analysed as for the data presented in Section 6.3. The advantage of this method is that the only variation in growth conditions between points is the growth rate; the substrate preparation, which has been shown to have a great effect on the structural perfection of the final layer[16], is the same for all recorded points.

6.6.2 Experimental Details

High Resolution X-ray rocking curves were recorded as a function of position across a single ZnTe/GaAs layer on a Bede Model 150 Diffractometer equipped with an automated XY scanning stage. The MOVPE growth conditions for (001) ZnTe/GaAs were given in Section 3.3.3.4. The symmetric 004 ZnTe reflection was used in the non-dispersive setting with a GaAs reference crystal. From Section 4.2.2.2, the effect of the difference in lattice parameter between reference crystal and layer is to broaden all ZnTe rocking curves by 5", assuming a fractional spread in wavelength of 2.6×10^{-4}, the intrinsic width of the $K\alpha_1$ line[6]. $CoK\alpha_1$ radiation was used as in Section 6.3, the $K\alpha_2$ component having been removed by a slit placed between the reference and specimen crystals. A beam size of 0.5mmx0.5mm was used, with the beam direction projecting onto $[1\bar{1}0]$, the orientation of the sample with respect to the incident beam is different to that assumed in Sections 6.2 and 6.3 due to the present substrate having zero offcut. Tilt optimisation of the sample (001) planes was carried out as described in Section 4.2.2.2.

The FWHM of HRXRD rocking curves over an area 12mmx12mm were recorded, with points every 2mm in both the X and Y directions. The thickness of the layer at each point was determined from the integrated intensity of the 004 reflection of the GaAs substrate recorded through the ZnTe over the same 12mmx12mm area. The layer thickness, h, may be calculated from equation 6.9 with ω=0 for zero offcut, $(\mu/\rho)_{cpd}$= 301cm^{2}g^{-1} for absorption of CoKα_1 radiation by Zn and Te[23], θ_B=39.3°, the Bragg angle for GaAs 004 reflection and ρ=5.64gcm^{-3} from the table of X-ray density, reference 24. The density of ZnTe was checked as described in the caption of table 6.4. I(x) is the integrated intensity of the GaAs peak measured through the ZnTe layer and I(0) is the integrated intensity of a clean GaAs wafer from the same boule as the substrate. Note that it is essential to use the same accelerating voltage and current settings on the X-ray generator when obtaining the values of I(0) and I(x).

6.6.3 Results and Discussion

XY maps of FWHM and thickness of the ZnTe layer after processing by grid and contour mapping software are shown in figure 6.18. The carrier gas flow is from the bottom to the top of the page with the downstream edge being the thicker. A smooth gradient in both thickness and FWHM is observed, with the thickest regions having the narrowest rocking curves. This is seen more clearly in figure 6.19a. Shtrikman et al.[34] have investigated HRXRD FWHM from (001)ZnTe/GaAs layers grown by low pressure MOVPE for thicknesses in the range 0.8-7μm and their findings are reproduced in figure 6.19b. They found that FWHM decreased with increasing thickness to a level of about 250" at 7μm. The rate of FWHM decrease with thickness reduces drastically at a thickness of about 2.5μm. This is in stark contrast to the layer investigated in this study, which gave a lowest FWHM of 190" for a thickness of 3.5μm. The gradient of the curve at 3.5μm suggests that FWHM will decrease significantly for thicker layers.

The values of FWHM in figure 6.19a were used to estimate threading dislocation density, as performed in Section 6.3, using the model by

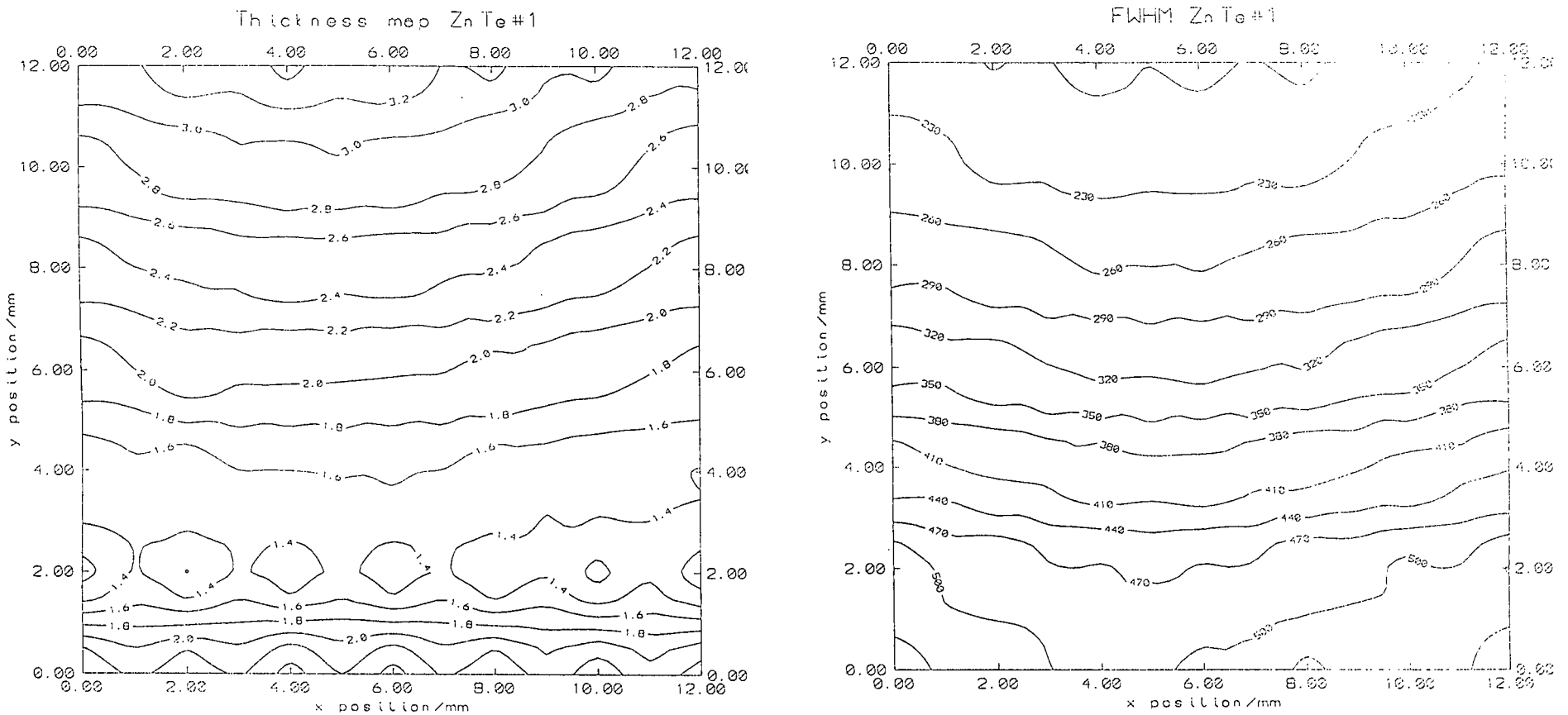

Figure 6.18 Contour maps of layer thickness (given in microns) and HRXRD FWHM (given in arcseconds) for one ZnTe/GaAs layer grown by MOVPE. Carrier gas flow is from the bottom to the top of the page. Measurement points were recorded every 2mm, beam size was 0.5mmx0.5mm.

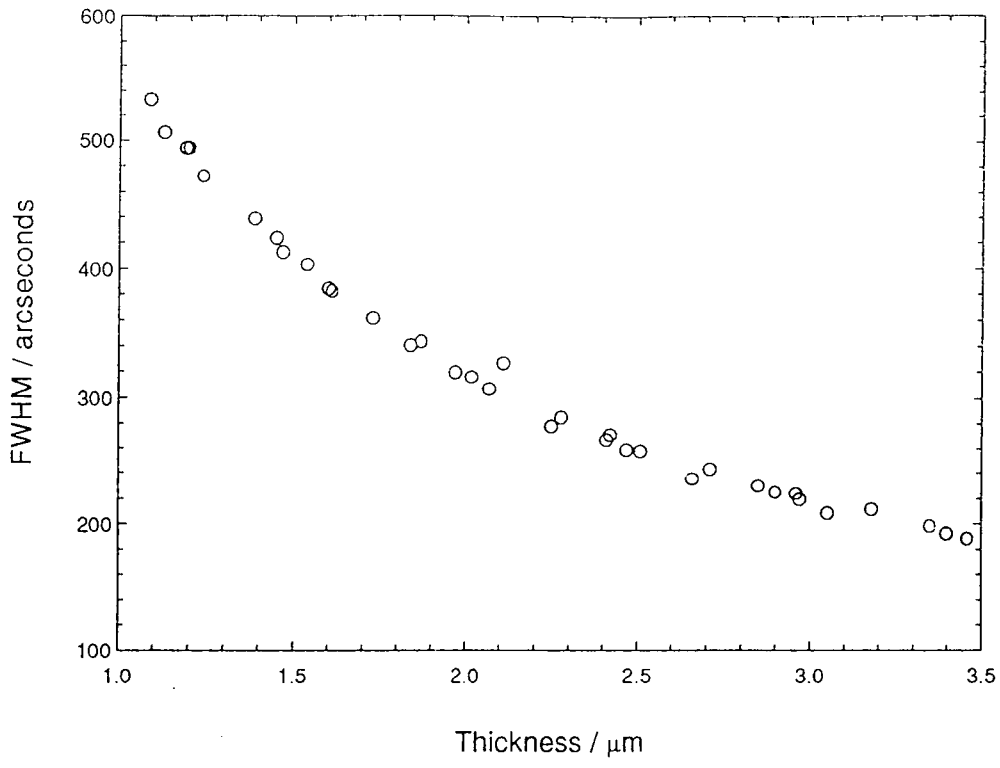

Figure 6.19a HRXRD FWHM as a function of layer thickness for the single ZnTe/GaAs MOVPE layer of figure 6.18.

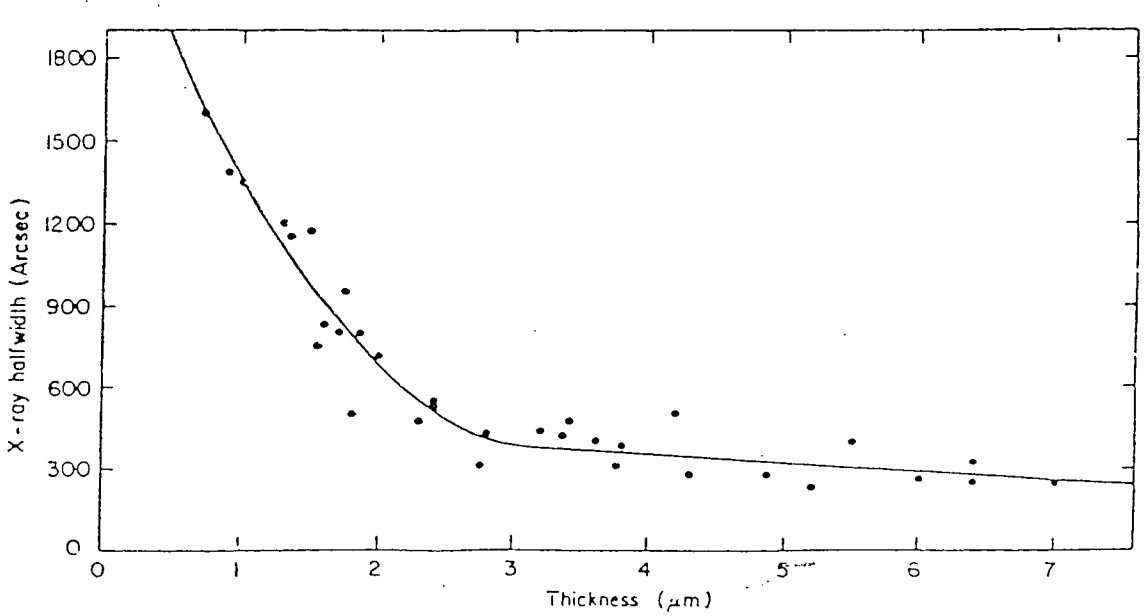

Figure 6.19b HRXRD FWHM as a function of layer thickness for ZnTe/GaAs layers grown by low pressure MOVPE. Figure is reproduced from Shtrikman et al.[34].

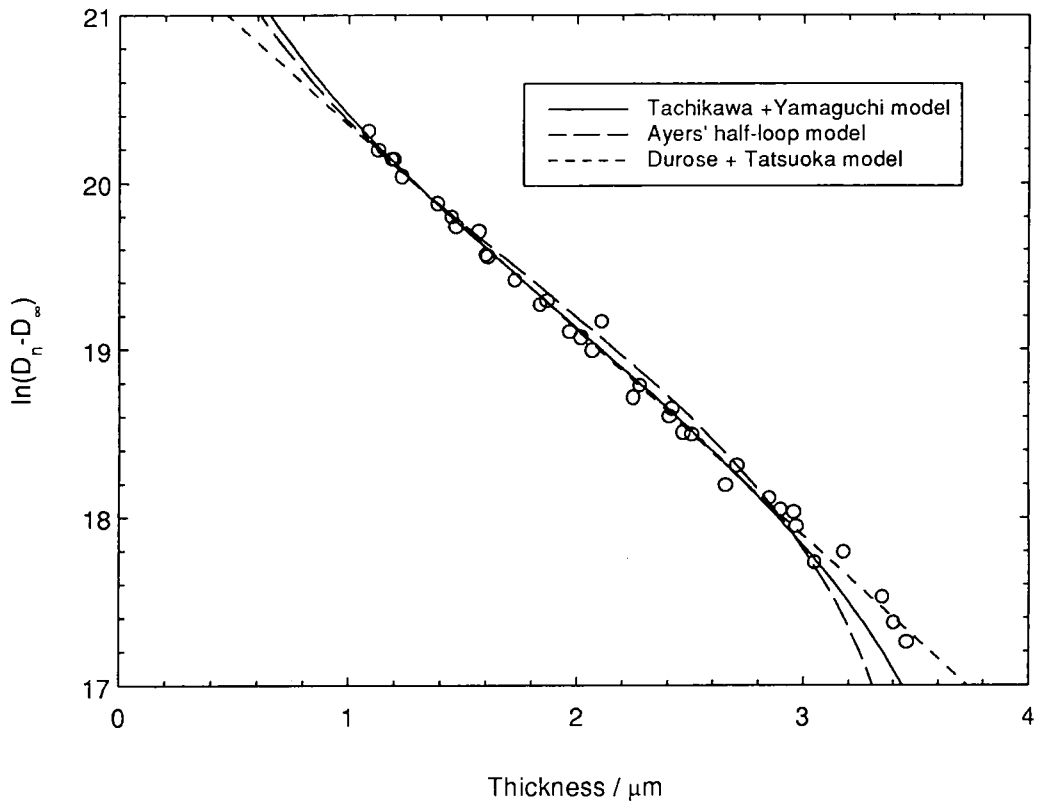

Figure 6.20 Dislocation density calculated from DCXRD FWHM versus thickness for a (001) ZnTe/GaAs epilayer. Comparison of best fit lines for the relationships predicted by Ayers et al.[20] (half-loop model), Durose and Tatsuoka[18] (strain relief by threading dislocations) and by Tachikawa and Yamaguchi[19] ('unimolecular' and bimolecular' annihilation mechanisms). $D(\infty) = 4.9 \times 10^{7} cm^{-2}$. Note that the agreement with Ayers' expession (equation 6.3) is very poor and a modified expression (equation 6.2) has been used in this graph.

Gay et al.[8], the same assumptions apply. Figure 6.20 shows best fit lines for relationships predicted by Ayers et al.[20], Durose and Tatsuoka[18] and by Tachikawa and Yamaguchi[19]. All three lines were plotted using the same axes so that the variances of the fits may be compared meaningfully. Note that $D(\infty)$ was taken to be $4.9 \times 10^7 cm^{-2}$ and best fits for the models by Ayers et al. and by Tachikawa and Yamaguchi were obtained on their own before being replotted on the axes required by the Durose and Tatsuoka model. As has consistently been the case for reciprocal thickness versus dislocation density plots, the best fit straight line did not pass through the origin as predicted by Ayers et al. The dislocation density predicted for infinite thickness (ie [1/h] =0) is $-2.3 \times 10^8 cm^{-2}$. A comparison of the variances of the three best fit lines is made in table 6.5.

Model	Half-loop model	Strain relief by threading dislocations	'Bimolecular' and 'Unimolecular' annihilation
Reference	Ayers et al.[20] modified-see equations 6.2 and 6.3	Durose and Tatsuoka[18]	Tachikawa and Yamaguchi[19]
Variance/ $(\ln[cm^{-2}])^2$	0.27	0.064	0.12

Table 6.5 Comparison of the variance of best fit lines for three models reviewed in Chapter 5.

When the findings for the thick CdTe/GaAs etched layer of Section 6.3 are compared with those for ZnTe/GaAs as shown in figure 6.21, there is a striking difference in the rates of threading dislocation reduction with increasing thickness. The ZnTe layer shows a far more rapid structural improvement than the CdTe layer, as well as having lower dislocation densities for all measured thicknesses (the second observation is expected due to the lower misfit in the ZnTe/GaAs case). If the rate of threading dislocation reduction with increasing thickness were determined by the number of dislocations present at a given thickness, and the probability of

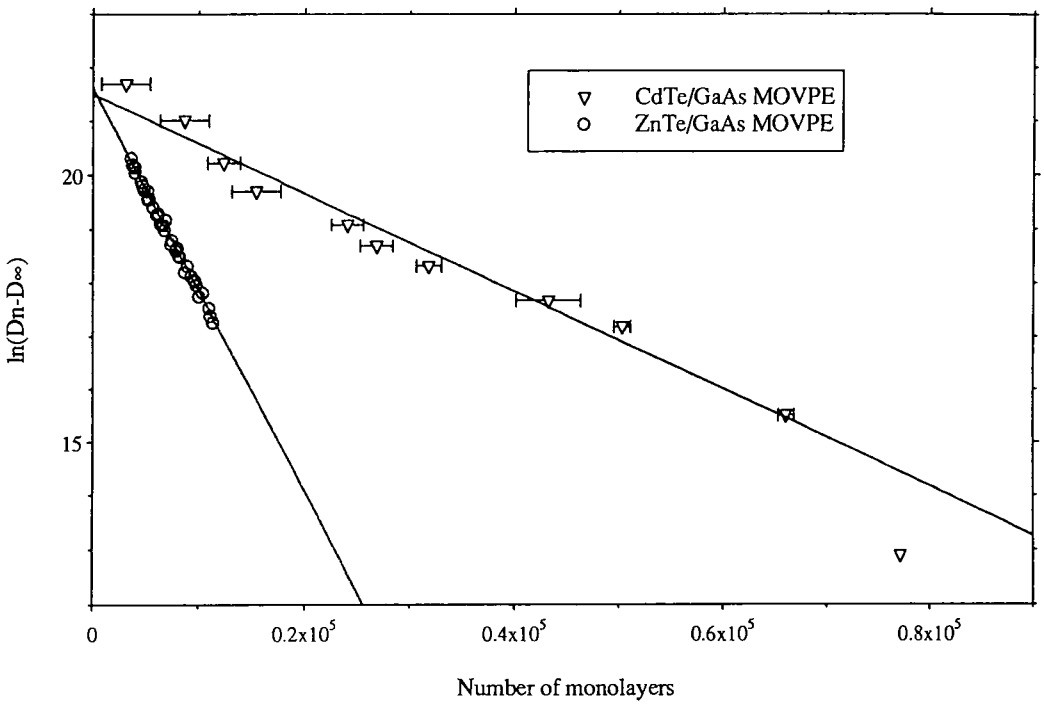

Figure 6.21 Comparison of dislocation density reduction with increasing thickness for ZnTe/GaAs and CdTe/GaAs epilayers grown by MOVPE.

'removing' a dislocation being greater the more dislocations there are, then one would expect that CdTe/GaAs would show a more rapid reduction than ZnTe, contrary to what has been shown. If the magnitude of the misfit at the growth temperature is considered for CdTe/GaAs and ZnTe/GaAs, an interesting difference may be noted. The thermal expansion coefficients of CdTe[39] and GaAs[40] are $4.5 \times 10^{-6} °C^{-1}$ and $6.86 \times 10^{-6} °C^{-1}$ respectively. This difference results in a smaller misfit at the growth temperature than at room temperature. As the layer cools, an additional compressive strain is put on the layer as the lattice parameter of the substrate decreases more than that of the layer. This may introduce additional dislocations which relieve compressive strain as the layer cools. The thermal expansion coefficients of ZnTe[41] and GaAs[40] are $8.3 \times 10^{-6} °C^{-1}$ and $6.86 \times 10^{-6} °C^{-1}$ respectively. This difference results in a larger misfit at the growth temperature than at room temperature. As the growth system cools, the lattice parameter of the layer decreases more than that of the substrate. This may result in the introduction into the layer of dislocations which relieve tensile strain, and since these are of opposite character to those formed during growth, the two types may annihilate. If this is the case, then a more rapid reduction in dislocation density with increasing thickness is expected as dislocations may be removed by an additional mechanism.

6.7 Conclusions

X-ray diffraction experiments using a limited acceptance angle detector have shown that the greatest source of HRXRD rocking curve broadening are mosaic tilts. The subsequent use of HRXRD FWHM to estimate threading dislocation density assumed that tilts are the sole factor governing the width of rocking curves. Investigation of the FWHM of CdTe/GaAs epilayers of different thickness and of a 25μm thick layer repeatedly etched and remeasured showed that structural quality improves with increasing thickness, the most rapid improvement occurring in the region nearest the interface. Comparison of the findings with data for CdTe/GaAs layers grown by HWE by Tatsuoka et al.[9] showed that the layers grown by HWE were of better structural quality than those grown by MOVPE at all thicknesses, but

more particularly for thin layers. It was suggested that this difference is caused by the HWE layers being grown under equilibrium conditions. Very little difference was observed between the FWHM of thin layers and a thick layer etched back and remeasured. This suggests that annealing near the growth temperature will yield little structural improvement, but does not discount the possibility of improvements for higher annealing temperatures since the dislocation reduction mechanism may be thermally activated.

It has been found that CdTe/GaAs layers thicker than 4.3μm give photoluminescence spectra which include excitonic features; no excitonic features were observed for layers thinner than 4.3μm. The width of the Cu°X line was found to increase with increasing dislocation density. Donor acceptor pair transitions were observed for layers of thickness 0.3-25μm with the thickest layer showing the greatest transition detail.

The thickness non-uniformity observed in the direction of carrier gas flow for MOVPE growth has been shown to cause a variation in structural quality in agreement with the expected relationship between HRXRD FWHM and layer thickness.

Three of the relationships between dislocation density and thickness presented in Chapter 5 were compared with the dislocation density profiles of CdTe/GaAs and ZnTe/GaAs. As predicted in Chapter 5, the relationship proposed by Durose and Tatsuoka[18] for strain relaxation by threading dislocations fitted the experimental data most closely. A large difference in the rate of threading dislocation reduction with increasing thickness for (001)ZnTe/GaAs and (001)CdTe/GaAs layers was observed. The ZnTe layer investigated in Section 6.6 showed a far more rapid structural improvement with increasing thickness than the thick CdTe layer investigated in Section 6.3; the ZnTe layer also had a lower dislocation density for all measured thicknesses. The difference is thought to be due to the differences in thermal expansion coefficient of CdTe, GaAs and ZnTe. CdTe/GaAs has a lower misfit at the growth temperature than at room temperature, which results in an increase in compressive strain on cooling. Conversely, ZnTe/GaAs has a higher misfit at the growth temperature than at room

temperature and this may lead to a tensile strain on the layer as it cools compared to the compressive strain during growth.

REFERENCES FOR CHAPTER 6

1. Ashenford D., Devine P., Hogg J. H. C., Lunn B. and Scott C. G., *J. Cryst. Growth* **117**, (1992), 233.

2. Kudlek G., Presser N., Gutowski J., Hingerl K., Abramof E., Pesek A., Pauli H. and Sitter H., *J. Cryst. Growth* **117**, (1992), 290.

3. Hudson J. M., Ph. D Thesis, *Specular and Diffuse X-Ray Scattering Studies of Surfaces and Interfaces*, University of Durham (1994).

4. Lafford T. A., Personal Communication, (1995).

5. Bates S., Hatton P. D., Lucas C. A., Ryan T. W., Miles S. J. and Taner B. K., *Adv. X-ray Anal.* **31**, (1988), 155.

6. Tanner B. K. and Bowen D. K., *J. Cryst. Growth* **126**, (1993), 1.

7. Keir A. M., Barnett S. J., Giess J., Walsh T. D. and Astles M. G., *Appl. Surf. Sci.* **50**, (1991), 103.

8. Gay P., Hirsch P. B. and Kelly A., *Acta Metallurgica* **1**, (1953), 315.

9. Tatsuoka H., Kuwabara H., Fujiyasu H. and Nakanishi Y., *J. Appl. Phys.* **65(5)**, (1989), 2073.

10. Irvine S. J. C., Gough J. S., Giess J., Gibbs M. J., Royle A., Taylor C. A., Brown G. T., Keir A. M. and Mullin J. B., *J. Vac. Sci. Technol. A* **7(2)**, (1989), 285.

11. Hwang J. S., Koo B. J., Chung I. H., Park H. L. and Chung C. H., *J. Cryst. Growth* **130**, (1993), 617.

12. Lopez-Otero A., *Thin Solid Films* **49**, (1978), 3.

13. Barnett S. J., Keir A. M. and Emeny M., *Semicond. Sci. Technol.* **7**, (1992), A158.

14. Keir A. M., Graham A., Barnett S. J., Giess J., Astles M. G. and Irvine S. J. C., *J. Cryst. Growth* **101**, (1990), 572.

15. Brown G. T., Keir A. M., Giess J., Gough J. S. and Irvine S. J. C., *Inst. Phys. Conf. Ser.* **100**, Section 6, (1989), 457.

16. Giess J., Hails J. E., Graham A., Blackmore G., Houlton M. R., Newey J., Young M. L., Astles M. G., Bell W. and Cole-Hamilton D. J., *J. Elec. Mat.* **24(9)**, (1995), in press.

17. Nishino H., Murakami S., Saito T., Nishijima Y. and Takigawa H., *J. Elec. Mater.* **24(5)**, (1995), 533.

18. Durose K. and Tatsuoka H., *Inst. Phys. Conf. Ser.* 134, Section 9, (1993), 581.

19. Tachikawa M. and Yamaguchi M., *Appl. Phys. Lett.* 56(5), (1990), 484.

20. Ayers J. E., Schowalter L. J. and Ghandhi S. K., *Mat. Res. Soc. Symp. Proc.* 209, (1991), 661.

21. Cullity B. D., *Elements of X-ray Diffraction*, (2nd edition), Addison-Wesley, 1978, Cohen M, Ed. Addison-Wesley Series in Metallurgy and Materials.

22. Azároff L. Z., *Elements of X-Ray Crystallography*, New York: McGraw Hill, 1968.

23. International Tables for X-ray Crystallography, , Birmingham: Kynoch, 1962; 3.

24. *Handbook of Physics and Chemistry*, CRC Press, 69th edition, 1988.

25. ASTM Powder Diffraction File

26. Holy V., Kubena J., Abramof E., Lischka K., Pesek A. and Koppensteiner E., *J. Appl. Phys.* 74(3), (1993), 1736.

27. Itoh N., *Appl. Phys. Lett.* 62(7), (1993), 690.

28. Qadri S. B. and Dinan J. H., *Appl. Phys. Lett.* 47, (1985), 1066.

29. Taguchi T. and Onodera C., *Mat. Sci. Forum* 65-66, (1990), 235.

30. Seto S., Tanaka A., Takeda F. and Matsuura K., *J. Cryst. Growth* 138, (1994), 346.

31. Molva E., Saminadayar K., Pautrat J. L. and Ligeon E., *Solid State Comm.* 48(11), (1983), 955.

32. Francou J. M., Saminadayar K. and Pautrat J. L., *Phys. Rev. B* 41(17), (1990), 12035.

33. Feldman R. D., Austin R. F., Dayem A. H. and Westerwick E. H., *Appl. Phys. Lett.* 49, (1986), 797.

34. Shtrikman H., Raizman A., Oron M. and Eger D., *J. Cryst. Growth* 88, (1988), 522.

35. Brown P. D., Loginov Y. Y., Mullins J. T., Durose K., Brinkman A. W. and Humphreys C. J., *J. Cryst. Growth* 138, (1994), 538.

36. Sugiyama I., Hobbs A., Ueda O., Shinohara K. and Takigawa H., *Appl. Phys. Lett.* 58(24), (1991), 2755.

37. Mullins J. T., Clifton P. A., Brown P. D., Brinkman A. W. and Woods J., *J. Cryst. Growth* **101**, (1990), 100.

38. Clifton P. A., Mullins J. T., Brown P. D., Russell G. J., Brinkman A. W. and Woods J., *J. Cryst. Growth* , 93, (1988), 726.

39. Cleveland Crystals Incorporated, *Internal Report,* (Ohio USA, 1984).

40. Sze S. M., *Physics of Semiconductor Devices,* (2nd edition), Wiley, 1981, pp. 850.

41. Soma T., *Solid State Commun.* **34**, (1980), 927.

CHAPTER 7

Microstructural Characterisation of (001)CdTe/GaAs Epilayers

7.1 Introduction

In this chapter, studies on the microstructure of layers of (001)CdTe on (001) GaAs substrates grown by MOVPE and investigated by TEM, HRXRD and double crystal X-ray topography (DCXRT) are presented. The MOVPE growth conditions for these layers were given in Section 3.3.3.1. In Section 7.2, tilt domains in CdTe epilayer are investigated and discussed. In Sections 7.3 and 7.4, layers are studied by both plan view and cross-section TEM. The findings of the TEM investigations are discussed in Section 7.5.

7.2 Tilt Domains in CdTe

Two types of tilt domain will be discussed in this section; the mosaic tilts which cause HRXRD rocking curve broadening and larger regions of misorientation which will be referred to as subgrains. Mosaic tilts were observed by plan view TEM (PTEM) and by DCXRT. It was shown in Chapters 5 and 6 that the spread of mosaic tilts decreases as a layer thickens. Subgrains were investigated by double crystal and triple axis XRD, DCXRT and PTEM.

HRXRD of a 2μm thick CdTe/GaAs layer using the experimental arrangement of Section 6.6 showed evidence of two subgrains misoriented by 2.1° with respect to each other, as shown in figure 7.1. The FWHM of the curves are 2300" and 2680" which suggest that each subgrain has approximately the same mosaic spread about its mean position. It is expected that the decrease in FWHM observed for increasing layer thickness will occur for all subgrains.

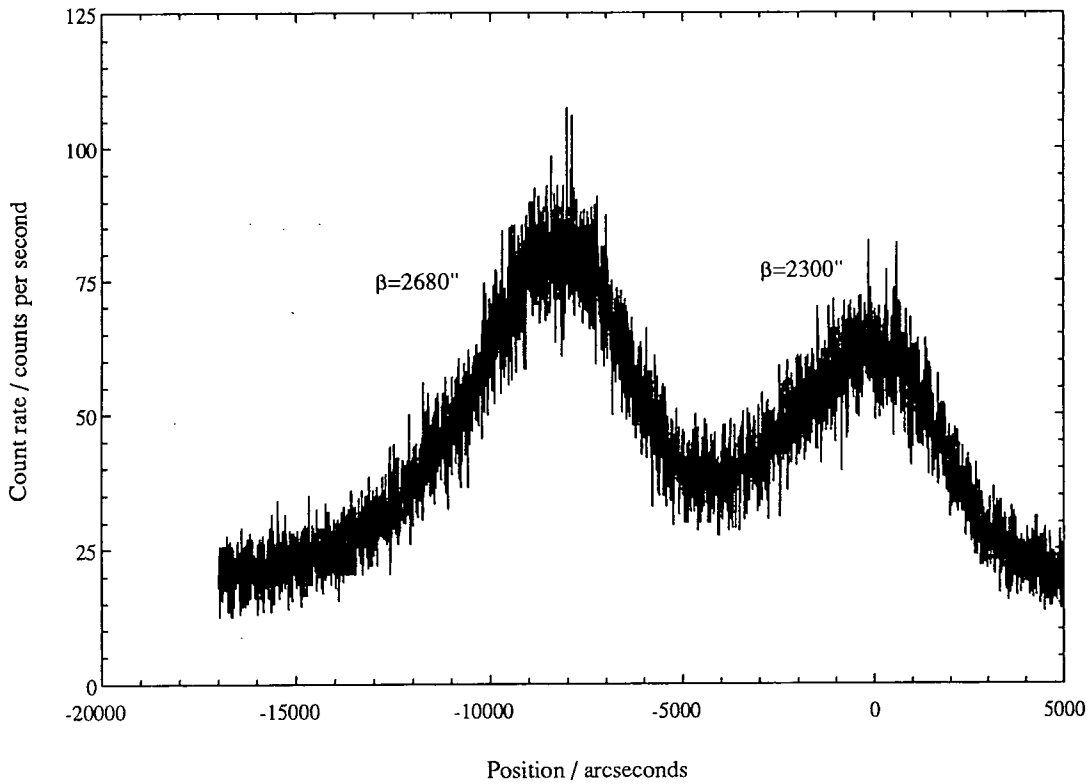

Figure 7.1 HRXRD rocking curve of a 2μm thick CdTe epilayer. The separation of the subgrain mean positions is 2.1°. The FWHM of the two peaks are 2680 and 2300 arcseconds.

The misorientation of subgrains was also estimated from the displacement of Kikuchi lines on moving across a subgrain boundary during PTEM examination. The angular misorientation can be determined, since the Bragg angle for reflections appearing in the electron diffraction pattern may be calculated for 200KV electrons (λ=0.0251Å), and this used to correlate the Kikuchi line displacement observed on the TEM screen with angular orientation. Using this method, subgrains tilted by 1.1° with respect to each other were observed in a 4.3μm thick layer.

Tilt boundaries can be thought of as arising from an array of edge dislocations with the same Burgers vector. This was first suggested by Burgers[1] and later developed by Vogel et al.[2]. An array of dislocations such as that shown in figure 7.2 produces a tilt between the grains on opposite sides of the boundary. If $b_{e\text{-}tilt}$ is the magnitude of the tilt component of the Burgers vectors and D is their separation, then the angle of misorientation, θ, is given in equation 7.1. If it is assumed that a threading dislocation has the same Burgers vector tilt component as a 60° misfit dislocation (see Sections 2.2.2 and 7.5), then $b_{e\text{-}tilt} = a_o/2$ [001] where a_o is the bulk lattice parameter of the CdTe layer. From equation 7.1, the dislocation separation required to produce the 1.1° misorientation measured in a 4.3μm layer by Kikuchi line displacement is 170 Å, corresponding to areal dislocation density of $1.2\text{x}10^6$ cm^{-2}. This is much less than the threading dislocation density of $9\text{x}10^8$ cm^{-2} measured for the top surface of a 4.3μm thick layer by PTEM.

$$\theta = \frac{b_{e\,tilt}}{D} \qquad \text{equation 7.1}$$

Following investigations using equation 7.1, Durose et al.[3] stated that if complete co-operative alignment of dislocation Burgers vectors occurred at a CdTe/GaAs interface, then a dislocation spacing of 15.7Å, corresponding to all misfit being accommodated by 60° dislocations, would give a subgrain tilt of 11.8°. This is far greater than any so far observed. They therefore concluded that the tilts and rotations observed experimentally could not be described solely by the complete co-operative alignment of Burgers vectors. Durose et al. assumed that the misfit dislocations were of 60° type, whereas

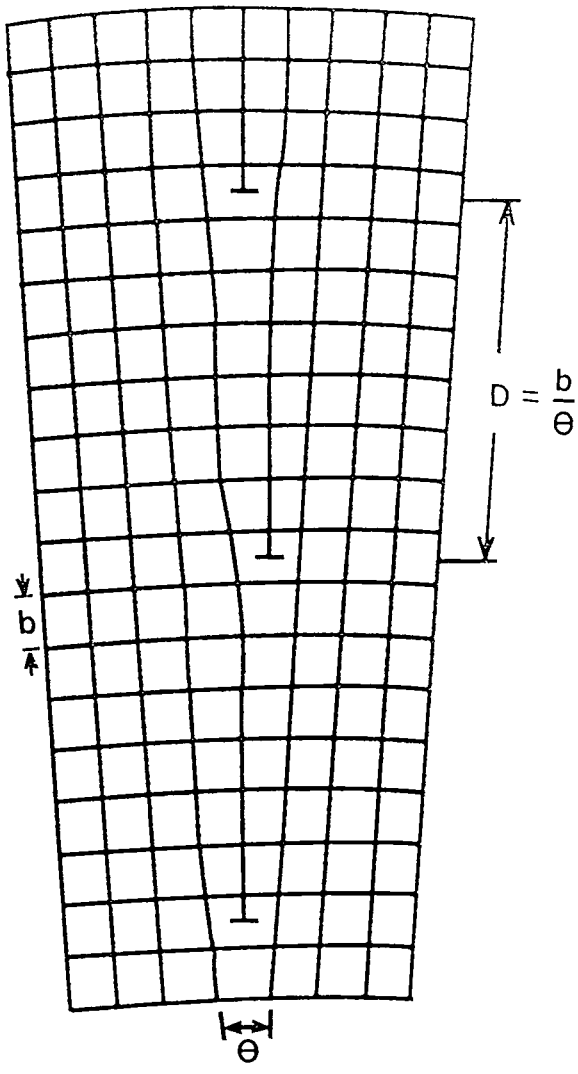

Figure 7.2 Diagrammatic representation of the arrangement of dislocations in a subgrain boundary. The dislocations are all edge type and $\mathbf{b}=\mathbf{b}_{e\text{-tilt}}$.

it is now generally accepted that edge type dislocations are the most abundant type of misfit dislocations to be found at the CdTe/GaAs interface (see for example Ponce et al.[4] for MBE grown (001)CdTe/GaAs or Cullis et al.[5] for MOVPE grown (001)CdTe/GaAs). Edge type dislocations do not have a tilt component and therefore seem unlikely to be the cause of subgrain tilts. However, most threading dislocations do have a tilt component to their Burgers vectors and the alignment of these components is likely to be the source of the subgrain tilts. The difference between the dislocation density required to support a 1.1° tilt in CdTe/GaAs (1.2×10^6 cm^{-2}) and the threading dislocation density actually observed by PTEM (9×10^8 cm^{-2}) indicates that very few dislocations contribute to large subgrain tilts, most are cancelled out by dislocations with opposite tilt components.

Keir et al.[6] have observed that subgrain boundaries in GaAs substrates are replicated in (001)$Cd_xHg_{(1-x)}Te$/CdTe/GaAs epitaxial layers but with greater tilt with respect to neighbouring regions. Barnett[7] reported a similar phenomenon for semi-insulating LEC GaAs substrates, where small lattice tilts of 1-2 arcsecond in the substrates gave rise to tilt boundaries of 10-100 arcseconds in layers grown on them.

A 25μm thick CdTe/GaAs layer was investigated by DCXRT using the experimental apparatus described in Section 6.4.3. A wavelength of 0.69Å was selected (Table 6.3) and a beam size of 3.5mmx2.5mm was used. Dental film was placed over the face of the detector shown in figure 6.10 to record the topograph. Dental film has low resolution compared to nuclear emulsion plates but requires only a fraction of the exposure time. A typical topograph is shown in figure 7.3. The double image was caused by the film not being quite perpendicular to the diffracted beam, resulting in an image from both sides of the film. The large elliptical feature which did not diffract has dimensions of 250μmx500μm. The smaller grains have dimensions of the order of 20-40μm and it is these which are thought to give rise to HRXRD rocking curve broadening and are termed 'mosaic' tilts. A contribution might also arise from domains having sizes below the resolution limit of the topograph.

Figure 7.3 A 004 double crystal topograph of the 25 µm thick (001)CdTe/GaAs epilayer investigated in Chapter 6. The topograph was recorded at a wavelength of 0.69Å at the diffraction peak maximum.

Thinner layers were investigated by PTEM and mosaic tilts were observed. An example of a PTEM micrograph of the top surface of a 0.6μm layer is shown in figure 7.4. The tilt domains are approximately 0.5-1μm wide, which is considerably smaller than those observed by DCXRT for the 25μm layer (20-40μm). Mosaic tilt domains of this type were not observed by PTEM for layers thicker than 0.6μm. The 25μm CdTe/GaAs epilayer was found to have a much narrower mosaic spread than the 0.6μm layer (Section 6.3). Brown et al.[8] have investigated the size of mosaic tilt domains and their spread with layer thickness for a (001)$Cd_xHg_{(1-x)}Te$/CdTe epilayer by etching followed by HRXRD and Lang topography. They found that as the layer was etched and remeasured, the HRXRD FWHM increased (as expected from earlier chapters) and the mosaic domain size decreased. This agrees with a model proposed by Turnbull[9] based on the random alignment of Burgers vectors. Turnbull derived an expression (equation 7.2) for the standard deviation tilt, ϕ_{SD} of an epilayer where N is the linear dislocation density, d is the domain size and $b_{e\text{-}tilt}$ is the tilt component of the Burgers vector considered to be producing the tilt. Equation 7.2 predicts that the standard deviation of mosaic spread increases as domain size decreases, as has been observed for (001)$Cd_xHg_{(1-x)}Te$/CdTe by Brown et al.[8] and for (001)CdTe/GaAs in the present work. It should be noted that the size of domains observed is in part dependent on the method of observation, with PTEM able to detect much smaller domains than the lower resolution DCXRT. It is possible that all layers contain domains of a wide range of dimensions but with a different distribution of sizes.

$$\tan\phi_{SD} \approx \phi_{SD} = b_{e\,tilt}\left(\frac{2N}{d}\right)^{\frac{1}{2}} \qquad \text{equation 7.2}$$

Subgrain tilts with a favoured direction were observed for a small region of the 25μm thick (001)CdTe/GaAs layer. Figures 7.5a and b show respectively the HRXRD curve and triple axis reciprocal space map of the region displaying subgrains. They were both recorded using the same experimental conditions as described in Section 6.2. The high angle (positive) side of the HRXRD rocking curve follows a Gaussian lineshape but the low angle (negative) side of the rocking curve displays a series of subsidiary

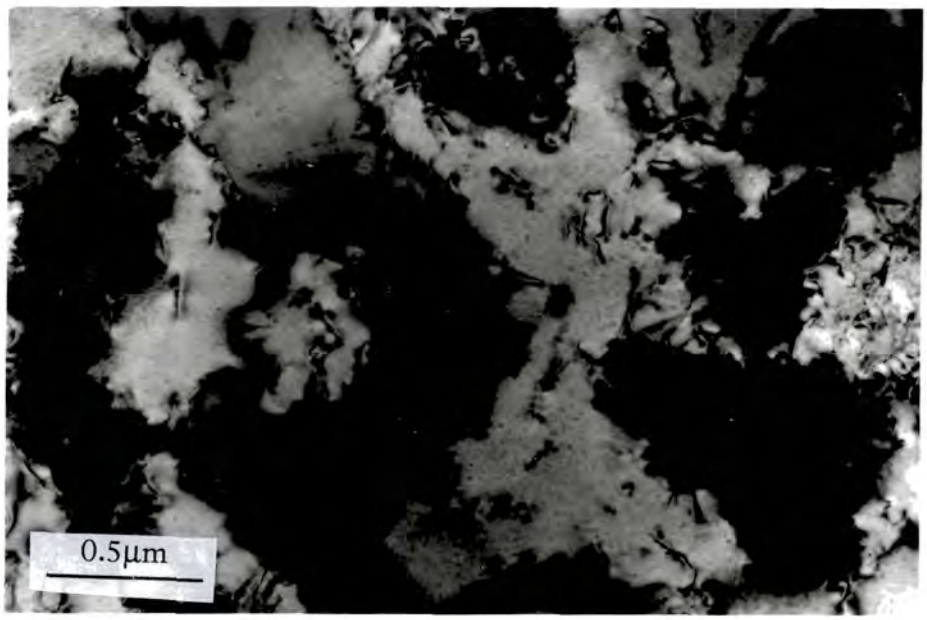

Figure 7.4 Plan view TEM micrograph of the top surface of the 0.6μm thick (001)CdTe/GaAs epilayer investigated in Chapter 6, showing the size of tilt domains which cause broadening of X-ray rocking curves.

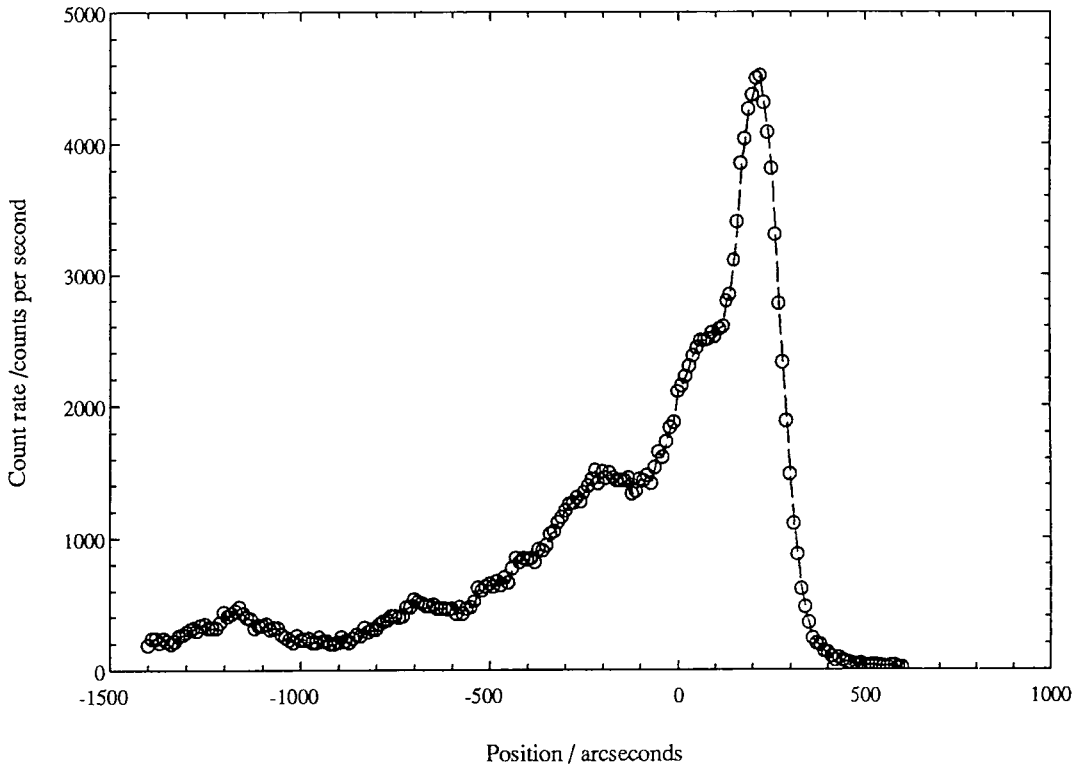

Figure 7.5a HRXRD rocking curve of a 25μm thick CdTe epilayer. Positive position is increasing Bragg angle. The direction of offcut is to smaller Bragg angle.

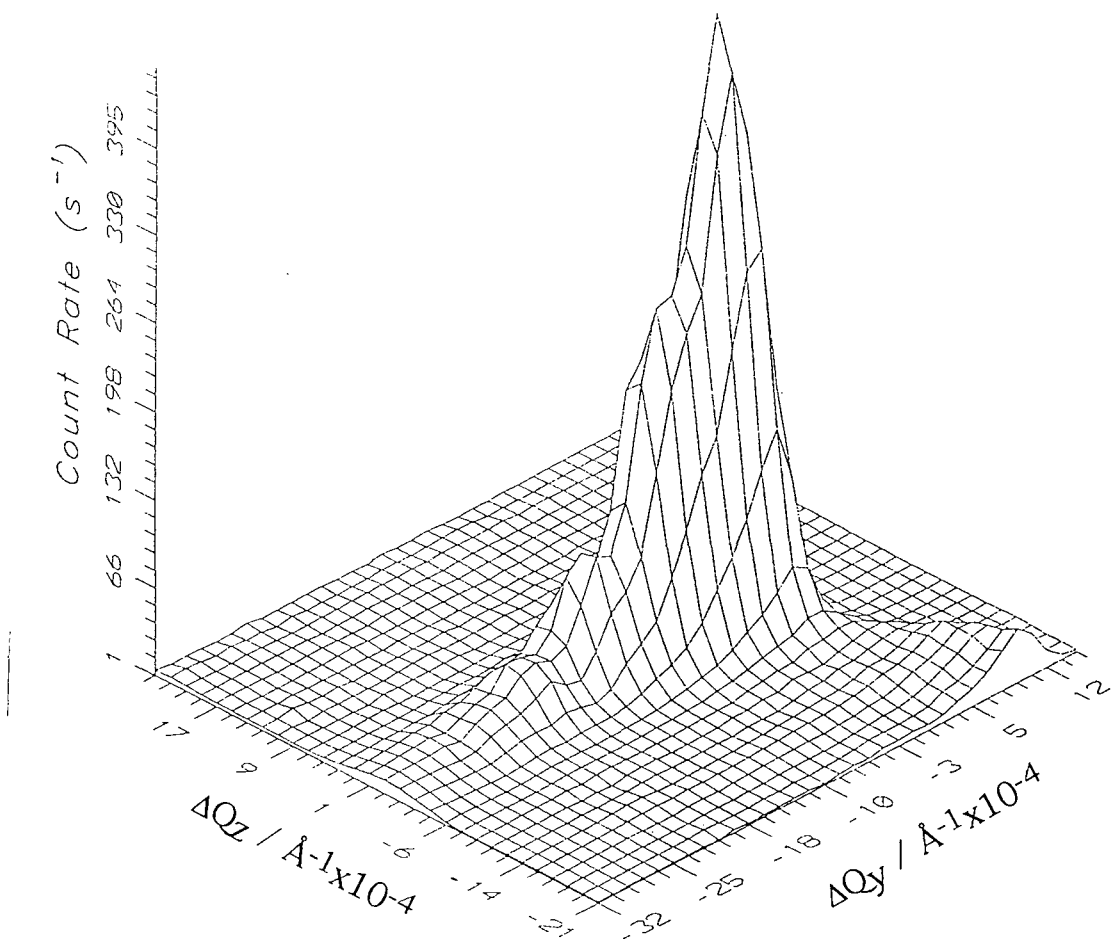

Figure 7.5b Reciprocal space plot of the scatter around the (004) reciprocal lattice point of a 25μm layer of (001)CdTe. Broadening in the ΔQ_y direction corresponds to mosaic and subgrain tilts

peaks, each assumed to be due to an individual subgrain. The subsidiary peaks are not well defined and it is difficult to ascertain whether each subgrain has the same mosaic spread. The reciprocal space map illustrates that broadening in the ΔQ_y direction is due to lattice and subgrain tilts. The additional tail towards positive ΔQ_y and negative ΔQ_z is an 'analyser streak'. The subgrain tilt direction is in the same direction as the substrate offcut.

Tilt of epitaxial layers with respect to the substrate has been investigated by many workers[10-12], whose models aim to predict the tilt of the entire layer and not just of isolated subgrains. Schowalter et al.[11] have predicted that layer tilt with respect to the substrate may be considered to increase or decrease the in plane lattice constant of the layer for compressive and tensile strain respectively and so reduce misfit strain. They predicted that for a layer in compression, the layer will tilt back towards the exact orientation. This is the opposite direction to that observed in the present work and by Yao et al.[13] for GaAs/Si layers grown on misoriented substrates. No explanation for the discrepancy has been found and this may be another example of high misfit three-dimensionally grown epilayers showing anomalous behaviour compared to low misfit two-dimensionally grown layers. Cheng et al.[14] have correlated the tilt of their (001)CdTe/GaAs layers to the offcut of their substrates and their novel heat treatment substrate preparation; conventional substrate preparation, which was used for the layers investigated in the present study, gave no tilt of the epilayer. They proposed that layer tilt was caused by the selective generation of misfit dislocations with the same Burgers vector. In the present study, the direction of the substrate offcut suggests that this is not the reason for the observed favoured tilt direction. Anisotropy of dislocations and the implication of this on layer tilts are discussed more fully in Section 7.5.

7.3 Threading Dislocations and their Interactions in CdTe Epilayers Investigated by PTEM

Threading dislocation density can be easily calculated by PTEM since all dislocations imaged in a PTEM foil thread through the plane of the foil, the

area of which can be measured easily. The small sampling area means that such an estimation is not necessarily representative of the whole sample. PTEM of (001) epilayers has the disadvantage that the incident beam direction is a four fold axis of symmetry, also the dislocation images are projected onto the (001) plane which makes absolute determination of their line direction difficult. The former problem cannot be overcome, but a compromise is made whereby one of the 220 diffraction spots is arbitrarily assigned and all others indexed relative to it. The second problem is partially overcome by calibrating the rotation of the image with respect to the diffraction pattern[15] (Section 4.3.2) and by establishing onto which directions certain common dislocation line directions will project in the (001) plane. Figure 7.6 shows the directions in the (001) plane which are expected for the projection of <011> and <112> threading dislocations. The projected line direction is determined from the relative rotation of the image and the diffraction pattern (whose reflections have been arbitrarily assigned), the actual line directions which could give the projected direction are then determined from figure 7.6.

It should be noted that all the line directions given in figure 7.6 are drawn from substrate to layer. This convention has been adopted, by the present author, since the reversal of either the line direction or Burgers vector gives a complementary dislocation while reversal of both line direction and Burgers vector gives the same dislocation[16]. It has been pointed out by Schwartzman and Sinclair[17] that for a layer in compression, dislocations which relieve misfit must have edge components which have extra half-planes pointing into the substrate. This can be expressed in terms of the cross product of line direction, ℓ, with Burgers vector, $\mathbf{b}$ having a negative [001] component as given in equation 7.3. All individual threading dislocations which are investigated in this and the following section are assumed to relieve misfit and have line directions and Burgers vectors which allow this. All micrographs are labelled for the electron beam passing into the plane of the paper, which is the orientation observed on the TEM screen. Individual straight dislocations were examined by $\mathbf{g}\cdot\mathbf{b}$ contrast analysis which was described in Section 4.3.1

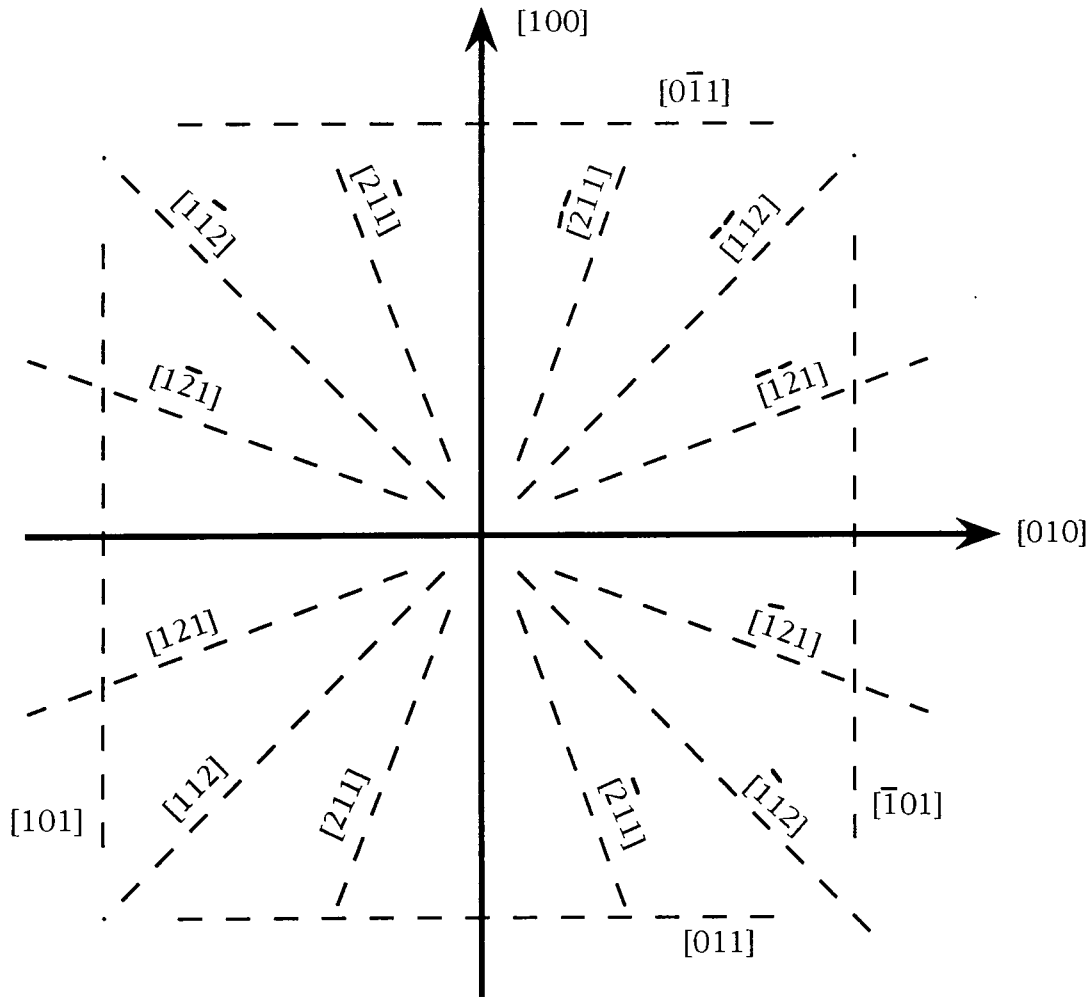

Figure 7.6 The projected line directions of threading dislocations onto the (001) interface plane as observed in plan view TEM. All line directions are out of the interface into the layer. Bold lines are those in the (001) plane, dashed lines are the projected line directions of threading dislocations, [001] is into the plane of the paper.

$[001] \cdot (\boldsymbol{\ell} \times \mathbf{b}) < 0$ equation 7.3

Many threading dislocations were identified as being of screw, 60° and 30° type in PTEM samples of the surface of CdTe/GaAs layers 0.6, 4.3 and 8.7μm thick. Many more were not identified since they were not straight or were in tangles with other dislocations. All characterised dislocations had Burgers vectors of type <011> and the line directions were of type <011> for the screw and 60° dislocations and <112> for the 30° dislocations. A more thorough analysis of the 30° dislocations is presented in Section 7.4. They are discussed in Section 7.5, along with a comparison with 60° dislocations, which are usually the more common type of dislocation in the sphalerite lattice.

Interactions between 30° dislocations were observed in PTEM; one such interaction for a 4.3μm layer is shown in figures 7.7a-d for four different diffraction vectors. The dislocation A was found to have $\mathbf{b}=(a_0/2)[0\bar{1}\bar{1}]$ with possible line directions [121] and $[12\bar{1}]$ while dislocation B was found to have $\mathbf{b}=(a_0/2)[\bar{1}0\bar{1}]$ with possible line directions $[2\bar{1}1]$ and $[2\bar{1}\bar{1}]$. The line directions [121] and $[2\bar{1}1]$ correspond to glide planes $(\bar{1}1\bar{1})$ and $(\bar{1}\bar{1}1)$ respectively and are thus more likely than line directions $[12\bar{1}]$ and $[2\bar{1}\bar{1}]$ which would have {311} glide planes. The line direction and Burgers vectors of these dislocations are summarised in table 7.1. When the two dislocations meet, they form a third, C which was out of contrast for $\mathbf{g}=220$. From the Burgers vectors of the two interacting dislocations, a dislocation with $\mathbf{b}=(ao/2)[1\bar{1}0]$ which is expected to be invisible for $\mathbf{g}=220$ can be formed. The line direction is uncertain. Several other similar interactions between 30° dislocations were observed in other CdTe/GaAs epilayers.

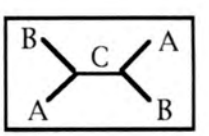

(a)

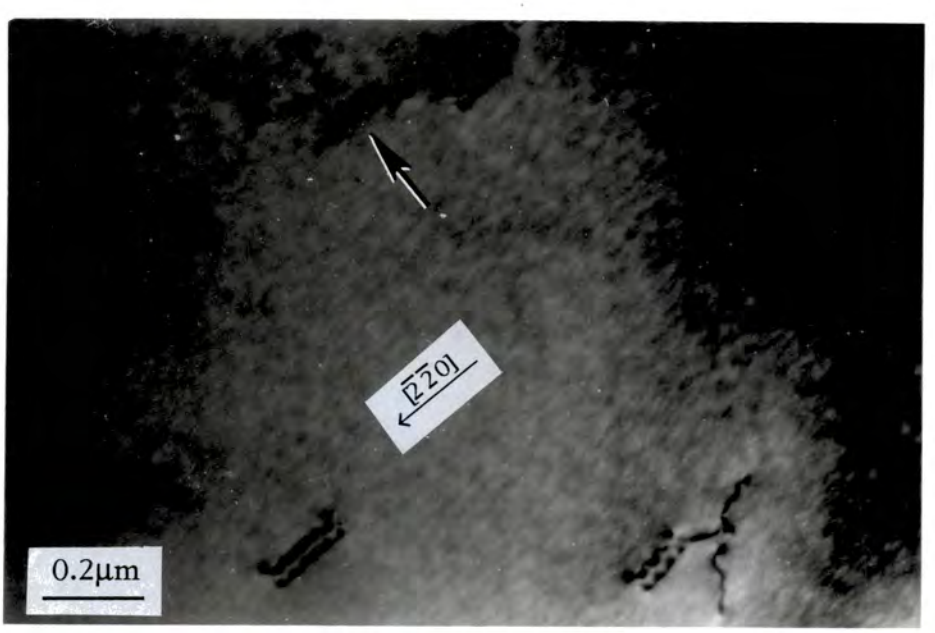

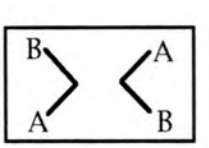

(b)

Figure 7.7 Plan view TEM micrographs showing the interaction of two 30° threading dislocations and dislocation dipoles. (a) **g**=2$\bar{2}$0, (b) **g**=$\bar{2}$2$\bar{2}$0.

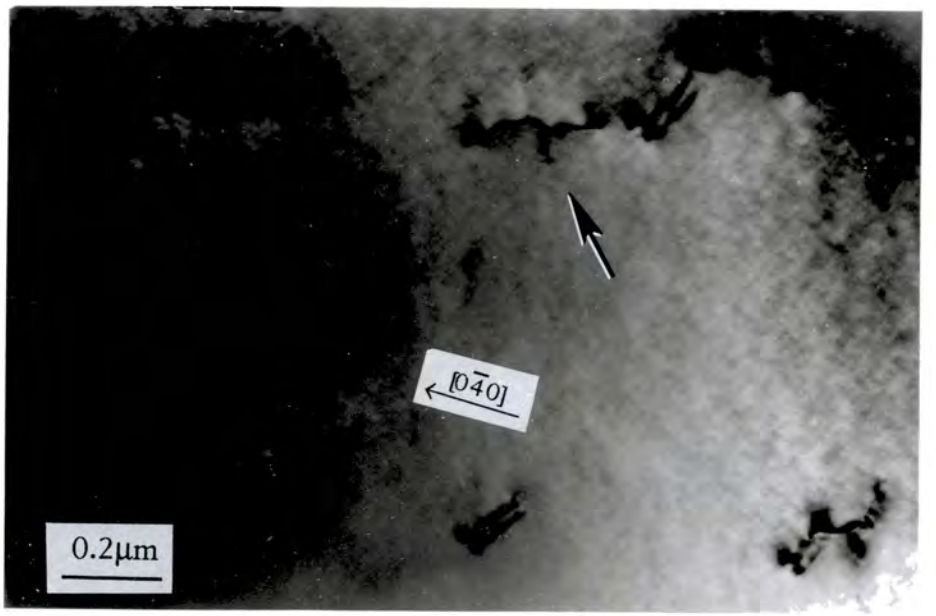

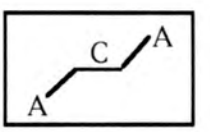

(c)

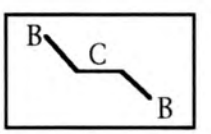

(d)

Figure 7.7 (cont) Plan view TEM micrographs showing the interaction of two 30° threading dislocations and dislocation dipoles. (c) $\mathbf{g}=0\bar{4}0$ (same parts invisible for $\mathbf{g}=11\bar{1}$), (d) $\mathbf{g}=\bar{4}00$ (same parts invisible for $\mathbf{g}=1\bar{1}1$).

Dislocation	Burgers vector, **b**	Line direction, ℓ	Glide plane
A	$[0\bar{1}\bar{1}]$	[121]	$(\bar{1}1\bar{1})$
B	$[\bar{1}0\bar{1}]$	$[2\bar{1}1]$	$(\bar{1}\bar{1}1)$

Table 7.1 Burgers vectors, line directions and glide planes for 30° dislocations shown in figures 7.7. All line directions are out of the substrate and into the layer. All Burgers vectors are given assuming that the dislocations relieve the misfit strain of a layer in compression and therefore the edge component of the Burgers vector corresponds to an extra half-plane in the substrate.

In figure 7.7, three dislocation dipoles can be seen which have a projected line direction of [220] which corresponds to an actual line direction of $[\bar{1}\bar{1}2]$ or [112] in figure 7.6, the dipoles disappear for $\mathbf{g}=2\bar{2}0$ giving Burgers vectors of $\pm(ao/2)[110]$. The two dislocations making up the dipole were found to thread in the same direction, since the same end of the dislocations reversed contrast in dark field imaging (the end of a dislocation emerging from the bottom of a TEM film shows reverse contrast in bright and dark field while the end emerging at the top of a foil shows no change of contrast). The two dislocations were found to have opposite Burgers vectors since they displayed complementary fringes in both bright and dark field images[18].

Two perpendicular sets of dipoles can be seen in figure 7.8 (micrographs taken of the surface of a 4.3μm thick layer), one set are the same as those seen in figure 7.7 while the other set is equivalent but lies on a perpendicular {110} plane. The line directions, Burgers vectors and glide planes of the dipoles are summarised in table 7.2. All the dipole dislocations have $[001].\ell x\mathbf{b}=0$, i.e. they do not participate in strain relief. The occurrence of these dipoles and their unusual glide plane will be discussed in Section 7.5. It should be pointed out that due to the dipoles having Burgers vectors parallel to one of the two <110> directions in the heterointerface, these dipoles cannot be analysed in <110>XTEM since their Burgers vector will always be either parallel or perpendicular to the electron beam direction and will therefore always be either visible or invisible.

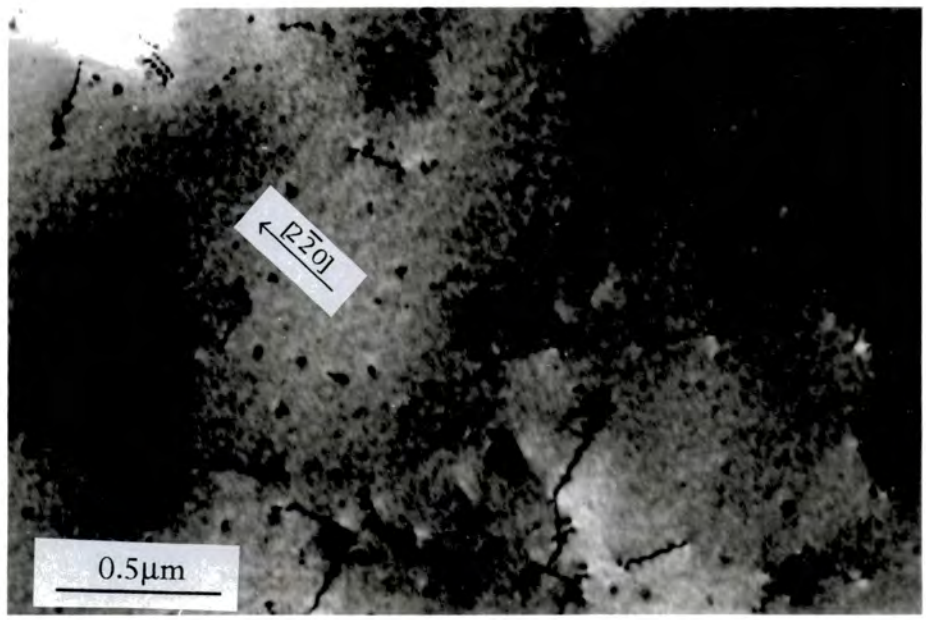

(a)

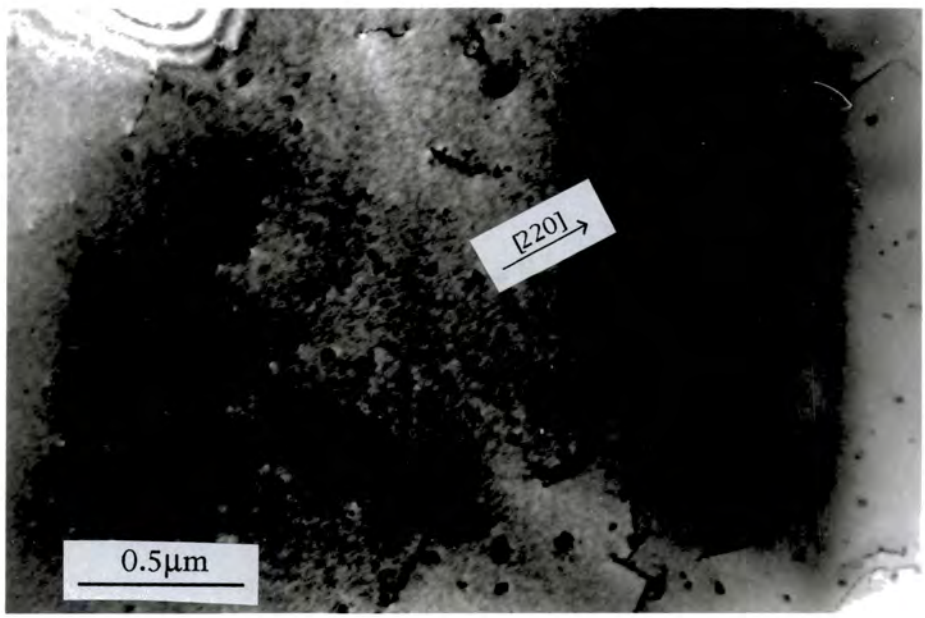

(b)

Figure 7.8 Plan view TEM micrographs showing two sets of dislocation dipoles. (a) **g**=2$\bar{2}$0, (b) **g**=220.

Line direction, ℓ	Burgers vector, **b**	Glide plane
[112]	$\pm$[110]	$(1\bar{1}0)$
or $[\bar{1}\bar{1}2]$	$\pm$[110]	$(1\bar{1}0)$
$[1\bar{1}2]$	$\pm[1\bar{1}0]$	(110)
or $[\bar{1}12]$	$\pm[1\bar{1}0]$	(110)

Table 7.2 Burgers vectors, line directions and glide planes for dislocation dipoles shown in figures 7.7 and 7.8. Dislocations within each dipole have opposing Burgers vectors.

The density of dislocation dipoles in figure 7.8 is estimated to be $7x10^7cm^{-2}$ and that of single threading dislocations is estimated to be $5x10^8cm^{-2}$ in the same region. Observation of many PTEM foils showed that dipoles such as those described here occur for all layers in the thickness range 0.6-8.7μm, but they tend to occur in certain isolated regions which means that the density quoted earlier is an upper limit. Stacking faults have been observed very rarely in these layers.

7.4 Threading Dislocations in CdTe Epilayers Investigated by XTEM

The micrographs presented in this section were all taken from the same XTEM specimen of an 8.7μm thick CdTe layer. The XTEM sample was prepared as described in Section 4.3.3 with opposite sides of the central glue line having normals parallel to the two <110> directions in the substrate surface. The polarity of each side of the foil was determined by microdiffraction[19] and the polar {111} planes were indexed according to the Gatos convention[20] (i.e. the Cd or A face is {111} and the Te or B face is $\{\bar{1}\bar{1}\bar{1}\}$). For details of this method see Section 4.3.2.

Cross-section TEM micrographs of the 8.7 μm layer in [110] projection (i.e. electron beam direction [110] into the plane of the paper) are shown in figures 7.9 a-c, for $\mathbf{g}=\bar{2}20$, $\bar{1}1\bar{1}$, and $1\bar{1}\bar{1}$ respectively. The dominant features are two sets of straight dislocations lying on oppositely inclined {111} planes and making angles of 54°44' with the interface. All dislocations lying on the same {111} plane will have an image which projects onto the (110) plane in the same orientation. For example [011], $[\bar{1}01]$ and $[\bar{1}12]$ line directions will all produce images in the (110) plane inclined at 54°44' to the interface. The $[\bar{1}12]$ line direction is contained in the plane of the TEM foil (110) and is therefore expected to show no oscillatory contrast along its length while [011] and $[\bar{1}01]$ line directions are inclined at 30° to the TEM foil and are thus expected to show oscillatory contrast due to the inclination of the dislocation with respect to the electron beam direction. Since these line directions are inclined to the TEM foil, they are not expected to remain in the foil for the whole of their length and will appear shorter than <112> dislocations. From figure 7.9, the long straight dislocations do not show any oscillatory contrast, and their length would require a foil thickness of approximately 0.5μm if the dislocations had <011> line directions; this would not give an observable image. For these reasons, the long straight dislocations were assigned <112> line directions.

Dislocation images, such as that marked D in figure 7.9a, are inclined at 54°44' to the interface, show oscillatory contrast and have a length, which if a line direction of <110> inclined to the TEM foil is assumed, corresponds to an expected foil thickness of about 900Å. Dislocations such as these, with <011> line directions appear to be less abundant than those with <112> line directions, although their shorter projected lengths make them harder to pick out.

Dislocations with line direction $[1\bar{1}2]$ which are on the $(1\bar{1}\bar{1})$ plane, disappear for $\mathbf{g}=1\bar{1}\bar{1}$ and therefore have Burgers vectors of either $(a_0/2)[0\bar{1}1]$ or $(a_0/2)[\bar{1}0\bar{1}]$ and are 30° dislocations. Those with line direction $[\bar{1}12]$ which are on the $(\bar{1}1\bar{1})$ plane, disappear for $\mathbf{g}=\bar{1}1\bar{1}$ and therefore have Burgers vectors of either $(a_0/2)[10\bar{1}]$ or $(a_0/2)[011]$, these are also 30° dislocations. Shorter dislocation segments which show oscillatory contrast and are assumed to

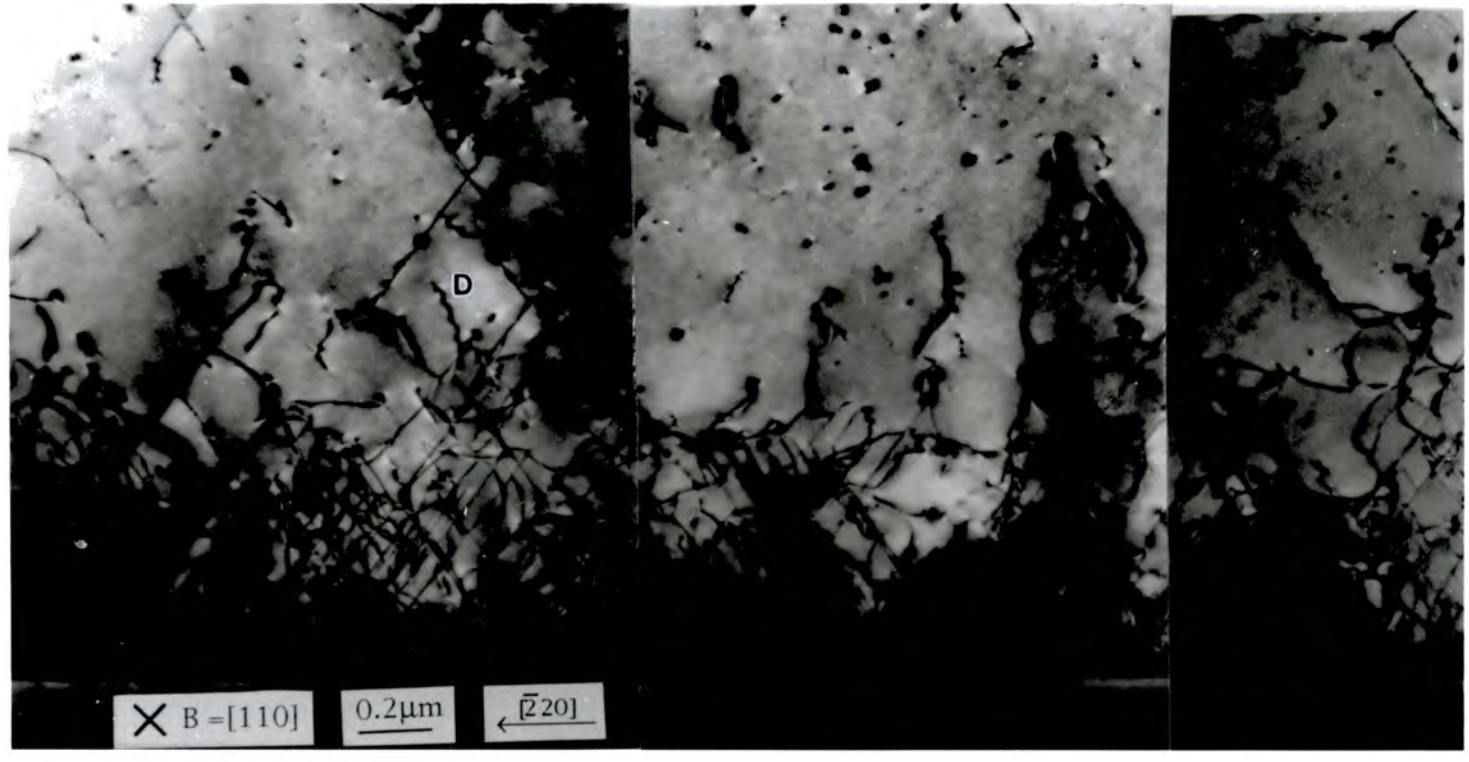

Figure 7.9a Cross-section TEM micrograph of a (001)CdTe/GaAs epilayer. The beam direction [110] is into the plane of the paper and **g**=$\bar{2}$20. Dislocations such as that labelled D are inclined to the TEM foil.

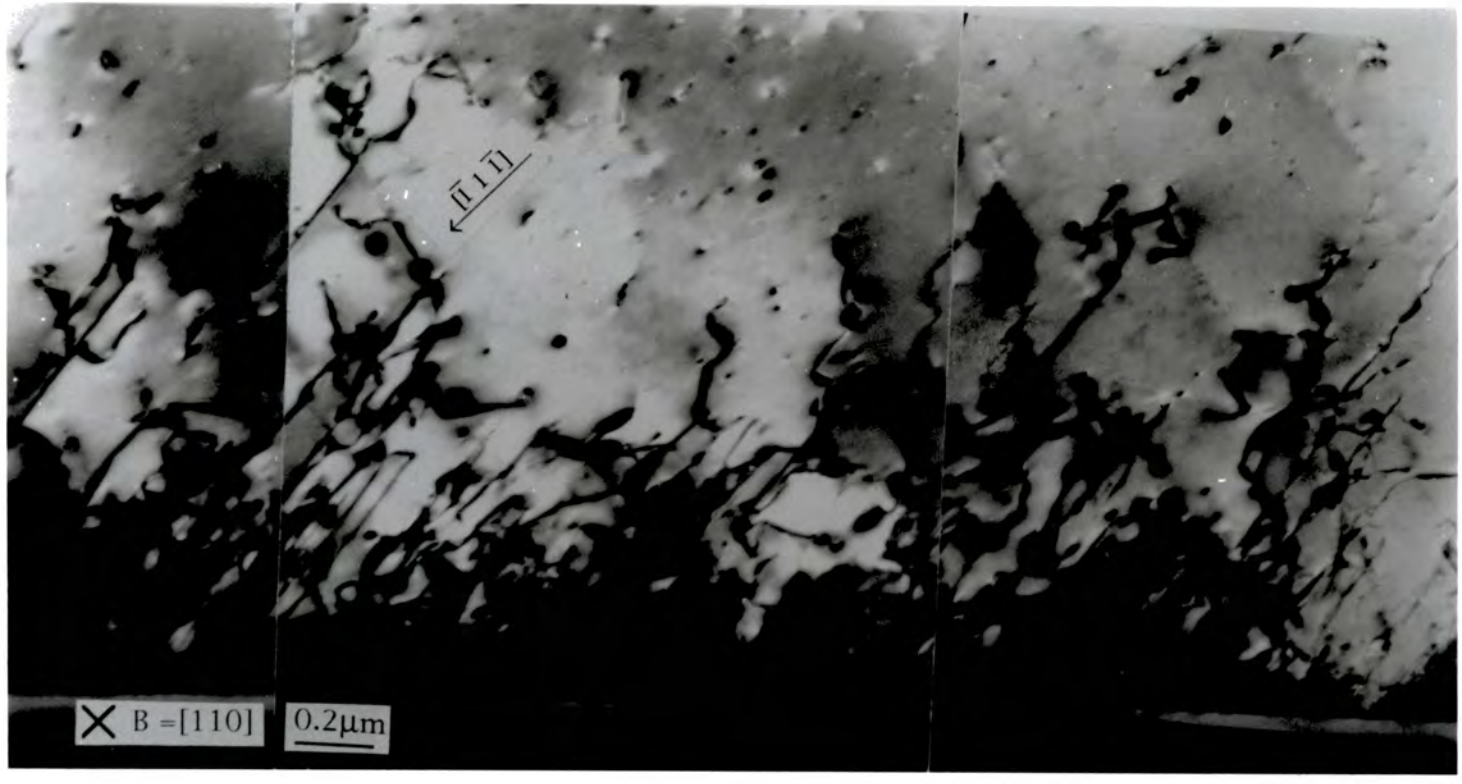

Figure 7.9b Cross-section TEM micrograph of a (001)CdTe/GaAs epilayer. The beam direction [110] is into the plane of the paper and $\mathbf{g}=\bar{1}1\bar{1}$.

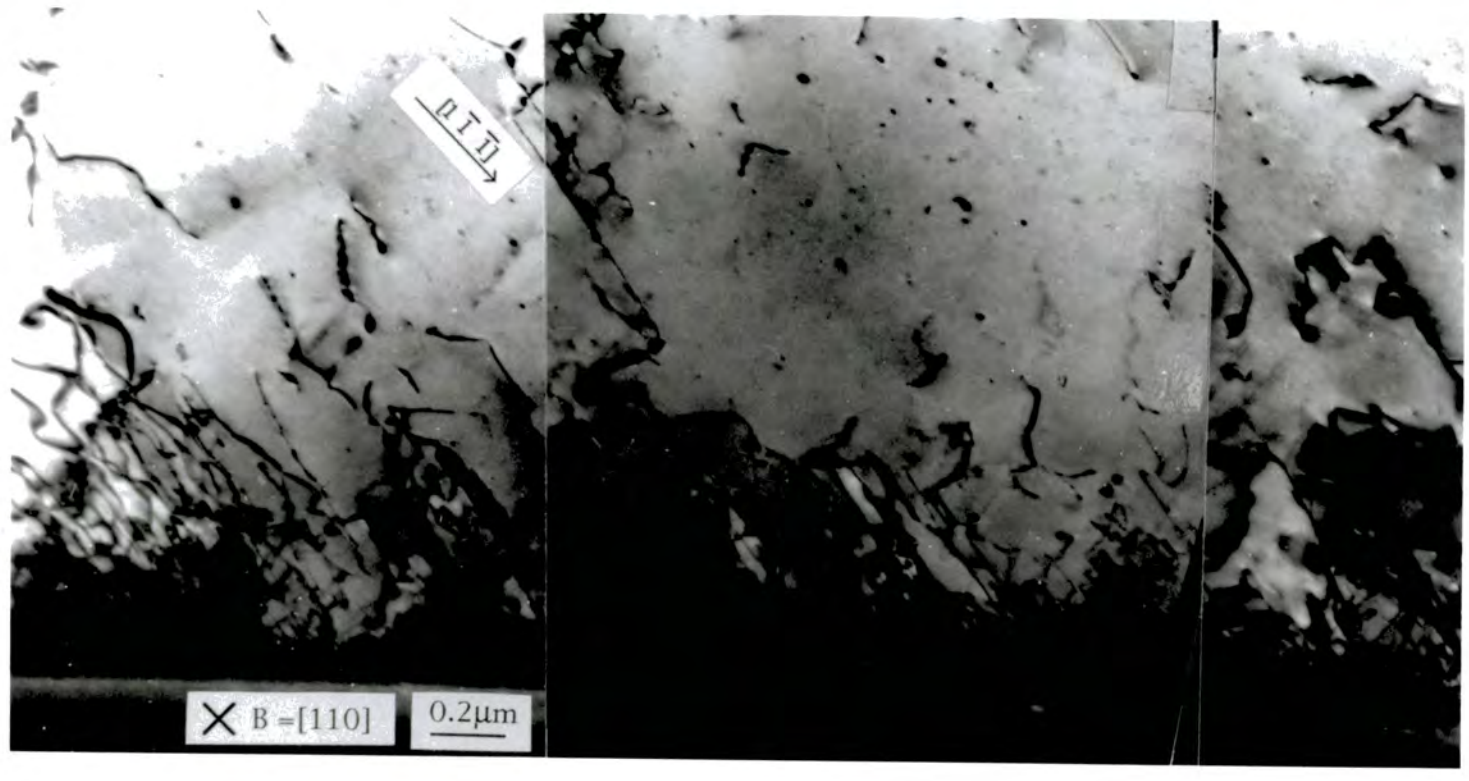

Figure 7.9c Cross-section TEM micrograph of a (001)CdTe/GaAs epilayer. The beam direction [110] is into the plane of the paper and $\mathbf{g}=1\bar{1}\bar{1}$.

have <011> line directions (e.g. the dislocation marked D in figure 7.9a), were analysed by **g.b** contrast; they were found to have the same Burgers vectors as the 30° dislocations. The inclination of these dislocations was determined by noting which end of the dislocation changed contrast between bright and dark field as described in Section 7.3. Although the inclination and, therefore, the line direction of these dislocations can be ascertained, the Burgers vectors cannot be determined definitely. From this analysis, the dislocations are of either 60° or screw type. Tables 7.3, 7.4 and 7.5 summarise the line directions, Burgers vectors and glide planes of 30°, 60° and screw type dislocations respectively, which were observed in XTEM.

Cross-section TEM micrographs of the 8.7 μm thick layer in $[\bar{1}10]$ projection (i.e. electron beam direction $[\bar{1}10]$ into plane of paper) are shown in figures 7.10 a-c, for **g**=220, 111, and $\bar{1}\bar{1}1$ respectively. Again the dominant feature was two sets of straight dislocations lying on oppositely inclined {111} planes. Assuming that the dislocations are once again contained in the plane of the TEM foil, their line directions are [112] and $[\bar{1}\bar{1}2]$ on the $(\bar{1}\bar{1}1)$ and (111) planes respectively; **g.b** analysis showed that the Burgers vectors were either $(a_o/2)[101]$ or $(a_o/2)[0\bar{1}\bar{1}]$ for those with line direction [112] and $(a_o/2)[01\bar{1}]$ or $(a_o/2)[\bar{1}01]$ for those with line direction $[\bar{1}\bar{1}2]$. The dislocations were 30° type as before. As for the [110] projection, 60° and screw type dislocations were also observed. The occurrence of 30° dislocations and the relative tilt components of 30°, 60° and screw type threading dislocations observed in XTEM are discussed in Section 7.5.

One interesting feature of this region is the dislocation segment marked E in figure 7.10a, which disappears for **g**=$\bar{1}\bar{1}1$ along with the two 30° dislocations which join it to the interface. This may be an example of the formation of a half-loop by dislocations with the same Burgers vector, as described in Section 5.3.2 and figure 5.14. Since dislocation E runs parallel to the interface, its line direction cannot be assigned by the convention adopted in this work. It has already been explained that the assignment of line direction is arbitrary due to the reversibility of both line direction and Burgers vector; dislocation E was arbitrarily assigned a line direction [110]. The two 30° dislocations which join E to the interface have Burgers vectors

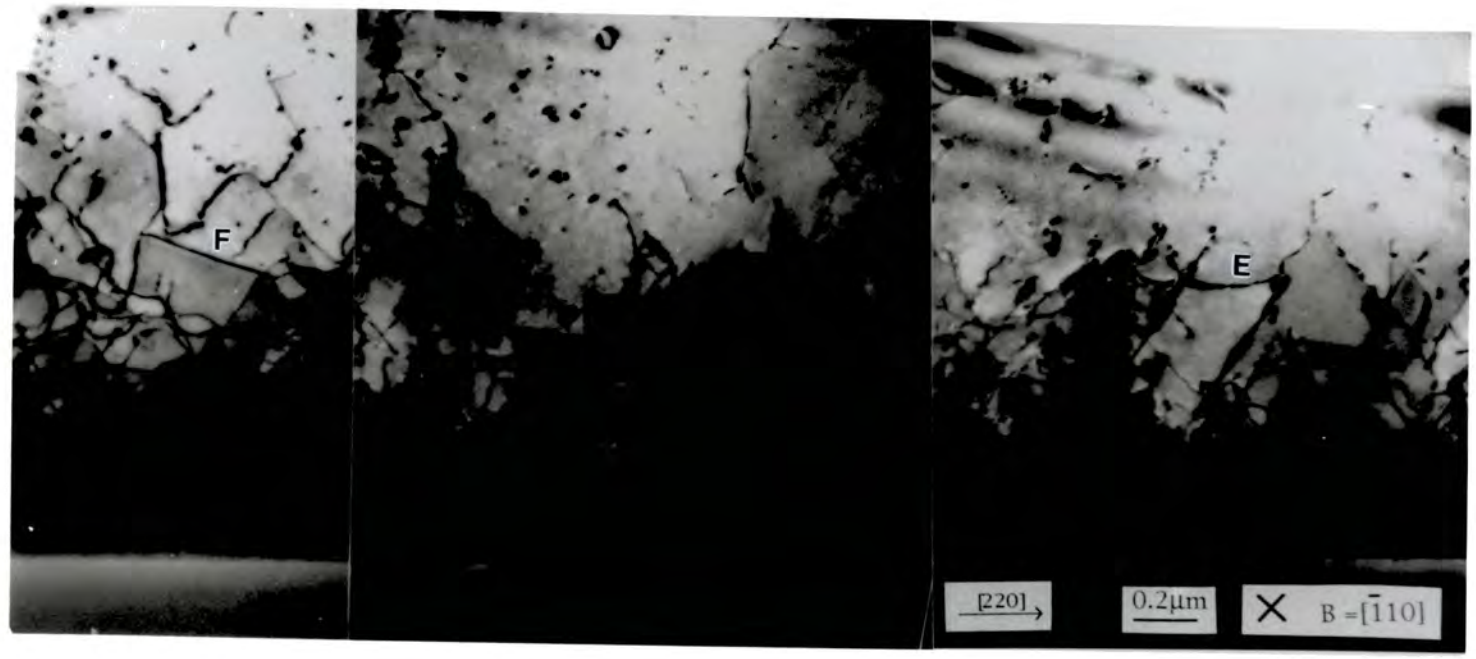

Figure 7.10a Cross-section TEM micrograph of a (001)CdTe/GaAs epilayer. The beam direction [$\bar{1}$10] is into the plane of the paper and **g**=220. Dislocation E is a 60° dislocation with the same Burgers vector as the two threading dislocations connecting it to the interface. The dislocation F did not disappear for any diffraction vectors of the [$\bar{1}$10] pole; its Burgers vector was not established.

Figure 7.10b Cross-section TEM micrograph of a (001)CdTe/GaAs epilayer. The beam direction [$\bar{1}$10] is into the plane of the paper and **g**=111.

Figure 7.10c Cross-section TEM micrograph of a (001)CdTe/GaAs epilayer. The beam direction [$\bar{1}10$] is into the plane of the paper and **g**=$\bar{1}\bar{1}1$. The contrast of dislocation E (labelled in figure 7.10a) is extinguished.

of either $(a_0/2)[101]$ or $(a_0/2)[0\bar{1}\bar{1}]$, if E has the same Burgers vector then E is a 60° dislocation. The feature F (also marked in figure 7.10a) which lies approximately parallel to the interface, did not disappear for any diffraction vectors of the $[\bar{1}10]$ pole. Dislocations running parallel to and up to 3.5μm from the interface were observed in both [110] and $[\bar{1}10]$ projection. Those whose Burgers vectors were determined were all of 60° type. Tables 7.3-7.6 summarise the line directions, Burgers vectors and glide planes of 30°, 60° (inclined to the interface), screw and 60° (parallel to the interface) type dislocations respectively. The tables summarise all the common dislocations observed in XTEM, although not all of them have been identified in the present work. Figure 7.11 shows the tetrahedron of {111} glide planes and all the dislocation line directions commonly encountered in the XTEM analysis.

Line direction ℓ	Burgers vector, **b**	Glide plane
Visible in [110]		
$[1\bar{1}2]$	$[0\bar{1}1]$ or $[\bar{1}0\bar{1}]$	$(1\bar{1}\bar{1})$
$[\bar{1}12]$	$[10\bar{1}]$ or $[011]$	$(\bar{1}1\bar{1})$
Visible in $[\bar{1}10]$		
$[112]$	$[101]$ or $[0\bar{1}\bar{1}]$	$(\bar{1}\bar{1}1)$
$[\bar{1}\bar{1}2]$	$[01\bar{1}]$ or $[\bar{1}01]$	(111)

Table 7.3 Summary of line directions, Burgers vectors and glide planes of 30° dislocations observed by XTEM in [110] and $[\bar{1}10]$ projections. All line directions are out of the substrate and into the layer. All Burgers vectors are given assuming that the dislocations relieve the misfit strain of a layer in compression and therefore the edge component of the Burgers vector corresponds to an extra half-plane in the substrate.

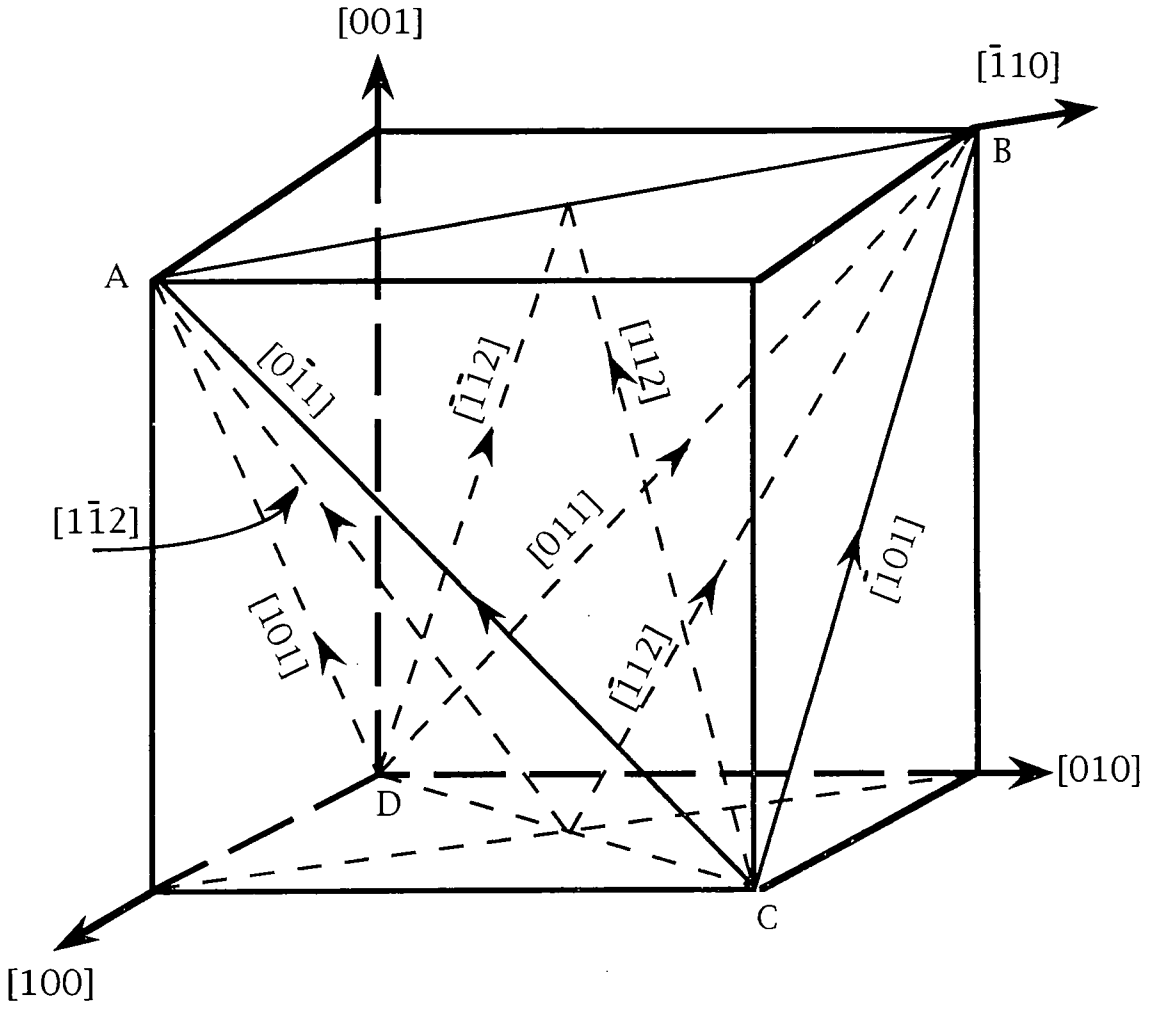

Figure 7.11 Tetrahedron of{111} planes showing all the <110> and <112> line directions analysed in this XTEM study.

Line direction ℓ	Burgers vector, **b**	Glide plane
[101]	$[0\bar{1}1]$ or $[0\bar{1}\bar{1}]$	$(1\bar{1}\bar{1})$ $(\bar{1}\bar{1}1)$
$[0\bar{1}1]$	$[\bar{1}0\bar{1}]$ or $[\bar{1}01]$	$(1\bar{1}\bar{1})$ (111)
[011]	$[10\bar{1}]$ or [101]	$(\bar{1}1\bar{1})$ $(\bar{1}\bar{1}1)$
$[\bar{1}01]$	[011] or $[01\bar{1}]$	$(\bar{1}1\bar{1})$ (111)

Table 7.4 Summary of line directions, Burgers vectors and glide planes of 60° dislocations. All these dislocations can be observed in both [110] and $[\bar{1}10]$ projections. All line directions are out of the substrate; all Burgers vectors correspond to an extra half-plane in the substrate. Note that no distinction has been made between 60° and screw type dislocations and the details given in this table and table 7.5 represent the two alternative characteristics of the dislocations threading the TEM foil.

Line direction ℓ	Burgers vector, **b**
[101]	± [101]
$[0\bar{1}1]$	± $[0\bar{1}1]$
[011]	± [011]
$[\bar{1}01]$	± $[\bar{1}01]$

Table 7.5 Summary of line directions and Burgers vectors of screw dislocations. All these dislocations can be observed in both [110] and $[\bar{1}10]$ projections. Note that no distinction has been made between 60° and screw type dislocations and the details given in this table and table 7.5 represent the two alternative characteristics of the dislocations threading the TEM foil.

Line direction ℓ	Burgers vector, **b**	Glide plane
Visible in [110]		
$[1\bar{1}0]$	$[\bar{1}0\bar{1}]$	$(\bar{1}\bar{1}1)$
	$[0\bar{1}1]$	(111)
$[\bar{1}10]$	$[10\bar{1}]$	(111)
	$[011]$	$(\bar{1}\bar{1}1)$
Visible in $[\bar{1}10]$		
$[110]$	$[101]$	$(1\bar{1}\bar{1})$
	$[0\bar{1}\bar{1}]$	$(\bar{1}1\bar{1})$
$[\bar{1}\bar{1}0]$	$[01\bar{1}]$	$(1\bar{1}\bar{1})$
	$[\bar{1}01]$	$(\bar{1}1\bar{1})$

Table 7.6 Summary of line directions, Burgers vectors and glide planes of 60° dislocations observed in [110] and $[\bar{1}10]$ projections which lie parallel to the interface. All Burgers vectors correspond to an extra half-plane in the substrate.

A comparison of the two orthogonal projections is made in figures 7.12a and b for [110] and $[\bar{1}10]$ respectively. The micrograph of the [110] projection is very ordered and the high density of dislocations extends approximately 0.7μm from the interface; that of the $[\bar{1}10]$ projection is much more tangled in comparison and the tangle extends approximately 1μm from the interface. This anisotropy and its possible origins are discussed in Section 7.5.

7.5 Discussion

Dislocation dipoles with <112> line directions and ±[110] Burgers vectors are present in CdTe/GaAs epilayers. The occurrence of such dipoles throws up some interesting questions; firstly, how and why dislocations with opposite character are formed in an epilayer under compressive strain, and secondly why such dislocations adopt an orientation on {110} glide planes rather than {111}.

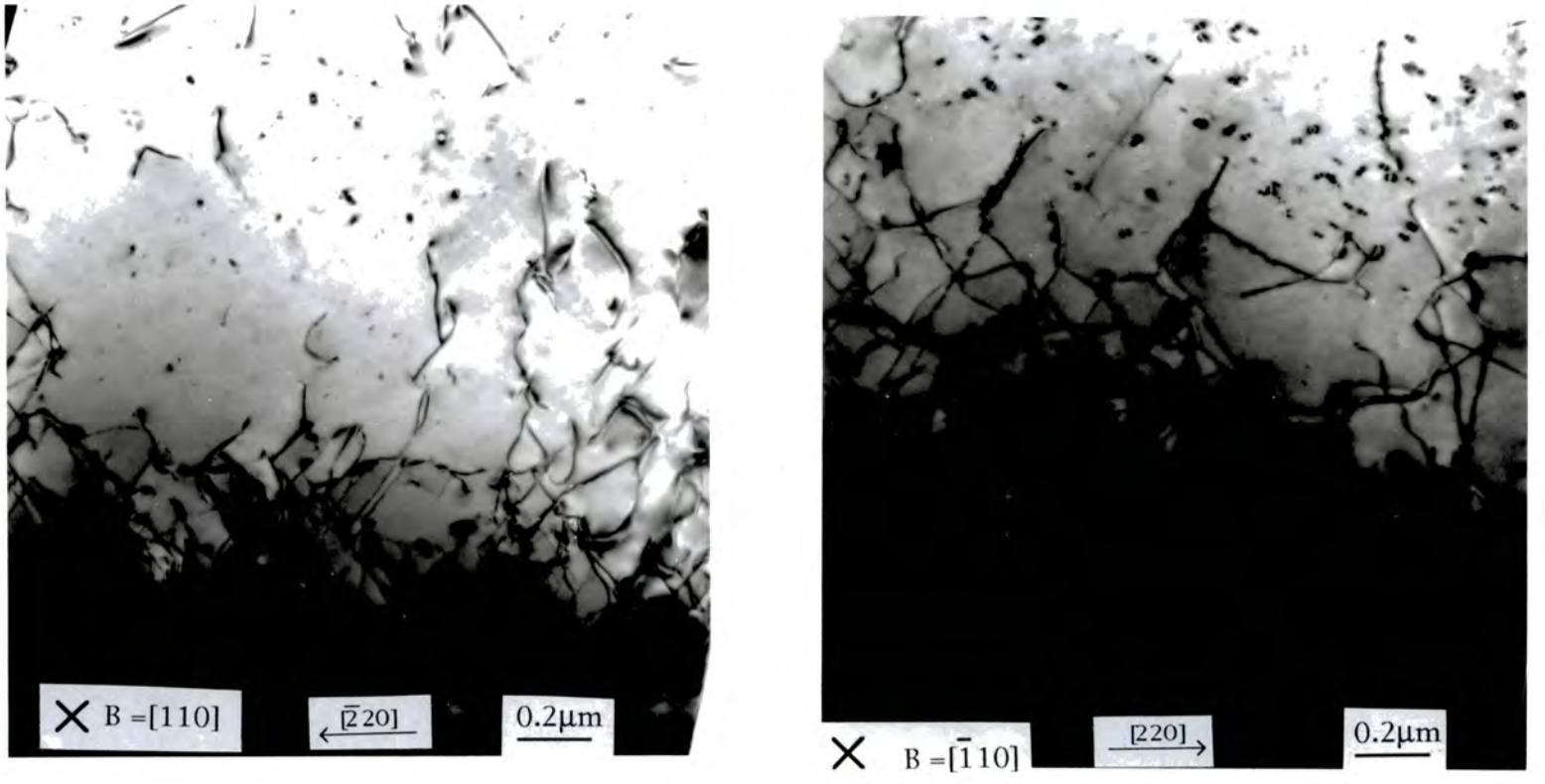

(a) (b)

Figure 7.12 Cross-section TEM micrograph of a (001)CdTe/GaAs epilayer. (a) [110] projection, **g**=2̄20, (b) [1̄10] projection, **g**=220. The beam directions (projections) given are into the plane of the paper.

The first question is posed because the formation of dislocations with opposite Burgers vectors suggests that one of the dislocations increases misfit strain while the other reduces it. It is not true in this case , however, since for misfit strain to be relieved, a dislocation must have an edge component perpendicular to the interface. Equation 7.3 formalises this by stating that for relief of compressive misfit strain, the cross product of the dislocation line direction and Burgers vector must have a negative component perpendicular to the interface. Since the line direction and Burgers vector of the dipoles are contained in a plane perpendicular to the interface, their cross product lies parallel to the interface and there is no extra half-plane in the direction of the substrate or the layer. The orientation which the dipole adopts is a low energy configuration since there is no extra half-plane in the layer from one of the dislocations which would increase misfit strain.

Dislocation dipoles lying in <112> and <110> directions have been observed by Holt and Dangor[21] in germanium, but they were unable to determine the Burgers vectors. Dipoles have been observed in (001)CdTe/GaAs grown by HWE by Hobbs et al.[22], who identified the dipoles as having <211> line directions and (ao/2)<110> Burgers vectors with {111} glide planes; the dipoles are, therefore, comprised of two 30° type dislocations with opposite Burgers vectors. Hobbs et al. suggested a formation mechanism for the dipoles which involved glide on the {111} planes. The mechanism presumed that dislocations of opposite Burgers vectors pass each other on parallel glide planes. Their opposite Burgers vectors result in an attractive interaction which tends to elongate them along the <211> direction. In the absence of climb, annihilation cannot occur since the dislocations are on different glide planes. An analogous mechanism, (illustrated in figure 7.13) could operate for the dipoles observed in this study although glide on the less common {110} plane is required. Glide on {110} planes has been observed by Albrecht et al.[23] in Ge(Si) on (001)Si and by Bonar et al.[24] in (Al)GaAs/$In_xGa_{(1-x)}As$/GaAs(001) both of which are relatively high misfit systems (3.6% and 2.9% respectively). Theoretical calculations of the elastic energy of straight dislocations in face centred cubic crystals for a variety of line directions and Burgers vectors have been made by Foreman[25], he found

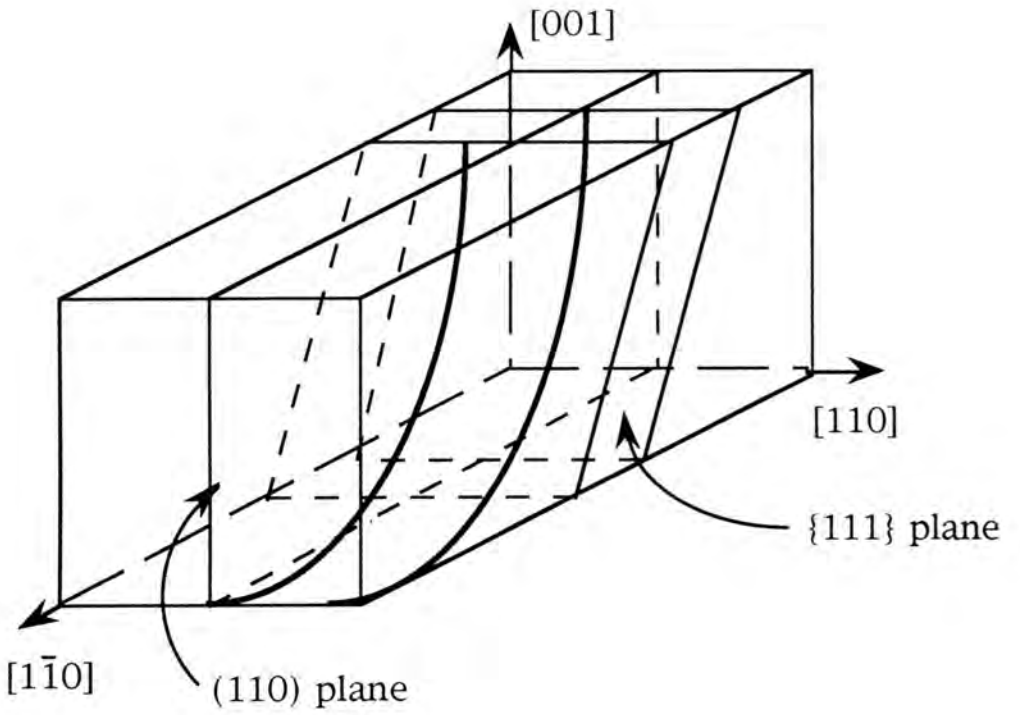

Figure 7.13 Model for the formation of dislocation dipoles observed in plan view TEM. The model is analogous to one proposed by Hobbs et al.[22] for 30° type dislocation dipoles. The Burgers vectors of the dipole are $\pm[1\bar{1}0]$, the slip plane is (110).

that dislocation energy was least for {110} planes but that dislocation core effects and dissociation on close packed {111} planes may be important factors in determining the plane in which glide occurs. Albrecht et al.[26] have made calculations for the introduction of misfit dislocations by half-loop glide on {110} planes and have found that for misfits > 6%, <112> threading segments on {110} glide planes are a more favoured orientation than glide on {111}. In the present study of CdTe/GaAs, the misfit is 14.6%, which is much greater than the lower limit for {110} glide suggested by Albrecht and co-workers.

The most obvious reason for the dipoles to adopt the unusual {110} glide plane is simply that it results in no extra half-plane in the layer compared to a line direction in the {111} glide plane which would increase misfit strain in the vicinity of the dipole (although this would be minimised by the close proximity of a dislocation of opposite character). Any energetic advantage of the more closely packed {111} glide plane for lower dislocation core energies and dissociation into partial dislocations is probably outweighed by the increase in misfit strain which would also occur.

The mechanism by which dislocations with opposite Burgers vectors are formed has not been ascertained, but since the dipoles tend to occur in isolated regions it may be due to the initial state of the GaAs substrate surface and the size and strain state of the islands nucleated during three-dimensional growth. The etching, rinsing, drying and pre-bake of the substrate prior to growth may lead to inhomogeneities in the GaAs surface; indeed anomalous regions of growth having poor surface morphology were observed and put down to poor substrate preparation.

In the PTEM and XTEM studies of CdTe/GaAs presented in Sections 7.3 and 7.4, 30°, 60° and screw type dislocations were observed. In most studies of semiconductor layers, the most common dislocations observed are of 60° type (see for example reviews by Hull and Bean[27] and by Beanland et al.[28]). 60° dislocations are said to arise by glide of half-loops on {111} planes (Section 2.2). In the case of high misfit systems, particularly when growth proceeds in a three-dimensional mode, Lomer dislocations are thought to be

generated at the edges of islands with 60° misfit dislocations and threading dislocations being formed when islands meet[29] (Section 2.3). It is anticipated that 60° misfit dislocations with their Burgers vectors inclined to the interface in <110> directions can be forced out of the interface by the high misfit strain on meeting other misfit dislocations or an island edge, thereby forming a threading segment. Both <110> and <211> are low energy line directions[30] and are expected to be the favoured orientations of the threading segments; their geometry is shown schematically in figure 7.14. For a given line direction there are two possible Burgers vectors which have not been determined explicitly for individual dislocations in this study.

It is not unusual for 30° dislocations to occur in high misfit systems: they have been observed by Tamura et al.[31] in MBE grown, indium doped GaAs/Si, by Shiba et al.[32] in MOVPE grown GaAs/Si and by Hobbs et al.[22] in HWE grown CdTe/GaAs. 30° dislocations have also been observed in bulk silicon by Patel[33] and by Geach et al.[34] who have also observed them in bulk germanium. The most extensive investigation of such dislocations has been performed by Tamura et al.[31] who studied the relative numbers of threading dislocations with <112> and <011> line directions by tilting about [110] and [1$\bar{1}$0]. They found that 30° threading dislocations along <112> were the most dense followed by 60° type along <110> and screw type along [001].

The effect of the tilt components of dislocations was used extensively in Chapters 5 and 6 to estimate the threading dislocation density in epilayers from HRXRD FWHM using the formula of Gay et al.[35]. It was assumed in these calculations that the threading dislocations had the same Burgers vector tilt component as a 60° misfit dislocation. In Section 2.2.2, the misfit, tilt and rotate components of a 60° misfit dislocation were calculated, a similar procedure will now be carried out for 30°, 60° and screw type threading dislocations. For reference and clarity, the effects of edge and screw components of a dislocation parallel and perpendicular to the heterointerface are illustrated in figures 7.15a-d.

A diagram of a 30° threading dislocation is shown in figure 7.16. It can be seen that the Burgers vector can be resolved into one screw component $\mathbf{b}_S$

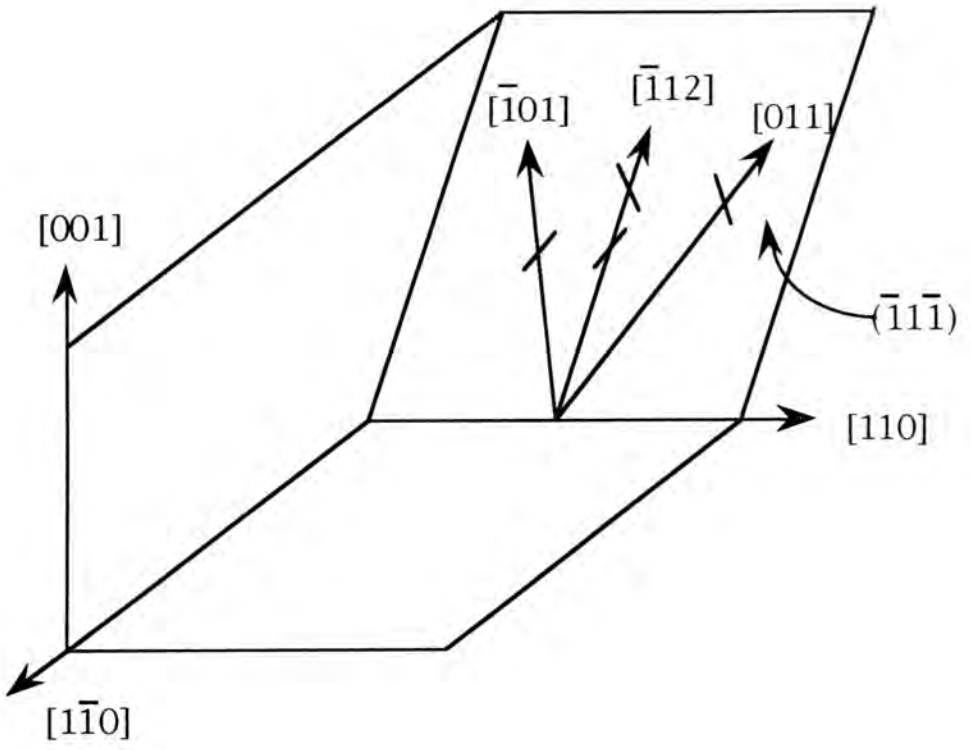

Figure 7.14 Geometry of 30°, 60° and screw type threading dislocations. Short lines represent Burgers vector directions. Burgers vectors are not shown for screw dislocations since the Burgers vector and line direction are parallel in this case.

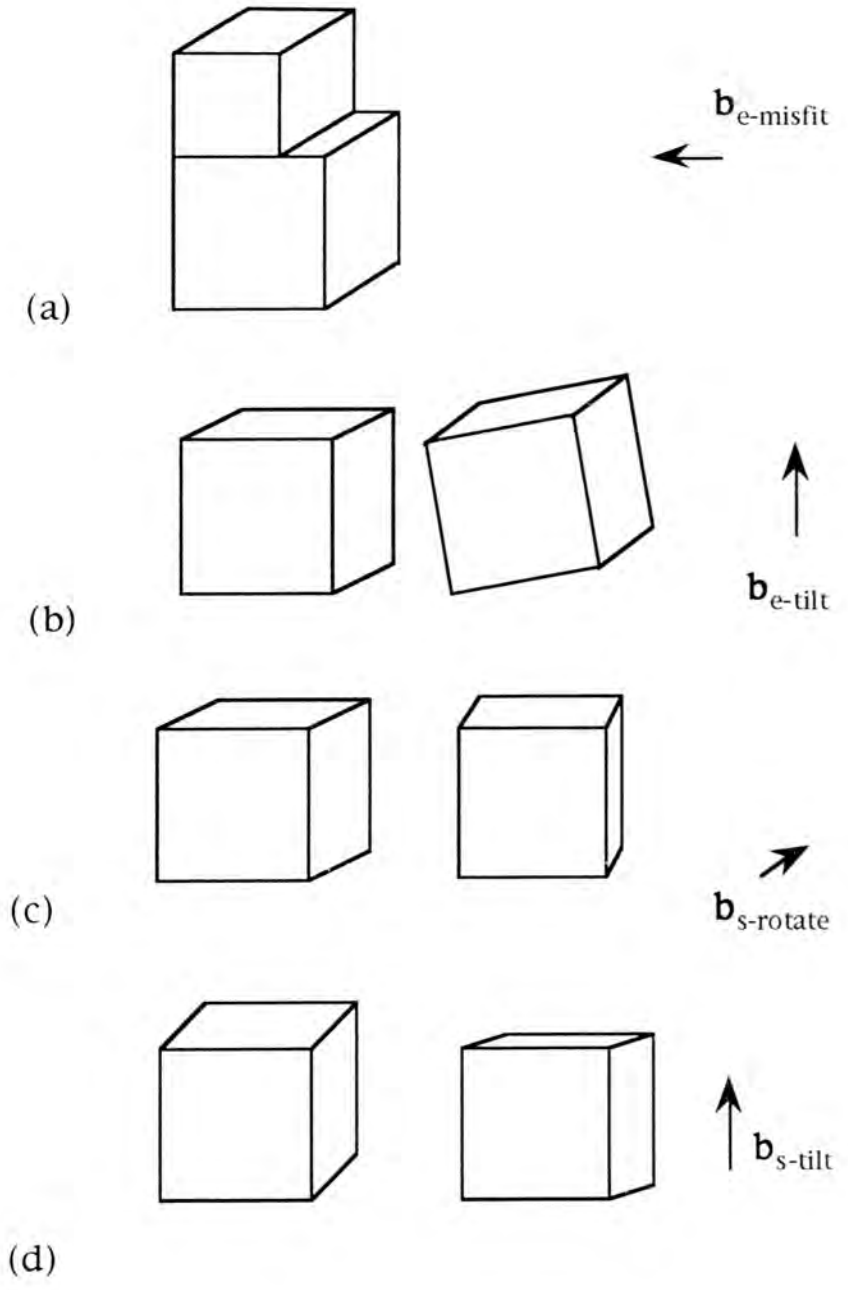

Figure 7.15 Effects of Burgers vector components parallel and perpendicular to the interface. (a) Edge component parallel to the interface relieves misfit strain, note that this figure shows relief of *tensile* strain. (b) Edge component perpendicular to the interface causes lattice tilts. (c) Screw component parallel to the interface causes a relative rotation of the layer with respect to the substrate. (d) Screw component perpendicular to the interface causes lattice tilts due to rotation.

and one edge component $\mathbf{b}_{e1}$. The edge component $\mathbf{b}_{e1}$ lies parallel to the interface and therefore relieves misfit strain. The screw component $\mathbf{b}_s$ is inclined to the interface and can be resolved further into components parallel and perpendicular to the interface ($\mathbf{b}_{s\text{-rotate}}$ and $\mathbf{b}_{s\text{-tilt}}$ respectively). The magnitudes of each component are summarised in table 7.7 along with those for 60° and screw type threading dislocations and 60° misfit dislocations.

A diagram of a 60° threading dislocation is shown in figure 7.17. The Burgers vector can be resolved into one screw component, $\mathbf{b}_s$ and two edge components, $\mathbf{b}_{e1}$ and $\mathbf{b}_{e2}$. The component $\mathbf{b}_{e2}$ is parallel to the interface and relieves misfit strain while both $\mathbf{b}_{e1}$ and $\mathbf{b}_s$ must be resolved into components parallel and perpendicular to the interface. The two Burgers vector components parallel to the interface are in opposite directions and therefore cancel with each other. The two components perpendicular to the interface both produce lattice tilts although one results from a twisting action ($\mathbf{b}_{s\text{-tilt}}$) while the other comes from a tilting action ($\mathbf{b}_{e\text{-tilt}}$). The magnitudes of the Burgers vector components are summarised in table 7.7.

A diagram of a screw type threading dislocation is shown in figure 7.18. The Burgers vector can be resolved into two screw components, one parallel to the interface, ($\mathbf{b}_{s\text{-rotate}}$) resulting in a rotation of the layer and one perpendicular to the interface, ($\mathbf{b}_{s\text{-tilt}}$) which results in a tilt of the layer. The magnitudes of the Burgers vector components are summarised in table 7.7.

Comparison of the sum of the tilt components given in table 7.7 shows that all four dislocations under consideration have the same magnitude of Burgers vector tilt component. The assumption made in calculating threading dislocation density from HRXRD FWHM, that the tilt component of the Burgers vector was of magnitude $a_o/2$, is therefore valid.

In developing the model by Tatsuoka et al.[36,37], Durose and Tatsuoka[38] proposed that misfit strain was relieved by threading dislocations rather than by 60° dislocations parallel to the interface (Section 5.3.1). They

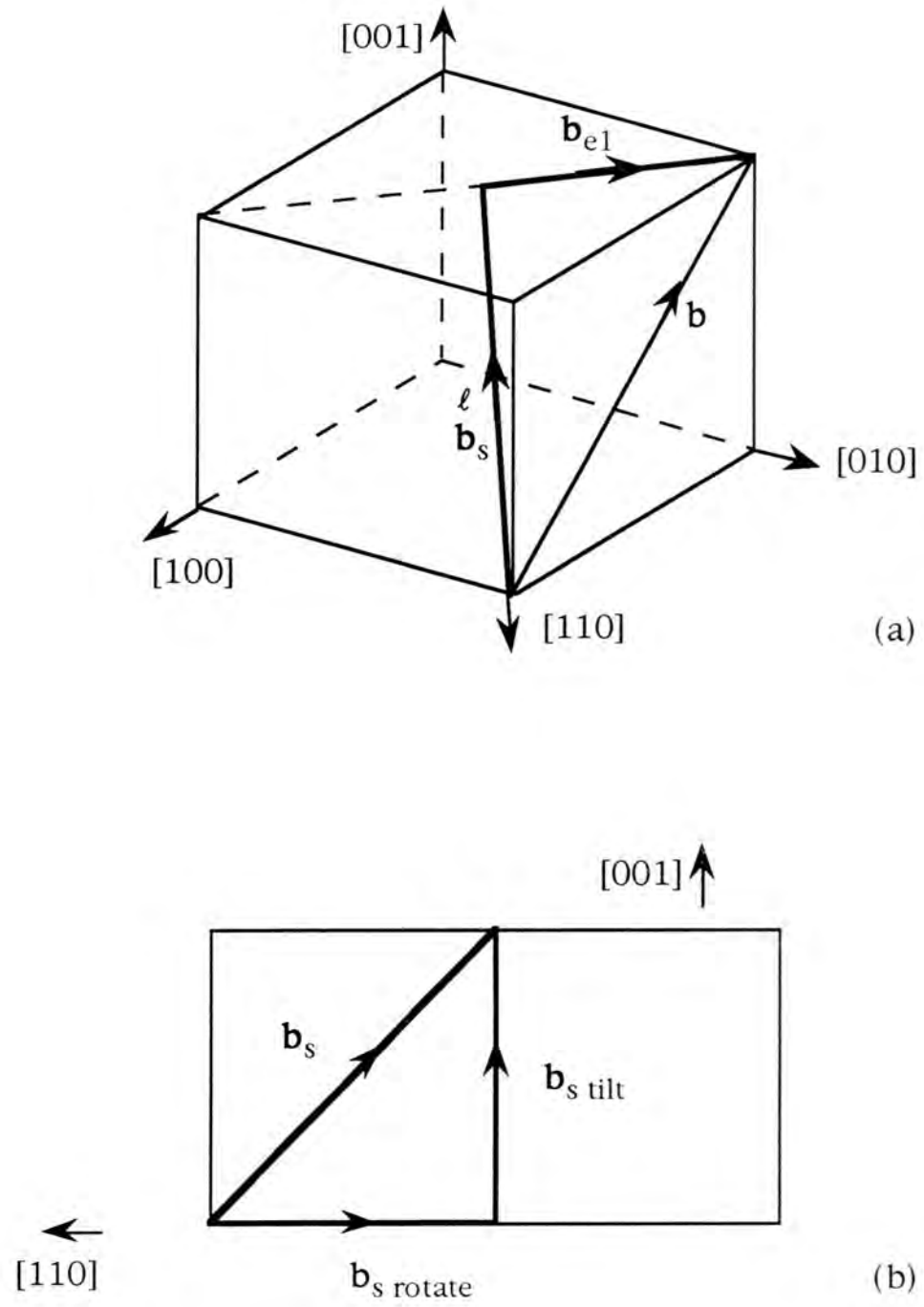

Figure 7.16 Burgers vector components of a 30° threading dislocation. (a) the Burgers vector can be resolved into one screw component, $\mathbf{b}_s$ and one edge component, $\mathbf{b}_{e1}$ which relieves misfit. (b) the screw component can be further resolved into tilt, $\mathbf{b}_{s\text{-tilt}}$ and rotate, $\mathbf{b}_{s\text{-rotate}}$ components. The magnitudes and directions of the components are summarised in table 7.7.

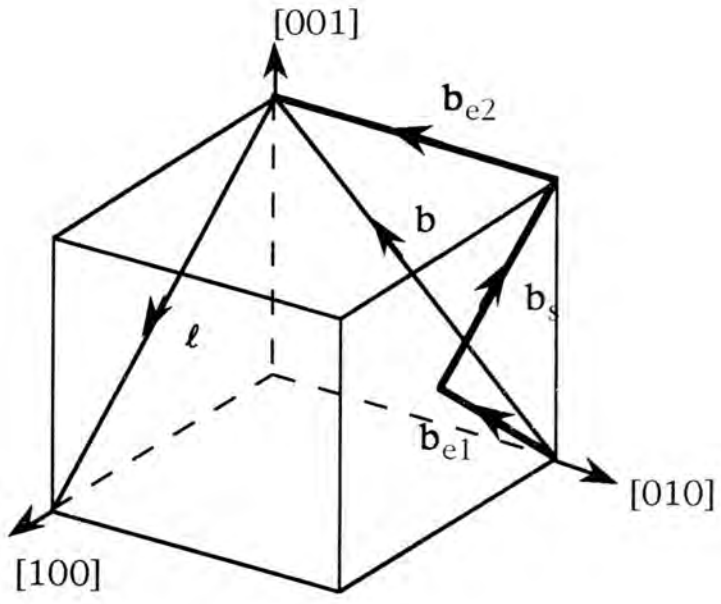

(a)

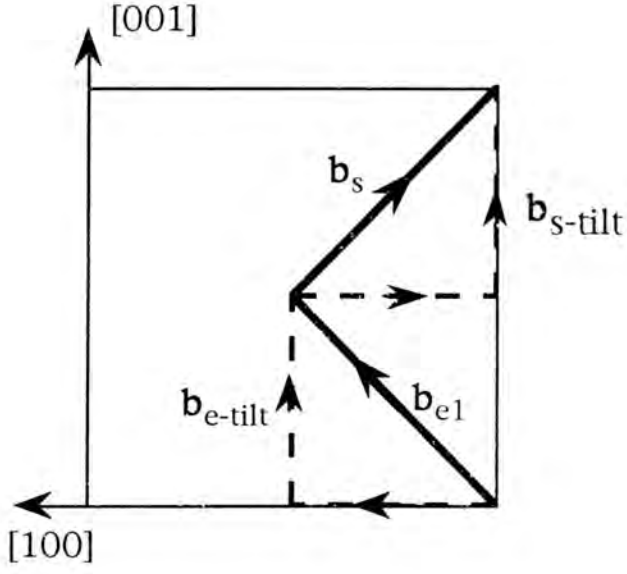

(b)

Figure 7.17 Burgers vector components of a 60° threading dislocation. (a) the Burgers vector can be resolved into one screw component, $\mathbf{b}_s$ and two edge components, $\mathbf{b}_{e1}$ and $\mathbf{b}_{e2}$. The edge component $\mathbf{b}_{e2}$ relieves misfit. (b) the components $\mathbf{b}_{e1}$ and $\mathbf{b}_s$ can be further resolved into components parallel and perpendicular to the interface, two components cancel, leaving two tilt components, $\mathbf{b}_{s\text{-tilt}}$ and $\mathbf{b}_{e\text{-tilt}}$. The magnitudes and directions of the components are summarised in table 7.7.

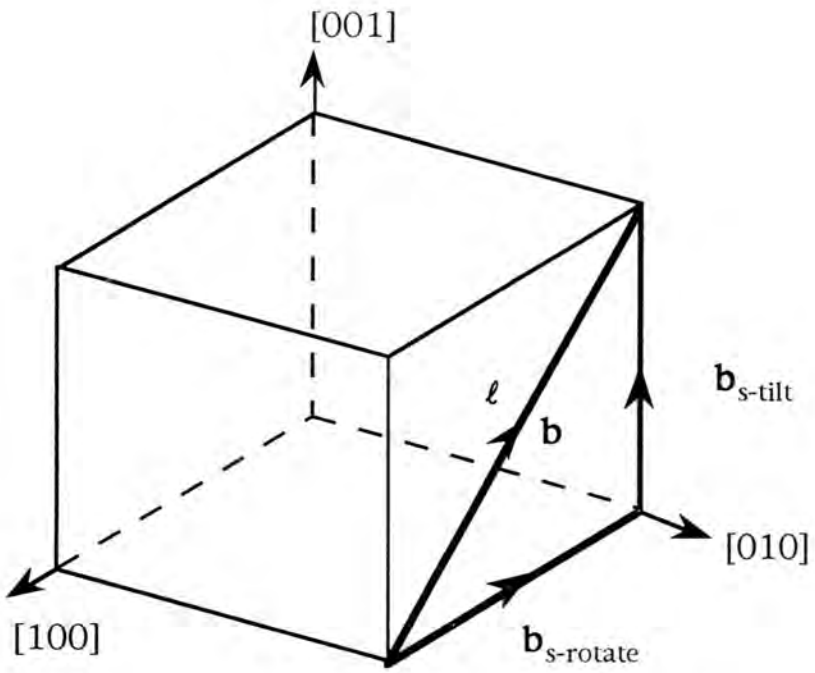

Figure 7.18 Burgers vector components of a screw type threading dislocation. The Burgers vector can be resolved into two components, $\mathbf{b}_{s\text{-tilt}}$ and $\mathbf{b}_{s\text{-rotate}}$, which produce layer tilt and rotation respectively. The magnitudes and directions of the components are summarised in table 7.7.

assumed that the threading dislocations had the same misfit relieving component ($b_{e\text{-misfit}}$) as 60° misfit dislocations. From table 7.7 it can be seen that only 30° threading dislocations have the same misfit relieving properties as 60° misfit dislocations. Screw dislocations relieve no misfit, while 60° threading dislocations have a larger $b_{e\text{-misfit}}$ than 60° misfit dislocations, this can be seen by comparing figures 2.4 and 7.17. Although the relative numbers of 30°, 60° and screw type threading dislocations were not determined for the CdTe/GaAs epilayers investigated in this study, both Hobbs et al.[22] and Tamura et al.[31] have found that the majority of threading dislocations are of 30° type for CdTe/GaAs and GaAs/Si respectively. If the majority of threading dislocations are of 30° type and if 60° and screw type threading dislocations occur in approximately equal numbers, then the average strain relief afforded by a threading dislocation is likely to be approximately the same as that of a 60° misfit dislocation, and the assumption made by Durose and Tatsuoka[38] is valid.

The reason why 60° threading dislocations bend over into the plane of a heterointerface despite $b_{e\text{-misfit}}$ decreasing in the process, can be explained by considering the effect of threading and misfit dislocations on the strain in the entire layer. A misfit dislocation relieves strain in the whole layer since it lies at the heterointerface. A threading dislocation also relieves all of the layer above it, but as the threading dislocation propagates further from the interface, the volume of layer which experiences strain relief decreases. The overall strain relief afforded by a threading dislocation over the entire thickness of the layer, is less per unit length than for a dislocation with a smaller strain relieving Burgers vector which lies in the interface. Also, by bending over at the heterointerface, the total dislocation length increases, since the threading arm of the misfit dislocation is the same length as a straight threading dislocation (this can be seen in figure 2.2). Therefore, additional strain relief is afforded by extending the dislocation in the interface.

Component	Threading dislocations						Misfit dislocations	
	30°		60°		Screw		60°	
	Magnitude	Direction	Magnitude	Direction	Magnitude	Direction	Magnitude	Direction
b_s	$a_o\sqrt{3}/2\sqrt{2}$	<211>	$a_o/2\sqrt{2}$	<110>	$a_o/\sqrt{2}$	<110>	$a_o/2\sqrt{2}$	<110>
b_{e1}	$a_o/2\sqrt{2}$	<110>	$a_o/2\sqrt{2}$	<110>	NONE		$a_o/2\sqrt{2}$	<110>
b_{e2}	NONE		$a_o/2$	<001>	NONE		$a_o/2$	<001>
b_{e_misfit}	$a_o/2\sqrt{2}$	<110>	$a_o/2$	<001>	NONE		$a_o/2\sqrt{2}$	<110>
b_{s_rotate}	$a_o/2\sqrt{2}$	<110>	NONE		$a_o/2$	<001>	$a_o/2\sqrt{2}$	<110>
b_{s_tilt}	$a_o/2$	<001>	$a_o/4$	<001>	$a_o/2$	<001>	NONE	
b_{e_tilt}	NONE		$a_o/4$	<001>	NONE		$a_o/2$	<001>
Σb_{tilt}	$a_o/2$	<001>	$a_o/2$	<001>	$a_o/2$	<001>	$a_o/2$	<001>

Table 7.7 Summary of Burgers vector components of 30°, 60° and screw type threading dislocations and 60° type misfit dislocations. In the main body of the text, the convention is, for example, $(a_o/2)$<110> for the most common Burgers vector. In this notation the vector <110> is taken to have a magnitude and a direction. In the table above, the total magnitude of the Burgers vector is given with the line direction being a unit vector. The effects of the components on the epitaxial layer are summarised in figures 7.15a-d. b_s, b_{e1} and b_{e2} are the screw and two edge components of each Burgers vector respectively, $b_{e\text{-misfit}}$ and $b_{s\text{-rotate}}$ are the edge and screw components resolved parallel to the interface, $b_{s\text{-tilt}}$ and $b_{e\text{-tilt}}$ are the screw and edge components resolved perpendicular to the interface, and Σb_{tilt} is the sum of $b_{s\text{-tilt}}$ and $b_{e\text{-tilt}}$.

Anisotropy in dislocation structure has been observed by TEM for many epitaxial layers, for example by Brown et al.[39] in MOVPE grown ZnTe/GaAs, by Diamond[40] in MBE grown CdTe-$Cd_xMn_{(1-x)}Te$ heterostructures, by Cheng et al.[14] in MOVPE grown CdTe/GaAs, by Zhu and Carter[41] in MBE grown GaAs/Si and by Lefebvre and Ulhaq-Bouillet[42] in MBE grown $In_xGa_{(1-x)}As$/GaAs heterostructures. Anisotropy in HRXRD FWHM has been observed for $Cd_xHg_{(1-x)}Te$/CdTe/GaAs by Barnett et al.[43] and by Bodin et al.[44] for $Cd_xMn_{(1-x)}Te/Cd_yZn_{(1-y)}Te$. The anisotropy in FWHM can be attributed to different densities of dislocations in the two orthogonal <110> projections. Several reasons for the asymmetric dislocation content of epitaxial layers within the sphalerite structure have been discussed by Fox and Jesser[45]. The reasons they considered were (i) substrate misorientation, (ii) thickness gradient of the epitaxial layer, (iii) differences in the nucleation barrier to form the two arrays of dislocations and (iv) differences in the Peierls barrier to move the two arrays of dislocations. Each of these possibilities will be considered for the layers investigated in earlier sections.

Misorientation of the substrate leads to an unequal resolved shear stress which favours one of the two glide systems, which leads to an asymmetric dislocation array. This was the reason suggested by Cheng et al.[14] for the occurrence of 60° misfit dislocations in only one <110> direction and of only one type. This anisotropy also resulted in a large tilt offset between the substrate and the layer. Substrates are misoriented in order to produce surface steps at which edge type misfit dislocations can nucleate; edge type dislocations are twice as effective as 60° dislocations in relieving misfit and therefore only half as many are required to relieve a given misfit. This method of dislocation reduction was discussed in Section 2.4. The substrates used in this study had surface normals misoriented 3.5° about [010] towards $[\bar{1}00]$, there is therefore equal offcut in both <110> directions (figure 7.19). This offcut will not result in anisotropy between the two <110> directions but might result in one of the two {111} glide planes being favoured in each <110> direction, i.e. anisotropy within each <110> direction but not anisotropy between them.

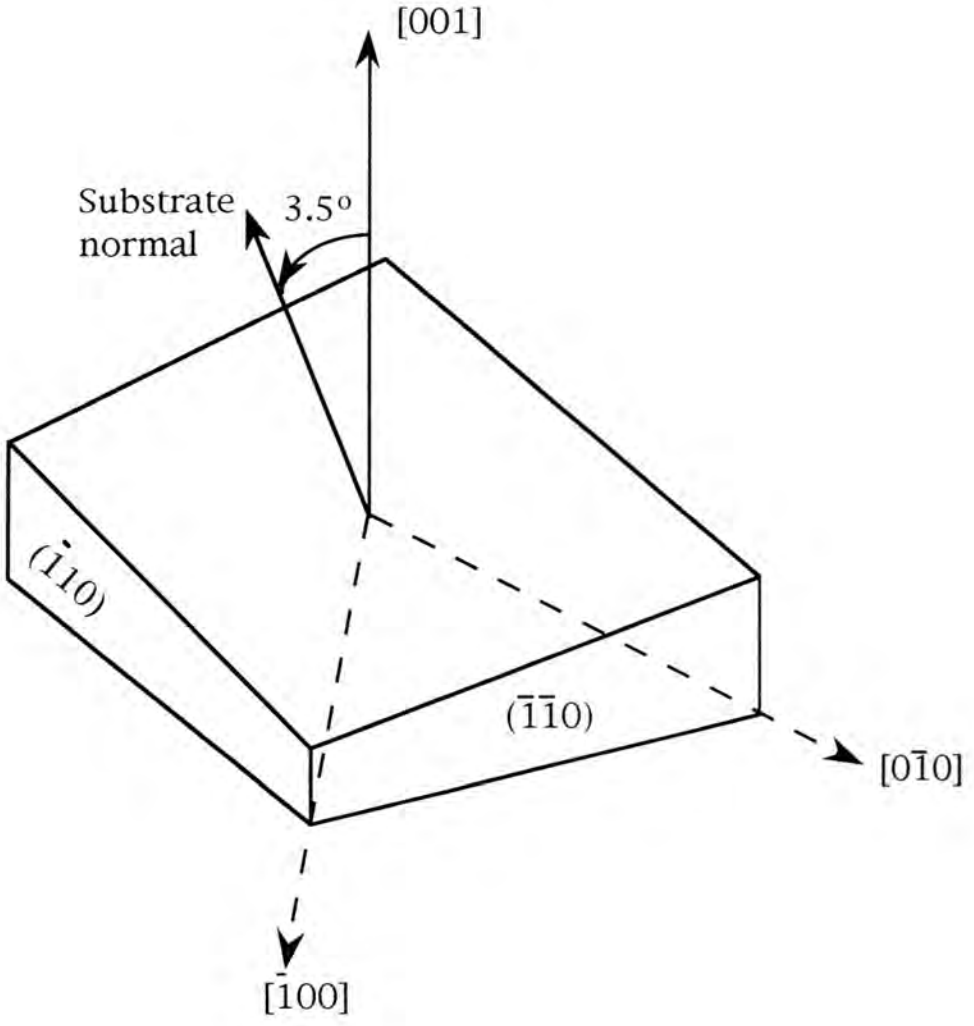

Figure 7.19 Schematic diagram of the substrate offcut used for layers examined in Chapter 7. The substrate normal is tilted 3.5° about [010] towards [$\bar{1}$00]. There is equal offcut in both orthogonal <110> directions in the interface.

The effect of a thickness gradient on defect structure was considered by Fox and Jesser since it gave rise to preferential nucleation of dislocations in thicker regions followed by glide to thinner areas. They found the same anisotropy between [110] and [1$\bar{1}$0] on rotation of the substrate by 90° in the growth chamber. In addition, for a high misfit system which displays three-dimensional growth, dislocations are formed at the edges of islands and the nucleation of dislocations at "thicker" regions is not meaningful in this case.

Before considering the differences in the nucleation barrier to form dislocations in the [110] and [1$\bar{1}$0] projections and the differences in the Peierls barrier to move the two arrays of dislocations, the reason why the differences occur should be clarified. In Section 2.5, the anisotropy of the sphalerite lattice was reviewed along with the different types of dislocations which may occur according to the nature of the dislocation core. It has already been explained that for relief of compressive misfit strain, dislocations must have an extra half-plane pointing into the substrate. In this work, it will be assumed that dislocations are of the glide set rather than the shuffle set[45-47]. For an α type dislocation (Cd core for glide set), the extra half-plane ends on a {111}A directed plane (i.e. (111), ($\bar{1}$1$\bar{1}$), ($\bar{1}\bar{1}$1) or (1$\bar{1}\bar{1}$)); for a β type dislocation (Te core for glide set), the extra half-plane ends on a {$\bar{1}\bar{1}\bar{1}$}B directed plane (i.e. ($\bar{1}\bar{1}\bar{1}$), (11$\bar{1}$), (1$\bar{1}$1) or ($\bar{1}$11)). Assuming that only dislocations with extra half-planes into the substrate occur, dislocations observed in the two <110> directions will be of different type and are expected to have different energies of nucleation and different Peierls barriers. The α and β dislocations with extra half-planes towards the substrate for the two orthogonal projections are illustrated in figure 7.20.

It is unlikely that the difference in nucleation energy of α and β dislocations will lead to a large anisotropy in misfit dislocation type for high misfit layers which display three-dimensional growth. This is because most of the misfit dislocations are formed at the edges of islands where nucleation is favoured[48]; this enhancement in nucleation occurs for both types of dislocation.

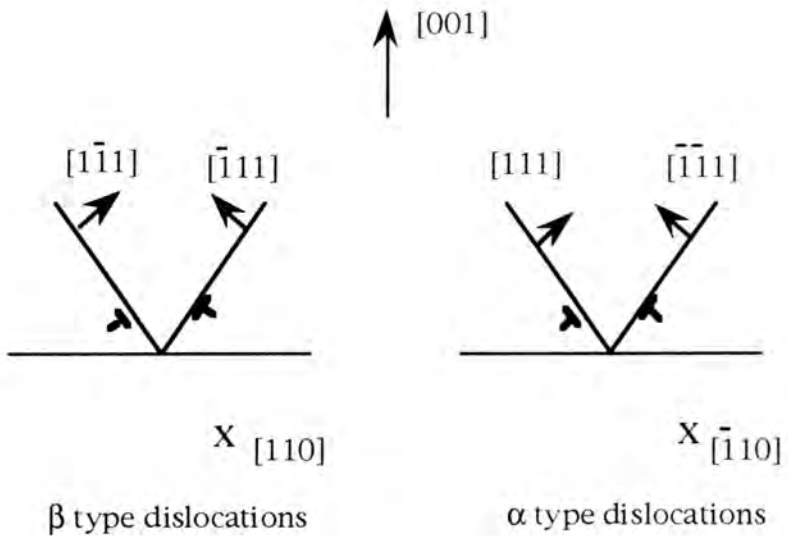

Figure 7.20 Diagram to show that for a layer in compression where dislocations have an extra half-plane pointing towards the substrate, dislocations are of different type in the two orthogonal <110> directions.

More important than the types of misfit dislocations which occur at the interface are the mechanisms by which dislocations are forced out of the interface into threading orientations, and the reactions which occur between threading dislocations. The difference in Peierls energy of α and β dislocations is the most likely cause of the different geometries of the extended dislocation network above the interface observed in the two orthogonal <110> directions. In the [110] projection, the dislocation structure is ordered and the dislocation density falls off rapidly with increasing thickness. In the [$\bar{1}$10] projection, the dislocation structure is tangled and extends much further into the layer before the dislocation density decreases significantly. A similar difference in dislocation geometry has been observed for ZnTe/GaAs epilayers by Brown et al.[39]. Keir et al.[6] reported an anisotropy in $Cd_xHg_{(1-x)}Te$/CdTe/GaAs HRXRD FWHM along projected beam directions of [110] (broad rocking curves) and [$\bar{1}$10] (narrow rocking curves). It should be noted that the more extended dislocation network observed in [$\bar{1}$10] XTEM projection will result in a broader mosaic spread being sampled for [110] X-ray beam projection as has been observed by Keir et al. The HRXRD data presented in Chapters 6 and 8 were collected for an X-ray beam direction of [$\bar{1}$00] when projected onto the interface, therefore both <110> directions were sampled equally.

Work by Brown[49] on II-VI layers under compression explained anisotropic twinning in terms of the difference in mobility of α and β dislocations. His work suggested that α type dislocations are the more mobile, which agrees with findings for the III-V materials InSb, InAs, GaSb and GaAs[47]. If α type dislocations are the more mobile, then threading dislocations observed in [$\bar{1}$10] projection on advancing {111}A planes will be more mobile than their counterparts observed in [110] projection. If being more mobile, α dislocations are more easily influenced by fluctuations in strain near the interface and neighbouring dislocations, then they are more likely to be bent over into less common orientations as is indeed found in [$\bar{1}$10] projection. The difference in mobility can, therefore, explain the more tangled dislocation structure observed in [$\bar{1}$10] projection, but it does not explain the extent to which the dislocations propagate into the layer.

7.6 Conclusions

HRXRD and the displacement of Kikuchi lines in PTEM have revealed large tilts between subgrains. The largest tilt recorded was 2.1°, for a 2μm thick CdTe/GaAs layer. The two subgrains had approximately the same HRXRD FWHM and it was concluded, therefore, that subgrains misoriented by a large angle with respect to each other are composed of a mosaic spread of small domains oriented about a mean position.

DCXRT and PTEM were used to measure the size of the small domains (mosaic spread) which result in the broadening of X-ray rocking curves. The tilt domains in a 0.6μm thick CdTe/GaAs layer measured by PTEM were found to be approximately 0.5-1μm in diameter, compared with 20-40μm in a 25μm thick layer, as measured by DCXRT. The relationship between tilt domain size and mosaic spread (as measured by HRXRD) was found to agree with a model by Turnbull[9] based on the random alignment of dislocation Burgers vectors. Turnbull's model predicts that smaller tilt domains will give rise to a larger standard deviation of tilt i.e. a broader mosaic spread.

Subgrain tilts with a favoured direction were observed for a small region of a 25μm thick (001)CdTe/GaAs layer. The subgrains were tilted in the same direction as the substrate offcut in agreement with some published data for GaAs/Si[13] but in disagreement with models proposed by Schowalter et al.[11] and by Ayers et al.[12].

Dislocation dipoles with <112> line directions and ±[110] Burgers vectors were observed in CdTe/GaAs epilayers by PTEM. The glide planes of the dipoles are {110} and are perpendicular to the interface. In this orientation the dipoles, whose two dislocations have opposite Burgers vectors, have no extra half-plane pointing towards or away from the interface. In this orientation, the dislocation Burgers vector has no misfit component and it is assumed that this is the reason for the dipole adopting this orientation.

In PTEM and XTEM studies of CdTe/GaAs, 30°, 60° and screw type threading dislocations were observed, all of which had $(a_0/2)<110>$ Burgers vectors. The 60° and screw type dislocations had <110> line directions while the 30° type had <211> line directions. 30° dislocations have been previously reported in In doped GaAs/Si[31], GaAs/Si[32], and CdTe/GaAs[22].

A comparison of the misfit relieving components and the sum of the tilt components of 30°, 60° and screw type threading dislocation and 60° type misfit dislocations has been made. All four dislocations under consideration were found to have the same magnitude of tilt component. The assumption made in Chapters 5 and 6, that a threading dislocation has the same Burgers vector tilt component as a 60° misfit dislocation is therefore valid. Only 30° threading dislocations have the same misfit relieving properties as 60° misfit dislocations; 60° threading dislocations relieve more misfit strain while screw type threading dislocations relieve none. The assumption in Section 5.3.1 of the average misfit relief afforded by a threading dislocation being approximately equal to that of a 60° dislocation is valid.

An anisotropy in the geometry of threading dislocations was observed in the two orthogonal <110> directions. In the [110] projection, the dislocation structure is ordered and the dislocation density falls off rapidly with increasing layer thickness. In the $[\bar{1}10]$ projection, the dislocation structure is tangled and extends much further into the layer before the dislocation density decreases significantly. It is thought that this difference in geometry is due to the different mobilities of α and β dislocations in the sphalerite lattice, although this does not explain the greater thickness to which the tangle extends in the case of the $[\bar{1}10]$ projection.

REFERENCES FOR CHAPTER 7

1. Burgers J. M., *Proc. Phys. Soc. (London)* **52**, (1940), 23.

2. Vogel F. L., Pfann W. G., Corey H. E. and Thomas E. E., *Phys. Rev.* **90**, (1953), 489.

3. Durose K., Turnbull A. and Brown P., *Mat. Sci. Eng.* **B16(1-3)**, (1993), 96.

4. Ponce F. A., Anderson G. B. and Ballingall J. M., *Surf. Sci.* **168**, (1986), 564.

5. Cullis A. G., Chew G., Irvine S. J. C. and Giess J., *Inst. Phys. Conf. Ser.* **87**, Section 2, (1987), 141.

6. Keir A. M., Graham A., Barnett S. J., Giess J., Astles M. G. and Irvine S. J. C., *J. Cryst. Growth* **101**, (1990), 572.

7. Barnett S. J., Ph. D. Thesis, *Structural Characterisation of Semi-insulating LEC Gallium Arsenide*, University of Durham (1987).

8. Brown G. T., Keir A. M., Giess J., Gough J. S. and Irvine S. J. C., *Inst. Phys. Conf. Ser.* **100**, Section 6, (1989), 457.

9. Turnbull A., Ph. D Thesis, *Relaxation in Epitaxial Layers of III-V Compounds*, University of Durham (1992).

10. Nagai H., *J. Appl. Phys.* **45**, (1974), 3789.

11. Schowalter L. J., Hall E. L., Lewis N. and Hashimoto S., *Thin Solid Films* **184**, (1990), 437.

12. Ayers J. E., Ghandhi S. K. and Schowalter L. J., *J. Cryst. Growth* **113**, (1991), 430.

13. Yao T., Okada Y., Kawanami H., Matsui S., Imagawa A. and Ishida K., *Mat. Res. Soc. Symp. Proc.* **91**, (1987), 63.

14. Cheng T. T., Aindow M., Jones I. P., Hails J. E., Williams D. J. and Astles M. G., *J. Cryst. Growth* **135**, (1994), 409.

15. Kay D. H., Ed., *Techniques for Electron Microscopy*, (Blackwell Scientific Publications, Oxford, 1965) .

16. Hull D. and Bacon D. J., *Introduction to Dislocations*, (3rd edition), Pergamon Press, 1989International Series on Materials Science and Technology, volume 37, chapter 1.

17. Schwartzman A. F. and Sinclair R., *J. Elec. Mat.* **20(10)**, (1991), 805.

18. Howie A. and Whelan M. J., *Proc. Roy. Soc. London* **A267**, (1962), 206.

19. Brown P. D., Durose K., Russell G. J. and Woods J., *J. Cryst. Growth* **101**, (1990), 211.

20. Gatos H. C. and Lavine M. C., *J. Electrochem. Soc.* **107**, (1960), 427.

21. Holt D. B. and Dangor A. E., *Phil. Mag.* **8**, (1963), 1921.

22. Hobbs A., Ueda O., Sugiyma I. and Takigawa H., *J. Cryst. Growth* **117**, (1992), 475.

23. Albrecht M., Strunk H. P., Hansson P. O. and Bauser E., *J. Cryst. Growth* **128**, (1993), 327.

24. Bonar J. M., Hull R., Walker J. F. and Malik R., *Appl. Phys. Lett.* **60(11)**, (1992), 1327.

25. Foreman A. J. E., *Acta Metallurgica* **3**, (1955), 322.

26. Albrecht M., Strunk H. P., Hull R. and Bonar J. M., *Appl. Phys. Lett.* **62(18)**, (1993), 2206.

27. Hull R. and Bean J. C., *Critical Reviews in Solid State and Materials Science* **17(6)**, (1992), 507.

28. Beanland R., Dunstan D. J. and Goodhew P. J., *in preparation* , .

29. Eaglesham D. J., Aindow M. and Pond R. C., *Mat. Res. Soc. Symp. Proc.* **116**, (1988), 267.

30. Hirth J. P. and Lothe J., *Theory of Dislocations*, McGraw-Hill, 1968.

31. Tamura M., Hashimoto A. and Sugiyama N., *J. Appl. Phys.* **70(9)**, (1991), 4770.

32. Shiba Y., Asai K., Kamel K. and Katahama H., *Jpn. J. Appl. Phys.* **34**, (1995), 1466.

33. Patel J. R., *J. Appl. Phys.* **29(2)**, (1958), 170.

34. Geach G. A., Irving B. A. and Phillips R., *Research (London)* **10**, (1957), 411.

35. Gay P., Hirsch P. B. and Kelly A., *Acta Metallurgica* **1**, (1953), 315.

36. Tatsuoka H., Kuwabara H., Nakanishi Y. and Fujiyasu H., *Thin Solid Films* **201**, (1991), 59.

37. Tatsuoka H., Kuwabara H., Nakanishi Y. and Fujiyasu H., *J. Cryst. Growth* **117**, (1992), 554.

38. Durose K. and Tatsuoka H., *Inst. Phys. Conf. Ser.* **134**, Section 9, (1993), 581.

39. Brown P. D., Loginov Y. Y., Clifton P. A., Simmons M. Y., Mullins J. T., Al-Allak H. M., Kelly H., Durose K., Brinkman A. W., Wagner H. P., Kuhn W., Gebhardt W. and Humphreys C. J., *J. Cryst. Growth* **submitted for publication**, (1995).

40. Diamond S., Ph. D. Thesis, *Electron Microscopy of Cadmium Telluride-Cadmium Manganese Telluride Heterostructures*, University of Bristol (1991).

41. Zhu J. G. and Carter C. B., *Phil. Mag.* **A62(3)**, (1990), 319.

42. Lefebvre A. and Ulihaq-Bouillet C., *Phil. Mag. A* **70(6)**, (1994), 999.

43. Barnett S. J., Keir A. M. and Emeny M., *Semicond. Sci. Technol.* **7**, (1992), A158.

44. Bodin C., Cibert J., Grieshaber W., Dang L. S., Marcenat F., Wasiela A., Jouneau P. H., Feuillet G., Hervé D. and Molva E., *J. Appl. Phys.* **77(3)**, (1995), 1069.

45. Fox B. A. and Jesser W. A., *J. Appl. Phys.* **68(6)**, (1990), 2739.

46. Alexander H., *J. de Physique (Paris) Colloque* **40**, (1979), C6-1.

47. Suzuki T., Takeuchi S. and Yoshinaga H., *Dislocation Dynamics and Plasticity*, Springer Series in Materials Science, 1985; **12**, chapter 7.

48. Guha S., Madhukar A. and Rajkumar K. C., *Appl. Phys. Lett.* **57(20)**, (1990), 2110.

49. Brown P. D., Ph. D Thesis, *Structural defects in II-VI epitaxial layers*, University of Durham (1988).

CHAPTER 8

Annealing of CdTe/GaAs Epilayers and Structural Quality of (CdHg)Te on CdTe/GaAs

8.1 Annealing Studies of CdTe/GaAs

8.1.1 Introduction

Various methods of reducing the threading dislocation density in high misfit epilayers were listed in Section 2.4. In Section 8.1.2 a more detailed review of the annealing of GaAs/Si will be presented and used to anticipate the conditions under which successful annealing of epitaxial CdTe may be carried out. In Section 8.1.3 a review of the annealing of bulk CdTe is presented from which the possible problems involved in the annealing of epitaxial material can be drawn. Annealing experiments on epitaxial CdTe/GaAs have been carried out both *in-situ* and *ex-situ* and the results are presented and discussed in Sections 8.1.4 and 8.1.5.

8.1.2 Review of annealing of GaAs/Si

Thermal annealing of GaAs/Si is a common procedure which has been found to be effective in the reduction of threading dislocation density[1]. Many different types of thermal anneal have been employed and, if annealing occurs at a significantly high temperature, all are effective. Results from several groups of workers will be presented, each of which have employed a different method of annealing. The work discussed in this section is summarised in table 8.1.

Yamaguchi et al.[2] have undertaken the *in-situ* annealing, under AsH_3, of MOVPE grown GaAs/Si using both single and multiple anneals at 800°C. The layer growth was terminated at a thickness of 2μm and the substrate cooled to near room temperature before being raised to 800°C for the times specified

in table 8.1. After annealing, the substrate was cooled to 700°C and growth was resumed. A further 2μm of GaAs was grown for the case of the single anneal. For the case of multiple annealing, a small thickness of GaAs was grown, the substrate was cooled to room temperature and was then heated to 800°C for the anneal time, after which the cycle was repeated. The final thickness of GaAs was 4μm in each case.

Yamaguchi et al.[2] commented that the improvement in structural quality resulting from thirteen anneal steps was remarkable; the etch pit density (EPD) dropped from $10^8 cm^{-2}$ to $3x10^6 cm^{-2}$ after 13 anneal steps. The effect of one anneal was less significant, with EPD reducing to approximately $4x10^7 cm^{-2}$. They observed a stepwise reduction in EPD for intermediate numbers of anneal steps. It appears that cooling down to room temperature played an important part in maximising the structural improvement in the GaAs/Si epilayers since a single anneal for 30 minutes gave no more improvement than one anneal for 5 minutes, but 6x5 minute anneals resulted in a greater improvement. Yamaguchi et al. noted most improvement for temperatures greater than 800°C and little improvement below 500°C.

Ayers et al.[3] have undertaken the *in-situ* annealing of MOVPE grown 1.5μm thick GaAs/Si layers under AsH_3 flow. The annealing was carried out at 850°C without cooling to room temperature prior to annealing. They found that increasing anneal time from 5 minutes to 15 minutes improved the layer quality further but that no further improvement occurred on annealing for more than 15 minutes. The improvement in structural quality on annealing was recorded by HRXRD with the FWHM decreasing from 470" to 290" for a 15 minute anneal.

Lee et al.[4] have annealed 3μm thick MBE grown GaAs/Si epilayers *ex-situ* under an arsenic overpressure at 850°C. The anneal time was 15 minutes and the structural improvement afforded was determined by HRXRD. The HRXRD FWHM decreased from 372" to 180" on annealing. The substrate was cooled down to room temperature before being raised to the annealing temperature.

2μm epilayers of GaAs grown on Si by MBE were annealed in sealed quartz ampoules under an arsenic overpressure at 1050°C for 100 seconds by Takagi et al.[5]. The substrate and layer were necessarily cooled to room temperature before being sealed in the quartz ampoule. The HRXRD FWHM decreased from 600" to 250" on annealing. They suggested that the reduction in threading dislocations density, which was confirmed by XTEM, was due to enhanced dislocation glide and climb at the elevated temperature; the concentration of vacancies also increased at the annealing temperature.

Deppe et al.[6] annealed 2μm thick, Zn-diffused MBE grown GaAs/Si epilayers in sealed quartz ampoules under an arsenic overpressure at 850°C for 30 minutes. The substrate and layer were cooled down to room temperature prior to being sealed in the ampoule. They found that the threading dislocation density observed by XTEM was significantly reduced and proposed that the climb motion of dislocations was enhanced by point defects produced by Zn-diffusion.

From the review above it seems that any annealing above the growth temperature will result in an improvement in structural quality for GaAs/Si. Most workers have cooled the specimen to room temperature after growth, to enable *ex-situ* annealing. However, Ayers et al. annealed the layers immediately after growth without cooling and, allowing for the difference in the thickness of the layers, found a similar improvement to Lee et al.. The literature data for annealing of GaAs/Si suggests that annealing of CdTe epilayers will be successful if a high enough temperature can be achieved. This will be discussed in the following sections.

Source of data	*In-situ* / *ex-situ*	Layer thickness /μm	Anneal temperature /°C	Anneal time	Number of anneals	Cool down before anneal?	Result of anneal	
							Before anneal	After anneal
Yamaguchi et al. ref 2	*In-situ* MOVPE reactor	4	800	30 min	1	YES	EPD $10^8 cm^{-2}$	EPD $4x10^7 cm^{-2}$
Yamaguchi et al. ref 2	*In-situ* MOVPE reactor	4	800	5 min	13	YES	EPD $10^8 cm^{-2}$	EPD $3x10^6 cm^{-2}$
Ayers et al. ref 3	*Ex-situ*	1.5	850	15 min	1	NO	HRXRD FWHM=470"	HRXRD FWHM=290"
Lee et al. ref 4	*Ex-situ*	3	850	15 min	1	YES	HRXRD FWHM=372"	HRXRD FWHM=180"
Takagi et al. ref 5	*Ex-situ*	2	1050	100 s	1	YES	HRXRD FWHM=600"	HRXRD FWHM=250"
Deppe et al. ref 6	Zn diffused *ex-situ*	2	850	30 min	1	YES	XTEM DD estimate	lower DD

Table 8.1 Summary of annealing of GaAs/Si. All annealing was carried out with an As overpressure. The structural improvement afforded by the annealing process was assessed by a decrease in the etch pit density (EPD), HRXRD FWHM or in threading dislocation density observed by XTEM.

8.1.3 Review of Annealing of Bulk CdTe

A very extensive study of phase equilibria of CdTe has been undertaken by de Nobel[7], and the equilibria for CdTe sublimation are given in equation 8.1. The concentration of gaseous CdTe species is negligible[8] and therefore sublimation can be effectively stopped by applying an overpressure of Cd or Te_2. According to de Nobel, the presence of an inert gas did not stop the sublimation of CdTe when a temperature gradient existed along the sealed ampoule. Atomic Cd and molecular Te_2 were able to diffuse along the ampoule and condense to form solid CdTe in the cooler regions of the ampoule. This drew the equilibria of equation 8.1 to the right, and resulted in further decomposition of CdTe.

$$CdTe_{(s)} \leftrightarrow CdTe_{(g)} \leftrightarrow Cd_{(g)} + \frac{1}{2} Te_{2\ (g)} \qquad \text{equation 8.1}$$

Annealing studies on CdTe substrates been carried out by Vydyanath et al.[9] and on bulk CdTe grown from the vapour phase by Loginov et al.[10]. In common with numerous other studies of annealed CdTe, an overpressure of Cd was employed. Arias et al.[11] found that annealing of $Cd_xHg_{(1-x)}Te$ on GaAs with a CdTe buffer layer under a Hg environment reduced the etch pit density.

Tatarenko et al.[12] have determined the sublimation activation energies of (001) and (111)B CdTe. They presented the sublimation rates of (001) and (111)B CdTe in $Å s^{-1}$ as a function of temperature. By extrapolation of their data, some rates of sublimation at temperatures above the MOVPE growth temperature for (001)CdTe have been estimated and are given in table 8.2.

From the available literature concerning the annealing of CdTe, it seems that a controlled environment is required to avoid sublimation of CdTe during annealing. In the following section, preliminary studies of the annealing of epitaxial CdTe are presented.

Temperature/°C	400	420	450	470
Sublimation rate/μm hr^{-1}	0.3	0.9	3.6	8.8

Table 8.2 Summary of sublimation rate of (001)CdTe without an overpressure of either constituent. Calculated by extrapolation of data by Tatarenko et al.[12].

8.1.4 Annealing of CdTe/GaAs Epilayers

8.1.4.1 *Ex-situ* Annealing

Before Tatarenko et al. published their work on the sublimation rates of (001) and (111)B CdTe, some annealing of CdTe epilayers was undertaken by the present author. A 4μm (001)CdTe/GaAs epilayer was cleaved into several pieces and each was sealed in a quartz ampoule at 10^{-5}mbar after flushing with Ar gas. The samples were annealed for 2 hours at temperatures of 550, 450, 400 and 350°C with the end of the ampoule containing the sample positioned away from the centre of the furnace. After calibration of the furnace temperature gradient, the difference in temperature between the two ends of the ampoule was estimated to be 5°C; the annealing temperatures quoted are those for the centre of the furnace. It was hoped that, by placing the sample in the cooler region of the furnace, sublimation would be minimised.

For annealing at all temperatures in the range 550°C-350°C, the surface of the epitaxial layers were observed to have been degraded. Figure 8.1 shows the worst example of surface degradation, after annealing for 2 hours at 550°C, where all of the layer has been lost in some regions. The micrograph was taken in backscattered (primary) electron mode which enhances the contrast between materials of different average atomic mass. In figure 8.1 the GaAs substrate can clearly be seen where all of the CdTe epilayer has sublimed

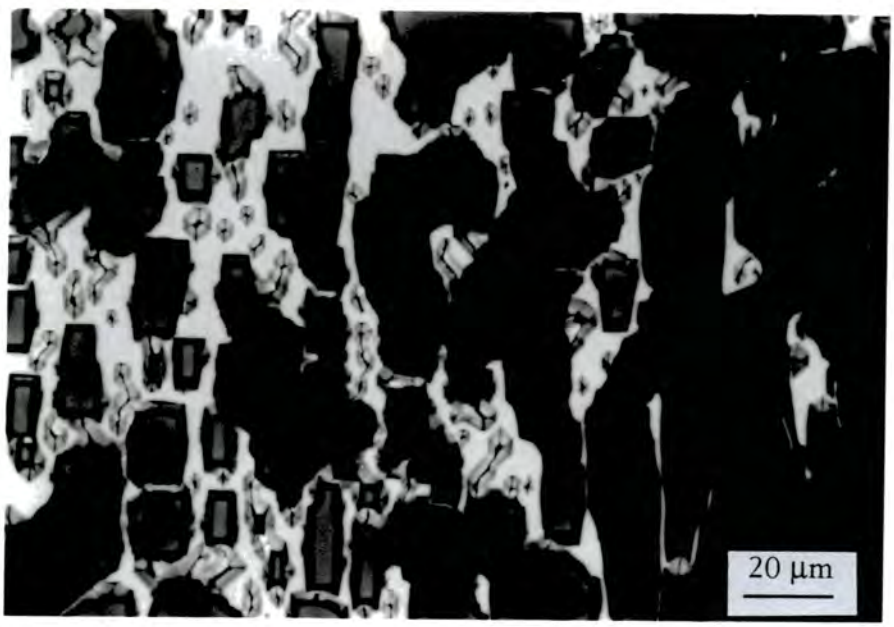

Figure 8.1 SEM micrograph (Backscattered mode) of a 4µm (001)CdTe/GaAs epilayer annealed for 2 hours at 550°C. The layer was sealed in a quartz ampoule at 10^{-5}mbar after flushing with Ar gas.

8.1.4.2 In-situ Annealing

In-situ annealing was carried out in an MOVPE reactor under a Cd overpressure maintained by a constant flow of Me_2Cd over the layer; the layer was maintained above the pyrolysis temperature for Me_2Cd. The substrate preparation and growth conditions were as given in Section 3.3.3.2. A Cd overpressure of 0.655 Torr (assuming complete breakdown of Me_2Cd at the anneal temperature) was maintained above the epilayer throughout heating, annealing and cooling back to the growth temperature. Two annealing temperatures were investigated, 420°C and 470°C with annealing times of 60 minutes and 20 minutes respectively. After annealing, the substrate was cooled to the growth temperature of 370°C and a further 9μm of CdTe was grown.

The quality of the layers was assessed by HRXRD with great care taken to record rocking curves for the same substrate position on the susceptor. This was particularly important since problems with growth uniformity were being experienced. Despite this it was thought that any improvement in structural quality would be quantifiable. The HRXRD experimental details are the same as those given in Section 6.3 but with a beam size of 0.5mmx1mm.

No visible degradation of either layer was observed; the surface morphology appeared the same when observed by Normarski interference microscopy for the unannealed and annealed layers.

No significant change in HRXRD FWHM was measured for either of the annealed layers (table 8.3). The possible reasons for this and suggestions for future annealing investigations are discussed in the following section. It is encouraging, however, that no surface degradation was observed even at 470°C when a sublimation rate of 8.8 $\mu m hr^{-1}$ is expected for no Cd overpressure[12].

Anneal temperature/°C	Anneal time/minutes	HRXRD FWHM /arcseconds
no anneal		174
420	60	186
470	20	161

Table 8.3 HRXRD FWHM for unannealed and annealed CdTe layers. The rocking curves were recorded for the same substrate position on the susceptor.

8.1.5 Discussion

Despite the apparent success of annealing GaAs/Si, the same procedure applied to CdTe/GaAs gave no observable improvement in structural quality. All of the GaAs/Si annealing was carried out at higher temperatures than were used for CdTe/GaAs (compare 850°C and 470°C). The cohesive energy per bond[13] is 1.63eV for GaAs and 1.03eV for CdTe, the melting points of GaAs[14] and CdTe[7] are 1238°C and 1090°C respectively. From these differences it is reasonable to suppose that dislocation rearrangement may occur at lower temperatures for CdTe than for GaAs but that annealing temperatures greater than 470°C may be required.

A major difference between GaAs/Si and CdTe/GaAs is the effect of the thermal expansion coefficients of the layer and substrate on misfit at growth and room temperatures. The linear expansion coefficients of Si[14], GaAs[14] and CdTe[15] at room temperature are $2.6\times10^{-6}°C^{-1}$, $6.86\times10^{-6}°C^{-1}$ and $4.5\times10^{-6}°C^{-1}$ respectively. The maximum misfit of GaAs/Si occurs at the higher of the growth or annealing temperatures since the linear expansion coefficient of GaAs is greater than that of Si and the layer is in compression. For CdTe/GaAs, the greatest misfit is at room temperature since CdTe expands less than GaAs on heating and the layer is in compression. With hindsight, it seems unlikely that an improvement in structural quality will occur for annealed CdTe/GaAs unless the layer has been cooled to room temperature first to allow for complete relaxation at the maximum misfit. Cooling of CdTe

epilayers prior to annealing is an obvious next step in determining whether epitaxial CdTe/GaAs can be structurally improved by annealing.

It may be necessary to increase the annealing temperature above those temperatures used in the present study, this could pose further problems since at temperatures above about 500°C, As is lost from GaAs. This may not be a problem if sufficiently thick CdTe epilayers are investigated, since CdTe would be deposited on the edges of the substrate, preventing loss of As.

8.1.6 Conclusions

In-situ and *ex-situ* annealing of CdTe/GaAs epilayers was unsuccessful at producing major improvements in structural quality. Severe degradation of CdTe epilayers was observed for *ex-situ* annealing in an Ar ambient but not for *in-situ* annealing with a Cd overpressure. It is thought that, owing to CdTe/GaAs having a higher misfit at room temperature than during growth, layers should be cooled prior to annealing to ensure complete relaxation. It is anticipated that annealing at temperatures above 500°C may introduce further problems, with As being lost from the GaAs substrate.

8.2 Study of $Cd_xHg_{(1-x)}Te$ on CdTe/GaAs Hybrid Substrates

8.2.1 Introduction

As was outlined in Chapter 1, $Cd_xHg_{(1-x)}Te$ (CMT) is an important semiconducting material for infrared devices. All of the investigations presented in earlier chapters were ultimately aimed at improving the structural quality of CMT which is grown on GaAs with (001)CdTe buffer layers. (001)CdTe/GaAs is not the only buffer structure used for the growth of CMT, therefore a brief review of published data on the structural quality of CMT on various buffer structures and using different growth methods is given in Section 8.2.2. The effect of CdTe buffer layer thickness on the structural quality of CMT grown by the interdiffused multilayer process (IMP) is briefly investigated in Section 8.2.3 and is compared to findings published by other workers.

The aim of Section 8.2 is to bring the work of Chapters 5, 6 and 7 to focus on the original aim of the investigation of CdTe/GaAs; that is to improve the structural quality of CMT epilayers.

8.2.2 Review of the Structural Quality of Epitaxial $Cd_xHg_{(1-x)}Te$

A common method of routine structural characterisation is the measurement of HRXRD FWHM. The narrowing of the double crystal rocking curve indicates that there is a reduction in mosaic spread and/or a decrease in lattice dilatations. Keir et al.[16] have studied CMT/CdTe/GaAs and found that HRXRD rocking curve broadening in CMT is dominated by mosaic spread. They studied CMT layers grown by IMP[17] which is known to give layers with good compositional uniformity[18]. In the following study it will be assumed that HRXRD rocking curve broadening indicates worsening structural quality and that broadening due to lattice dilatations can be ignored. In tables 8.4 and 8.5, the effects of substrate material, buffer layer structure, lattice mismatch and growth technique on HRXRD FWHM of CMT layers are presented. The data has been taken from published literature and the

references are given in the tables. The methods of CMT growth known as IMP (interdiffused multilayer process) and DAG (direct alloy growth), referred to in the tables, were described in Section 3.3.2.

Gouws et al.[19] have recorded CMT HRXRD rocking curves for four different buffer layers on GaAs substrates; the details are given in table 8.4. They found that CdTe buffer layers on GaAs with a thin ZnTe layer to force the (001) orientation gave the narrowest HRXRD rocking curve for a 12μm CMT layer grown on the buffer layers. $Cd_{0.22}Hg_{0.78}Te$ on $Cd_{0.96}Zn_{0.04}Te$ did not give a better layer despite being lattice matched.

CMT Orientation	Buffer layer Structure	Total buffer thickness /μm	FWHM buffer /arcseconds	FWHM of 12μm CMT layer on buffer
$(\bar{1}\bar{1}\bar{1})$B	CdTe/GaAs	3	350-400	110-145
(001)	CdTe/ZnTe/GaAs	3.05	200-250	90-120
(001)	CdTe/graded (CdZn)Te/GaAs	3.5-3.9	500-650	170-200
(001)	$Cd_{0.96}Zn_{0.04}Te$/ ZnTe/GaAs	3.05	250-300	85-110

Table 8.4 The effect of buffer layer structure on the HRXRD FWHM of a 12μm CMT layer grown by IMP MOVPE. The CMT composition was 22% Cd. The data is taken from work published by Gouws et al.[19].

In table 8.5 the effect of growing CMT on a variety of different substrates is presented; the data has been published by Irvine et al.[20], Ghandi et al.[21] and Sugiyama et al.[22]. It is not advisable to compare exact values of HRXRD FWHM published by different research groups since the growth and characterisation conditions employed will affect the FWHM recorded. It is better to compare data by the same authors to determine the effect of changing growth conditions.

Layer structure	$Cd_xHg_{(1-x)}Te$ x value	Growth technique	Buffer thickness/ μm	$Cd_xHg_{(1-x)}Te$ thickness/ μm	FWHM / arcseconds	Reference
CMT/CdTe	0.22	MOVPE (IMP)	N/A	12	67-135	Irvine et al. ref 20
CMT/CdTe/GaAs	0.235	MOVPE (IMP)	3	12	< 84, best 55	
CMT/CdTe	0.18	MOVPE (DAG)	N/A	12	151±15	Ghandi et al. ref 21
CMT/$CdSe_{0.04}Te_{0.96}$	0.182	MOVPE (DAG)	N/A	12	47±21	
CMT/CdTe/SLS*/CdTe /SLS$/CdTe/GaAs	0.28	buffer-HWE CMT-MOVPE	7.4	8	124	Sugiyama et al. ref 22
CMT/CdTe/GaAs	0.28		4.3	8	185	

Table 8.5 Comparison of CMT FWHM for different substrates and misfits. All layers are (001) oriented. Sugiyama et al. did not specify whether their CMT layers were grown by IMP or DAG.

* SLS consists of 5x{120nm CdTe, 120nm $Cd_{0.97}Zn_{0.03}Te$}

$ SLS consists of 8x{30nm CdTe, 210nm $Cd_{0.97}Zn_{0.03}Te$}

Irvine et al.[20] have shown that high quality CMT can be grown on (001)CdTe buffered GaAs substrates. Some of the layers were of better quality than those grown directly onto CdTe substrates, this suggests that lattice mismatch is not the only factor governing dislocation density in CMT layers. Ghandi et al.[21] compared the growth of CMT on CdTe and $CdTe_{0.96}Se_{0.04}$ substrates (Cd(TeSe) is lattice matched to $Cd_{0.2}Hg_{0.8}Te$) and found that the lattice matched substrate gave a superior quality layer. They concluded that although the initial quality of the substrate was important in determining the quality of CMT grown on it, the most important factor in reducing HRXRD FWHM was lattice mismatch.

Buffer layers including strained layer superlattices (SLSs) were employed by Sugiyama et al.[22] to decrease the dislocation density in CMT layers, (table 8.5). The CdTe/(CdZn)Te SLSs blocked the propagation of threading dislocations by bending them at the SLS interfaces. It should be noticed that the buffer layer thickness decreases from 7.4 to 4.3μm for CMT layers grown with and without SLSs; this is not mentioned explicitly by the authors but is assumed in the absence of further detail in the published text. It is estimated from data presented in Section 6.3 that the threading dislocation density of a CdTe buffer layer will decrease by a factor of 2 on increasing its thickness from 4.3 to 7.4μm. This compares to the decrease by a factor of 2.5 which is reported by Sugiyama et al.

Edwall et al.[23] have observed a twofold increase in FWHM for IMP grown $(\bar{1}\bar{1}\bar{1})$B CMT compared to DAG grown, the substrates used being (0001) sapphire. Poorer structural quality IMP layers compared to DAG have also been reported by Shigenaka[18] for CMT grown on (111)B (CdZn)Te substrates. However better compositional uniformity has been reported by both authors named above for IMP grown CMT and by Hallam et al.[24,25]for IMP (HgMn)Te.

The thickness dependence of HRXRD FWHM within a 15μm CMT layer on GaAs with a 3μm CdTe buffer layer has been studied by Irvine et al.[20]. They etched the layer and remeasured the X-ray rocking curve. The FWHM

remained low until close to the interface, whereupon it increased rapidly. For a CdTe layer of equal thickness, the FWHM increased gradually towards the CdTe/GaAs interface. They had shown earlier[16] that the HRXRD FWHM gives a measure of mosaic spread and hence dislocation density[26]. The rapid decrease in FWHM for small distances from the CMT/CdTe interface corresponds, therefore, to a rapid decrease in dislocation density in the same region. Irvine et al.[20] suggested that this was due to the bending over of threading dislocations as a change in lattice parameter occurs at the interface.

The overwhelming weight of published data shows that for any CdTe buffer layer thickness, the dislocation density in CMT grown on the CdTe buffer will be less than that of the buffer (this will be discussed further in the following section). The only exception found in the literature was by Peng et al.[27] who reported an increase in HRXRD FWHM from 240" to 450" on going from a 2-3μm CdTe buffer to a 4μm CMT layer.

8.2.3 Results and Discussion

CMT layers were grown on (001)CdTe/GaAs hybrid substrates using IMP according to the conditions given in Section 3.3.3.3. A cross-section TEM micrograph of the CMT/CdTe interface of one of these layers is shown in figure 8.2. Threading dislocations are bent into directions parallel to the interface and were found to have Burgers vectors inclined to the interface in <110> directions. The dislocations lying parallel to the interface are all of 60° type, and are the same as those described in table 7.6. The dislocations are not all confined to a narrow region, but rather are distributed over a thickness of approximately 0.5μm. This is probably due to the diffusion of Hg into the buffer layer leading to a compositional gradient. It is unlikely that the distribution of dislocations is caused by the incomplete interdiffusion of the HgTe and CdTe layers since the region nearest the interface has been maintained at the growth temperature for the longest time, and is expected to be uniform in composition with depth. Yoshikawa[28] has observed a similar effect at CMT/CdTe heterojunctions with interdiffusion occurring over

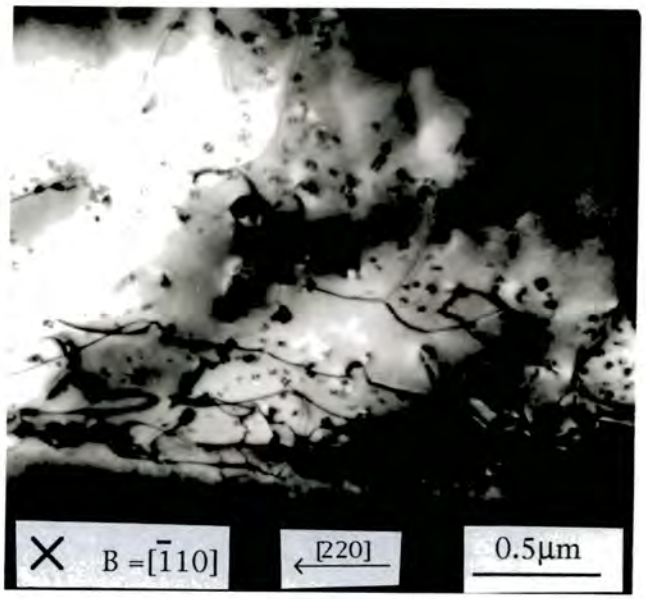

Figure 8.2 XTEM micrograph of the CMT/CdTe interface of a CMT epilayer grown on (001)CdTe buffered GaAs. The dislocations lying parallel to the interface are of 60° type. The electron beam direction is [$\bar{1}$10] into the plane of the paper.

nearly 4μm at 500°C. Tunnicliffe et al.[17], who developed the IMP process, found interdiffusion at the CMT/CdTe interface occurring over approximately 2μm at 410°C. Interdiffusion has also been shown to be responsible for the spreading out of interfacial dislocation by Watson[29] in LPE grown CMT on $(\bar{1}\bar{1}\bar{1})$(CdZn)Te substrates.

Two CMT/CdTe/GaAs epilayers were grown with the growth conditions given in Section 3.3.3.3. Buffer thicknesses of 6.5 and 11μm were used. The details of composition, layer thickness and etch pit density (EPD) are given in table 8.6 along with the HRXRD FWHM (which were recorded using the same experimental arrangement as in Section 6.3 but using a beam size of 0.5mmx1mm).

CdTe thickness /μm	CMT thickness /μm	$Cd_xHg_{(1-x)}Te$ x value	HRXRD FWHM /arcseconds	CMT EPD /10^7cm^{-2} *
6.5	12.2	0.23	137	2.4
11	11	0.29	124	2.3

Table 8.6 The effect of buffer layer thickness on the FWHM and EPD of IMP grown CMT on CdTe buffered GaAs.

From Section 6.3 it is estimated that the difference in FWHM between a 6.5 and 11μm CdTe buffer layer is 100". It seems that this improvement is not replicated to the same degree when a CMT layer is grown on the buffer. As well as a difference in buffer thickness, there is also a difference in CMT composition between the two layers described in table 8.6. The lattice parameters of CdTe and HgTe are 6.481Å and 6.461Å respectively[30], giving a misfit of 3.1% between the CdTe buffer and the first HgTe IMP layer at room temperature, the HgTe layer being in tension. The thermal expansion coefficients of CdTe and HgTe are $4.9x10^{-6}°C^{-1}$ and $4x10^{-6}°C^{-1}$ respectively[31]

* Etch pit densities were measured by Mrs A. B. Smith, Defence Research Agency, Malvern.

leading to a higher misfit at the growth temperature than at room temperature. Basson and Booyens[32] have estimated the critical thickness of HgTe on CdTe to be approximately 0.05μm between 300 and 400°C using the equation for critical thickness by Matthews and Blakeslee[33]. The CMT layer with 0.23% Cd has HgTe IMP layers of 0.109μm thickness compared with 0.091μm for the layer with 0.29% Cd. Both of these HgTe IMP layers are thicker than that required for the bending over of threading dislocations into misfit orientations, as proposed by Matthews and Blakeslee[33]. It is possible that more threading dislocations are bent over by the thicker HgTe layer than by the thinner layer, while no new misfit dislocations are introduced by half-loop formation in either case. Since the bending over of threading dislocations has a greater effect in reducing dislocation density than simply increasing the buffer thickness, the decrease in FWHM and EPD expected when increasing the buffer thickness from 6.5 to 11μm may be counteracted by the increased dislocation reduction occurring at the interface of the 6.5μm CdTe/$Cd_{0.23}Hg_{0.77}Te$ layer.

Nishino et al.[34] have undertaken a very extensive investigation of the effect of CdTe buffer layer thickness on the EPD of DAG grown CMT on CdTe buffered GaAs. There was no difference in CMT composition because all CMT layers were deposited at the same time onto previously grown CdTe buffer layers of different thicknesses. They grew CMT layers 2, 6, 10 and 14μm thick onto 4, 8 and 18μm thick CdTe buffer layers. They also etched back and remeasured thick CMT layers which had been grown on buffer layers of different thickness. The findings are in accordance with the present work, that is that dislocation density decreases with thickness. Their data also agrees with workers who propose that a lower dislocation density buffer layer will lead to a less dislocated CMT layer. Little improvement in structural quality was observed on increasing buffer layer thickness beyond 8μm; also from the trend observed, little improvement would have been measured on increasing the buffer thickness from 6 to 11μm as was indeed the case in the present study.

8.2.4 Conclusions

A sharp reduction in threading dislocation density occurs at the CMT/CdTe interface which results in CMT epilayers having narrower HRXRD rocking curves than the CdTe buffer layers on which they were grown. The reduction is caused by the bending over of threading dislocations when the first HgTe IMP layer is deposited on the CdTe buffer. The threading dislocations are bent into orientations parallel to the interface and were found to be of 60° type.

Very little reduction in CMT/CdTe/GaAs HRXRD FWHM was observed on increasing the CdTe buffer layer thickness from 6.5 to 11μm. The small reduction observed was less than might be expected from the difference in FWHM of the buffer layers alone, and may be due to the different compositions of CMT grown on the two buffer layers.

From the present work and that by Nishino et al.[34] it seems that another method of dislocation reduction needs to be found in order to decrease MOVPE CMT dislocation density below $10^6 cm^{-2}$. Sugiyama et al.[22] have reported that a reduction in threading dislocation density by a factor of 2.5 has been achieved by the use of SLSs, however a reduction by a factor of 2 is anticipated simply by increasing the CdTe thickness by the thickness of the SLSs (predicted from data presented in Section 6.3).

REFERENCES FOR CHAPTER 8

1. Kroemer H., Liu T. Y. and Petroff P. M., *J. Cryst. Growth* **95**, (1989), 96.

2. Yamaguchi M., Yamamoto A., Tachikawa M., Itoh Y. and Sugo M., *Appl. Phys. Lett.* **53(23)**, (1988), 2293.

3. Ayers J. E., Schowalter L. J. and Ghandhi S. K., *J. Cryst. Growth* **125**, (1992), 329.

4. Lee J. W., Shichijo H., Tsai H. L. and Matyi R. J., *Appl. Phys. Lett.* **50(1)**, (1987), 31.

5. Takagi Y., Yonezu H., Hachiya Y. and Pak K., *Jpn. J. Appl. Phys.* **33**, (1994), 3368.

6. Deppe D. G., Holonyak N., Hsieh Jr K. C., Nam D. W., Plano W. E., Matyi R. J. and Shichijo H., *Appl. Phys. Lett.* **52(21)**, (1988), 1812.

7. de Nobel D., *Philips Res. Reports* **14**, (1959), 361.

8. Goldfinger P. and Jennehomme M., *Trans. Faraday Soc.* **59(492)**, (1963), 2851.

9. Vydyanath H. R., Ellsworth J., Kennedy J. J., Dean B., Johnson C. J., Neugebauer G. T., Sepich J. and Liao P.-K., *J. Vac. Sci. Technol. B* **10(4)**, (1992), 1476.

10. Loginov Y. Y., Brown P. D., Durose K., Thompson N., Alnajjar A. A., Brinkman A. W. and Woods J., *J. Cryst. Growth* **117**, (1992), 259.

11. Arias J. M., Zandian M., Shin S. H., McLevige W. V., Pasko J. G. and DeWames R. E., *J. Vac. Sci. Technol. B* **9(3)**, (1991), 1646.

12. Tatarenko S., Daudin B. and Brun D., *Appl. Phys. Lett.* **65(6)**, (1994), 734.

13. Harrison W. A., *Electronic Structure and the Properties of Solids*, San Francisco: Freeman, 1980, Section beginning page 173.

14. Sze S. M., *Physics of Semiconductor Devices*, (2nd edition), Wiley, 1981, pp. 850.

15. Cleveland Crystals Incorporated, *Internal Report*, (Ohio USA, 1984).

16. Keir A. M., Barnett S. J., Giess J., Walsh T. D. and Astles M. G., *Appl. Surf. Sci.* **50**, (1991), 103.

17. Tunnicliffe J., Irvine S. J. C., Dosser O. D. and Mullin J. B., *J. Cryst. Growth* **68**, (1984), 245.

18. Shigenaka K., Uemoto T., Sugiura L., Ichizono K. and Hirahara K., *J. Cryst. Growth* **117**, (1992), 37.

19. Gouws G. J., Muller R. J. and Bowden R. S., *J. Cryst. Growth* **130**, (1993), 209.

20. Irvine S. J. C., Gough J. S., Giess J., Gibbs M. J., Royle A., Taylor C. A., Brown G. T., Keir A. M. and Mullin J. B., *J. Vac. Sci. Technol. A* **7(2)**, (1989), 285.

21. Ghandhi S. K., Bhat I. B. and Fardi H., *Appl. Phys. Lett.* **52**, (1988), 392.

22. Sugiyama I., Hobbs A., Saito T., Ueda O., Shinohara K. and Takigawa H., *J. Cryst. Growth* **117**, (1992), 161.

23. Edwall D. D., Gertner E. R. and Bubulac L. O., *J. Cryst. Growth* **86**, (1988), 240.

24. Hallam T. D., Oktik S., Funaki M., Moore C., Brinkman A. W., Durose K. and Tanner B. K., *J. Cryst. Growth* **146**, (1995), 604.

25. Hallam T. D., Personal Communication, (1995).

26. Gay P., Hirsch P. B. and Kelly A., *Acta Metallurgica* **1**, (1953), 315.

27. Peng R. W., Ding Y. Q. and Wang G. Y., *J. Cryst. Growth* **103**, (1990), 380.

28. Yoshikawa M., *J. Appl. Phys.* **63(5)**, (1988), 1533.

29. Watson C. C. R., Ph. D Thesis, *Structural Defects in CdTe and Related Materials*, University of Durham (1993).

30. ASTM Powder Diffraction File

31. Madelung O., Ed., *Semiconductors: Physics of II-VI and I-VII Compounds*, Landolt-Börnstein, New Series, **Volume 17b**, (Springer, Berlin, 1982).

32. Basson J. H. and Booyens H., *Phys. Stat. Sol.* **80**, (1983), 663.

33. Matthews J. W. and Blakeslee A. E., *J. Cryst. Growth* **27**, (1974), 118.

34. Nishino H., Murakami S., Saito T., Nishijima Y. and Takigawa H., *J. Elec. Mater.* **24(5)**, (1995), 533.

CHAPTER 9

Conclusions

The aim of this thesis was to investigate the threading dislocations in thick (>3μm) CdTe buffer layers grown on (001)GaAs by MOVPE, with the aim of finding ways to reduce the threading dislocation density in CMT grown on top of them. A thorough experimental study of CdTe/GaAs using X-ray diffraction and electron microscopy has been presented, the conclusions of which are summarised later in this chapter.

An important aspect of work with CdTe/GaAs is that the layer grows by a 3-D island mechanism. The commonly accepted mechanisms for the formation of misfit dislocations, glide of threading dislocations and half-loop nucleation, are not valid for 3-D growth. Nucleation of misfit dislocations at island edges is thought[1] to occur for CdTe/GaAs, with threading dislocations being formed when islands coalesce and by half-loop nucleation once a complete layer has formed.

Although the MOVPE growth of II-VI Te based materials is a mature technology, a number of problems were encountered. Thickness non-uniformity across wafers was observed for all the layers investigated in this work; susceptor temperature gradient non-uniform carrier gas flow and external cooling effects were all found to cause variations in thickness with position on the susceptor[2,3]. Improvements in the quality of CdTe epitaxy is ongoing. For example, a significant development was reported recently by Giess et al.[4] who have developed a final substrate treatment which they have shown to reduce hillock density on (001) CMT/CdTe/GaAs to less than $10cm^{-2}$.

A significant portion of this thesis has addressed the distribution of threading dislocations with depth in a thick layer and the change in dislocation density as a layer thickens. Several models which attempt to describe dislocation density reduction or strain relaxation with increasing

layer thickness were reviewed in Chapter 5, and a new geometrical model was developed. The approximate relationships between dislocation density (or strain) and thickness for these models are summarised in table 9.1. Several of the models approximate to the same relationship between dislocation density and layer thickness, even though they are based on different physical principles. This demonstrates that although a particular set of data may be described accurately by a given equation, this does not in itself mean that the mechanism from which the expression was derived is correct.

Model reference	Approximate relationship	Section number in thesis
Dunstan[5]	$\varepsilon \alpha \frac{1}{t}$	5.2.1
Tatsuoka[6,7]	$\varepsilon \alpha (1 - C_1)^{n-1}$	5.2.2
Durose and Tatsuoka[8]	$D \approx C_1(1 - C_2)^n + C_3$	5.3.1
Ayers[9]	$D \alpha \frac{1}{t}$	5.3.2
Kroemer[10]	$D \alpha \frac{1}{t}$	5.3.3
Tachikawa and Yamaguchi[11]	$D = \frac{1}{\left(\frac{1}{C_1} + C_2\right) \exp(C_3 t) - C_2}$	5.3.3
Present work	$D \alpha \frac{1}{t}$	5.4.2

Table 9.1 Summary of the approximate relationships between dislocation density, D, strain, ε, thickness, t and number of monolayers, n for models reviewed in Chapter 5. C_n are constants.

Dislocation density and strain distributions as a function of layer thickness published by other authors, covering the misfit range 0.23-14.6%, were compared to the models summarised in table 9.1. For high misfit systems, the models by Tatsuoka[6,7], Durose and Tatsuoka[8] and by Tachikawa and Yamaguchi[11] agreed most closely with literature data. The latter two models

were found to describe the reduction in threading dislocation density with increasing layer thickness most accurately for the CdTe/GaAs and ZnTe/GaAs epilayers studied in Chapter 6. Threading dislocation densities were estimated from HRXRD FWHM according to the relationship proposed by Gay, Hirsch and Kelly[12].

A new model which attempts to describe the dislocation density reduction which occurs on increasing thickness was presented in Section 5.4.2. The model assumes that the threading dislocations are static and all of the same character. They may intersect and react as a layer thickens, thus reducing the threading dislocation density. The expression derived from this treatment approximates to an inverse relationship between dislocation density and layer thickness.

Triple axis X-ray diffraction of CdTe/GaAs epilayers confirmed that the major contribution to HRXRD rocking curve broadening was mosaic spread. Large subgrains tilted significantly away from the mean position were found to have individual mosaic spreads comparable to that of the rest of the layer. HRXRD was performed as a function of layer thickness on CdTe/GaAs and ZnTe/GaAs epilayers and showed that mosaic spread, and by implication dislocation density[12], decreased rapidly in the region close to the interface and the rate of reduction slowed with increasing thickness. From the study of CdTe/GaAs, an optimum buffer layer thickness of 8μm is recommended for subsequent growth of CMT. As a result of this study, 8μm buffers are now routinely used by the team at D.R.A, Malvern.

HRXRD is not surface sensitive, the depth to which the beam penetrates into the layer depending on the X-ray wavelength and the layer material. It was demonstrated in Section 6.4 using synchrotron radiation, that rocking curve measurement as a function of wavelength and extrapolation to infinite absorption, enables the FWHM representative of the surface of an epilayer to be determined.

The interfacial structure of CdTe/GaAs epilayers has been studied by a number of workers, see for example references 1,13-15. These references

report that misfit dislocations are of two types, 60° and 90°. In this work, CdTe/GaAs epilayers were studied by XTEM in two orthogonal <110> projections. A dense tangle of dislocations which could not be resolved was observed close to the interface, with the dislocation density decreasing further from the interface. Diffraction contrast experiments indicated that a high proportion of threading dislocations were of 30° type, although this may be an artefact of the cross-section chosen, since 60° dislocations with <011> line directions are only visible in <110> projection for a short distance, making them difficult to observe. A detailed comparison of the Burgers vector components of 30°, 60° and screw type threading dislocations was presented in table 7.7. It was found that all three types of threading dislocation have a Burgers vector tilt component of magnitude ($a_0/2$). This is the value of Burgers vector which should be used when dislocation density is calculated from HRXRD FWHM using the expression by Gay, Hirsch and Kelly[12].

A further aim of the study was to propose and implement new methods of threading dislocation density reduction. Annealing of CdTe/GaAs epilayers, both *in-situ* and *ex-situ* was reported in Section 8.1. These studies demonstrated that CdTe sublimes disproportionately at relatively low temperature and that this can be prevented by *in-situ* annealing under Me_2Cd flow. Two layers were interrupted during growth, annealed, and growth resumed to a predetermined thickness. No reduction in HRXRD FWHM was recorded for layers annealed at 420 or 470°C compared to a standard layer which had not been annealed. Future studies of the annealing of CdTe/GaAs may involve temperatures above the 470°C employed in the present study and cooling down to room temperature prior to annealing.

The latter procedure may result in further improvements on account of the difference in the thermal expansion coefficients of CdTe and GaAs which are such that CdTe/GaAs has greatest misfit at room temperature. ZnTe/GaAs and GaAs/Si systems are most highly mismatched at the growth temperature, with a decrease in misfit occurring on cool down. Dislocation density decreased more rapidly in ZnTe/GaAs than in CdTe/GaAs, as reported in Section 6.6.3. It is thought that dislocations of opposite Burgers vector to

those formed during growth may be nucleated in ZnTe/GaAs during cooling, and may annihilate some of those dislocations already present. It is possible that any reduction in dislocation density achievable by annealing CdTe/GaAs will be less than that observed for GaAs/Si, simply because additional dislocations of the same sign as those introduced during growth may be formed during cooling.

Increasing the CdTe buffer layer thickness from 6.5 to 11μm did not noticeably improve the structural quality of CMT grown on it. This is thought to be due to the different compositions of CMT which were grown. However, independent work by Nishino et al.[16] has demonstrated a reduction in EPD in CMT layers grown on progressively thicker CdTe buffer layers.

The aim for the future of CMT epitaxy is to decrease the threading dislocation density in CMT layers to below $2x10^5 cm^{-2}$, since minority carrier lifetime is not dominated by dislocations below this density[17]. The most promising techniques for achieving this objective would appear to be those methods which have proved effective for reducing the dislocation densities of GaAs/Si epilayers, i.e. the use of substrate offcut, annealing and SLSs.

It was pointed out in Chapter 2, that substrate offcut can enhance the formation of efficient 90° type misfit dislocations and increase the probability of dislocation alignment when islands coalesce. The optimum offcut for CdTe/GaAs was calculated to be 5.1° away from [001] towards [010]. To date the present author has been unable to find any reference to such a large offcut being used for CMT/CdTe/GaAs epitaxy.

There are numerous literature reports (see summary table 8.1) that annealing of GaAs/Si reduces threading dislocation density, provided the annealing temperature is sufficiently high enough. It is likely that annealing of CdTe/GaAs will be less successful than for GaAs/Si, simply because additional dislocations may be introduced during cooling. To the author's knowledge, the greatest reduction in dislocation density by annealing of GaAs/Si was reported by Yamaguchi et al.[18]. They reported a reduction by a factor of 33 for 13 annealing steps. If an etch pit density

(EPD) reduction of this magnitude were to be achieved for a CMT layer grown on a CdTe/GaAs buffer, then the EPD of the CMT layers investigated in Chapter 8 would still be of the order of $7x10^5cm^{-2}$ (based upon the EPD of $2.3x10^7cm^{-2}$ for an unannealed layer).

Strained layer superlattices have been reported to reduce the dislocation density in CdTe buffer layers. In Chapter 2, the success of SLSs for subsequent growth of CMT was reviewed (table 2.1). The greatest decrease in dislocation density was reported by Petruzzello et al.[19] who observed an order of magnitude reduction by a (HgZn)Te/CdTe SLS. This is a small decrease compared to those reported for annealing of GaAs/Si and suggests that SLSs must be used in conjunction with other methods if the target of $2x10^5cm^{-2}$ is to be reached.

The most consistent reduction in threading dislocation density reported for CMT/CdTe/GaAs is when CMT is grown on CdTe buffer layers. For example, Sugiyama et al.[20] reported a factor of 2.5 reduction in the dislocation density of CdTe buffer layers with and without SLSs, but observed a reduction by a factor of 87 simply by growing 8μm of CMT on the buffer layer.

Threading dislocations and their distribution in CdTe buffer layers grown on GaAs by MOVPE are understood better as a result of this thesis. There is still considerable progress to be made before CMT layers with dislocation densities below $2x10^5cm^{-2}$ can be achieved. The very different thermal expansion coefficients of the substrate, GaAs and the epilayer materials CdTe and HgTe may be a limiting factor in all attempts to reduce dislocation density in CMT/CdTe/GaAs epilayers. Whatever growth strategies might be employed, the layers are likely to deteriorate on cooling.

REFERENCE FOR CHAPTER 9

1. Eaglesham D. J., Aindow M. and Pond R. C., *Mat. Res. Soc. Symp. Proc.* **116**, (1988), 267.

2. Hallam T. D., Oktik S., Funaki M., Moore C., Brinkman A. W., Durose K. and Tanner B. K., *J. Cryst. Growth* **146**, (1995), 604.

3. Oktik S., Personal Communication, (1995).

4. Giess J., Hails J. E., Graham A., Blackmore G., Houlton M. R., Newey J., Young M. L., Astles M. G., Bell W. and Cole-Hamilton D. J., *J. Elec. Mat.* **24(9)**, (1995), in press.

5. Dunstan D. J., Young S. and Dixon R. H., *J. Appl. Phys.* **70(6)**, (1991), 3038.

6. Tatsuoka H., Kuwabara H., Nakanishi Y. and Fujiyasu H., *Thin Solid Films* **201**, (1991), 59.

7. Tatsuoka H., Kuwabara H., Nakanishi Y. and Fujiyasu H., *J. Cryst. Growth* **117**, (1992), 554.

8. Durose K. and Tatsuoka H., *Inst. Phys. Conf. Ser.* **134**, Section 9, (1993), 581.

9. Ayers J. E., Schowalter L. J. and Ghandhi S. K., *Mat. Res. Soc. Symp. Proc.* **209**, (1991), 661.

10. Kroemer H., Liu T. Y. and Petroff P. M., *J. Cryst. Growth* **95**, (1989), 96.

11. Tachikawa M. and Yamaguchi M., *Appl. Phys. Lett.* **56(5)**, (1990), 484.

12. Gay P., Hirsch P. B. and Kelly A., *Acta Metallurgica* **1**, (1953), 315.

13. Ponce F. A., Anderson G. B. and Ballingall J. M., *Surf. Sci.* **168**, (1986), 564.

14. Petruzzello J., Olego D., Ghandhi S. K., Tasker N. R. and Bhat I. B., *Appl. Phys. Lett.* **50**, (1987), 1423.

15. Cheng T. T., Aindow M., Jones I. P., Hails J. E., Williams D. J. and Astles M. G., *J. Cryst. Growth* **135**, (1994), 409.

16. Nishino H., Murakami S., Saito T., Nishijima Y. and Takigawa H., *J. Elec. Mater.* **24(5)**, (1995), 533.

17. Yamamoto T., Miyamoto Y. and Tanikawa K., *J. Cryst. Growth* **72**, (1985), 270.

18. Yamaguchi M., Yamamoto A., Tachikawa M., Itoh Y. and Sugo M., *Appl. Phys. Lett.* **53(23)**, (1988), 2293.

19. Petruzzello J., Olego D., Chu X. and Faurie J. P., *J. Appl. Phys.* 66(7), (1989), 2980.

20. Sugiyama I., Hobbs A., Saito T., Ueda O., Shinohara K. and Takigawa H., *J. Cryst. Growth* 117, (1992), 161.